frontiers | Research Topics

Construction of inorganic-organic hybrid materials and application as antibacterials

Edited by
He Xiaojun, Hong Chen, Runming Wang, Yu Huo and Haibo Wang

Published in
Frontiers in Chemistry

ISSN 1664-8714
ISBN 978-2-8325-2707-8
DOI 10.3389/978-2-8325-2707-8

About Frontiers

Frontiers is more than just an open access publisher of scholarly articles: it is a pioneering approach to the world of academia, radically improving the way scholarly research is managed. The grand vision of Frontiers is a world where all people have an equal opportunity to seek, share and generate knowledge. Frontiers provides immediate and permanent online open access to all its publications, but this alone is not enough to realize our grand goals.

Frontiers journal series

The Frontiers journal series is a multi-tier and interdisciplinary set of open-access, online journals, promising a paradigm shift from the current review, selection and dissemination processes in academic publishing. All Frontiers journals are driven by researchers for researchers; therefore, they constitute a service to the scholarly community. At the same time, the *Frontiers journal series* operates on a revolutionary invention, the tiered publishing system, initially addressing specific communities of scholars, and gradually climbing up to broader public understanding, thus serving the interests of the lay society, too.

Dedication to quality

Each Frontiers article is a landmark of the highest quality, thanks to genuinely collaborative interactions between authors and review editors, who include some of the world's best academicians. Research must be certified by peers before entering a stream of knowledge that may eventually reach the public - and shape society; therefore, Frontiers only applies the most rigorous and unbiased reviews. Frontiers revolutionizes research publishing by freely delivering the most outstanding research, evaluated with no bias from both the academic and social point of view. By applying the most advanced information technologies, Frontiers is catapulting scholarly publishing into a new generation.

What are Frontiers Research Topics?

Frontiers Research Topics are very popular trademarks of the *Frontiers journals series*: they are collections of at least ten articles, all centered on a particular subject. With their unique mix of varied contributions from Original Research to Review Articles, Frontiers Research Topics unify the most influential researchers, the latest key findings and historical advances in a hot research area.

Find out more on how to host your own Frontiers Research Topic or contribute to one as an author by contacting the Frontiers editorial office: frontiersin.org/about/contact

Construction of inorganic-organic hybrid materials and application as antibacterials

Topic editors

He Xiaojun — Wenzhou Medical University, China
Hong Chen — Luoyang Normal University, China
Runming Wang — Tsinghua University, China
Yu Huo — Sichuan Normal University, China
Haibo Wang — University of Zurich, Switzerland

Citation

Xiaojun, H., Chen, H., Wang, R., Huo, Y., Wang, H., eds. (2023). *Construction of inorganic-organic hybrid materials and application as antibacterials*. Lausanne: Frontiers Media SA. doi: 10.3389/978-2-8325-2707-8

Table of contents

04 Silk peptide-hyaluronic acid based nanogels for the enhancement of the topical administration of curcumin
Jiangxiu Niu, Ming Yuan, Yao Liu, Liye Wang, Zigui Tang, Yihan Wang, Yueheng Qi, Yansong Zhang, Huiyuan Ya and Yanli Fan

18 An "on-off-on" fluorescence probe for glyphosate detection based on Cu^{2+} modulated g-C_3N_4 nanosheets
Yingfeng Qin, Ruiqi Huang and Gao-Jie Ye

26 Nanoengineered, magnetically guided drug delivery for tumors: A developmental study
Tieyu Chen, Yanyu Kou, Ruiling Zheng, Hailun Wang and Gang Liang

40 Enhancement of fluorescence and anti-tumor effect of ZnO QDs by La doping
Ruixin Hao, Shanshan Luo, Feiyan Wang, Xinyu Pan, Jing Yao, Jielian Wu, Haihong Fang and Wenkui Li

53 Ruthenium polypyridine complexes with triphenylamine groups as antibacterial agents against *Staphylococcus aureus* with membrane-disruptive mechanism
Li Jiang, Yuanyuan Ma, Yanshi Xiong, Yanhui Tan, Xuemin Duan, Xiangwen Liao and Jintao Wang

69 Gallium ions incorporated silk fibroin hydrogel with antibacterial efficacy for promoting healing of *Pseudomonas aeruginosa*-infected wound
Hui Zheng, Zhida Huang, Tongxin Chen, Yafeng Sun, Shouqing Chen, Guangming Bu and Hongcai Guan

79 Synthesis, biological evaluation, and molecular docking of novel hydroxyzine derivatives as potential AR antagonists
Yueheng Qi, Baoli Xue, Shijin Chen, Wang Wang, Haifeng Zhou and Hong Chen

88 Multifunctional phototheranostic agent ZnO@Ag for anti-infection through photothermal/photodynamic therapy
Enoch Obeng, Jiayao Feng, Danyan Wang, Dongyang Zheng, Bailin Xiang and Jianliang Shen

102 Mo@ZIF-8 nanozyme preparation and its antibacterial property evaluation
Zheng Lian, Chunqing Lu, Jiangqi Zhu, Xining Zhang, Ting Wu, Youlin Xiong, Zhiyi Sun and Rong Yang

110 Peroxidase-like MoS_2/Ag nanosheets with synergistically enhanced NIR-responsive antibacterial activities
Huiying Chen, Xinshuo Zhao, Bingbing Cui, Haohao Cui, Mengyang Zhao, Jun Shi, Jingguo Li and Zhan Zhou

frontiers | Frontiers in Chemistry

TYPE Original Research
PUBLISHED 19 September 2022
DOI 10.3389/fchem.2022.1028372

OPEN ACCESS

EDITED BY
He Xiaojun,
Wenzhou Medical University, China

REVIEWED BY
Lei Xing,
China Pharmaceutical University, China
Yuna Qian,
University of Chinese Academy of Sciences, China

*CORRESPONDENCE
Liye Wang,
liye2009314@163.com
Zigui Tang,
tang_zigui@163.com
Huiyuan Ya,
yahuiyuan@lynu.edu.cn

†These authors have contributed equally to this work

SPECIALTY SECTION
This article was submitted to Medicinal and Pharmaceutical Chemistry, a section of the journal Frontiers in Chemistry

RECEIVED 25 August 2022
ACCEPTED 05 September 2022
PUBLISHED 19 September 2022

CITATION
Niu J, Yuan M, Liu Y, Wang L, Tang Z, Wang Y, Qi Y, Zhang Y, Ya H and Fan Y (2022), Silk peptide-hyaluronic acid based nanogels for the enhancement of the topical administration of curcumin. *Front. Chem.* 10:1028372. doi: 10.3389/fchem.2022.1028372

Silk peptide-hyaluronic acid based nanogels for the enhancement of the topical administration of curcumin

Jiangxiu Niu[1†], Ming Yuan[1†], Yao Liu[1], Liye Wang[1*], Zigui Tang[2*], Yihan Wang[1], Yueheng Qi[1], Yansong Zhang, Huiyuan Ya[1*] and Yanli Fan[1]

[1]College of Food and Drug, Henan Functional Cosmetics Engineering and Technology Research Center, Luoyang Normal University, Luoyang, Henan, China, [2]Department of Pharmacy, Henan Medical College, Zhengzhou, China

The present study focused on the development of Cur-loaded SOHA nanogels (Cur-SHNGs) to enhance the topical administration of Cur. The physiochemical properties of Cur-SHNGs were characterized. Results showed that the morphology of the Cur-SHNGs was spherical, the average size was 171.37 nm with a zeta potential of −13.23 mV. Skin permeation experiments were carried out using the diffusion cell systems. It was found that the skin retention of Cur-SHNGs was significantly improved since it showed the best retention value (0.66 ± 0.17 μg/cm^2). In addition, the hematoxylin and eosin staining showed that the Cur-SHNGs improved transdermal drug delivery by altering the skin microstructure. Fluorescence imaging indicated that Cur-SHNGs could effectively deliver the drug to the deeper layers of the skin. Additionally, Cur-SHNGs showed significant analgesic and anti-inflammatory activity with no skin irritation. Taken together, Cur-SHNGs could be effectively used for the topical delivery of therapeutic drugs.

KEYWORDS

silk peptide, hyaluronic acid, curcumin, nanogels, topical administration

1 Introduction

Topical transdermal drug delivery is one of the important methods for the treatment of local diseases (such as contact dermatitis, psoriasis, etc.) (Dasht Bozorg et al., 2022). For some locally effective drugs, compared with oral and injection routes, topical transdermal administration can reduce the entry of drugs into the blood circulation, thereby reducing systemic adverse reactions (Hanna et al., 2019). Besides, the slow release of topical drugs into the skin tissue can prolong the efficacy time, reduce the number of doses, provide patients with greater comfort (Jiang et al., 2018). Although topical transdermal administration has many advantages, the stratum corneum of the skin limits the transdermal penetration of external agents, resulting in drug waste and poor clinical efficacy (Truong et al., 2022; Uner et al., 2022). Therefore, for topical drug formulations,

the primary goal of formulation development is to maximize drug penetration through the skin while maximizing drug retention in the skin.

To improve the transdermal penetration and the retention of drugs in the skin, various nanocarriers (such as solid lipid nanoparticles, ethosomes, and emulsions) have been developed to improve topical transdermal delivery (Ilic et al., 2021; El-Hashemy, 2022; Niu et al., 2022). Among various types of nanocarriers, nanogels have attracted increasing attention due to their unique advantages, including great colloidal stability, tunable size, large surface area for biological coupling, and porous structure for loading large amounts of drugs (Sivaram et al., 2015; Liu et al., 2021a). In addition, due to the unique structure, nanogels can bind a large amount of water to moisturize and enhance the hydration of the stratum corneum, which is conducive to its role in the field of transdermal drug delivery (Kim et al., 2021). A variety of natural and synthetic polymer nanogels have been prepared and used as transdermal drug delivery vehicles to date (Uk Son et al., 2020; Wang et al., 2022).

Hyaluronic acid (HA) is a linear polysaccharide consisting of repeating units of D-glucuronic acid and N-acetyl-D-glucosamine (Jiang et al., 2022). As a natural polymer, HA has been widely studied in drug delivery due to its outstanding biological function (Yu et al., 2021b). It is well known that HA can overcome the skin barrier by hydrating the stratum corneum, and effectively delivering drugs to the deeper layers of the skin (Chen et al., 2020). In addition, some studies have proved the applicability of HA based nanocarriers in enhancing topical drug delivery due to the interaction between HA based nanocarriers and keratin components in skin (Liu et al., 2021b; Kim et al., 2021; Sharma et al., 2022). However, HA is hydrophilic and is not suitable as a carrier for hydrophobic drugs. It has been reported that intramolecular and/or intermolecular hydrophobic interactions can self-aggregate in aqueous solutions to form nanogels when HA is hydrophobized, and the hydrophobic regions inside the nanogels are beneficial for the loading and topical delivery of hydrophobic drugs (Son et al., 2017).

In recent years, silk fibroin has attracted great interest due to its biological adhesion and its application in drug stabilization, and is currently used in various drug delivery systems such as nanoparticles, hydrogels and nanofibers (Chen et al., 2015; Sakunpongpitiporn et al., 2022; Selvaraj et al., 2022). Silk peptide is produced by hydrolysis of silk fibroin. It is non-toxic to human skin and has high affinity, water retention and anti-inflammatory properties (Eom et al., 2020).

Curcumin (Cur), a natural polyphenol extracted from the rhizome of turmeric with various pharmacological effects. The topical application of Cur to the skin has long been of great interest in anti-oxidation, anti-inflammatory and light protection (Shi et al., 2020). However, chemical instability, low water solubility, and poor skin penetration are major obstacles to their application as topical therapeutics (Granata et al., 2020). Therefore, finding novel formulations aimed at overcoming these limitations and enhancing the topical pharmacological properties of Cur remains a challenge. Currently, Cur-loaded nanoparticles (such as solid lipid nanoparticles, liposomes, emulsions, micelles, etc.) seem to be a very promising formulation method to effectively improve the topical efficacy of Cur (Vater et al., 2020; Yu et al., 2021a; Zhou et al., 2021; Prabhu et al., 2022).

In this study, silk peptide conjugated OHA (SOHA) was successfully synthesized on the basis of octadecylamine conjugated hyaluronic acid (OHA), and Cur-loaded SOHA nanogels (Cur-SHNGs) were developed to enhance the topical administration of Cur for better treatment of localized diseases (Figure 1). The physicochemical properties of micelles were characterized in term of particle size, zeta potential, morphology, stability, and *in vitro* release. In addition, the *in vitro* transdermal penetration and skin retention, effect of the preparation on skin structure, intradermal drug distribution, *in vivo* analgesic and anti-inflammatory activities were also investigated. Finally, biocompatibility assessments were performed using *in vivo* skin irritation test.

2 Materials and methods

2.1 Materials

Hyaluronic acid (HA, molecular weight <10 *k*Da) was purchased from Freda Biochem Co., Ltd. (Shandong, China). Silk peptide (Protein hydrolyzates, molecular weight is between 500 and 1,000 Da) was purchased from Shanghai McLean Biochemical Technology Co., Ltd. (Shanghai, China). Octadecylamine was purchased from Aladdin reagent Co., Ltd. (Shanghai, China). (3-dimethylaminopropyl)-3-ethylcarbodiimide hydrochloride (EDC.HCL) and N-hydroxysuccinimide (NHS) were purchased from Nanjing dulai Biotechnology Co., Ltd. (Nanjing, China). Curcumin was purchased from Ivy Biotechnology Co. Ltd. (Xian, China). Haematoxylin and Eosin staining were purchased from Sigma-Aldrich (Shanghai, China). All other reagents were analytical grade preparation.

2.2 Animals

Female SD rats (180–220 g) and female ICR mice (18–22 g) were used as the experimental animals. Animals were raised in the animal care facility of the Pharmacology Laboratory of Luoyang Normal University. Animal room was kept at 22°C ± 3°C and under a 12 h light cycle, with free access food and water. All animal feeding and experimental procedures were guided by the guidelines of Henan Provincial Experimental Animal

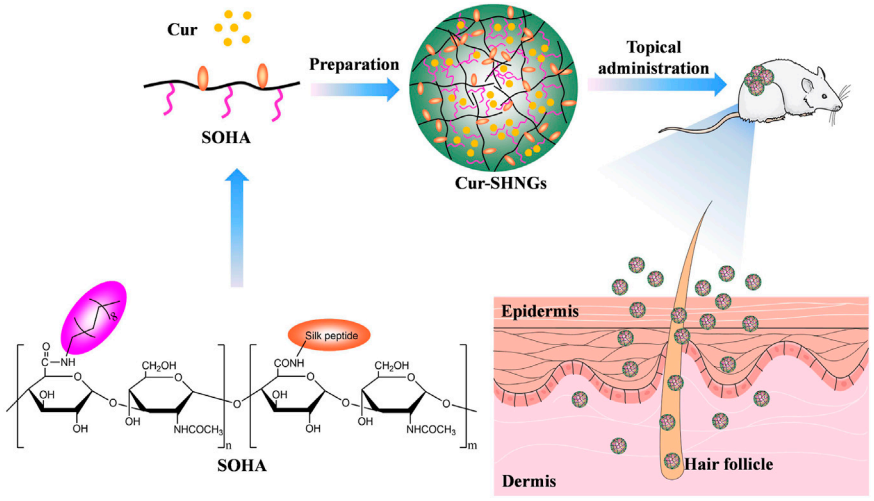

FIGURE 1
Schematic illustration of the Cur-loaded nanogels (Cur-SHNGs) based on SOHA conjugate for the enhancement of the topical administration of Cur.

Management Committee and approved by the Animal Ethics Committee of Luoyang Normal University.

2.3 Synthesis of SOHA conjugate

Octadecylamine conjugated hyaluronic acid (OHA) was formed by covalently combining the $-NH_2$ group in octadecylamine with the −COOH group of HA through an amide reaction using EDC and NHS as catalysts (Son et al., 2017). Briefly, hyaluronic acid solution (1%, w/v) was prepared in deionized water by naturally swell. A double molar excess of EDC and NHS was added to activate the −COOH groups in HA, followed by the addition of octadecylamine (dissolved in DMF). The molar ratio of HA subunit: octadecylamine was 1:1. The reaction was first run at 60°C for 5 h, and then at room temperature for 24 h. After the reaction was stopped, the mixture was dialyzed in ethanol/deionized water (V/V, 7:3, 5:5, 3:7) for 2 days and further freeze-dried to obtain dry purified OHA conjugate. The structure of OHA was characterized by ^{1}H NMR using an instrument (AVANCE500, Bruker, Germany).

Silk peptide (440 mg) was dissolved in 5 ml of DMF. OHA conjugate (100 mg) was fully dissolved in 10 ml of dimethylformamide (DMF), followed by addition of EDC (100 mg) and NHS (60 mg), the mixture was stirred at room temperature for 6 h and then the silk peptide solution was slowly dropped into the OHA activated solution. The reaction was run at room temperature for 24 h under stirring. The ultimate reaction solution was dialyzed against an excess amount of deionized water for 48 h, and then the solution was filtered to remove impurities through a 0.45 μm millipore filter. Finally, silk peptide conjugated OHA (SOHA) was collected by freeze-drying. The structure of SOHA was characterized by ^{1}H NMR.

2.4 Preparation and characterization of Cur-SHNGs

2.4.1 Preparation of Cur-SHNGs

Cur-SHNGs were prepared by dialysis-sonication method. Briefly, 160 mg of SOHA and 8 mg of Cur were mixed in 10 ml of deionized water and 3 ml of DMSO, respectively. The mixture was dialyzed against deionized water in the dark for 48 h using a dialysis bag (MWCO 3.5 kDa) with stirring. After dialysis, the mixture was subjected to ultrasonic treatment for 20 min. Subsequently, the sample was freeze-dried with a freeze dryer (SCIENTZ-18ND, Ningbo Xinzhi Biotechnology Co., Ltd., China) to obtain Cur-SHNGs powder. Nanogels consisting of Cur and formulated by OHA (Cur-HNGs) were prepared in the same way.

2.4.2 Quantitation of Cur using HPLC

Cur in the formulation was quantified using a high performance liquid chromatography (HPLC) system (U-3000, Thermo, United States) equipped with a UV detector and a reversed-phase WondaSil C18 column (5 mm, 200 mm × 4.6 mm). The mobile phase was composed of acetonitrile and 0.5% phosphoric acid (58:42, V/V), and the flow rate was 1.0 ml/min. The wavelength of the UV detector and the temperature of the column oven

were set to 423 nm and 30°C, respectively. The injection volume was 20 μl. The Cur content (%) in the nanogels was calculated according to following formula: Cur content (%) = (mass of Cur loaded in nanogels/mass of Cur loaded nanogels) × 100%.

2.4.3 Measurement of particle size and zeta potential

The particle size and zeta potential of the nanogels were determined using a dynamic light scattering instrument (Zetasizer ZS90, Malvern Instruments, United Kingdom). Samples were diluted to 3.0 mg/ml with deionized water prior to determination. Each sample was placed in a zeta potential cell and the zeta potential of the particles was measured at 25°C. The results were the average of three measurements for each sample.

2.4.4 Morphological observations of Cur-SHNGs

To observe the morphology of the Cur-SHNGs particles, scanning electron microscope (SEM) was performed using (Sigma 500, ZEISS, Germany). The Cur-SHNGs were diluted to 2 mg/ml, the diluted sample was dropped on the surface of the silicon wafer and kept at room temperature until completely dry. A small amount of freeze-dried Cur-SHNGs was placed on the conductive glue. The samples were coated with gold before observing. The SEM images of dispersed and lyophilized Cur-SHNGs were scanned and recorded, respectively.

2.4.5 Stability of Cur-SHNGs

To investigate the stability of Cur-SHNGs, lyophilized Cur-SHNGs powder was re-dispersed in deionized water and stored at 4°C in the dark for 0, 7, 14, and 21 days. At predetermined time points, the content of Cur was determined by HPLC system, the particle size and zeta potential were measured by dynamic light scattering instrument.

2.5 *In vitro* release

In vitro release studies were conducted in triplicate in phosphate buffered saline (PBS, pH 7.4) containing ethanol (40%, v/v). 2 ml of Cur solution, Cur-HNGs or Cur-SHNGs (0.5 mg/ml) were transferred into dialysis bags (MWCO 3500). Subsequently, the bags were sealed and immersed in 20 ml of release medium. The release medium was continuously stirred at 300 rpm at 37°C. At preset sampling time points (0.5, 1, 2, 4, 8, 12, 24, and 48 h), 2 ml samples were withdrawn and an equal amount of corresponding fresh release medium was placed back. The concentration of Cur in the samples was measured using a fluorescence spectrophotometer (Ex = 442 nm, Em = 475 nm) (F-7000, Hitachi High-Tech, Japan). The cumulative release of Cur was calculated by the following formula: (Liu et al., 2021a)

$$\text{Cumulative release of Cur (\%)} = \frac{V_i \sum_1^{n-1} C_i + V_0 C_n}{m} \times 100\%$$

Where: V_i is the volume of samples (ml), V_0 is the total volume of the release medium (ml), C_i is the drug concentration of the samples (mg/ml), m is the initial amount of the Cur in the dialysis bags (mg), and n is the number of samples (n > 0).

2.6 *In vitro* skin permeation studies

2.6.1 Preparation of rat skin

After the abdominal hair of the rats was shaved with an electric shaver, the animals were sacrificed by ether inhalation anesthesia, the abdominal skin was excised, adipose tissue and adhesions were removed, and then the skin was hydrated with physiological saline and stored at 4°C for use (Daryab et al., 2022).

2.6.2 *In vitro* permeation studies in rat skin

In vitro skin penetration study of Cur from Cur solutions, Cur-HNGs and Cur-SHNGs on rat skin was implemented using the transdermal diffusion cell systems (Ali et al., 2021; Sudhakar et al., 2021). The skin membrane was fixed between the donor chamber and receiving chamber of the diffusion cell, with the epidermis facing the donor chamber and the dermis facing the receiving chamber. The receiving chamber was filled with phosphate buffered saline (PBS, pH 7.4) containing ethanol (40%, v/v). Subsequently, 0.3 ml of Cur solution, Cur-HNGs or Cur-SHNGs (equivalent to 0.15 mg Cur) was added to the donor chamber. The glass tube was suspended in a water bath at 37°C ± 0.5°C and agitated at 300 rpm. Samples of 1.0 ml were taken from the receiver chamber at predetermined time intervals up to 24 h and immediately replenished with an equal amount of receiving solution. The amount of Cur was quantified using HPLC as described above.

After the penetration experiment was completed, the skin samples were removed from the diffusion cell and rinsed with deionized water to remove residual formulation from the surface of the skin. The skin was then cut into pieces and subjected to intermittent sonication in 2 ml of methanol for 120 min to extract the drug in the skin. The Cur retained in the skin was quantitatively analyzed by HPLC.

2.7 Hematoxylin and eosin staining

The back hair of the mice was depilated 1 day before the experiment, and then Cur solutions, Cur-HNGs and Cur-

SHNGs (containing 0.15 mg of Cur) were applied in the depilation area. 6 h after application of the formulations, the mice were killed and the skin was immediately collected. After washing with physiological saline, the skin was placed in a 4% paraformaldehyde solution at 4°C for fixation. The fixed skin was embedded in paraffin, and serial longitudinal sections were obtained with a thickness of 5 μm using a microtome (LEICA RM2235, Nussloch, Germany). Photographs of paraffin sections were obtained using a digital slide scanner (3DHISTECH, Ltd.), and the effect of formulations on skin microstructure was analyzed using the matching analysis software of CaseViewer 2.3.

2.8 Fluorescence imaging

Different Cur formulation (Cur solution, Cur-HNGs, and Cur-SHNGs) was respectively administered to the skin of living mice as described in section of "Hematoxylin and eosin staining." After 1 and 6 h of administration, the skin samples were excised and thoroughly washed with physiological saline. Subsequently, the treated skin samples were cut longitudinally using a freezing slicer (Leica CM 1950, Germany). The skin sections were nuclear counterstained with DAPI, fluorescent images were acquired using a digital slide scanner (3DHISTECH, Ltd.).

2.9 *In vivo* hot plate test in mice

In vivo analgesic activity studies in mice were performed using the hot plate method (Abdallah et al., 2021). Briefly, each mouse was individually placed on the hot plate of a smart hot plate apparatus (YLS-6B, Jinan, China) maintained at 55°C ± 1°C. The time elapsed from the onset of mouse exposure to the hot plate to eliciting a response (including paw licking, paw withdrawal, limb lift, or jumping) was recorded as the latency (Muangnoi et al., 2018). Female mice with a basal latency of 5–30 s were selected for testing. The mice were divided into four groups with 10 mice in each group. After the determination of the basal latency, the hot plate latencies were recorded at different time points (30, 60, and 120 min) post the administration of Cur solution, Cur-HNGs or Cur-SHNGs at a dose of 15 mg/kg. The cutoff time was set at 60 s.

2.10 Dimethyl benzene induced mice ear edema test

The mice were randomly divided into four groups with 10 mice in each group. Cur solution, Cur-HNGs or Cur-SHNGs were uniformly applied to the two sides of the right ear in each group at the dose of 0.4 mg/kg. After treatment for 1 h, 30 μl of dimethyl benzene was applied topically on both sides of the right ear (15 μl on each side) to induce ear edema. The mice were humanely killed after treatment with dimethyl benzene for 30 min, and then the same area of the left and right ears of the mice were carefully cut off with a puncher, the ears (8 mm in diameter) of all mice were harvested and weighed accurately. The ear edema and ear swelling inhibition rate were calculated.

2.11 Acute dermal irritation test

The hairs on both sides of the spine (approximately 3 cm × 3 cm) were shaved 24 h before the experiment. The mice were divided into four groups of six mice each. Then 0.5 ml of Cur solution, Cur-HNGs or Cur-SHNGs was administered on depilated dorsal surface of the mice, the formulation was removed after 4 h of exposure, and any visible changes in the skin (such as erythema, edema, etc.) were observed at 1, 4, 24, 48, and 72 h.

2.12 Statistical analysis

Results were expressed as mean ± standard deviations (SD) of triplicate experiments. The statistical differences among groups were analyzed using Student's *t*-test, and $p < 0.05$ was considered significant.

3 Results and discussions

3.1 Synthesis and characterizations of SOHA conjugate

The synthetic scheme of SOHA conjugate is shown in Figure 2A. Under the catalysis of EDC and NHS, a new conjugate SOHA was synthesized through the amide reaction between the –COOH groups of HA and the $-NH_2$ groups of octadecylamine and silk peptide. Figure 2B showed the ^{1}H NMR spectra of silk peptide, OHA, and SOHA. The characteristic peak of SOHA at 0.95 ppm was the chemical shift corresponding to protons of the $-CH_3-$ group in octadecylamine (Yuan et al., 2022), the peak at 1.24 ppm was attributed to the chemical shifts of the $-CH-NH_2CH_3$ proton in alanine of silk peptide (Zainuddin et al., 2008), and peaks ranging from 2.94 to 3.85 ppm were the chemical shift corresponding to protons of the glycosides in HA (Yuan et al., 2022). The ^{1}H-NMR spectrum indicating that SOHA conjugate was successfully synthesized. The substitution degree (DS) of octadecylamine and silk peptide was

10.3389/fchem.2022.1028372

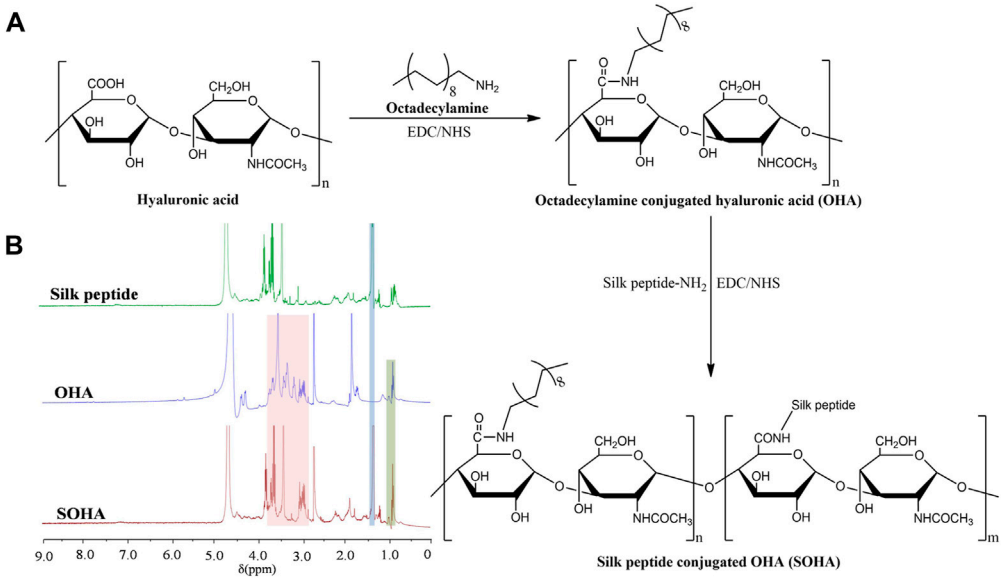

FIGURE 2
(A) Synthetic scheme of SOHA. **(B)** ^{1}H NMR spectra of silk peptide, OHA and SOHA.

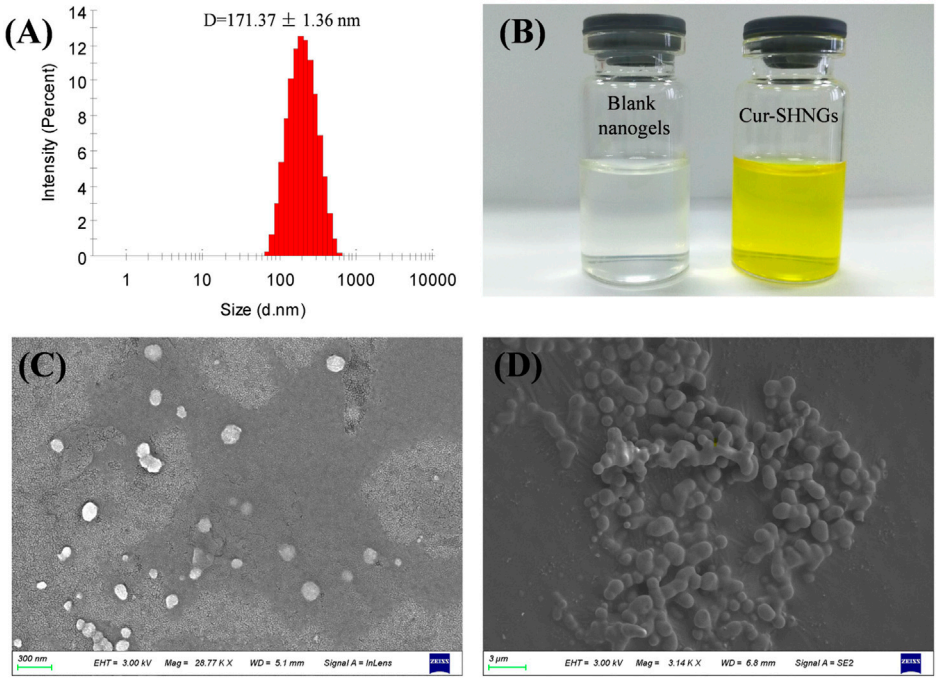

FIGURE 3
Characterization of Cur-SHNGs. **(A)** Particle size distribution of Cur-SHNGs. **(B)** Appearance of blank nanogels and Cur-SHNGs. **(C)** SEM image of Cur-SHNGs dispersion.**(D)** SEM image of lyophilized Cur-SHNGs powder.

14.82% ± 0.27% and 9.46% ± 0.15% in SOHA conjugate, respectively.

3.2 Preparation and characterization of the Cur-SHNGs

3.2.1 Preparation of Cur-SHNGs

Hyaluronic acid is a water-soluble polymer that could form gels with a network structure (Zhang et al., 2019). It has been reported that when HA polymers are hydrophobized by hydrophobic groups, self-aggregating nanogels could be formed (Zoratto et al., 2021). In this study, Cur-loaded SOHA nanogels (Cur-SHNGs) were formulated by dialysis-sonication method. This method could not only easily embed a large amount of highly lipophilic drugs, but also form nanogels with small and uniform particle size. When the weight ratio of Cur to SOHA was 1:20, the content of Cur was 4.26%, which showed a satisfactory drug content and no precipitation was found during preparation.

3.2.2 Particle size and zeta potential

In skin application, the particle size of the formulation plays an important role. Usually, when the particle size of the formulation is less than 300 nm, it is easy to penetrate the stratum corneum and form a drug reservoir in the skin. However, when the particle size is less than 100 nm, it is easier to enter the blood circulation through the dermis (Verma et al., 2003). The particle size of blank nanogels was 163.16 ± 2.31 nm with a PDI of 0.15 ± 0.02. After loading Cur, Cur-SHNGs presented a slightly increased particle size of 171.37 ± 1.36 nm with a PDI of 0.23 ± 0.01. Only one peak was observed in the diagram of particle size distribution of the Cur-SHNGs (Figure 3A), which indicated the uniform particle size distribution of the formulation. The loading of Cur did not significantly change the particle size of the nanogels. The particle size of Cur-SHNGs is between 100 and 300 nm. Therefore, Cur-SHNGs might enter deeper skin through the stratum corneum and form a drug reservoir in the skin. The average size of Cur-HNGs was around 165 nm, so the conjugation of silk peptide did not obviously change the size.

The zeta potential of nanoparticles might be one of the important factors affecting their stability and skin deposition (Kahraman et al., 2018). The zeta potentials of blank nanogels, Cur-HNGs and Cur-SHNGs were −12.90 ± 0.21, −27.08 ± 1.34, and −13.23 ± 0.90 mV, respectively. Compared with Cur-HNGs, the negative charge of Cur-SHNGs was weakened, which might be due to the binding of silk protein peptides. It was found that nanoparticle systems with a zeta potential greater than ±30 mV can produce good stability of the suspension, while less than ±15 mV might lead to the problem of aggregation and sedimentation (Deng et al., 2021). Nevertheless, the stability experiments showed that the stability of the Cur-SHNGs was not affected by the surface zeta potential (discussed in section of "Stability of Cur-SHNGs"). Since skin cells are negatively charged, lower repulsion between Cur-SHNGs with less negative charge and skin cells might result in better cell adsorption and intradermal drug deposition (Zhang et al., 2020).

3.2.3 Morphology of Cur-SHNGs

The prepared blank nanogels were uniform and transparent in appearance, while the formulated Cur-SHNGs were yellow and homogeneous (Figure 3B). As shown in Figure 3C, the Cur-SHNGs dispersion appeared as a single nanoparticle with spherical shape. The lyophilized powder of Cur-SHNGs also presented a spherical shape with a smooth surface (Figure 3D).

3.2.4 Stability of Cur-SHNGs

After 21 days of storage in the dark at 4°C, the particle size, zeta potential value and Cur content of Cur-SHNGs were not statistically different from those observed at 0 days of storage, indicating that the gel network formed by Cur-SHNGs could protect Cur from degradation and oxidation, and effectively improve the physicochemical stability of the formulation Figures 4A–C.

3.3 *In vitro* release

The *in vitro* release curves were shown in Figure 4D. It was obvious that almost 95.06% ± 1.87% of the Cur was released from the Cur solution within 48 h, while the cumulative release of the Cur-HNGs and Cur-SHNGs was only 70.05% ± 3.39% and 60.23% ± 2.18%, respectively. The Cur-HNGs and Cur-SHNGs showed a significantly lower cumulative release compared to that of Cur solution at 48 h ($p < 0.01$). The slower release rate of Cur loaded nanogels might be attributed to the unique grid structure of the nanogels formed by the entanglement of OHA or SOHA chains, which affected the drug diffusion and slowed down drug release. This might be beneficial for the formulation to act as an intradermal drug depot and to release the drug continuously in the skin, rather than releasing the drug before the nanogels penetrate into the skin.

3.4 *In vitro* skin penetration and retention

Figure 5A showed the cumulative amount of Cur permeated through the unit area of abdominal rat skin from the Cur solution, Cur-HNGs and Cur-SHNGs. At each time point, the cumulative permeability of Cur-HNGs and Cur-SHNGs was much higher

10.3389/fchem.2022.1028372

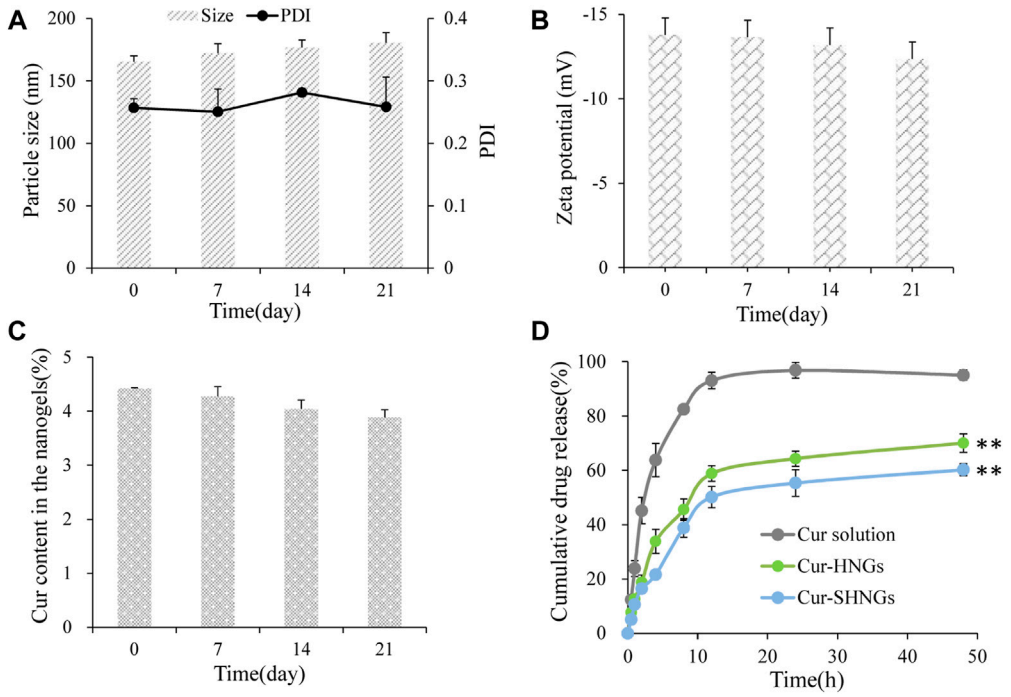

FIGURE 4
The storage stability of Cur-SHNGs at 4°C by **(A)** particle size and PDI, **(B)** zeta potential and **(C)** Cur content in the nanogels. **(D)** The *in vitro* release of Cur from Cur solution, Cur-HNGs, and Cur-SHNGs in PBS (pH 7.4) containing ethanol (40%, v/v) (results were presented as mean ± SD, $n = 3$; $^{**}p < 0.01$ compared with the Cur solution).

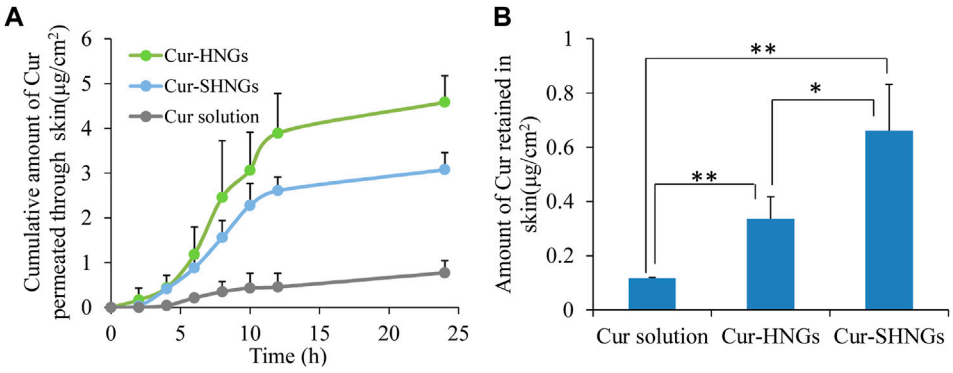

FIGURE 5
In vitro skin permeation studies of Cur solution, Cur-HNGs and Cur-SHNGs in rat skin after 24 h of topical administration. **(A)** The *in vitro* skin cumulative permeation of Cur through the skin. **(B)** Cur retention in the skin (results were presented as mean ± SD, $n = 3$; $^{*}p < 0.05$, $^{**}p < 0.01$).

than that of Cur solution, no lag phase was observed for the Cur-HNGs and Cur-SHNGs, and Cur could be detected in the receiving chambers at the first time point of 2 h, indicated that the nanogels could quickly cross the stratum corneum and penetrate through the skin. While, only a small amount of drugs could be detected in the receiving chambers at 4 h for Cur solution. After 24 h of percutaneous penetration, the cumulative amount of Cur permeated through the skin from the Cur solution, Cur-HNGs and Cur-SHNGs was 0.77 ± 0.27, 4.58 ± 0.59, and 3.08 ± 0.38 μg/cm^2, respectively. It was obvious that Cur permeated through rat skin from Cur-HNGs and Cur-SHNGs was significantly higher than that of Cur solution ($p <$

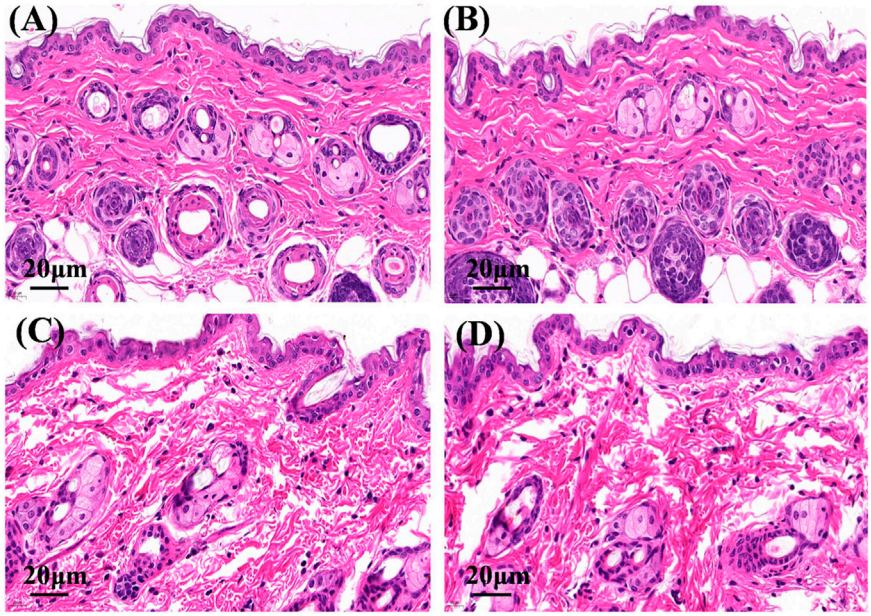

FIGURE 6
Micrographs of hematoxylin and eosin stained mice skin sections after the mice were treated with physiological saline **(A)**, Cur solution **(B)**, Cur-HNGs **(C)**, and Cur-SHNGs **(D)** (n = 3).

0.01). The small particle size of the formulated nanogels provided a large surface area that promotes the transdermal penetration of drugs (Elmataeeshy et al., 2018). In addition, it has been reported that HA has an unusually strong ability to absorb water and can bind 1,000 times its own volume of water (Zhu et al., 2020), so it can greatly hydrate the stratum corneum, thereby causing swelling of keratinocytes and reducing the compactness of the stratum corneum structure, ultimately increasing permeation efficiency of the drug (Zhu et al., 2020). The efficacy of topical therapeutic drugs depends on the amount of drugs in the skin, which is related to the ability of drugs to penetrate the stratum corneum into the skin tissue. Cur loaded nanogels had a stronger percutaneous permeability than that of the Cur solution, indicated that more Cur would be retained in skin, which is beneficial to the treatment of local diseases (Zheng et al., 2016; Faisal et al., 2018). The cumulative permeation of Cur through the skin at 24 h was found to be significantly reduced in the case of Cur-SHNGs compared to Cur-HNGs ($p < 0.05$). This result indicated that Cur-SHNGs might be more beneficial to keep the drug in the skin layer and reduce the further penetration of Cur into the systemic circulation. Therefore, Cur-SHNGs would be more effective in targeting local skin sites than Cur-HNGs.

The amounts of Cur retained in the skin after applying Cur solution, Cur-HNGs and Cur-SHNGs were shown in Figure 5B. After 24 h of transdermal penetration, the amount of Cur retained in skin were 0.12 ± 0.01, 0.34 ± 0.08, and 0.66 ± 0.17 μg/cm^2 for Cur solution, Cur-HNGs and Cur-SHNGs, respectively. It was obvious that the amount of Cur retained in skin for Cur-HNGs and Cur-SHNGs was 2.83 and 5.50 times higher than that of Cur solution, respectively. It is beneficial when Cur retention in the skin is needed in some local skin diseases such as dermatitis, psoriasis, and burn pain. The significant increase in skin retention of Cur loaded nanogels might be attributed to: 1) The HA molecule has a strong affinity for keratin in the skin and the viscoelasticity of the HA molecule chain allows the formulation to remain in the skin for a longer time (Cilurzo et al., 2014). 2) The nano-sized nanogels is easy to penetrate into the deep layer of the skin through the stratum corneum, and forms a drug depot in the skin to exert a slow-release effect, which is conducive to the accumulation of drugs in the skin tissue to achieve better treatment of local skin diseases (Faisal et al., 2018). 3) Negatively charged drug-loaded nanoparticles could interact with negatively charged skin membranes to increase the transdermal flux of drugs, which in turn could improve drug accumulation in the skin layer (Maione-Silva et al., 2019). Cur-SHNGs showed a significantly higher ($p < 0.05$) drug deposition in skin than that of Cur-HNGs, this might be due to that the helical silk peptide in SOHA chains has special ultrastructure and multi-level structure, which makes Cur-SHNGs have good skin affinity and biological adhesives properties (Dong et al., 2015; Mao et al., 2017). In conclusion, we could say that the increased retention of Cur-SHNGs in the skin is mainly due to the characteristics of the carrier material and the formulation in which the drug is dispersed.

10.3389/fchem.2022.1028372

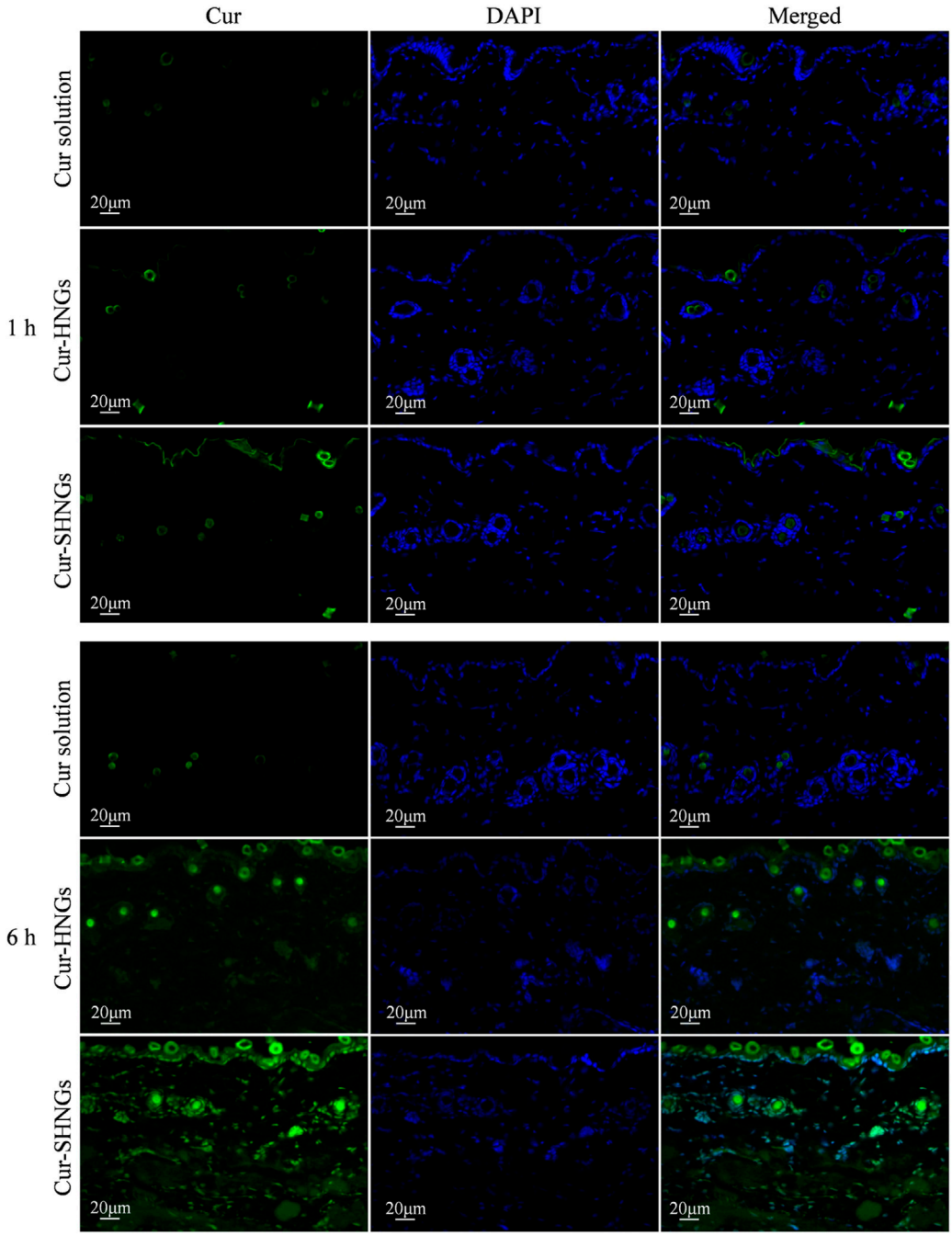

FIGURE 7
Fluorescence images of longitudinal sections of the skin incubated with Cur solution, Cur-HNGs and Cur-SHNGs at 1 and 6 h (n = 3).

3.5 Hematoxylin and eosin staining

On hematoxylin and eosin staining analysis, the nucleus and cytoplasm appeared blue and red (Figure 6), respectively. The structure of the skin tissue in the physiological saline group and the Cur solution group was compact and complete, the epidermal cells were closely arranged, and the edge of cells were difficult to distinguish (Figures 6A,B). After administration of Cur-HNGs or Cur-SHNGs, the skin structure was loose, the intercellular spaces and epidermal cracks of the skin increased, and the cell arrangement in the stratum corneum was disordered (Figures 6C,D). Taken

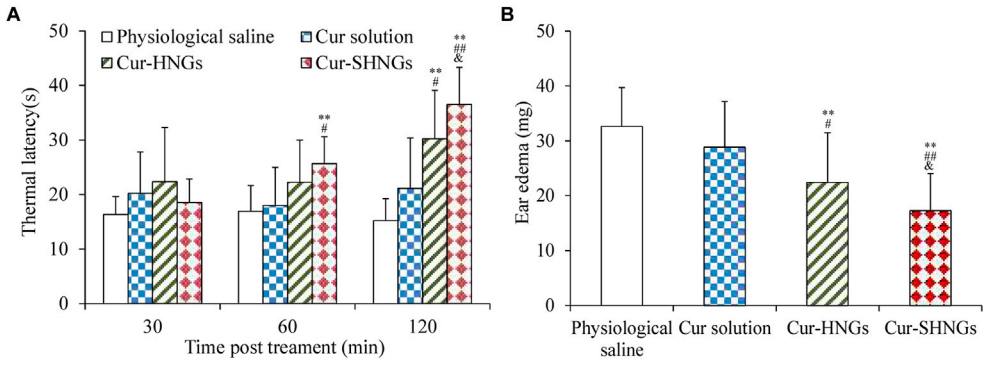

FIGURE 8
(A) Thermal latency of physiological saline, Cur solution, Cur-HNGs, and Cur-SHNGs in mice at various time intervals on the hot plate; **(B)** Effect of physiological saline, Cur solution, Cur-HNGs, and Cur-SHNGs on the weight of dimethyl benzene induced mice ear edema. (**$p < 0.01$ as compared to physiological saline group, $^{\#}p < 0.05$ and $^{\#\#}p < 0.01$ as compared to Cur solution group, $^{\&}p < 0.05$ as compared to Cur-HNGs group).

together, Cur-HNGs and Cur-SHNGs altered the skin microstructure, increased skin permeability, and improved transdermal drug delivery, which might be related to the reduced skin density due to the intense skin hydration of HA (Taieb et al., 2012; Taweechat et al., 2020).

3.6 Fluorescence imaging

In order to effectively improve the topical efficacy of Cur, it is necessary to improve the penetration of the drug into the deep layers of the skin after administration of the formulation. Taking advantage of the characteristic of spontaneous green fluorescence of Cur, *in vivo* skin penetration studies were performed using fluorescence images to confirm the skin permeation and retention enhancement effect of developed formulation, as well as to study the distribution of formulations in the skin. Fluorescence images of mouse skin after treatment with Cur solution, Cur-HNGs and Cur-SHNGs for 1 and 6 h were shown in Figure 7. After 1 h of permeation, only showed weak fluorescence in hair follicles was observed in the skin treated with Cur solution, while in Cur-HNGs group and Cur-SHNGs group, fluorescence was observed in both the upper epidermis and hair follicles, and the fluorescence intensity was stronger than Cur solution. In the case of Cur loaded nanogels, the enhancement of skin fluorescence intensity indicated that they could effectively penetrate the stratum corneum and deliver the drug to the deeper layers of the skin. The fluorescence intensity of all formulations in the skin increased with the extension of permeation time. After 6 h of penetration, the Cur solution group was still mainly distributed in the hair follicles, indicating that it did not penetrate the stratum corneum into the deep layer of the skin, which might be due to the poor permeability of Cur molecules (Yu et al., 2021a), and the hair follicle pathway might be the main pathway for the percutaneous penetration of free Cur. The Cur-HNGs group and the Cur-SHNGs group were distributed in the epidermis, dermis and hair follicles, and showed stronger fluorescence intensity compared with the Cur solution group, indicating that the transdermal penetration ability of the nanogels formulation was much better than that of the Cur solution. The fluorescence intensity of the skin samples from the Cur-SHNGs group was significantly higher than that of Cur-HNGs group, indicating that more drugs were retained in the skin tissue after percutaneous administration of Cur-SHNGs, which might be due to the skin affinity and biological adhesives properties (Yang et al., 2020), these phenomena further confirmed the favorable performance of Cur-SHNGs for transdermal drug delivery.

3.7 Assessment of analgesic activity

The results of analgesic effects were shown in Figure 8A. From the obtained results, we noticed that the developed Cur-SHNGs formulation exhibited significant analgesic activity at both the 60 and 120 min time points ($p < 0.05$), compared with the physiological saline group and the Cur solution group. At 120 min following topical application of the formulation, the Cur-SHNGs group showed significant analgesic activity compared to the Cur-HNGs group ($p < 0.05$). These results suggested that the Cur-SHNGs treated group had a significantly higher anti-nociceptive effect, which might be due to the fact that Cur-SHNGs improved the penetration of Cur through the stratum corneum and enhanced intradermal retention.

TABLE 1 Appearance of mice belonging to the physiological saline (control) group and to the groups treated with Cur solution, Cur-HNGs, and Cur-SHNGs. Experiments were completed on six animals for each group.

Group	Erythema (Normal for "√")	Edema (Normal for "√")	Death/total animals
Control	√	√	0/6
Cur solution	√	√	0/6
Cur-HNGs	√	√	0/6
Cur-SHNGs	√	√	0/6

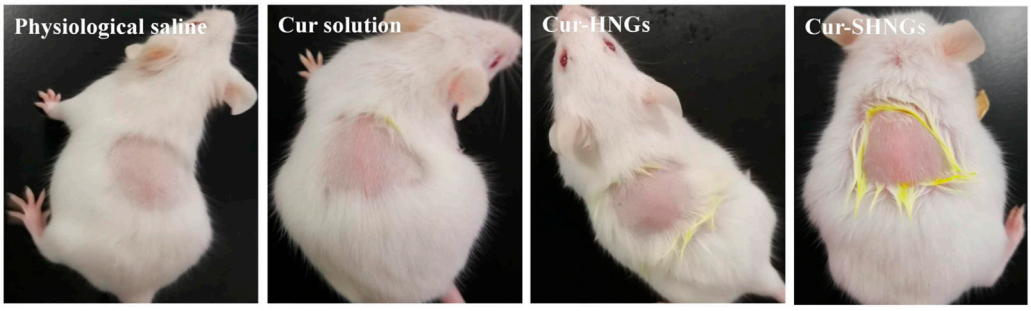

FIGURE 9
Observation of mice skin appearance at 72 h after exposure to physiological saline, Cur solution, Cur-HNGs, or Cur-SHNGs (n = 6).

3.8 Assessment of anti-inflammatory activity

As can be seen from Figure 8B, the ear edema of the Cur-SHNGs group was 17.26 ± 6.7 mg, while the ear edema of the Cur solution group and the Cur-HNGs group were 28.12 ± 8.58 and 22.43 ± 9.05 mg, respectively. Compared with the Cur solution group and Cur-HNGs group, the ear edema in the Cur-SHNGs group was significantly reduced ($p < 0.05$) when the same dose was topically administered to mice. The ear swelling inhibition rate of Cur-SHNGs was 47.07%, which was 3.41 times and 1.51 times better than that of Cur solution and Cur-HNGs, respectively. These results indicated that Cur-SHNGs had stronger protective and therapeutic effects on dimethyl benzene induced mice ear skin edema when compared with Cur solution and Cur-HNGs. This also further confirmed the advantages of Cur-SHNGs as a transdermal drug delivery system for topical inflammatory diseases.

3.9 *In vivo* skin irritation test

As shown in Table 1 and Figure 9, all mice tested showed no signs of edema or erythema during the testing period, indicating that the Cur-SHNGs had good biocompatibility and can be safely used as a topical product, which will facilitate improved skin acceptability and patient compliance. In conclusion, despite the Cur-SHNGs exhibited high skin retention of Cur as previously described, no skin irritation was found.

4 Conclusion

In this study, Cur-loaded SOHA nanogels (Cur-SHNGs) were successfully prepared as a novel drug carrier for the enhancement of the topical administration of Cur. The physical properties, *in vitro* release behavior, *in vitro* skin penetration and retention, effects of formulations on skin microstructure, *in vivo* drug activity and biocompatibility of the newly developed nanogels were investigated. *In vitro* skin penetration and retention study revealed higher skin penetration of Cur-SHNGs than that of Cur solution and the highest retention than that of Cur-HNGs and Cur solution. Fluorescence imaging further confirmed the skin permeation and retention enhancement effect of developed Cur-SHNGs. Hematoxylin and eosin staining indicated that nanogels formulation improved transdermal drug delivery by reducing skin density due to the intense skin hydration of HA. In addition, *in vivo* activity tests indicated that Cur-SHNGs had favorable analgesic and anti-inflammatory activity. *In vivo* skin irritation test implied the good biocompatibility of Cur-SHNGs. In

conclusion, the Cur-SHNGs should be a promising formulation in the topical drug delivery.

Data availability statement

The original contributions presented in the study are included in the article/supplementary material, further inquiries can be directed to the corresponding authors.

Ethics statement

The animal study was reviewed and approved by the Animal Ethics Association of Luoyang Normal University. Written informed consent was obtained from the owners for the participation of their animals in this study.

Author contributions

JN and LW: Conceptualization, methodology, writing-original draft. MY and YL: Conceptualization, methodology, writing-original draft, resources. YQ and YW: Conceptualization, methodology. YZ: Methodology, investigation. YF: Methodology, investigation. ZT and HY: Resources, writing-review and editing, validation, supervision.

Funding

This research was funded by the Key Scientific Research Project of Higher Education of Henan Province (No. 20B180006), the National project cultivation fund of Luoyang Normal University (No. 2019-PYJJ-012) and key scientific and technological project of Henan of China (No. 202102110103). Henan Province Science and Technology Attack Plan Foundation (Nos. d222102310356), the Key Scientific Research Project of Higher Education of Henan Province (Nos. 22B350004).

Conflict of interest

The authors declare that the research was conducted in the absence of any commercial or financial relationships that could be construed as a potential conflict of interest.

Publisher's note

All claims expressed in this article are solely those of the authors and do not necessarily represent those of their affiliated organizations, or those of the publisher, the editors and the reviewers. Any product that may be evaluated in this article, or claim that may be made by its manufacturer, is not guaranteed or endorsed by the publisher.

Supplementary material

The Supplementary Material for this article can be found online at: https://www.frontiersin.org/articles/10.3389/fchem.2022.1028372/full#supplementary-material

References

Abdallah, M. H., Abu Lila, A. S., Unissa, R., Elsewedy, H. S., Elghamry, H. A., and Soliman, M. S. (2021). Preparation, characterization and evaluation of anti-inflammatory and anti-nociceptive effects of brucine-loaded nanoemulgel. *Colloids Surfaces B Biointerfaces* 205, 111868. doi:10.1016/j.colsurfb.2021.111868

Ali, M. K., Moshikur, R. M., Wakabayashi, R., Moniruzzaman, M., and Goto, M. (2021). Biocompatible ionic liquid-mediated micelles for enhanced transdermal delivery of paclitaxel. *ACS Appl. Mat. Interfaces* 13 (17), 19745–19755. doi:10.1021/acsami.1c03111

Chen, A. Z., Chen, L. Q., Wang, S. B., Wang, Y. Q., and Zha, J. Z. (2015). Study of magnetic silk fibroin nanoparticles for massage-like transdermal drug delivery. *Int. J. Nanomedicine* 10, 4639–4651. doi:10.2147/ijn.s85999

Chen, Y., Zhang, Z., Xin, Y., Zhou, R., Jiang, K., Sun, X., et al. (2020). Synergistic transdermal delivery of nanoethosomes embedded in hyaluronic acid nanogels for enhancing photodynamic therapy. *Nanoscale* 12 (28), 15435–15442. doi:10.1039/d0nr03494k

Cilurzo, F., Vistoli, G., Gennari, C. G., Selmin, F., Gardoni, F., Franze, S., et al. (2014). The role of the conformational profile of polysaccharides on skin penetration: The case of hyaluronan and its sulfates. *Chem. Biodivers.* 11 (4), 551–561. doi:10.1002/cbdv.201300130

Daryab, M., Faizi, M., Mahboubi, A., and Aboofazeli, R. (2022). Preparation and characterization of lidocaine-loaded, microemulsion-based topical gels. *Iran. J. Pharm. Res.* 21 (1), e123787. doi:10.5812/ijpr.123787

Dasht Bozorg, B., Bhattaccharjee, S. A., Somayaji, M. R., and Banga, A. K. (2022). Topical and transdermal delivery with diseased human skin: Passive and iontophoretic delivery of hydrocortisone into psoriatic and eczematous skin. *Drug Deliv. Transl. Res.* 12 (1), 197–212. doi:10.1007/s13346-021-00897-7

Deng, S., Iscaro, A., Zambito, G., Mijiti, Y., Minicucci, M., Essand, M., et al. (2021). Development of a new hyaluronic acid based redox-responsive nanohydrogel for the encapsulation of oncolytic viruses for cancer immunotherapy. *Nanomater. (Basel)* 11 (1), 144. doi:10.3390/nano11010144

Dong, Y., Dong, P., Huang, D., Mei, L., Xia, Y., Wang, Z., et al. (2015). Fabrication and characterization of silk fibroin-coated liposomes for ocular drug delivery. *Eur. J. Pharm. Biopharm.* 91, 82–90. doi:10.1016/j.ejpb.2015.01.018

El-Hashemy, H. A. (2022). Design, formulation and optimization of topical ethosomes using full factorial design: *In-vitro* and *ex-vivo* characterization. *J. Liposome Res.* 32 (1), 74–82. doi:10.1080/08982104.2021.1955925

Elmataeeshy, M. E., Sokar, M. S., Bahey-El-Din, M., and Shaker, D. S. (2018). Enhanced transdermal permeability of Terbinafine through novel nanoemulgel formulation; Development, *in vitro* and *in vivo* characterization. *Future J. Pharm. Sci.* 4 (1), 18–28. doi:10.1016/j.fjps.2017.07.003

Eom, S. J., Lee, N. H., Kang, M. C., Kim, Y. H., Lim, T. G., and Song, K. M. (2020). Silk peptide production from whole silkworm cocoon using ultrasound and enzymatic treatment and its suppression of solar ultraviolet-induced skin inflammation. *Ultrason. Sonochem.* 61, 104803. doi:10.1016/j.ultsonch.2019.104803

Faisal, W., Soliman, G. M., and Hamdan, A. M. (2018). Enhanced skin deposition and delivery of voriconazole using ethosomal preparations. *J. Liposome Res.* 28 (1), 14–21. doi:10.1080/08982104.2016.1239636

Granata, G., Petralia, S., Forte, G., Conoci, S., and Consoli, G. M. L. (2020). Injectable supramolecular nanohydrogel from a micellar self-assembling calix[4] arene derivative and curcumin for a sustained drug release. *Mater. Sci. Eng. C* 111, 110842. doi:10.1016/j.msec.2020.110842

Hanna, P. A., Ghorab, M. M., and Gad, S. (2019). Development of betamethasone dipropionate-loaded nanostructured lipid carriers for topical and transdermal delivery. *Antiinflamm. Antiallergy. Agents Med. Chem.* 18 (1), 26–44. doi:10.2174/1871523017666181115104159

Ilic, D., Cvetkovic, M., and Tasic-Kostov, M. (2021). Emulsions with alkyl polyglucosides as carriers for off-label topical spironolactone - safety and stability evaluation. *Pharm. Dev. Technol.* 26 (3), 373–379. doi:10.1080/10837450.2021.1874011

Jiang, K., Zhao, D., Ye, R., Liu, X., Gao, C., Guo, Y., et al. (2022). Transdermal delivery of poly-hyaluronic acid-based spherical nucleic acids for chemogene therapy. *Nanoscale* 14 (5), 1834–1846. doi:10.1039/d1nr06353g

Jiang, T., Wang, T., Li, T., Ma, Y., Shen, S., He, B., et al. (2018). Enhanced transdermal drug delivery by transfersome-embedded oligopeptide hydrogel for topical chemotherapy of melanoma. *ACS Nano* 12 (10), 9693–9701. doi:10.1021/acsnano.8b03800

Kahraman, E., Nesetoglu, N., Gungor, S., Unal, D. S., and Ozsoy, Y. (2018). The combination of nanomicelles with terpenes for enhancement of skin drug delivery. *Int. J. Pharm. X.* 551 (1-2), 133–140. doi:10.1016/j.ijpharm.2018.08.053

Kim, H., Lee, S., and Ki, C. S. (2021). Modular formation of hyaluronic acid/β-glucan hybrid nanogels for topical dermal delivery targeting skin dendritic cells. *Carbohydr. Polym.* 252, 117132. doi:10.1016/j.carbpol.2020.117132

Liu, L., Luan, S., Zhang, C., Wang, R., Zhang, Y., Zhang, M., et al. (2021a). Encapsulation and pH-responsive release of bortezomib by dopamine grafted hyaluronate nanogels. *Int. J. Biol. Macromol.* 183, 369–378. doi:10.1016/j.ijbiomac.2021.04.161

Liu, Y., Han, Y., Zhu, T., Wu, X., Yu, W., Zhu, J., et al. (2021b). Targeting delivery and minimizing epidermal diffusion of tranexamic acid by hyaluronic acid-coated liposome nanogels for topical hyperpigmentation treatment. *Drug Deliv. (Lond).* 28 (1), 2100–2107. doi:10.1080/10717544.2021.1983081

Maione-Silva, L., de Castro, E. G., Nascimento, T. L., Cintra, E. R., Moreira, L. C., Cintra, B. A. S., et al. (2019). Ascorbic acid encapsulated into negatively charged liposomes exhibits increased skin permeation, retention and enhances collagen synthesis by fibroblasts. *Sci. Rep.* 9 (1), 522. doi:10.1038/s41598-018-36682-9

Mao, K. L., Fan, Z. L., Yuan, J. D., Chen, P. P., Yang, J. J., Xu, J., et al. (2017). Skin-penetrating polymeric nanoparticles incorporated in silk fibroin hydrogel for topical delivery of curcumin to improve its therapeutic effect on psoriasis mouse model. *Colloids Surfaces B Biointerfaces* 160, 704–714. doi:10.1016/j.colsurfb.2017.10.029

Muangnoi, C., Jithavech, P., Ratnatilaka Na Bhuket, P., Supasena, W., Wichitnithad, W., Towiwat, P., et al. (2018). A curcumin-diglutaric acid conjugated prodrug with improved water solubility and antinociceptive properties compared to curcumin. *Biosci. Biotechnol. Biochem.* 82 (8), 1301–1308. doi:10.1080/09168451.2018.1462694

Niu, J., Yuan, M., Li, H., Liu, Y., Wang, L., Fan, Y., et al. (2022). Pentapeptide modified ethosomes for enhanced skin retention and topical efficacy activity of indomethacin. *Drug Deliv. (Lond).* 29 (1), 1800–1810. doi:10.1080/10717544.2022.2081739

Prabhu, A., Jose, J., Kumar, L., Salwa, S., Vijay Kumar, M., and Nabavi, S. M. (2022). Transdermal delivery of curcumin-loaded solid lipid nanoparticles as microneedle patch: An *in vitro* and *in vivo* study. *AAPS PharmSciTech* 23 (1), 49. doi:10.1208/s12249-021-02186-5

Sakunpongpitiporn, P., Naeowong, W., and Sirivat, A. (2022). Enhanced transdermal insulin basal release from silk fibroin (SF) hydrogels via iontophoresis. *Drug Deliv. (Lond).* 29 (1), 2234–2244. doi:10.1080/10717544.2022.2096717

Selvaraj, S., Inbasekar, C., Pandurangan, S., and Nishter, N. F. (2022). Collagen-coated silk fibroin nanofibers with antioxidants for enhanced wound healing. *J. Biomater. Sci. Polym. Ed.*, 1–18. doi:10.1080/09205063.2022.2106707

Sharma, T., Thakur, S., Kaur, M., Singh, A., and Jain, S. K. (2022). Novel Hyaluronic Acid ethosomes based gel formulation for topical use with reduced toxicity, better skin permeation, deposition, and improved pharmacodynamics. *J. Liposome Res.* 1-15, 1–15. doi:10.1080/08982104.2022.2087675

Shi, T., Lv, Y., Huang, W., Fang, Z., Qi, J., Chen, Z., et al. (2020). Enhanced transdermal delivery of curcumin nanosuspensions: A mechanistic study based on co-localization of particle and drug signals. *Int. J. Pharm. X.* 588, 119737. doi:10.1016/j.ijpharm.2020.119737

Sivaram, A. J., Rajitha, P., Maya, S., Jayakumar, R., and Sabitha, M. (2015). Nanogels for delivery, imaging and therapy. *WIREs. Nanomed. Nanobiotechnol.* 7 (4), 509–533. doi:10.1002/wnan.1328

Son, S. U., Lim, J. W., Kang, T., Jung, J., and Lim, E. K. (2017). Hyaluronan-based nanohydrogels as effective carriers for transdermal delivery of lipophilic agents: Towards transdermal drug administration in neurological disorders. *Nanomater. (Basel).* 7 (12), 427. doi:10.3390/nano7120427

Sudhakar, K., Mishra, V., Jain, S., Rompicherla, N. C., Malviya, N., and Tambuwala, M. M. (2021). Development and evaluation of the effect of ethanol and surfactant in vesicular carriers on Lamivudine permeation through the skin. *Int. J. Pharm. X.* 610, 121226. doi:10.1016/j.ijpharm.2021.121226

Taieb, M., Gay, C., Sebban, S., and Secnazi, P. (2012). Hyaluronic acid plus mannitol treatment for improved skin hydration and elasticity. *J. Cosmet. Dermatol.* 11 (2), 87–92. doi:10.1111/j.1473-2165.2012.00608.x

Taweechat, P., Pandey, R. B., and Sompornpisut, P. (2020). Conformation, flexibility and hydration of hyaluronic acid by molecular dynamics simulations. *Carbohydr. Res.* 493, 108026. doi:10.1016/j.carres.2020.108026

Truong, T. H., Alcantara, K. P., Bulatao, B. P. I., Sorasitthiyanukarn, F. N., Muangnoi, C., Nalinratana, N., et al. (2022). Chitosan-coated nanostructured lipid carriers for transdermal delivery of tetrahydrocurcumin for breast cancer therapy. *Carbohydr. Polym.* 288, 119401. doi:10.1016/j.carbpol.2022.119401

Uk Son, S., Jang, S., Choi, Y., Park, M., Son, H. Y., Huh, Y. M., et al. (2020). Distinctive nanogels as high-efficiency transdermal carriers for skin wound healing. *J. Biomed. Nanotechnol.* 16 (3), 304–314. doi:10.1166/jbn.2020.2893

Uner, B., Ozdemir, S., Tas, C., Ozsoy, Y., and Uner, M. (2022). Development of lipid nanoparticles for transdermal loteprednol etabonate delivery. *J. Microencapsul.* 39 (4), 327–340. doi:10.1080/02652048.2022.2079744

Vater, C., Hlawaty, V., Werdenits, P., Cichon, M. A., Klang, V., Elbe-Burger, A., et al. (2020). Effects of lecithin-based nanoemulsions on skin: Short-time cytotoxicity MTT and BrdU studies, skin penetration of surfactants and additives and the delivery of curcumin. *Int. J. Pharm. X.* 580, 119209. doi:10.1016/j.ijpharm.2020.119209

Verma, D. D., Verma, S., Blume, G., and Fahr, A. (2003). Particle size of liposomes influences dermal delivery of substances into skin. *Int. J. Pharm. X.* 258 (1-2), 141–151. doi:10.1016/s0378-5173(03)00183-2

Wang, Y., Fu, S., Lu, Y., Lai, R., Liu, Z., Luo, W., et al. (2022). Chitosan/hyaluronan nanogels co-delivering methotrexate and 5-aminolevulinic acid: A combined chemo-photodynamic therapy for psoriasis. *Carbohydr. Polym.* 277, 118819. doi:10.1016/j.carbpol.2021.118819

Yang, X., Wang, X., Hong, H., Elfawal, G., Lin, S., Wu, J., et al. (2020). Galactosylated chitosan-modified ethosomes combined with silk fibroin nanofibers is useful in transcutaneous immunization. *J. Control. Release* 327, 88–99. doi:10.1016/j.jconrel.2020.07.047

Yu, F., Zhang, Y., Yang, C., Li, F., Qiu, B., and Ding, W. (2021a). Enhanced transdermal efficiency of curcumin-loaded peptide-modified liposomes for highly effective antipsoriatic therapy. *J. Mat. Chem. B* 9 (24), 4846–4856. doi:10.1039/d1tb00557j

Yu, M., Lu, Z., Shi, Y., Du, Y., Chen, X., and Kong, M. (2021b). Systematic comparisons of dissolving and swelling hyaluronic acid microneedles in transdermal drug delivery. *Int. J. Biol. Macromol.* 191, 783–791. doi:10.1016/j.ijbiomac.2021.09.161

Yuan, M., Niu, J., Xiao, Q., Ya, H., Zhang, Y., Fan, Y., et al. (2022). Hyaluronan-modified transfersomes based hydrogel for enhanced transdermal delivery of indomethacin. *Drug Deliv. (Lond).* 29 (1), 1232–1242. doi:10.1080/10717544.2022.2053761

Zainuddin, Le, T. T., Park, Y., Chirila, T. V., Halley, P. J., and Whittaker, A. K. (2008). The behavior of aged regenerated *Bombyx mori* silk fibroin solutions studied by (1)H NMR and rheology. *Biomaterials* 29 (32), 4268–4274. doi:10.1016/j.biomaterials.2008.07.041

Zhang, Y., Jing, Q., Hu, H., He, Z., Wu, T., Guo, T., et al. (2020). Sodium dodecyl sulfate improved stability and transdermal delivery of salidroside-encapsulated niosomes via effects on zeta potential. *Int. J. Pharm. X.* 580, 119183. doi:10.1016/j.ijpharm.2020.119183

Zhang, Y., Xia, Q., Li, Y., He, Z., Li, Z., Guo, T., et al. (2019). CD44 assists the topical anti-psoriatic efficacy of curcumin-loaded hyaluronan-modified ethosomes: A new strategy for clustering drug in inflammatory skin. *Theranostics* 9 (1), 48–64. doi:10.7150/thno.29715

Zheng, J., Shen, C. Y., Pang, J. Y., Xu, F. C., Liao, W. B., Hu, C. X., et al. (2016). Preparation of tanshinone A loaded nanostructured lipid carrier and its *in vitro* transdermal permeation characteristics. *Zhongguo Zhong Yao Za Zhi* 41 (17), 3232–3238. doi:10.4268/cjcmm20161718

Zhou, P., Zhou, H., Shu, J., Fu, S., and Yang, Z. (2021). Skin wound healing promoted by novel curcumin-loaded micelle hydrogel. *Ann. Transl. Med.* 9 (14), 1152. doi:10.21037/atm-21-2872

Zhu, J. Y., Tang, X. D., Jia, Y., Ho, C. T., and Huang, Q. R. (2020). Applications and delivery mechanisms of hyaluronic acid used for topical/transdermal delivery - a review. *Int. J. Pharm.* 578, 119127. doi:10.1016/j.ijpharm.2020.119127

Zoratto, N., Forcina, L., Matassa, R., Mosca, L., Familiari, G., Musaro, A., et al. (2021). Hyaluronan-cholesterol nanogels for the enhancement of the ocular delivery of therapeutics. *Pharmaceutics* 13 (11), 1781. doi:10.3390/pharmaceutics13111781

frontiers | Frontiers in Chemistry

TYPE Original Research
PUBLISHED 30 September 2022
DOI 10.3389/fchem.2022.1036683

OPEN ACCESS

EDITED BY
He Xiaojun,
Wenzhou Medical University, China

REVIEWED BY
Yu Huo,
Sichuan Normal University, China
You Zhang,
Dongguan University of Technology, China
Hua Yao,
Nanning Normal University, China

*CORRESPONDENCE
Gao-Jie Ye,
gaojieygj@163.com

SPECIALTY SECTION
This article was submitted to Medicinal and Pharmaceutical Chemistry, a section of the journal Frontiers in Chemistry

RECEIVED 05 September 2022
ACCEPTED 14 September 2022
PUBLISHED 30 September 2022

CITATION
Qin Y, Huang R and Ye G-J (2022), An "on-off-on" fluorescence probe for glyphosate detection based on Cu^{2+} modulated g-C_3N_4 nanosheets. *Front. Chem.* 10:1036683. doi: 10.3389/fchem.2022.1036683

An "on-off-on" fluorescence probe for glyphosate detection based on Cu^{2+} modulated g-C_3N_4 nanosheets

Yingfeng Qin, Ruiqi Huang and Gao-Jie Ye*

Guangxi Key Laboratory of Bioactive Molecules Research and Evaluation, Key Laboratory of Biological Molecular Medicine Research (Guangxi Medical University), Education Department of Guangxi Zhuang Autonomous Region, Pharmaceutical College and School of Basic Medical Sciences, Guangxi Medical University, Nanning, China

The analysis of glyphosate is essential to agricultural production, environment protection and public health. Herein, we proposed a fast and convenient "on-off-on" fluorescence platform for sensitive detection of glyphosate *via* Cu^{2+} modulated g-C_3N_4 nanosheets. The fluorescence of the system was quenched by Cu^{2+}. With the presence of glyphosate, the fluorescence could be restored due to the formation of Cu^{2+}- glyphosate complex. The proposed method was cost-effective with label-free and enzyme-free. Moreover, it exhibits high sensitivity with a low detection limit of 0.01 μg/ml. Furthermore, the proposed method has been successfully monitored glyphosate in real samples.

KEYWORDS

glyphosate, G-C3N4 nanosheets, Cu^{2+}, fluorescence, on-off-on

1 Highlights

- A fast and convenient "on-off-on" fluorescence platform based on Cu^{2+} modulated g-C3N4 nanosheets for sensitive detection of glyphosate was developed.
- This method is cost-effective and does not need any labeling, enzyme or other complex processes.
- The proposed method exhibits high sensitivity and has a good analysis performance in complex samples.

2 Introduction

The use of pesticides is highly merited to improve crop yields and products quality. Among many pesticides, glyphosate has become one of the most widely applied herbicides because of its high efficiency, broad-spectrum, non-selective, and low toxicity (Valle et al., 2019). Nevertheless, the misuse of glyphosate can cause its high residues in soil, water, and food, and then produce some problems regarding environmental pollution and health hazards. Moreover, glyphosate exposure has adverse effects on the endocrine system, central nervous system and cell cycle

(Gasnier et al., 2009; Wozniak et al., 2020). Besides that, glyphosate has been listed as a potential carcinogen (Guyton et al., 2015). Therefore, constructing a facile, low-cost, and high-efficiency method for glyphosate detection is of great importance for public health and environmental protection.

Currently, some traditional approaches have been applied to analyze glyphosate such as capillary electrophoresis (Muñoz et al., 2019), gas chromatography (Royer et al., 2000; Ding et al., 2015), high-performance liquid chromatography (Sun et al., 2017; Surapong and Burakham, 2021), Chromatography-mass spectrometry (Schütze et al., 2021; Pérez-Mayán et al., 2022), and enzyme-linked immunosorbent assay (González-Martínez et al., 2005). However, these methods tend to require sophisticated instrumentation, tedious pretreatments, long testing times or tedious operation. To overcome such limitations, several techniques have been proposed (Xu et al., 2018; Qin et al., 2020; Ding et al., 2021; Wu et al., 2022; Zhao et al., 2022). Among them, fluorescence methods have been receiving great attention owing to their superior analytical performances such as simplistic, rapid, and sensitive. Especially, fluorescent probes can be applied to develop label-free fluorescent platforms for target analysis (Liu et al., 2020; Zhang et al., 2020; Liu et al., 2021).

As a promising kind of 2D nanomaterials, g-C3N4 nanosheets (CN NNS) have attracted much attention because of their low cost, easy synthesis, excellent catalytic performance, metal-free, water solubility and excellent biocompatibility (Dong et al., 2016). Up to now, CN NNS have emerged in biosensor, imaging and photocatalysis (Guo et al., 2011; Salehnia et al., 2017; Zhang et al., 2021; Zheng et al., 2021). Intriguingly, CN NNS not only have excellent fluorescence properties, but also the fluorescence can be quenched by some metal ions including Fe^{3+}, Hg^{2+}, Eu^{3+}, and Cr^{6+}(Rong et al., 2015a; Zhuang et al., 2017; Ti et al., 2021; Wang et al., 2021). Recently, Chen group reported a label-free fluorescence sensor for detection of Fe^{3+} and ascorbic acid *via* CN NNS (Guo et al., 2018). Duan group used CN NNS to establish a facile fluorescence approach for 6-Thioguanine and Hg^{2+} (Duan et al., 2018). This property can be used to develop novel sensor strategies for metal ion detection or some other targets detection which were mediated by these metal ions.

In the present work, a facile and effective "on-off-on" fluorescence sensor based on CN NNS was developed for glyphosate. The CN NNS were prepared by one-step process. The fluorescence of the CN NNS could be quenched by Cu^{2+}. Then, the fluorescence gradually increased with the addition of glyphosate due to Cu^{2+} preferentially coordinated with glyphosate. The quantitation of glyphosate could be achieved according to the change of fluorescence. Thus, the proposed approach not only provided a novel sensor platform for glyphosate but also exhibited a potential application in environmental safety and biological fields.

3 Materials and methods

3.1 Reagents and materials

Glyphosate, dicyanamide, copper chloride ($CuCl_2$), and other pesticides (such as carbendazim, carbaryl, parathion, malathion, chlorpyrifos, diazinon, omethoate) were gained from Aladdin Reagent Co., Ltd. (Shanghai, China). Tris was purchased from Solarbio Science and Technology Co., Ltd. (Beijing, China). Ultrapure water was gained from a Milli-Q Integral 15 system (Millipore) and used throughout the work. Water samples were obtained from Yongjiang river in Nanning City and the lake water of Guangxi Medical University campus.

3.2 Preparation of CN NNS nanosheets

The CN NNS were synthesized according to the previously reported literature (Rong et al., 2015b). Briefly, the alumina crucible containing 10 g of ground dicyandiamide was placed in a muffle furnace, heated to 550°C at a heating rate of 3°C/min, reacted for 2 h, and then cooled to 25°C at the same rate. As a result, the bulk CN NNS was acquired. After that, 1 g of bulk CN NNS was put into 100 mL10 M HNO_3 and refluxed for 16 h at 25°C. Then, the refluxed product was collected through centrifugation at 10000 rpm and washed to neutrality with water. The obtained precipitate was dispersed in 50 ml water for 6 h through a 2D nanomaterial stripper. Finally, the CN NNS solution was stored at 4°C.

3.3 Analysis of glyphosate

First, the stock solution of glyphosate was diluted with water to different concentrations. Then, 2 μL of 0.2 mM Cu^{2+}, 10 μL of different concentrations of glyphosate, 5 μL CN NNS and 183 μL 20 mM Tris-HCl buffer (pH 6.0) reacted at room temperature for 10 min with a total volume of 200 μL. Subsequently, the fluorescence spectra of the samples were collected using an FL-8500 fluorescence spectrometer (PerkinElmer, United States) with the excitation wavelength at 308 nm.

3.4 Determination of glyphosate in real samples

First, the samples of river water and lake water were filtered with 0.22 μm membrane to remove solid impurities, respectively. After that, the analysis of glyphosate in the real water samples were carried out as described above processing procedure (2.3 Analysis of glyphosate).

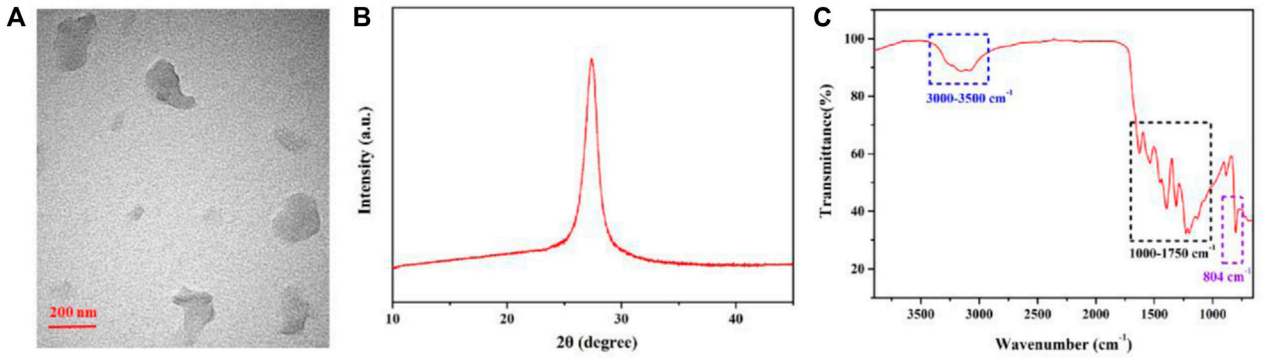

FIGURE 1
The Characterization of CN NNS **(A)** TEM image; **(B)** XRD image; **(C)** FT-IR spectrum.

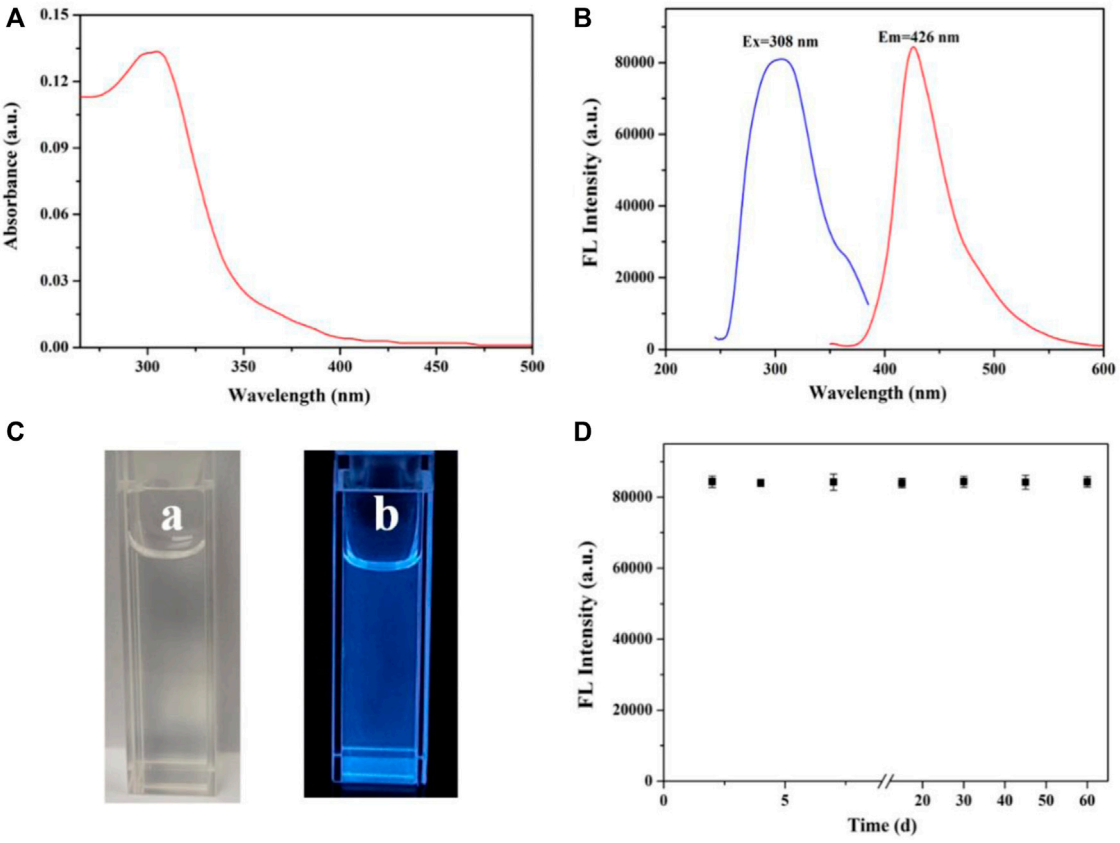

FIGURE 2
(A) UV-Vis spectra of CN NNS; **(B)** The fluorescence excitation and emission spectra of CN NNS; **(C)** The photos of the dispersion under room light **(A)** and 365 nm UV light **(B)**; **(D)**The fluorescence photostability of the dispersion.

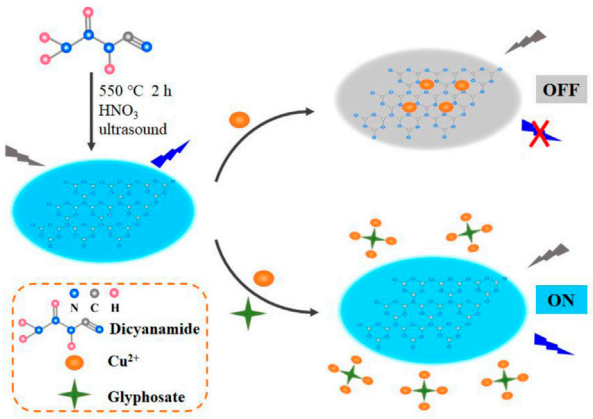

FIGURE 3
Schematic illustration of fluorescence sensor for glyphosate detection *via* CN NNS.

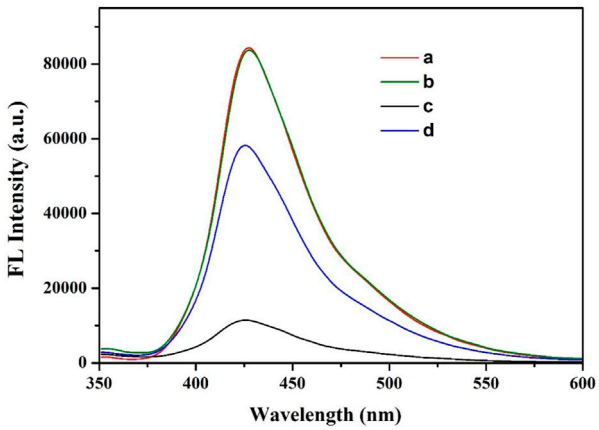

FIGURE 4
Fluorescence emission spectra of different sample solutions. Sample a: CN NNS; Sample b: CN NNS + glyphosate; Sample c: CN NNS + Cu^{2+}; Sample d: CN NNS +Cu^{2+}+ glyphosate. The concentrations of CN NNS, Cu^{2+} and glyphosate were 5 μg/mL, 2 μM and 5 μg/mL, respectively.

4 Results and discussion

4.1 Characterization

The morphology of the obtained CN NNS was characterized through transmission electron microscopy (TEM). Figure 1A exhibited a lamellar structure and a well-dispersed state by TEM image. The XRD image displayed a broad diffraction peak (002) at 27.6° in Figure 1B, which was consistent with previous reports (Sun et al., 2020). As shown in Figure 1C, FT-IR spectrum of the obtained CN NNS was analyzed. The broad bands peaked at 3,000 to 3,500 cm^{-1} were ascribed to N-H stretching. The bands peaked at 1,000 to 1750 cm^{-1} were attributed to C=N stretching and C=O stretching. A characteristic peak of appeared at 804 cm^{-1}, which was due to the vibration of the triazine ring. The FT-IR results indicated the presence of carboxyl, amino and hydroxy groups.

4.2 Optical properties of CN NNS nanosheets

In this work, the UV-Vis absorption spectroscopy and fluorescence spectra are used to reveal the optical properties of CN NNS. The UV-Vis absorption possessed a characteristic absorption peak at 308 nm in Figure 2A. In addition, Figure 2B shows the solution emitted a strong fluorescence emission at 426 nm with the excitation wavelength at 308 nm. Compared with daylight, brilliant blue fluorescence of the solution was clearly observed under the irradiation of 365 nm UV light (Figure 2C). Meanwhile, the fluorescence stability of the CN NNS dispersion was also researched. As displayed in Figure 2D, there is no obvious change in the intensity after the solution was stored for more than 2 months, implying outstanding stability of the dispersion.

4.3 Principle of the proposed sensor

The principle of this novel enzyme-free fluorescence sensor for glyphosate assay based on CN NNS is illustrated in Figure 3. Firstly, the blue CN NNS were prepared by simple synthesis using dicyanamide. In the absence of glyphosate, the fluorescence of system was greatly quenched by Cu^{2+}, lending to a low fluorescence signal. In contrast, upon the addition of glyphosate, Cu^{2+} preferentially coordinated with glyphosate to form glyphosate-Cu^{2+}complex due to the stronger interaction than CN NNS-Cu^{2+}. As a result, a high fluorescence signal was obtained. Thus, the concentrations of glyphosate could be detected by the fluorescence change.

4.4 Feasibility of the sensor

In order to verify the feasibility of this sensor strategy, the fluorescence emission spectra of the reaction solutions were detected. Figure 4 showed that the CN NNS had very high current fluorescence (curve a). After the introduction of glyphosate, no obvious change in fluorescence intensity at 426 nm was observed in curve a and curve b, manifesting that glyphosate had no effect on CN NNS. However, when Cu^{2+} was added to the system, the fluorescence intensity decreased significantly (curve c) due to the formation of the Cu^{2+}-CN NNS complex. After glyphosate and Cu^{2+} were added, we

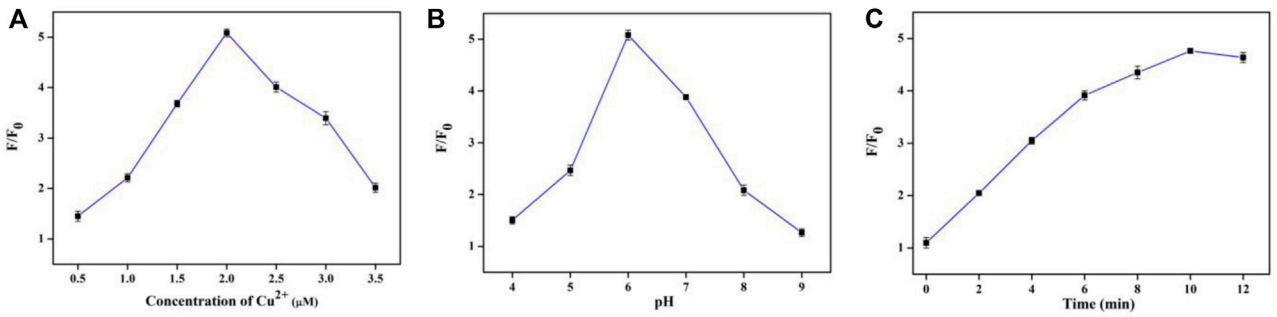

FIGURE 5
Optimization of assay conditions. The effect of Cu^{2+} concentration **(A)**, pH value **(B)**, and incubation time **(C)**.

observed that the fluorescence intensity of system increased significantly (curve d) because glyphosate exhibits a stronger combination ability with Cu^{2+}. Above results illustrated that the fluorescence method using CN NNS and Cu^{2+} was feasible for glyphosate detection.

4.5 Optimization of assay conditions

For achieving the best assay performances, several main factors including the concentration of Cu^{2+}, pH of reaction system, and the reaction time were optimized.

The concentration of Cu^{2+} was first investigated. As seen in Figure 5A, the value of F/F_0 increases with Cu^{2+} concentration from 0.5 μM to 2 μM. The maximum F/F_0 value was obtained at 2 μM. Afterwards, the value of F/F_0 decreased gradually. Thus, 2 μM was the optimal concentrations of Cu^{2+}. In addition, the pH of reaction system was also optimized. The value of F/F_0 increased on increasing pH from 4.0 to 6.0, and the F/F_0 value reached a maximum when the pH was 6.0. However, after the pH exceeds 6.0, the F/F_0 value gradually decreases as the pH value increases (Figure 5B). Thus, 6.0 was used as the optimum pH of the reaction system. Finally, effect of incubation time was also examined. The value of F/F_0 increased with the increase reaction time and sustained a stable value at 10 min (Figure 5C). So, the optimal incubation time was 10 min.

4.6 Fluorescence assay for glyphosate

Based on the optimal conditions, various concentrations of glyphosate were analyzed. As illustrated in Figure 6A, the fluorescence intensity at 426 nm increases as the concentration of glyphosate increased from 0 to 8.0 μg/ml.

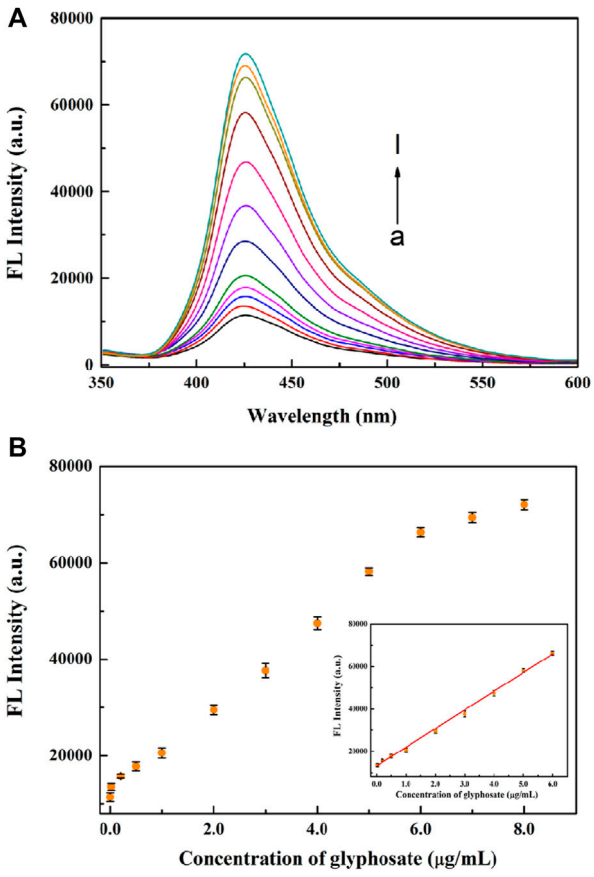

FIGURE 6
(A) The response of fluorescence emission spectra with different concentrations of glyphosate. The concentrations of glyphosate from a to I were 0, 0.02, 0.2, 0.5, 1, 2, 3, 4, 5, 6, 7 and 8 μg/ml, respectively. **(B)** The relationship between the fluorescence intensity and glyphosate concentrations. Inset: linear curve for glyphosate (0.02–6 μg/ml).

10.3389/fchem.2022.1036683

TABLE 1 Detection of glyphosate in river water and lake water samples.

Samples	Added (μg/mL)	Found (μg/mL)	Recovery (%)	RSD (%, n = 3)
river water				
1	0.200	0.205	102.7	2.1
2	1.000	0.972	97.2	3.5
3	5.000	5.218	104.4	2.9
lake water				
1	0.200	0.193	96.5	2.6
2	1.000	1.026	102.6	2.2
3	5.000	5.162	103.2	3.3

The fluorescence intensity and the glyphosate concentration in the ranged from 0.02 μg/ml to 6.0 μg/ml shows a good linear relationship (inset of Figure 6B). The linear equation was F = 8,814.14C + 13143.35 (C: the concentration of glyphosate, F: the fluorescence intensity at 426 nm, R^2 = 09968). The limit of detection is 0.01 μg/ml, which is substantially lower than the maximum residue of 0.7 μg/ml in drinking water by the US EPA and GB5749-2022 (Drinking Water Standards and Health Advisories., 2018; Standardization Administration of China., 2022). The sensitivity is comparable to or better than most other methods for glyphosate assay (Chang et al., 2016; Hou et al., 2020; Tai et al., 2022).

4.7 Selectivity study

The selectivity of this sensor was verified by detecting other pesticides including carbendazim, carbaryl, parathion, malathion, chlorpyrifos, diazinon and omethoate. As displayed in Figure 7, compared to other pesticides, only glyphosate could induce a remarkable fluorescence enhancement. These results indicated that the present assay has good selectivity for glyphosate detection.

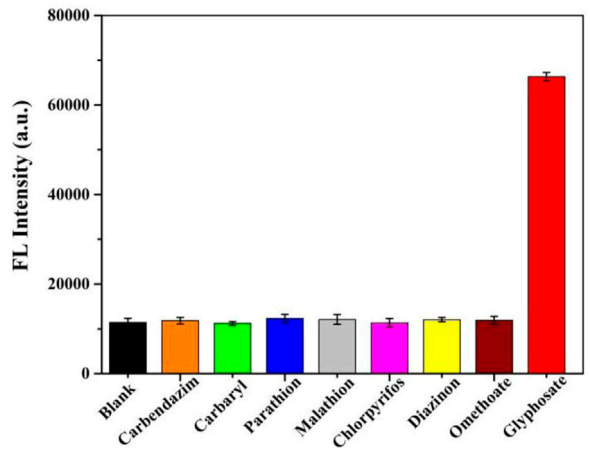

FIGURE 7
Selectivity of the present method for glyphosate. The concentration was 5 μg/ml for glyphosate, and the concentrations were 100 μg/ml for other pesticides.

4.8 Analysis of real samples

To evaluate the applicability of the present method in real samples, the recovery experiments were estimated in river water and lake water samples. The samples were spiked with different concentrations of glyphosate and detected. As can be seen in Table 1, The recoveries ranged from 96.5 to 104.4%. These results indicated the proposed method had great potential for glyphosate detection in complicated real samples.

5 Conclusion

In summary, we constructed a novel "on-off-on" sensor for sensitive detection of glyphosate *via* CN NNS as fluorescence probe. The fluorescence change of system can be obtained by the combination between copper ions and nanosheets or glyphosate, achieving the detection of glyphosate. The developed method was convenient, low-cost and rapid without tedious procedures. It exhibits a high sensitivity with a detection limit of 0.01 μg/ml. Besides that, a satisfactory performance in actual samples was also obtained. Therefore, the developed approach is expected to possess potential ;application in environmental safety and biological fields.

Data availability statement

The original contributions presented in the study are included in the article/supplementary material, further inquiries can be directed to the corresponding author.

Author contributions

YQ and GY conceived this work. YQ and RH contributed to the experimental efforts and collected the data. YQ and GY drafted and reviewed the manuscript.

Funding

This work was supported by Guangxi Scientific and Technological Base and Personnel Project (Grant No. GUIKEAD22035051); Open Project of Key Laboratory of Longevity and Aging-related Diseases (Guangxi Medical University), Ministry of Education (Grant No. KLLAD202103); The Basic Ability Enhancement Program for Young and Middle-aged Teachers of Guangxi (Grant No. 2022KY0098).

Conflict of interest

The authors declare that the research was conducted in the absence of any commercial or financial relationships that could be construed as a potential conflict of interest.

Publisher's note

All claims expressed in this article are solely those of the authors and do not necessarily represent those of their affiliated organizations, or those of the publisher, the editors and the reviewers. Any product that may be evaluated in this article, or claim that may be made by its manufacturer, is not guaranteed or endorsed by the publisher.

References

Chang, Y., Zhang, Z., Hao, J., Yang, W., and Tang, J. (2016). A simple label free colorimetric method for glyphosate detection based on the inhibition of peroxidase-like activity of Cu(II). *Sensors Actuators B Chem.* 228, 410–415. doi:10.1016/j.snb.2016.01.048

Ding, J., Guo, H., Liu, W., Zhang, W., and Wang, J. (2015). Current progress on the detection of glyphosate in environmental samples. *J. Sci. Appl. Biomed.* 3 (6), 88–95.

Ding, S., Lyu, Z., Li, S., Ruan, X., Fei, M., Zhou, Y., et al. (2021). Molecularly imprinted polypyrrole nanotubes based electrochemical sensor for glyphosate detection. *Biosens. Bioelectron. X.* 191, 113434. doi:10.1016/j.bios.2021.113434

Dong, Y., Wang, Q., Wu, H., Chen, Y., Lu, C-H., Chi, Y., et al. (2016). Graphitic carbon nitride materials: Sensing, imaging and therapy. *Small* 12 (39), 5376–5393. doi:10.1002/smll.201602056

Drinking Water Standards and Health Advisories (2018). *United States environmental protection Agency*. Washington, DC: US EPA.

Duan, J., Zhang, Y., Yin, Y., Li, H., Wang, J., and Zhu, L. (2018). A novel "on-off-on" fluorescent sensor for 6-thioguanine and Hg2+ based on g-C3N4 nanosheets. *Sensors Actuators B Chem.* 257, 504–510. doi:10.1016/j.snb.2017.10.071

Gasnier, C., Dumont, C., Benachour, N., Clair, E., Chagnon, M. C., and Seralini, G. E. (2009). Glyphosate-based herbicides are toxic and endocrine disruptors in human cell lines. *Toxicology* 262 (3), 184–191. doi:10.1016/j.tox.2009.06.006

González-Martínez, M. A., Brun, E. M., Puchades, R., Maquieira, A., Ramsey, K., and Rubio, F. (2005). Glyphosate immunosensor. Application for water and soil analysis. *Anal. Chem.* 77 (13), 4219–4227. doi:10.1021/ac048431d

Guo, X., Yue, G., Huang, J., Liu, C., Zeng, Q., and Wang, L. (2018). Label-free simultaneous analysis of Fe(III) and ascorbic acid using fluorescence switching of ultrathin graphitic carbon nitride nanosheets. *ACS Appl. Mat. Interfaces* 10 (31), 26118–26127. doi:10.1021/acsami.8b10529

Guo, Y., Deng, L., Li, J., Guo, S., Wang, E., and Dong, S. (2011). Hemin-graphene hybrid nanosheets with intrinsic peroxidase-like activity for label-free colorimetric detection of single-nucleotide polymorphism. *ACS Nano* 5 (2), 1282–1290. doi:10.1021/nn1029586

Guyton, K. Z., Loomis, D., Grosse, Y., Grosse, F. E., Benbrahim-Tallaa, L., Guha, N., et al. (2015). Carcinogenicity of tetrachlorvinphos, parathion, malathion, diazinon, and glyphosate. *Lancet Oncol.* 16 (5), 490–491. doi:10.1016/S1470-2045(15)70134-8

Hou, J., Wang, X., Lan, S., Zhang, C., Hou, C., He, Q., et al. (2020). A turn-on fluorescent sensor based on carbon dots from Sophora japonica leaves for the detection of glyphosate. *Anal. Methods* 12, 4130–4138. doi:10.1039/d0ay01241f

Liu, H., Zhang, P., Zhang, C., Chen, Jian., and Jiang, J-H. (2020). Self-assembly of a dual-targeting and self-calibrating ratiometric polymer nanoprobe for accurate hypochlorous acid imaging. *ACS Appl. Mat. Interfaces* 12 (41), 45822–45829. doi:10.1021/acsami.0c13857

Liu, P., Li, B., Zheng, J., Liang, Q., Wu, C., Huang, L., et al. (2021). A novel N-nitrosation-based ratiometric fluorescent probe for highly selective imaging endogenous nitric oxide in living cells and zebrafish. *Sensors Actuators B Chem.* 329, 129147. doi:10.1016/j.snb.2020.129147

Muñoz, R., Guevara-Lara, A., Santos, J. L. M., Miranda, J. M., and Rodriguez, J. A. (2019). Determination of glyphosate in soil samples using CdTe/CdS quantum dots in capillary electrophoresis. *Microchem. J.* 146, 582–587. doi:10.1016/j.microc.2019.01.059

Pérez-Mayán, L., Castro, G., Ramil, M., Cela, R., and Rodríguez, I. (2022). Approaches to liquid chromatography tandem mass spectrometry assessment of glyphosate residues in wine. *Anal. Bioanal. Chem.* 414, 1445–1455. doi:10.1007/s00216-021-03775-w

Qin, Y., Wu, G., Guo, Y., Ke, D., Yin, J., Wang, D., et al. (2020). Engineered glyphosate oxidase coupled to spore-based chemiluminescence system for glyphosate detection. *Anal. Chim. Acta X.* 1133, 39–47. doi:10.1016/j.aca.2020.07.077

Rong, M., Lin, L., Song, X., Wang, Y., Zhong, Y., Yan, J., et al. (2015a). Fluorescence sensing of chromium (VI) and ascorbic acid using graphitic carbon nitride nanosheets as a fluorescent "switch. *Biosens. Bioelectron. X.* 68, 210–217. doi:10.1016/j.bios.2014.12.024

Rong, M., Lin, L., Song, X., Zhao, T., Zhong, Y., Yan, J., et al. (2015b). A label-free fluorescence sensing approach for selective and sensitive detection of 2, 4, 6-trinitrophenol (TNP) in aqueous solution using graphitic carbon nitride nanosheets. *Anal. Chem.* 87 (2), 1288–1296. doi:10.1021/ac5039913

Royer, A., Beguin, S., Tabet, J. C., Hulot, S., Reding, M. A., and Communal, P. Y. (2000). Determination of glyphosate and aminomethylphosphonic acid residues in water by gas chromatography with tandem mass spectrometry after exchange ion resin purification and derivatization. Application on vegetable matrixes. *Anal. Chem.* 72 (16), 3826–3832. doi:10.1021/ac000041d

Salehnia, F., Hosseini, M., and Ganjali, M. R. (2017). A fluorometric aptamer based assay for cytochrome C using fluorescent graphitic carbon nitride nanosheets. *Microchim. Acta* 184, 2157–2163. doi:10.1007/s00604-017-2130-6

Schütze, A., Morales-Agudelo, P., Vidal, M., Calafat, A. M., and Ospina, M. (2021). Quantification of glyphosate and other organophosphorus compounds in human urine *via* ion chromatography isotope dilution tandem mass spectrometry. *Chemosphere* 274, 129427. doi:10.1016/j.chemosphere.2020.129427

Standardization Administration of China (2022). *Standardization Administration of China*. GB 5749-2022. Available at: https://openstd.samr.gov.cn/bzgk/gb/newGbInfo?hcno=99E9C17E3547A3C0CE2FD1FFD9F2F7BE.

Sun, L., Kong, D., Gu, W., Guo, X., Tao, W., Shan, Z., et al. (2017). Determination of glyphosate in soil/sludge by high performance liquid chromatography. *J. Chromatogr. A* 1502, 8–13. doi:10.1016/j.chroma.2017.04.018

Sun, Y., Zhang, Y., Zhang, H., Liu, M., and Liu, Y. (2020). Integrating highly efficient recognition and signal transition of g-C3N4 embellished Ti3C2 MXene hybrid nanosheets for electrogenerated chemiluminescence analysis of protein kinase activity. *Anal. Chem.* 92, 10668–10676. doi:10.1021/acs.analchem.0c01776

Surapong, N., and Burakham, R. (2021). Magnetic molecularly imprinted polymer for the selective enrichment of glyphosate, glufosinate, and aminomethylphosphonic acid prior to high-performance liquid chromatography. *ACS Omega* 6 (41), 27007–27016. doi:10.1021/acsomega.1c03488

Tai, S., Qian, Z., Ren, H., Barimah, A. O., Peng, C., and Wei, X. (2022). Highly selective and sensitive colorimetric detection for glyphosate based on β-CD@DNA-CuNCs enzyme mimics. *Anal. Chim. Acta X.* 1222, 339992. doi:10.1016/j.aca.2022.339992

Ti, M., Li, Y., Li, Z., Zhao, D., Wu, L., Yuan, L., et al. (2021). A ratiometric nanoprobe based on carboxylated graphitic carbon nitride nanosheets and Eu3+ for the detection of tetracyclines. *Analyst* 146 (3), 1065–1073. doi:10.1039/d0an01826k

Valle, A. L., Mello, F. C. C., Alves-Balvedi, R. P., Rodrigues, L. P., and Goulart, L. R. (2019). Glyphosate detection: Methods, needs and challenges. *Environ. Chem. Lett.* 17, 291–317. doi:10.1007/s10311-018-0789-5

Wang, X., Xiong, H., Chen, T., Xu, Y., Bai, G., Zhang, J., et al. (2021). A phosphorus-doped g-C3N4 nanosheets as an efficient and sensitive fluorescent probe for Fe3+ detection. *Opt. Mat. (Amst).* 119, 111393. doi:10.1016/j.optmat.2021.111393

Wozniak, E., Reszka, E., Jablonska, E., Balcerczyk, A., Broncel, M., and Bukowska, B. (2020). Glyphosate affects methylation in the promoter regions of selected tumor suppressors as well as expression of major cell cycle and apoptosis drivers in PBMCs (*in vitro* study). *Toxicol. Vitro* 63, 104736. doi:10.1016/j.tiv.2019.104736

Wu, J., Chen, X., Zhang, Z., and Zhang, J. (2022). "Off-on" fluorescence probe based on green emissive carbon dots for the determination of Cu2+ ions and glyphosate and development of a smart sensing film for vegetable packaging. *Microchim. Acta* 189 (3), 131. doi:10.1007/s00604-022-05241-5

Xu, M., Gao, Y., Li, Y., Li, X., Zhang, H., Han, X. X., et al. (2018). Indirect glyphosate detection based on ninhydrin reaction and surface-enhanced Raman scattering spectroscopy. *Spectrochimica Acta Part A Mol. Biomol. Spectrosc.* 197, 78–82. doi:10.1016/j.saa.2018.01.014

Zhang, X., Yang, P., and Jiang, S. P. (2021). The edge-epitaxial growth of yellow g-C3N4 on red g-C3N4 nanosheets with superior photocatalytic activities. *Chem. Commun.* 57, 3119–3122. doi:10.1039/d1cc00209k

Zhang, Y., Zhang, Y., Yue, Y., Chao, J., Huo, F., and Yin, C. (2020). Based on morpholine as luminescence mechanism regulation and organelle targeting dual function Cys NIR specific biological imaging probe. *Sensors Actuators B Chem.* 320, 128348. doi:10.1016/j.snb.2020.128348

Zhao, Y., Yan, Y., Liu, C., Zhang, D., Wang, D., Ispas, A., et al. (2022). Plasma-assisted fabrication of molecularly imprinted NiAl-LDH layer on Ni nanorod arrays for glyphosate detection. *ACS Appl. Mat. Interfaces* 14 (31), 35704–35715. doi:10.1021/acsami.2c08500

Zheng, Y., Liu, Y., Wei, F., Xiao, H., Mou, J., Wu, H., et al. (2021). Functionalized g-C3N4 nanosheets for potential use in magnetic resonance imaging-guided sonodynamic and nitric oxide combination therapy. *Acta Biomater.* 121, 592–604. doi:10.1016/j.actbio.2020.12.011

Zhuang, Q., Sun, L., and Ni, Y. (2017). One-step synthesis of graphitic carbon nitride nanosheets with the help of melamine and its application for fluorescence detection of mercuric ions. *Talanta* 164, 458–462. doi:10.1016/j.talanta.2016.12.004

frontiers | Frontiers in Chemistry

TYPE Original Research
PUBLISHED 04 October 2022
DOI 10.3389/fchem.2022.1013994

OPEN ACCESS

EDITED BY
He Xiaojun,
Wenzhou Medical University, China

REVIEWED BY
Jin Huang,
Guangxi Medical University, China
Si-Yang Liu,
Sun Yat-sen University, China

*CORRESPONDENCE
Gang Liang,
lianggang@gxmu.edu.cn

SPECIALTY SECTION
This article was submitted to Nanoscience, a section of the journal Frontiers in Chemistry

RECEIVED 08 August 2022
ACCEPTED 02 September 2022
PUBLISHED 04 October 2022

CITATION
Chen T, Kou Y, Zheng R, Wang H and Liang G (2022), Nanoengineered, magnetically guided drug delivery for tumors: A developmental study. *Front. Chem.* 10:1013994. doi: 10.3389/fchem.2022.1013994

Nanoengineered, magnetically guided drug delivery for tumors: A developmental study

Tieyu Chen, Yanyu Kou, Ruiling Zheng, Hailun Wang and Gang Liang*

Pharmaceutical College, Guangxi Medical University, Nanning, China

Fighting against tumors is an ongoing challenge in both medicinal and clinical applications. In recent years, chemotherapy, along with surgery, has significantly improved the situation to prolong life expectancy. Theoretically, and regardless of dosage, we now have drugs that are strong enough to eliminate most tumors. However, due to uncontrollable drug distribution in the body, it is difficult to increase treatment efficiency by simply increasing dosages. For this reason, the need for a drug delivery system that can release "bombs" at the target organ or tissue as precisely as possible has elicited the interest of researchers. In our work, we design and construct a silica-based nanocomposite to meet the above demand. The novel nanocomposite drug carrier can be guided to target tumors or tissue by a magnetic field, since it is constructed with superparamagnetic Fe_3O_4 as the core. The Fe_3O_4 core is clad in a mesoporous silica molecular sieve MCM-41 (represented as MS, in this article), since this MS has enormous ordered hexagonal caves providing sufficient space to hold the drug molecules. To modify the magnetically guided carriers so that they become both magnetically guided and light-responsive, benzophenone hydrazone is coupled into the molecular sieve tunnel. When a certain wavelength of light is imposed on the gating molecules, C=N double bonds vibrate and swing, causing the cavity that holds the drug molecules to change size and open the tunnels. Hence, the nanocomposite has the ability to release loaded drugs with light irradiation. The structure, loading abilities, and the size of the nanocomposite are inspected with a scanning electron microscope, a transmission electron microscope, thermogravimetry analysis, N_2 adsorption/desorption, and dynamic light scattering The biocompatibility and *in vitro* drug molecule controlled release are tested with an SMMC-7721 cell line.

KEYWORDS

stimuli-responsive, superparamagnetic, drug delivery, daunorubicin, magnetic guided, nanocomposite

Introduction

Hepatocellular carcinoma (HCC) is a commonly found cancer, the third largest cause of cancer-related deaths worldwide, and the largest in Southeast Asia (Han et al., 2011; Yen et al., 2020; Zheng et al., 2022). Surgery and chemotherapy are significant in the battle against hepatocellular carcinoma, saving millions of patients. Daunorubicin (DNR) is a kind of anthracycline used clinically as a chemotherapy reagent, mainly curing cancers such as acute myeloid leukemia, acute lymphoblastic leukemia, and Kaposi's sarcoma (Deng et al., 2021; Samosir et al., 2021; Shepherd et al., 2021). However, it is not the first drug of choice for HCC because daunorubicin can be turned into daunorubicinol in the liver with serious cardiac effects. However, the situation has changed since researchers discovered that the combination of DNR with epigallocatechin-3-gallate (EGCG) and its derivatives, can reduce the production of daunorubicinol (Li et al., 2014; Zhou et al., 2020). This brings relief to those patients who have relapsed after treatment with doxorubicin, as well as to patients with multidrug-resistant liver cancer. Yet simply replacing doxorubicin with DNR, or combining the two drugs for chemotherapy, cannot alter the shortcomings in this traditional treatment for liver cancer: i.e., short half-life, inadequate lipid/water partition, and non-selective release to tumor tissue (Chang and Wang, 2018; Qiu et al., 2020). Some researchers have thus devoted themselves to the modification of novel DNR using advanced carriers. The most commonly seen proposal is liposomal modifying methods, which mainly involve improving the lipid-water partition coefficiency or bioavailability (Krauss et al., 2019; Bewersdorf et al., 2022). Some research groups have realized that the "smart-release" of the drug can offer another more important improvement, and have proposed a series of conditionally sensitive formulations (Zhang et al., 2012; Uematsu et al., 2018). Regrettably, few research groups have designed drug carriers for DNR that can achieve all the necessary requirements.

In recent years, silica-based mesoporous nanocomposites have been adopted as the most focused functional drug delivery system (DDS). The major reason is that the silanols in molecular sieves are easily modified, so that some additional properties can be easily introduced by connecting certain functional groups or molecules. Another reason is that these mesoporous materials have an extremely large surface area and pore space and are inherently suitable as supports for catalysts and some other molecules (Sun et al., 2009; Meireles et al., 2021). It is generally accepted that a successful composite for a drug should be able to load sufficient drug molecules; it should also tightly lock the drug molecules when they do not need to be released. Furthermore, the ability to deliver drug molecules to specific tissues or organs and hence minimize the possibility of wrong transport to other sites is also essential. Moreover, if the DDS can respond to certain stimuli, including light, heat, or a change in solution pH, it can then utilize this response as a "switch" to release host molecules. Most of the recent research has been devoted to meeting one or two of the requirements mentioned above, and research into a DDS that can fully achieve the ideal state, especially one suitable for DNR, has rarely been seen.

Hence, in our search, we constructed a novel "smart" nanocomposite for drug delivery. As mentioned above, the drug carrier should be able to target the morbid tissue in the first place, and therefore superparamagnetic Fe_3O_4 nanoballs were chosen to act as the core. The nanocomposite can be freely dispersed in the solution in the absence of an externally strong magnetic field and can aggregate to the tumor site when a strong magnetic field is applied. As the host molecule holder, the ferrous oxide was modified and coated with the MCM-41 molecular sieve. In the next step, the silica-based molecular sieve shell was further coupled with an irradiation-sensitive organic ligand which acts as "smart" caps for the MCM-41 tunnels, allowing the DDS to manifest different behavior with/without light stimulation. Additionally, biocompatibility as well as the *in vitro* release feather were tested using the MTT method. Preliminary studies show that our DDS has good biocompatibility, and its "smart" controlled release ability also achieves our desired result. According to our design, the site-specific and stimuli-responsive drug delivery system for DNR could now provide an opportunity for hepatocellular carcinoma treatment.

Experiment details

Materials

Daunorubicin hydrochloride (DNR·HCl, purity>98%) was purchased from Chengdu Desite Biological Technology; benzophenone hydrazine was purchased from Shanghai Macklin, and 3-(4,5-dimethyl-2-thiazolyl)-2,5-diphenyltetrazoliumbromide (MTT) was purchased from Beijing Suolaibao Technology. PBS (phosphate buffered saline), Dulbecco's modified Eagle's medium (DMEM), fetal bovine serum (FBS), and trypsin (0.25% in EDTA) were purchased from Wuhan Boside Biological Technology. Penicillin and streptomycin solution with 10,000 units per ml of penicillin, 10,000 μg per ml of streptomycin, tetraethoxysilane (TEOS, AR), 3:1 poly (4-styrenesulfonic acid-co-maleic acid) sodium salt, and (3-chloropropyl) trimethoxysilane (CPTS, purity>98%), were all purchased through Sigma-Aldrich. DCM, absolute ethanol, ethylene glycol, and $NH_3{\cdot}H_2O$ (28 wt %) were purchased from Qingdao Marine Chemicals. Cetyltrimethylammonium bromide (CTAB, AR), $FeCl_3{\cdot}6H_2O$ (AR), and NaOH were purchased from Huai'an Kelong

Chemicals. All solvents or reagents received from the companies were used directly without additional purification.

Instrumental information

A Perkin-Elmer Spectrum-100 FT-IR spectrometer was used for IR testing via the KBr protocol. The morphology and nanocomposite sizes were obtained with a transmission electron microscope (TEM, JEM-2010, JEOL), a scanning electron microscope (SEM, S4800, Hitachi), and dynamic light scattering (DLS, Zetasizer Nano ZS, Malvern). The magnetism was studied via a sample magnetometer (MPM5-XL-5, Quantum Design). In the MTT assay, the OD value was recorded via a microplate reader (Synergy H1, Biotek, wavelength at 490 nm). XRD features were probed with an X-ray diffractometer (Rigaku Multiflex, λ = 1.5418 Å). DNR concentration was tested with UV-Vis and UV-Vis-NIR spectroscopy (UV-1900i, Shimadzu). Pore size and volume were tested by N_2 adsorption/desorption, then calculated by BJH via a Nova-l000 analyzer. DNR loading was obtained via thermogravimetric analysis (TGA, STA-6000, Perkin-Elmer) without specifications. All operations were performed at room temperature.

Synthesis of stimuli-responsive and magnetically guided nanocomposite

For convenience, the nanocomposite in our research was denoted as BEN@MS@Fe_3O_4, since it included the major functions or components of the carrier and was synthesized via a five-step procedure as follows.

The magnetic-guided property of our nanocomposite was introduced by the superparamagnetic Fe_3O_4 core, using a procedure modified from the literature (Gao et al., 2013). 80 ml of the glycol and 2 g of PSS:MA = 3:1 were added to a beaker and stirred supersonically until the solution became clear. To the above solution was added 2.16 g $FeCl_3{\cdot}6H_2O$ and 6 g anhydrous sodium acetate, which was then stirred in r.t. until it became a homogeneous solution. The above mixture was then transferred into a Teflon flask and sealed in an autoclave. The reaction was initiated at 200°C in an oven for 10 h and then terminated by cooling the solution to room temperature. The black Fe_3O_4 product was collected with the help of a magnet, and the product was then purified with ultra-pure water and ethanol and vacuum-dried overnight.

In order to wrap the MCM-41 molecular sieve onto the Fe_3O_4 nanosphere smoothly, the core must first be pre-coated with amorphous silica (Mirzajani et al., 2018). The dried 0.16 g Fe_3O_4 was dissolved into a solution with 40 ml absolute ethanol, 2 ml water, and 2 ml ammonia. The solution was ultrasonicated for 15 min to achieve a homogeneous mixture. In 30 min, through stirring and ultrasonication, a TEOS solution (0.8 ml TEOS in 10 ml ethanol) was uniformly added to the above mixture with a syringe. Ultrasonication continued for another 60 min and the reaction quenched by removing the product, $SiO_2@Fe_3O_4$, with a magnet. The $SiO_2@Fe_3O_4$ was further purified with ultra-pure water and ethanol and vacuum-dried overnight.

In the third step, the MCM-41 mesoporous molecular sieve was wrapped onto the surface of the $SiO_2@Fe_3O_4$ nanosphere where it formed a new shell. Then 0.1 g $SiO_2@Fe_3O_4$ was placed in 10 ml ultrapure water and ultrasonicated for 20 min, before the above suspension was added to a solution of 40 ml 0.1 mol/L of CTAB (1.46 g CTAB dissolved in 40 ml ultrapure water), and a solution of 0.6 ml NaOH (1 g NaOH in 20 ml ultrapure water), and mixed together. Under continuous ultrasonication, 50 μl of TEOS was injected into the mixture every 5 min to a total amount of 0.3 ml (Vetrivel et al., 2010). Ultrasonication continued for another 60 min, and the reaction was then quenched by removing the product with a magnet. In order to remove the CTAB used as a template while forming the molecular sieve tunnels, the product was transferred into a solution with 30 ml absolute ethanol and 4 ml concentrated HCl, and stirred continuously under ultrasonication for 1 h. The reaction was then quenched by collecting the product (denoted as MS@Fe_3O_4) with a magnet, before the composite was rinsed with ultra-pure water and vacuum-dried overnight.

In our nanocomposite, CPTS acts as a bridge between the molecular sieve and the gating molecule as a silane coupling reagent. 0.5 g MS@Fe_3O_4 was dispersed in a solution of 5 ml CPTS and 75 ml dried toluene with the help of ultrasonication, and the temperature increased to reflux for 8 h. The reaction was quenched by cooling to r.t., and the product (named CPTS@MS@Fe_3O_4) was rinsed with ultra-pure water and ethanol and vacuum-dried at 50°C overnight.

The CPTS@MS@Fe_3O_4 was coupled with a gating molecule to yield the final nanocomposite as a drug carrier. To a flask with 100 ml DMF, 0.25 g CPTS@MS@Fe_3O_4 and 0.5 g benzophenone hydrazone were added. The mixture was ultrasonicated for 30 min, and then the flask was heated to reflux for 8 h. The reaction was quenched by cooling to r.t., then the final product (named BEN@MS@Fe_3O_4) was rinsed with ultra-pure water and ethanol, and vacuum-dried at 50°C overnight.

DNR loading and release feature of BEN@MS@Fe_3O_4

DNR was loaded onto the nanocomposite under 310 nm light irradiation to activate the gating ligand. To a 3 ml aquatic solution of 20 mg/ml DNR, 20 mg BEN@MS@Fe_3O_4 was added. After being fully dispersed under ultrasonication, it was irradiated and stirred overnight in order for the DNR to reach a loading and release balance.

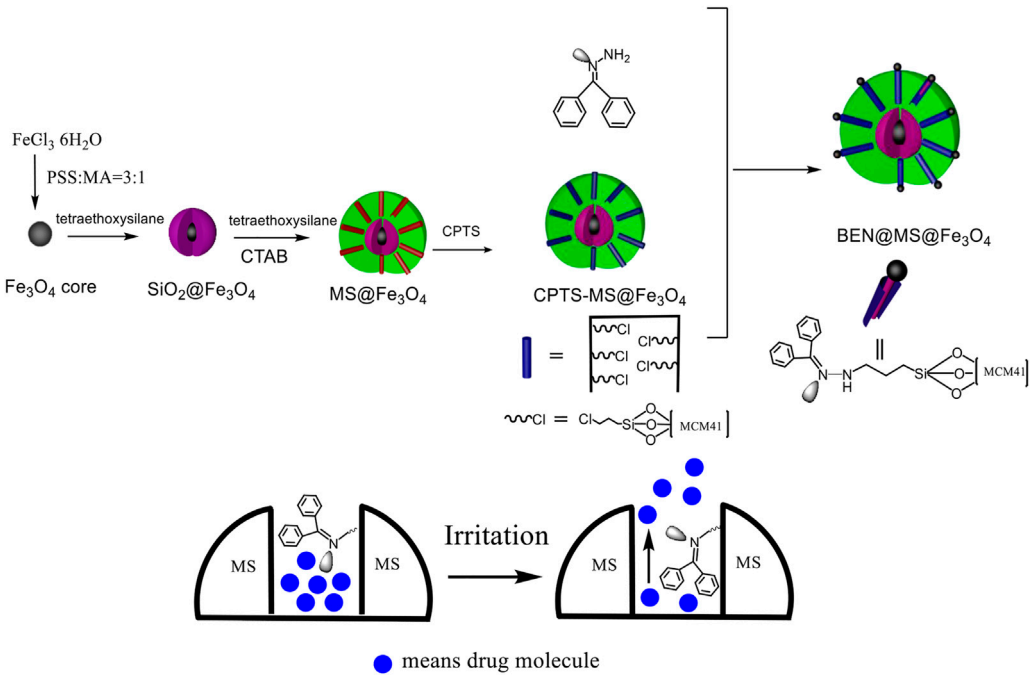

SCHEME 1
Construction of drug carrier and molecules release process.

The carriers loaded with the drug molecule (denoted as DNR@MS@Fe_3O_4) were gathered with a magnet, and the nanocomposite was rinsed with ultrapure water to remove the DNR from the surface. The DNR@MS@Fe_3O_4 was vacuum-dried at 50°C overnight and tested via TGA. The loading rate of DNR on BEN@MS@Fe_3O_4 was calculated as 1.25% from the difference between DNR@MS@Fe_3O_4 and BEN@MS@Fe_3O_4 revealed in the TGA.

In order to provide data references for the following *in vitro* cell experiments, the release property of drug carriers under light/non-light stimulation was firstly tested in the pure solvent state without cells. To a 10 ml quartz vial with 5 ml PBS solution, 5 mg DNR@MS@Fe_3O_4 was added and continuously stirred and irritated. At 0.25, 0.5, 1, 1.5, 2, 3, 6, and 8 h, the DNR concentration was obtained via spectrometer at 480 nm. In the case of irradiation, the early release rate was more rapid. An increase of up to 39% can be seen in the results section.

Biocompatibility of BEN@MS@Fe_3O_4

The cytotoxicity of BEN@MS@Fe_3O_4 was checked by MTT assay (Ye et al., 2020). In order to exclude the possibility that the carrier may kill hepatocellular carcinoma tissues or cells when using DNR loaded on the nanocomposite during the chemo treatment, SMMC-7721 (human hepatocarcinoma cells, purchased from the Shanghai Institute of Cell Research, Chinese Academy of Sciences) were chosen for our experiment. The cells were cultured in a full DMEM medium, which contained FBS, 89% RPMI 1640, and 1% penicillin-streptomycin. The viability of the cell line when treated with different concentrations of added BEN@MS@Fe_3O_4 was evaluated by MTT testing. The SMMC-7721 cell line of 180 µl was seeded into a 96-well plate when it reached the exponential growth state, then put into the incubator for another 24 h to allow the cells to adhere to the base of the wells. When around 70 to 80 percent coverage of the well area was observed under microscopy, a solution of BEN@MS@Fe_3O_4 (concentrations sequenced at 1.562, 3.12, 6.25, 12.5, 25.0, 50.0 µg/ml) was added to each well. After that, the 96-well plate with cell line and nanocomposite was returned to the incubator for 24 h in 5% CO_2 at 37°C. The biocompatibility can be seen in the following: the medium with nanocomposite was replaced with MTT and incubated for another 4 h, then the incubation was quenched with 100 µl DMSO added to each of the wells. The OD reading was recorded at a wavelength of 490 nm.

$$\text{cell viability (\%)} = [A]_{test}/[A]\text{control} \times 100\%$$

All tests were performed with 3 repeated wells and the cell viability was calculated using the above equation.

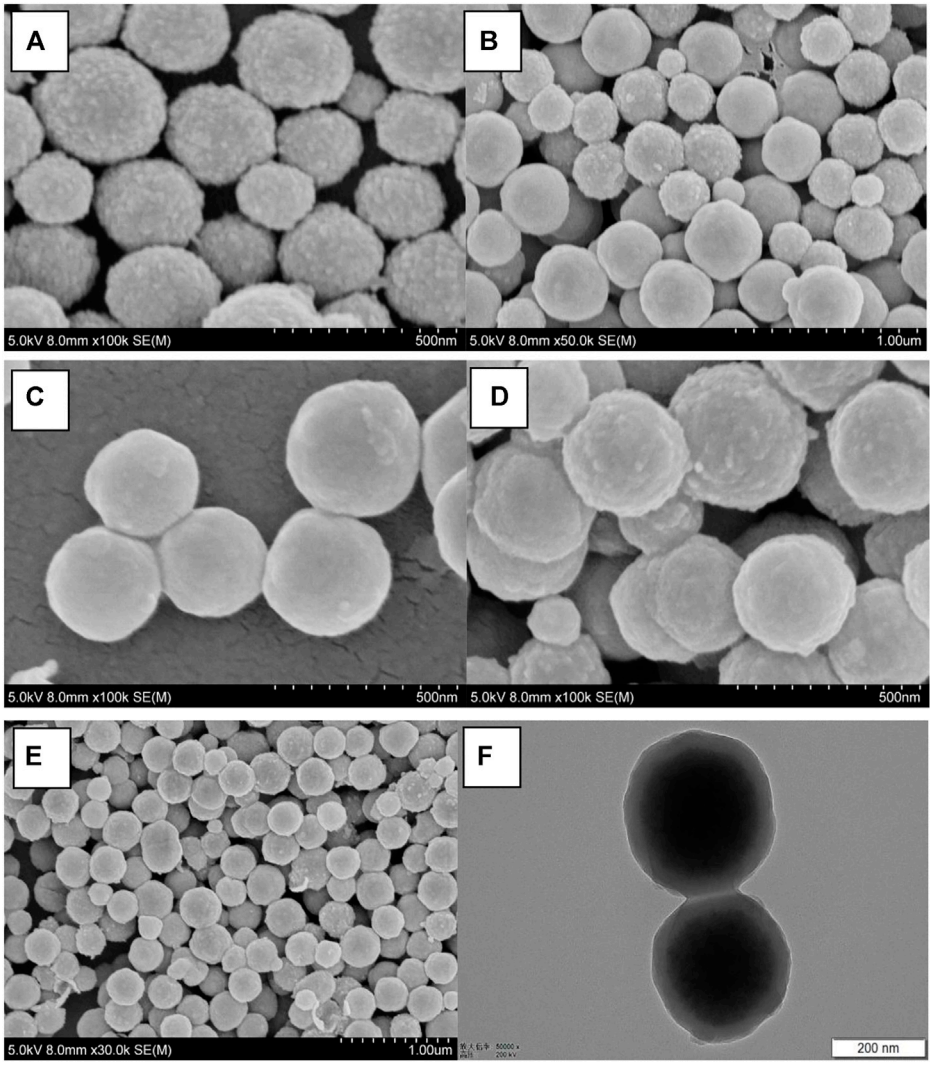

FIGURE 1
SEM micrographs of **(A)** Fe_3O_4 particles, **(B)** SiO_2@Fe_3O_4, **(C)** MS@Fe_3O_4, **(D)** BEN@MS@Fe_3O_4, **(E)** DNR@MS@Fe_3O_4, and the TEM image of **(F)** BEN@MS@Fe_3O_4.

In vitro release performance of DNR@MS@Fe_3O_4

The stimuli release performance of DNR@MS@Fe_3O_4 and the stimuli and magnetic-guided release were carried forward upon a 96-well plate and 6-well plate with MTT protocols. In the stimuli release performance experiment, the SMMC-7721 cell line was used and divided into stimuli and non-stimuli groups. The 96-well plate was prepared with the same procedure mentioned above in part 2.5. When the 96-well plate was ready, different amounts of DNR@MS@Fe_3O_4 were added to the well to reach a final concentration of 3.8 mg/ml, 3.0 mg/ml, and 2.3 mg/ml, acting as high, medium, and low dosages, respectively. Considering that 60% of the DNR will be released within 3 h from DNR@MS@Fe_3O_4, this is equivalent to DNR dosages of 50 μM, 40 μM, and 30 μM at 3 h. Both groups were then incubated for 6 h while the stimuli group received extra irritation. The OD reading was performed, as mentioned in part 2.5.

In the stimuli release and magnetic-guided performance experiment, a 6-well plate was chosen in order to visualize the result. 1 ml of SMMC-7721 cell-line medium solution containing, 30,000 cells, was seeded into each well of the plate when it reached the exponential growth state and placed into the incubator for another 24 h to allow the cells to adhere to the base of the well. For the magnetic-guided group, the dual functional group, and the control group, DNR@MS@Fe_3O_4 was added to reach a final concentration of 3.0 mg/ml, and then the plate was

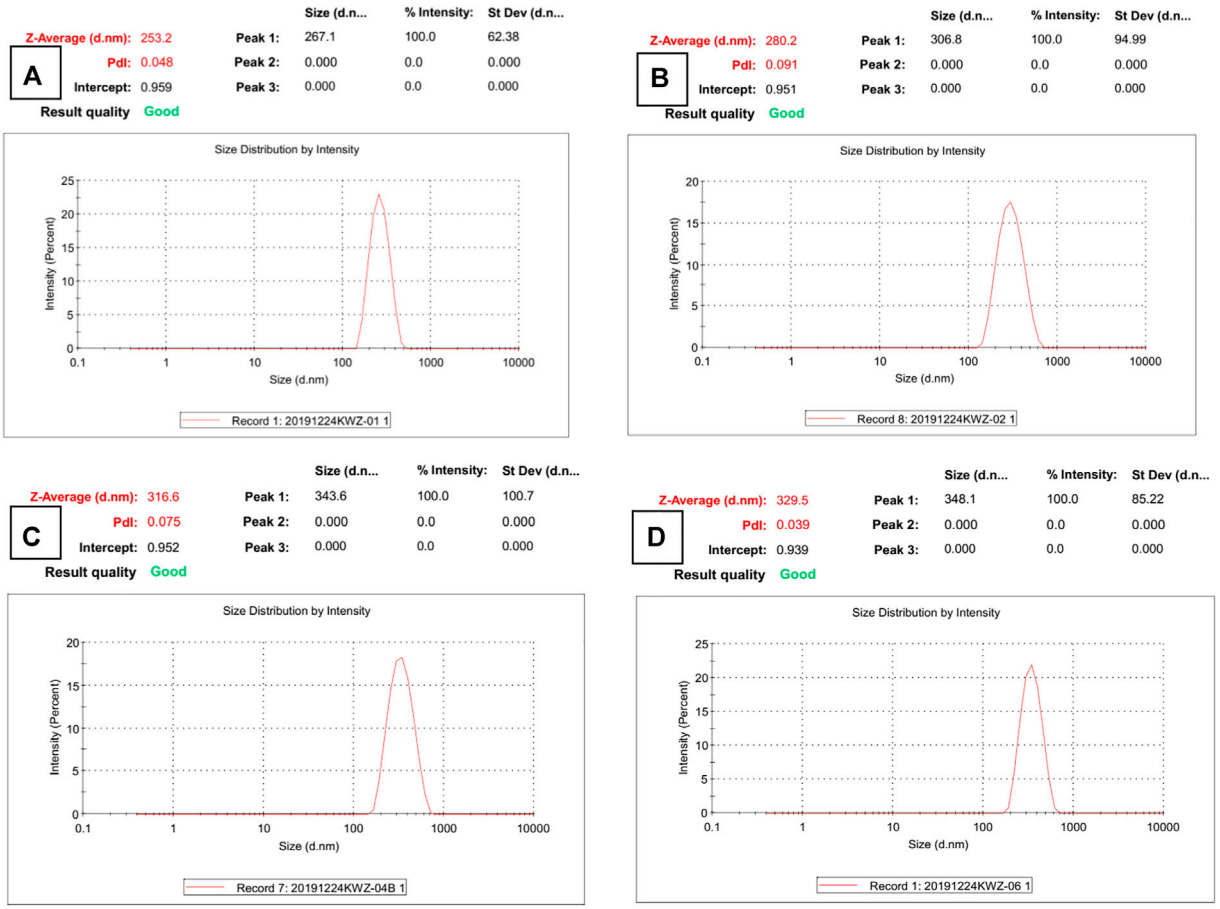

FIGURE 2
DLS results of **(A)** Fe_3O_4 particles, **(B)** SiO_2@Fe_3O_4, **(C)** MS@Fe_3O_4, and **(D)** BEN@MS@Fe_3O_4.

returned to the incubator for 6 h. In the final step, the medium with DNR@MS@Fe_3O_4 was replaced by MTT and incubated for another 4 h, before rejecting the MTT solution to visualize the result.

Results and discussion

Design and synthesis scheme of nanocomposites: BEN@MS@Fe_3O_4

The drug carrier in our research was firstly constructed with $FeCl_3{\cdot}6H_2O$ as the starting material, as shown in Scheme 1. The superparamagnetic core was formed via a hydrothermal reaction to grant the drug carrier the ability to be magnetically guided. This means the drug carrier can be easily switched from aggregation to dispersion status depending upon the presence/absence of the magnetic field and thus can be site-specific to the morbid tissues or organs. With the additional coating of a SiO_2 crust and molecular shell, a typical core-shell nanocomposite was obtained. The mesoporous MCM-41 can offer plenty of room for host molecules. In the following steps, by linking CPTS and gating molecules, the final drug carrier was formed. The gating molecule bonded to the MCM-41 has a C=N bonding which can flip over under certain irritation. This allows the molecular sieve channels to change their size and adjust the release rate of molecules.

Size, morphology, and distributional features of the nanocomposite

The micrograph (SEM and TEM) images are shown in Figure 1, and the DLS result is shown in Figure 2. The surface of Fe_3O_4, as prepared by the hydrothermal reaction, is relatively rough. In fact, each large nano ball is actually made up of smaller spheres, which is a major feature of Fe_3O_4 prepared via hydrothermal reaction. The size of the Fe_3O_4 nanoparticle

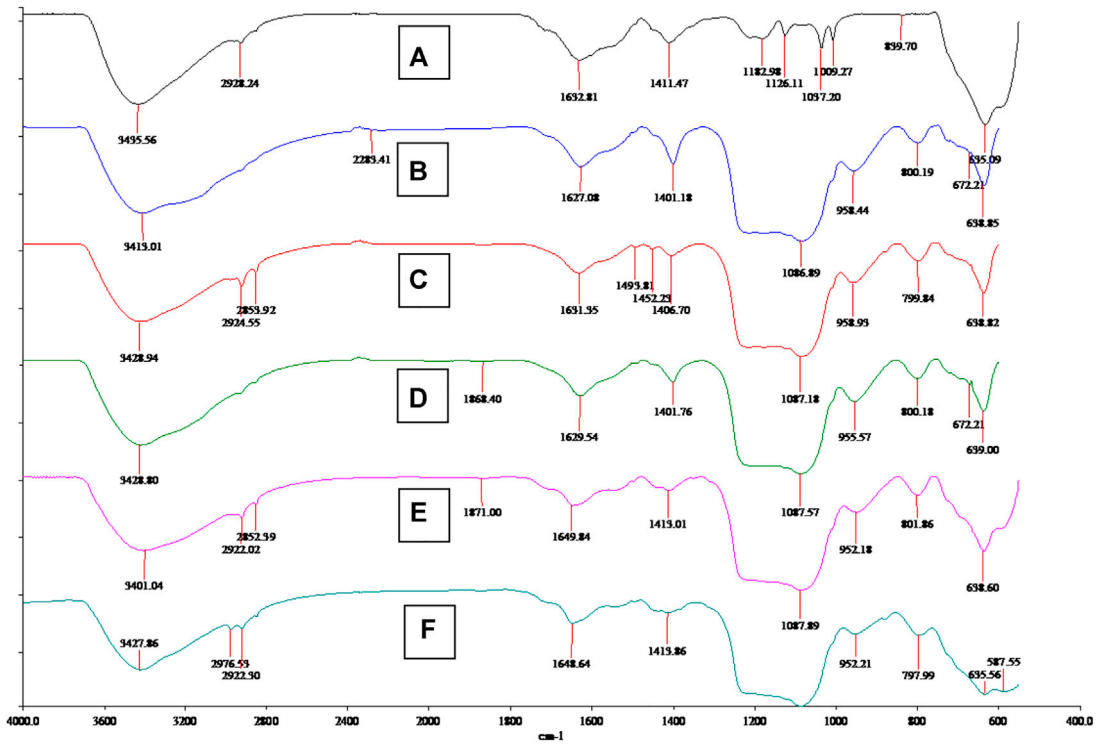

FIGURE 3
FT-IR spectrum of **(A)** Fe_3O_4 particles, **(B)** SiO_2@Fe_3O_4, **(C)** MS@Fe_3O_4 (with template), **(D)** MS@Fe_3O_4 (without template), **(E)** CPTS@MS@Fe_3O_4, and **(F)** BEN@MS@Fe_3O_4.

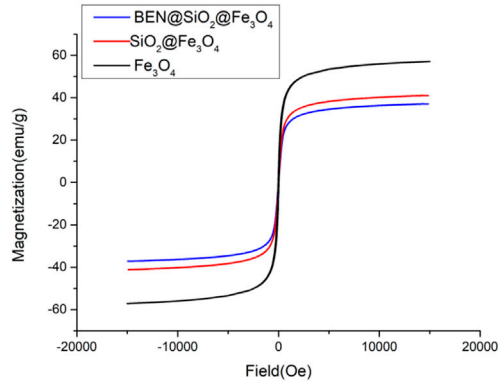

FIGURE 4
Magnetization loops for BEN@MS@Fe_3O_4, SiO_2@Fe_3O_4, and Fe_3O_4.

core prepared in the first step is about 250 nm (Figure 1A), which is consistent with the DLS testing result. The Pdi value is much less than 0.1 (Figure 2A), indicating that particle size uniformity, as well as the dispersion of the particles in the solution, is excellent, which will benefit the subsequent modification. After being wrapped in amorphous silica, the surface of the nanospheres became smoother (Figure 1B), and the average diameter of the nanospheres increased from 250 to 280 nm (Figure 2B). After further modification by molecular sieve wrapping, the diameter of the nanosphere exceeded 300 nm (Figure 2C), and the surface was smoother, close to a perfect sphere (Figure 1C). From the above, it can be inferred that the thicknesses of the amorphous silica shell and the molecular sieve shell are about 13 and 18 nm, respectively. In the subsequent reaction, both the organosilicon ligand reagent and the gating molecule were combined with the silanol groups in the molecular sieve tunnels. In the meanwhile, the DNR was mainly loaded into the MCM-41 hexagonal tunnels. Therefore, the shape and size of the subsequent nanocomposite (BEN@MS@Fe_3O_4, DNR@MS@Fe_3O_4) did not show significant change.

The final image of Figure 1F presents a perspectival view of the drug carrier BEN@MS@Fe_3O_4 by TEM. From the image, we can easily see the core-shell structure of the carrier. The darker sphere in the figure is the superparamagnetic core, and the lighter outer ring is the amorphous silica layer along with the molecular sieve layer. The thickness and dimensions of each component are also consistent with SEM and DLS.

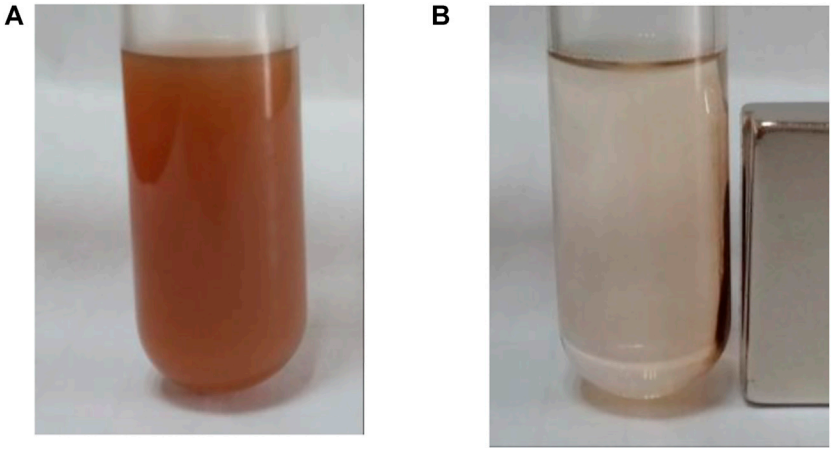

FIGURE 5
BEN@MS@Fe_3O_4 in ethanol solution **(A)** without magnetic field, and **(B)** with the presence of a magnet.

FT-IR spectrum

Besides the morphological analysis, FT-IR analysis also strongly confirmed the nanocomposite structures and organic ligand grafting step. As shown in Figure 3, the Fe_3O_4 spectrum is quite simple, showing Fe-O signal peaks at 3,435 and 635 cm^{-1} (Palomino et al., 2004). After SiO_2 and molecular coating, nanocomposite (B) SiO_2@Fe_3O_4, (C) (with template) MS@Fe_3O_4, (D) (without template) MS@Fe_3O_4, (E) CPTS@MS@Fe_3O_4, and (F) BEN@MS@Fe_3O_4, all showed additional peaks at about 800 and 1,087 cm^{-1}, which was caused by the Si-O vibration (Kefayati et al., 2016). The MCM-41 molecular sieve in our research was prepared with CTAB as a template, therefore before the removal of the CTAB, two obvious peaks at 2,924 and 2,853 cm^{-1} can be seen in the composite (C) (with template) MS@Fe_3O_4. When the CTAB was removed, the above two peaks disappeared, as shown at (D) (without template) MS@Fe_3O_4. The reappearance of the peaks at 2,922 and 2,852 cm^{-1} on CPTS@MS@Fe_3O_4, resorted to the alkyl chain of CPTS, and an additional peak of 2,976 cm^{-1}, indicated that C=N bonding had been successfully established on the final composite (Ravikumar et al., 2008).

Nanocomposite magnetic behavior and features

The carriers prepared in this study should be dispersed without a magnetic field and aggregated with a magnetic field. They must therefore be superparamagnetic. From Figure 4, it can be inferred that the nano core obtained by using the hydrothermal reaction method with PSS: MA as the surfactant is superparamagnetic with a saturation magnetization reading of 58.7 emu/g. After the coating of amorphous silica, the subsequent coating of the molecular sieve, and the coupling modification of the organic ligands, the hysteresis of SiO_2@Fe_3O_4 and BEN@MS@Fe_3O_4 was still zero, suggesting the superparamagnetic property still existed. It is quite reasonable that the magnetic saturation dropped to 41.1 emu/g and 37.2 emu/g, respectively, since the proportion of Fe_3O_4 that endowed the two nanocomposites with superparamagnetic properties had been diluted. Meanwhile, in order to visualize the magnetic behavior of the nano-carrier, we tested the aggregation behavior of BEN@MS@Fe_3O_4 with/without a magnetic field in an ethanol solution. It can be seen from Figure 5 that the nano-carrier prepared in our research can be automatically dissolved in polar solvents and forms a stable solution. The nanocomposite can be automatically led to a specific place when a magnetic field is used, and release drugs under stimuli.

XRD (X-ray diffraction) analysis

In order to further confirm the core structure of the drug carrier BEN@MS@Fe_3O_4 and its precursors, as well as the type of the outer shell, the nanocomposites were tested with wide-angle XRD (WAXRD) and small-angle XRD (SAXRD). As shown in Figure 6, the superparamagnetic core, the MS@Fe_3O_4, and the BEN@MS@Fe_3O_4, have similar XRD patterns, and five Fe_3O_4 characteristic peaks marked as 220, 311, 400, 440, and 551 can be seen in all 3 samples (Gao et al., 2013). As reported in previous literature, the above peaks stand for the face center cubic structures of the superparamagnetic Fe_3O_4 cores. Combining the test results in the FT-IR results, we can

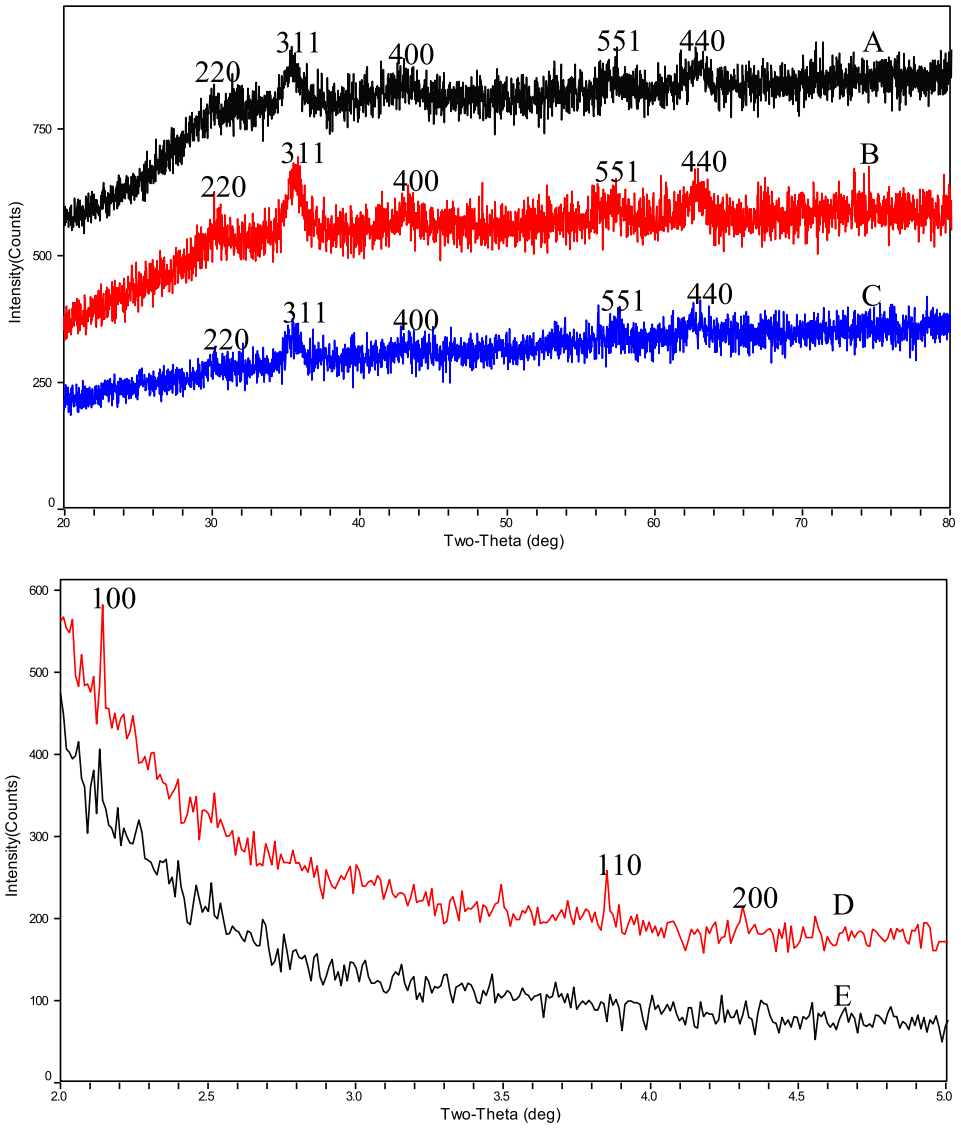

FIGURE 6
WAXRD results of **(A)** BEN@MS@Fe_3O_4, **(B)** MS@Fe_3O_4, **(C)** Fe_3O_4 particles and SAXRD results of **(D)** MS@Fe_3O_4, **(E)** BEN@MS@Fe_3O_4.

infer that the core of the final nanocomposite BEN@MS@Fe_3O_4 was composed of superparamagnetic Fe_3O_4. In the SAXRD testing, MS@Fe_3O_4 and BEN@MS@Fe_3O_4 all showed a high Bragg reflection peak at 100, and two weak peaks at 110 and 200 (Vetrivel et al., 2010). Especially in the case of BEN@MS@Fe_3O_4, the two weak peaks were barely seen. This is most likely because the original regular molecular sieve channels were occupied by organic ligands and photosensitive molecules after subsequent chemical modifications. Therefore, the ordered hexagonal tunnel characteristic peaks of molecular sieves were weakened in the XRD test.

Nitrogen adsorption–desorption isotherms of the outer shell

The nitrogen adsorption–desorption isotherms of BEN@MS@Fe_3O_4 and MS@Fe_3O_4 are shown in Figure 7. The two samples showed the same pattern as type IV according to the literature (Huang et al., 2012). In conclusion, the MS@Fe_3O_4 retained its hexagonal mesophases even after template removal, organic ligand coupling, and further gating molecules modification. However, after subsequent reactions, the major feather value of the MS@Fe_3O_4 declined. For MS@Fe_3O_4, the surface area, pore diameter, and pore volume were 28.6 m^2/g, 6.9 nm, and 0.042 cm^3/g, respectively, and shrunk to

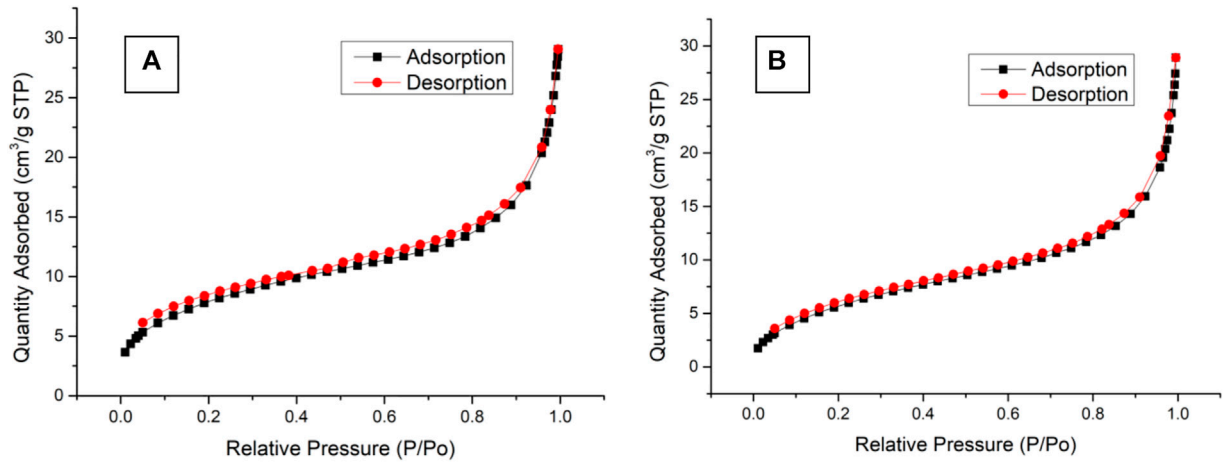

FIGURE 7
Nitrogen adsorption/desorption isotherms of **(A)** MS@Fe_3O_4 and **(B)** BEN@MS@Fe_3O_4.

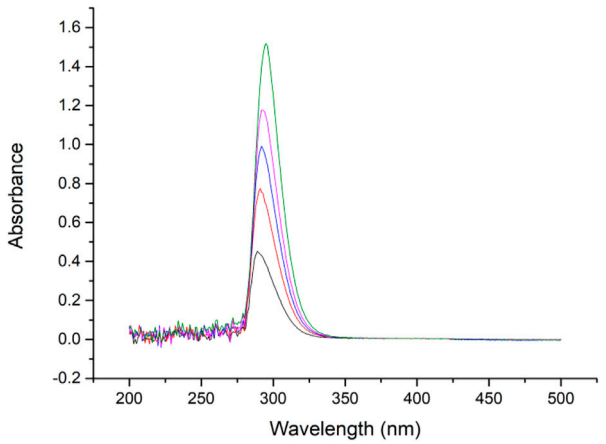

FIGURE 8
Absorbance spectrum of gating molecule (0.01–0.05 mg/ml in ethanol).

22.2 m^2/g, 5.7 nm, and 0.038 cm^3/g correspondingly. This is mainly due to the fact that the pores and tunnels in the molecular sieve had been partly occupied by organic ligands and photosensitive molecules.

Drug loading and determination

Benzophenone hydrazine connected to the MCM-41 was used for gating molecules, and can swing its C=N bond under certain irritations. Previous papers indicate that C=N bonding

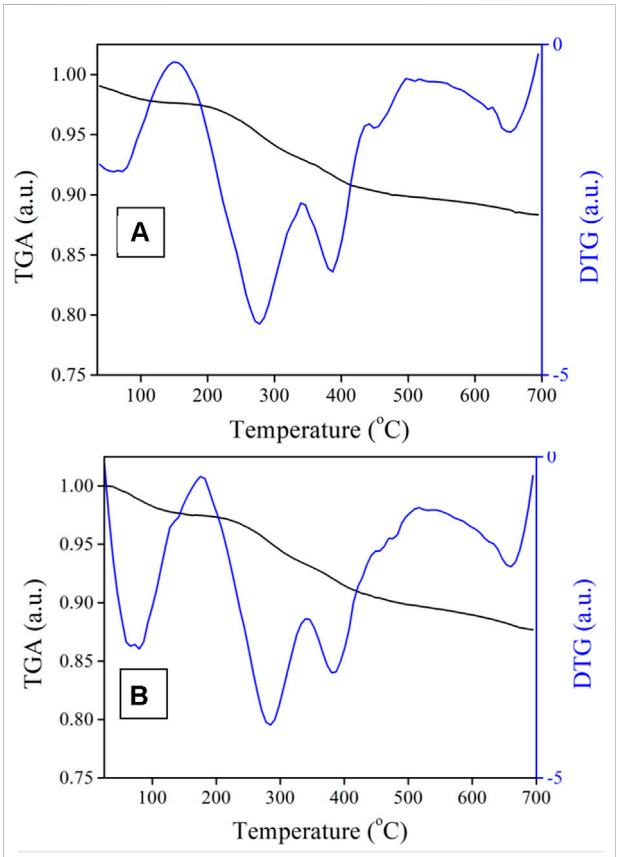

FIGURE 9
TGA of **(A)** BEN@MS@Fe_3O_4 and **(B)** DNR@MS@Fe_3O_4.

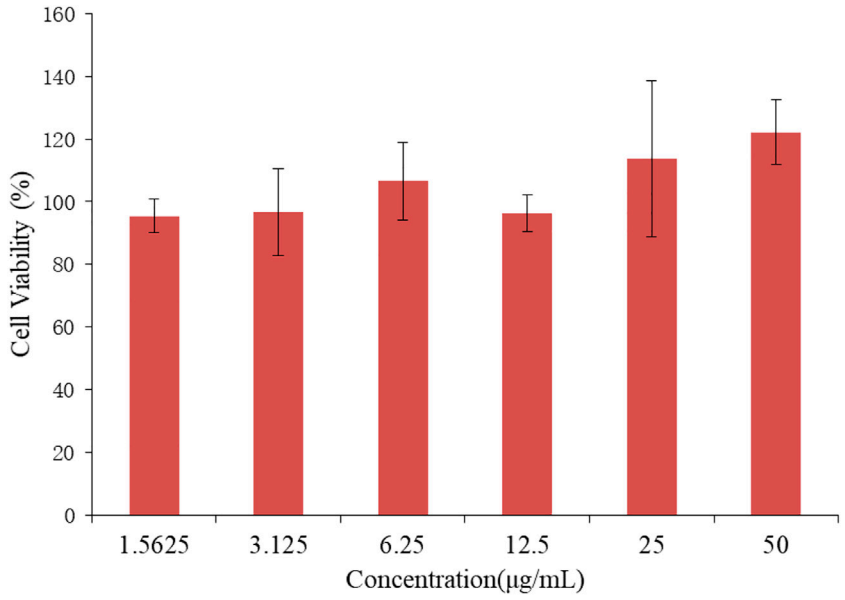

FIGURE 10
Cell viability of SMMC-7721 cell line treated with BEN@MS@Fe_3O_4 nanoparticle (n = 3).

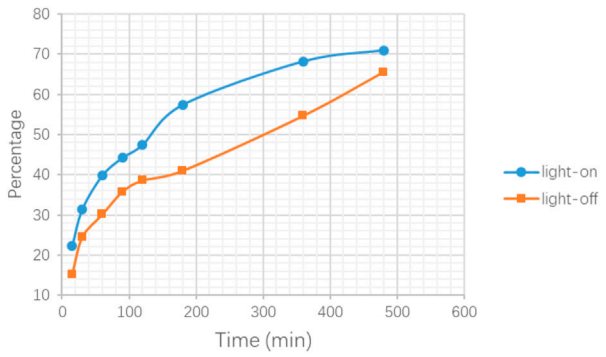

FIGURE 11
Release testing in PBS for DNR@MS@Fe_3O_4 with light-on and light-off.

has a peak absorbance at approximately 300 nm (Thurston et al., 2004; Romero et al., 2015), and therefore the absorbance curve was tested. It can be seen in Figure 8 that the benzophenone hydrazine has a maximum peak at about 297 nm, hence in our research 310 nm LED was selected as an irritation source.

The DNR loading was studied by TGA with N_2 as a working gas, where the temperature rising rate was 10°C per minute (Figure 9). In general, the DNR@MS@Fe_3O_4 lost 1.25% more weight than the BEN@MS@Fe_3O_4 at the final temperature; hence, we prudently concluded that the DNR loaded on the drug carrier was 1.25%.

Cytotoxicity and analysis of the DNR@MS@Fe_3O_4 nanocomposite

As a carrier of drug molecules, the nanocomposite prepared in research must satisfy a fundamental property, that is, the carrier must be nontoxic and bio-safe. In this regard, BEN@MS@Fe_3O_4 was firstly checked for biocompatibility using the MTT method. The SMMC-7721 cell line was used to perform the testing. As is shown in Figure 10, the SMMC-7721 cell line that was exposed to the nanocomposite with a concentration of up to 50 μg/ml did not show obvious growth inhibition in this experiment. This indicates that our carrier has no cytotoxicity for the morbid tissues. We prudently believe that our drug carrier could be used as a candidate for a drug delivery system.

In vitro release and performance

In order to provide a reference for subsequent cell experiments, a preliminary exploration was made of the release performance upon the carrier with different conditions and different times. The result shown in Figure 11 illustrates that, under light stimulation, the drug molecules loaded on the nano-carriers were released more quickly, especially at 3 h, and the concentration increased by 39% compared with the non-light counterpart. However, the difference in drug concentration between the two experimental conditions gradually narrowed over time. On the one hand, when the drug molecules in the light-on group were rapidly released into the solution, the concentration difference between the inside and outside of the

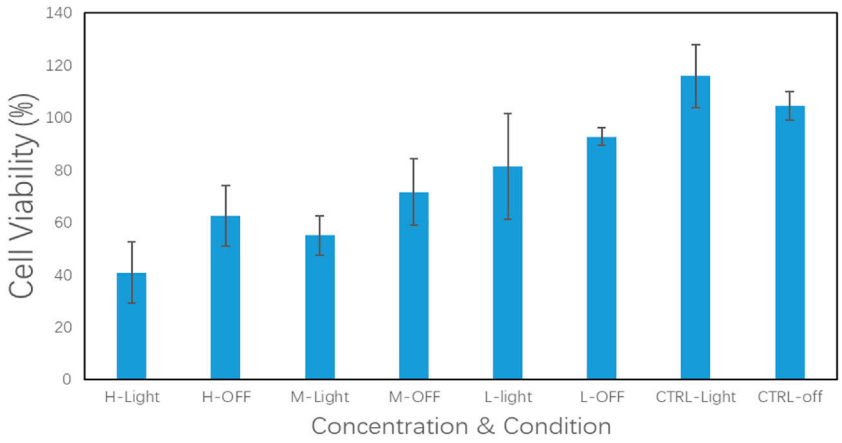

FIGURE 12
DNR@MS@Fe_3O_4 *in vitro* release testing upon SMMC-7721 cell line with irritation on and off (n = 3)

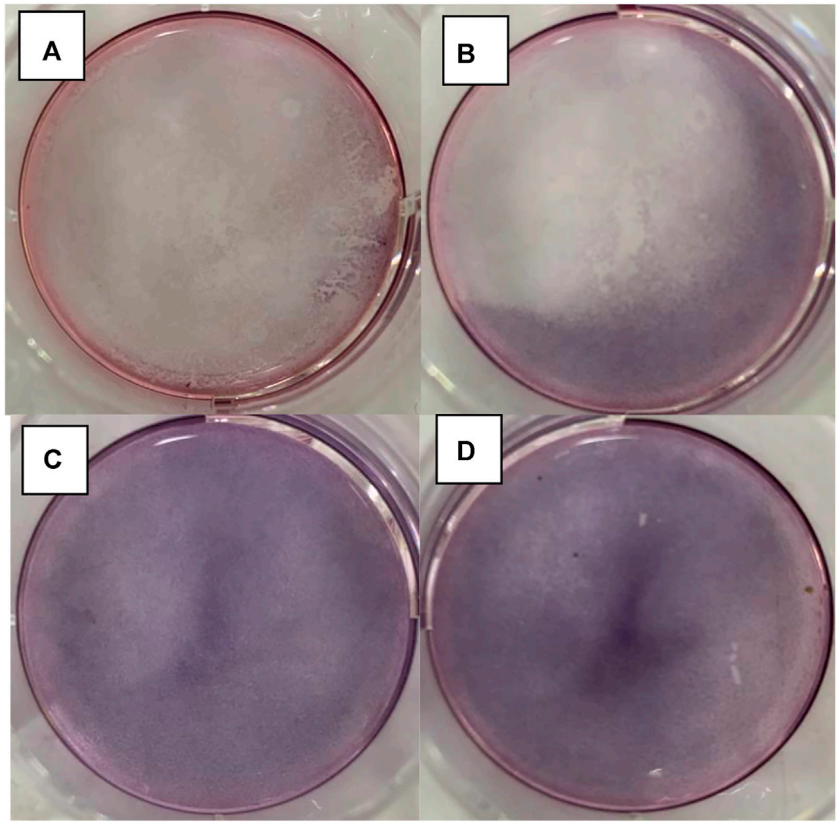

FIGURE 13
DNR@MS@Fe_3O_4 *in vitro* release testing upon 6-well plate method. **(A)** Light and magnetic, **(B)** magnetic only, **(C)** without light or magnetic, and **(D)** control group.

molecular sieve pores became smaller, which delayed the further release of the drug molecules. On the other hand, in the light-off counterpart, the drug molecules could also be slowly released from the molecular sieve pores through thermal motion and diffusion. Therefore, for the *in vitro* experiments, the administration time using the nano-carrier should be the time needed to reach the maximum release concentration difference between light on/off.

In Figure 12, the results of the *in vitro* experiments based on the 96-well plate show that under light irritation conditions, cell viability decreased obviously at each concentration. The cell line was treated with high, medium, and low dosages and the control groups are denoted as "H, M, L, and Ctrl," respectively in Figure 12. In the meanwhile, the "Light" and "OFF" stand for the condition with and without irritation. This indicates that the drug carrier can release DNR molecules more quickly under light conditions. In the *in vitro* experiments based on the 6-well plate, the intelligent release effect of the carrier on light and magnetic guidance was more obvious. Under the same DNR@MS@Fe_3O_4 concentration, in the well treated by magnetic guidance and light at the same time, the cells were obviously inhibited, and the color of MTT produced was lighter. The magnetic field was applied from the left side of the well in this study, so cells near the left side were almost completely inhibited. In Figure 13A, only a few cells on the right side were left. In Figure 13B, since there was only magnetic guidance present during the test, and since no light stimulation was used, the drug concentration was not as high as in Figure 13A. However, the concentration of the drug on the left side was significantly increased, because the drug-loaded carrier was guided to the left side by the magnetic field. This made the inhibition rate on the left side significantly higher than that on the right side. In Figure 13C, since the drug was not treated with either light or a magnetic field, the drug molecules were neither stimulated to release nor locally aggregated. Hence, it is reasonable that the color depth showed as only slightly faded compared with the control group, as seen in Figure 13D.

Conclusion

In conclusion, a novel nanocomposite with a core-shell structure was synthesized in our research. The core of the carrier was constructed for its ability to be magnetically guided, and the outer shell was designed to hold drug molecules. The detailed messages of core-shell structure in the nanocomposite were characterized by means of SEM, TEM, X-RAY, and DLS. The biocompatibility and drug loading/release properties of the carrier were preliminarily determined by using the MTT method with a 96-well plate and a 6-well plate. The results show that the nanocomposite prepared in our project has a core-shell structure. The inner core was superparamagnetic, and the outer shell was composed of SiO_2 and molecular sieves. The 7721 cell line was used to perform the *in vitro* cytotoxicity experiment via the MTT method, and no obvious cytotoxicity was observed in the experimental result. The carriers can be aggregated under a magnetic field and can respond to irritation stimuli. Test results show that the release rate of DNR under light stimuli was significantly faster than that without light. Our nanocomposite could be a new candidate for DDS.

Data availability statement

The original contributions presented in the study are included in the article/Supplementary Material, and further inquiries can be directed to the corresponding author.

Author contributions

TC, YK, RZ, and HW synthesized the chemical compounds. TC performed the *in vitro* experiments and wrote the first draft of the manuscript. GL supervised the project and revised the manuscript.

Funding

This work was supported by grants from the National Natural Science Foundation of China (nos. 81160532 and 81960737).

Acknowledgments

The authors would like to express gratitude to the university for its support with facilities.

Conflict of interest

The authors declare that the research was conducted in the absence of any commercial or financial relationships that could be construed as a potential conflict of interest.

Publisher's note

References

Bewersdorf, J. P., Patel, K. K., Goshua, G., Shallis, R. M., Podoltsev, N. A., Huntington, S. F., et al. (2022). Cost-effectiveness of liposomal cytarabine/daunorubicin in patients with newly diagnosed acute myeloid leukemia. *Blood* 139 (11), 1766–1770. doi:10.1182/blood.2021014401

Chang, V. Y., and Wang, J. J. (2018). Pharmacogenetics of chemotherapy-induced cardiotoxicity. *Curr. Oncol. Rep.* 20 (7), 52. doi:10.1007/s11912-018-0696-8

Deng, L., Zhang, C., Ying, S., Cai, B., and Zhou, F. (2021). Effect of dose ratio on mitoxantrone and daunorubicin in acute myeloid leukemia: A systematic review and meta-analysis of randomized controlled trials. *Clin. Lymphoma Myeloma Leuk.* 21 (1), e10–e20. doi:10.1016/j.clml.2020.08.001

Gao, J., Ran, X., Shi, C., Cheng, H., Cheng, T., and Su, Y. (2013). One-step solvothermal synthesis of highly water-soluble, negatively charged superparamagnetic Fe_3O_4 colloidal nanocrystal clusters. *Nanoscale* 5 (15), 7026–7033. doi:10.1039/c3nr00931a

Han, K. H., Kudo, M., Ye, S. L., Choi, J. Y., Poon, R. T., Seong, J., et al. (2011). Asian consensus workshop report: Expert consensus guideline for the management of intermediate and advanced hepatocellular carcinoma in Asia. *Oncology* 81 (1), 158–164. doi:10.1159/000333280

Huang, S., Li, C., Cheng, Z., Fan, Y., Yang, P., Zhang, C., et al. (2012). Magnetic Fe3O4@ mesoporous silica composites for drug delivery and bioadsorption. *J. Colloid Interface Sci.* 376 (1), 312–321. doi:10.1016/j.jcis.2012.02.031

Kefayati, H., Bazargard, S. J., Vejdansefat, P., Shariati, S., and Kohankar, A. M. (2016). Fe_3O_4@ MCM-41-SO_3H@[HMIm] [HSO_4]: An effective magnetically separable nanocatalyst for the synthesis of novel spiro [benzoxanthene-indoline] diones. *Dyes Pigm.* 125, 309–315. doi:10.1016/j.dyepig.2015.10.034

Krauss, A. C., Gao, X., Li, L., Manning, M. L., Patel, P., Fu, W., et al. (2019). FDA approval summary: (Daunorubicin and cytarabine) liposome for injection for the treatment of adults with high-risk acute myeloid leukemia. *Clin. Cancer Res.* 25 (9), 2685–2690. doi:10.1158/1078-0432.CCR-18-2990

Li, L., Tang, Y. X., Ou, B. N., Zhou, H. D., Chen, R. L., Liu, B. M., et al. (2014). Effects of (-)-epigallocatechin-3-gallate peracetylated derivative on daunorubicin-induced cardiotoxicity in mice. *Chin. Pharmacol. Bull.* 3, 345–348. doi:10.3969/j.issn.1001-1978.2014.03.012

Meireles, I., Cipreste, M. F., Gastelois, P. L., Macedo, W., Gomes, D. A., and de Sousa, E. (2021). Synthesis and characterization of gold nanorods coated by mesoporous silica MCM-41 as a platform for bioapplication in photohyperthermia. *Nanotechnology* 32 (50), 505720. doi:10.1088/1361-6528/ac28db

Mirzajani, R., Pourreza, N., and Burromandpiroze, J. (2018). Fabrication of magnetic Fe_3O_4@nSiO_2@mSiO_2-NH_2 core-shell mesoporous nanocomposite and its application for highly efficient ultrasound assisted dispersive μSPE-spectrofluorimetric detection of ofloxacin in urine and plasma samples. *Ultrason. Sonochem.* 40, 101–112. doi:10.1016/j.ultsonch.2017.06.027

Palomino, G. T., Pascual, J. J. C., Delgado, M. R., Parra, J. B., and Areán, C. O. (2004). FT-IR studies on the acidity of gallium-substituted mesoporous MCM-41 silica. *Mat. Chem. Phys.* 85 (1), 145–150. doi:10.1016/j.matchemphys.2003.12.020

Qiu, L., Zhou, G., and Cao, S. (2020). Targeted inhibition of ULK1 enhances daunorubicin sensitivity in acute myeloid leukemia. *Life Sci.* 243, 117234. doi:10.1016/j.lfs.2019.117234

Ravikumar, C., Joe, I. H., and Jayakumar, V. S. (2008). Charge transfer interactions and nonlinear optical properties of push–pull chromophore benzaldehyde phenylhydrazone: A vibrational approach. *Chem. Phys. Lett.* 460 (4-6), 552–558. doi:10.1016/j.cplett.2008.06.047

Romero, E. L., D'Vries, R. F., Zuluaga, F., and Chaur, M. N. (2015). Multiple dynamics of hydrazone based compounds. *J. Braz. Chem. Soc.* 26, 1265–1273. doi:10.5935/0103-5053.20150092

Samosir, S. M., Utamayasa, I., Andarsini, M. R., Rahman, M. A., Ontoseno, T., Hidayat, T., et al. (2021). Risk factors of daunorubicine induced early cardiotoxicity in childhood acute lymphoblastic leukemia: A retrospective study. *Asian pac. J. Cancer Prev.* 22 (5), 1407–1412. doi:10.31557/APJCP.2021.22.5.1407

Shepherd, S. J., Issadore, D., and Mitchell, M. J. (2021). Microfluidic formulation of nanoparticles for biomedical applications. *Biomaterials* 274, 120826. doi:10.1016/j.biomaterials.2021.120826

Sun, G., Chang, Y., Li, S., Li, Q., Xu, R., Gu, J., et al. (2009). pH-responsive controlled release of antitumour-active polyoxometalate from mesoporous silica materials. *Dalton Trans.* 23, 4481–4487. doi:10.1039/b901133a

Thurston, T. J., Brereton, R. G., Foord, D. J., and Escott, R. E. (2004). Principal components plots for exploratory investigation of reactions using ultraviolet-visible spectroscopy: Application to the formation of benzophenone phenylhydrazone. *Talanta* 63 (3), 757–769. doi:10.1016/j.talanta.2003.12.027

Uematsu, N., Zhao, Y., Kiyomi, A., Yuan, B. O., Onda, K., Tanaka, S., et al. (2018). Chemo-sensitivity of two-dimensional monolayer and three-dimensional spheroid of breast cancer MCF-7 cells to daunorubicin, docetaxel, and arsenic disulfide. *Anticancer Res.* 38 (4), 2101–2108. doi:10.21873/anticanres.12450

Vetrivel, S., Chen, C. T., and Kao, H. M. (2010). The ultrafast sonochemical synthesis of mesoporous silica MCM-41. *New J. Chem.* 34 (10), 2109–2112. doi:10.1039/C0NJ00379D

Ye, L., Zhu, L., Wang, J., and Li, F. (2020). Inhibition of vitamin D analog eldecalcitol on hepatoma *in vitro* and *in vivo*. *Open Med. (Wars).* 15 (1), 663–671. doi:10.1515/med-2020-0137

Yen, Y. H., Cheng, Y. F., Wang, J. H., Lin, C. C., Chen, Y. Y., Yong, C. C., et al. (2020). Real world clinical practice in treating advanced hepatocellular carcinoma: When East meets West. *PLoS One* 15 (3), e0230005. doi:10.1371/journal.pone.0230005

Zhang, H., Wang, C., Chen, B., and Wang, X. (2012). Daunorubicin-TiO2 nanocomposites as a "smart" pH-responsive drug delivery system. *Int. J. Nanomedicine* 7, 235–242. doi:10.2147/IJN.S27722

Zheng, R., Zhang, S., Zeng, H., Wang, S., Sun, K., Chen, R., et al. (2022). Cancer incidence and mortality in China, 2016. *J. Natl. Cancer Cent.* 2 (1), 1–9. doi:10.1016/j.jncc.2022.02.002

Zhou, H., Fu, L. X., Li, L., Chen, Y. Y., Zhu, H. Q., Zhou, J. L., et al. (2020). The epigallocatechin gallate derivative Y6 reduces the cardiotoxicity and enhances the efficacy of daunorubicin against human hepatocellular carcinoma by inhibiting carbonyl reductase 1 expression. *J. Ethnopharmacol.* 261, 113118. doi:10.1016/j.jep.2020.113118

frontiers | Frontiers in Chemistry

TYPE Original Research
PUBLISHED 10 October 2022
DOI 10.3389/fchem.2022.1042038

OPEN ACCESS

EDITED BY
Yu Huo,
Sichuan Normal University, China

REVIEWED BY
Jiuxin Jiang,
Hubei University of Technology, China
Xipeng Pu,
Liaocheng University, China

*CORRESPONDENCE
Shanshan Luo,
Luoss82@163.com
Wenkui Li,
liwenkui1976@163.com

SPECIALTY SECTION
This article was submitted to Medicinal and Pharmaceutical Chemistry, a section of the journal Frontiers in Chemistry

RECEIVED 12 September 2022
ACCEPTED 27 September 2022
PUBLISHED 10 October 2022

CITATION
Hao R, Luo S, Wang F, Pan X, Yao J, Wu J, Fang H and Li W (2022), Enhancement of fluorescence and anti-tumor effect of ZnO QDs by La doping. *Front. Chem.* 10:1042038. doi: 10.3389/fchem.2022.1042038

Enhancement of fluorescence and anti-tumor effect of ZnO QDs by La doping

Ruixin Hao[1], Shanshan Luo[1]*, Feiyan Wang[2], Xinyu Pan[1], Jing Yao[1], Jielian Wu[1], Haihong Fang[1] and Wenkui Li[2]*

[1]Jiangxi Provincial Key Laboratory of Drug Design and Evaluation, Jiangxi Science and Technology Normal University, Nanchang, China, [2]Jiangxi Provincial Key Laboratory of Surface Engineering, Jiangxi Science and Technology Normal University, Nanchang, China

ZnO quantum dots (QDs) have received much attention as biomarkers and drug delivery systems in cancer treatment, due to their low cost, ease of preparation, and pH-responsive degradation. However, its applications are limited by the low quantum yield and light absorption. In this work, a lanthanum-doped zinc oxide (La-ZnO) QDs-based drug delivery platform was constructed. The results show that 4% La doping is the most beneficial for improving the fluorescent properties of the ZnO QDs. After loading the drug, the cell activity was 15% at ZnO@DOX and 12% at La-ZnO@DOX. According to *in vitro* and *in vivo* experiment results, the La-ZnO QDs show enhancement of the antitumor effect. Dual enhancement of fluorescence and anti-tumor effects make La-ZnO QDs promising as a drug delivery system in cancer treatment.

KEYWORDS

ZnO, quantum dots, fluorescence, ion doping, drug delivery

1 Introduction

Nanomaterial composites, combined functions such as imaging, targeting, drug delivery, and cancer treatment, show great potential for applications in anticancer medicine (Liu et al., 2007; Wang et al., 2020; Sahu et al., 2021; Khan et al., 2022). Last decades, quantum dot clusters attracted high interest in bioimaging and drug delivery (Zrazhevskiy et al., 2010; Probst et al., 2013). Quantum dots (QDs) mainly play two roles in the drug transport system. Firstly, QDs can serve as drug carriers to bring drugs to the target. Secondly, QDs can help elucidate the drug metabolism kinetics and pharmacodynamics as fluorescent probes to trace the distribution of drugs *in vivo* (Probst et al., 2013). ZnO is a promising candidate for fluorescent probes due to its low cost, ease of preparation, and pH-responsive degradation (Xiong, 2013; Cai et al., 2016). However, Using ZnO as a biological label in tumor therapy applications is limited by the unstable emission intensity and low quantum yields. The quantum yield of ZnO QDs prepared by the conventional method is usually less than 10% (Gulia and Kakkar, 2013; Verma et al., 2021). How to effectively improve the photoluminescent (PL) properties of ZnO QDs remains to be studied.

Ion-doping is an effective way to improve the electronic, optical, and magnetic properties of semiconductor devices (Thangeeswari et al., 2015; Zheng et al., 2022). As common semiconductor dopants, rare earth (RE) elements have attracted widespread interest because of their unique effect on optical properties (Huang W et al., 2019; Prakash et al., 2021). Zong et al. (2014) prepared Eu-doped ZnO QDs, and the results show that Eu-doped ZnO QDs exhibited better photocatalytic activity than pure ZnO, and they are promising for applications for photodegradation of organic contaminants in wastewater. Cao et al. (2017) prepared Ga-doped ZnO NPs (nanoparticles) and found that charge transfer at the interface of the nanoparticles was attenuated by doped Ga. A few studies have been devoted to the preparation of lanthanum-doped ZnO QDs. Huang P et al. (2019) prepared La-doped ZnO QDs with stable fluorescence performance. Ge et al. (2007) studied the gas sensitivity of La-doped ZnO QDs, and found that proper La doping could enhance the gas-sensitive properties. However, few studies are available on the use of La-doped ZnO QDs as a drug delivery system (DDS) for cancer therapy.

This research aims to develop a ligand/receptor-based targeted drug delivery system using La-ZnO QDs as the core material. Hyaluronic Acid (HA) was used to modify the La-ZnO because HA can specifically bind to the major receptor CD44 (Gomez et al., 2020; Maksoudian et al., 2020; Yusupov et al., 2021). Besides, Polyethylene glycol (PEG) was introduced to stabilize the La-ZnO QDs under physiological conditions (Zhao et al., 2014; Reisch et al., 2015; Cai et al., 2018). Finally, DOX (Adriamycin), an anti-tumor drug, was loaded to HA-La-ZnO-PEG through covalent interactions and the formation of Zn2+-DOX chelating complexes. The results show that the doping of lanthanum achieves a dual enhancement of fluorescence and anti-tumor effect for the drug delivery system. The La-ZnO QDs have good prospects for application in drug delivery systems for cancer therapy.

2 Materials and method

2.1 Materials

Zinc acetate dihydrate (Zn(CH3COO)2·2H2O) was obtained from Shanghai Titan Co., Ltd. 3-aminopropyl triethoxysilane (APTES) was purchased from Shanghai RHAWN Co., Ltd. Lithium hydroxide (LiOH), N-N-dimethylformamide (DMF), 1-(3-dimethylaminopropyl)-3-Ethyl carbodiimide salt (EDC), N-hydroxysuccinimide (NHS), Hyaluronic acid (HA) were obtained from Aladdin Reagents (Shanghai) Co., Ltd. Adriamycin (DOX) was purchased from Bide Pharmatech Ltd.

2.2 Preparation of pure and La-doped ZnO QDs

Figure 1 is the schematic illustration of the preparation of PEG-HA-La-ZnO and its antitumor effects investigate in both *in vitro* and *in vivo*. The steps of synthesizing pure and La-doped ZnO QDs are shown in Figure 2. In the first step, 2.20 g of Zn(CH3COO)2·2H2O and 0%, 2%, 4%, 6%, and 8% lanthanum acetate were dissolved in 100 ml of absolute ethanol solution, then refluxed and stirred for 2 h under 80°C in a water bath until the solution was colorless and transparent. Then the above solution was placed in an ice bath. At the same time, according to the ratio of RZn-OH = 1:1, LiOH was weighed and dissolved in 150 ml of absolute ethanol solution, then heated to 85°C and stirred for 2 h until the solution was colorless and transparent. Then the solution was cooled to room temperature, before adding them to zinc acetate ethanol solution in an ice bath drop by drop for 8 h. It was observed that the zinc acetate solution quickly turned white and then gradually became clear, indicating that ZnO quantum dots had been formed. In the second step, n-hexane was added to precipitate a large amount of white precipitation. The precipitation was then centrifuged for 15 min under the condition of 4500 R/min and finally dried in a vacuum at 60°C to obtain ZnO quantum dots.

2.3 Preparation of APTES-modifified La-ZnO QDs

Firstly, 100 mg pure or La-ZnO QDs were dispersed in 15 ml DMF solution under ultrasonic conditions. After heating to 120°C, 50 μL APTES was added and stirred for 15 min, followed by centrifuging at 1,000 rpm for 5 min and washing with DMF twice. Then the amino ZnO QDs were collected and dispersed in 10 ml of water and then stored at 4°C.

2.4 Surface modification of La-ZnO QDs with PEG (PEG-La-ZnO)

COOH-PEG-COOH (Mw: 2000) was used to modify the surface of NH2-La-ZnO QDs through amide reaction. At first, 0.2 g EDC/NES was added to 1 ml of ultrapure water containing 25 mg PEG, followed by adjusting the pH value of the mixture to 7 with NaOH. The solution was shaken at 25°C for 30 min to active COOH-PEG-COOH. After activation, 2.5 ml of NH2-ZnO QDs dispersion was slowly added, then the mixture was stirred at room temperature in dark for 4 h. The final product was freeze-dried and preserved after removing the unmodified COOH-PEG-COOH.

10.3389/fchem.2022.1042038

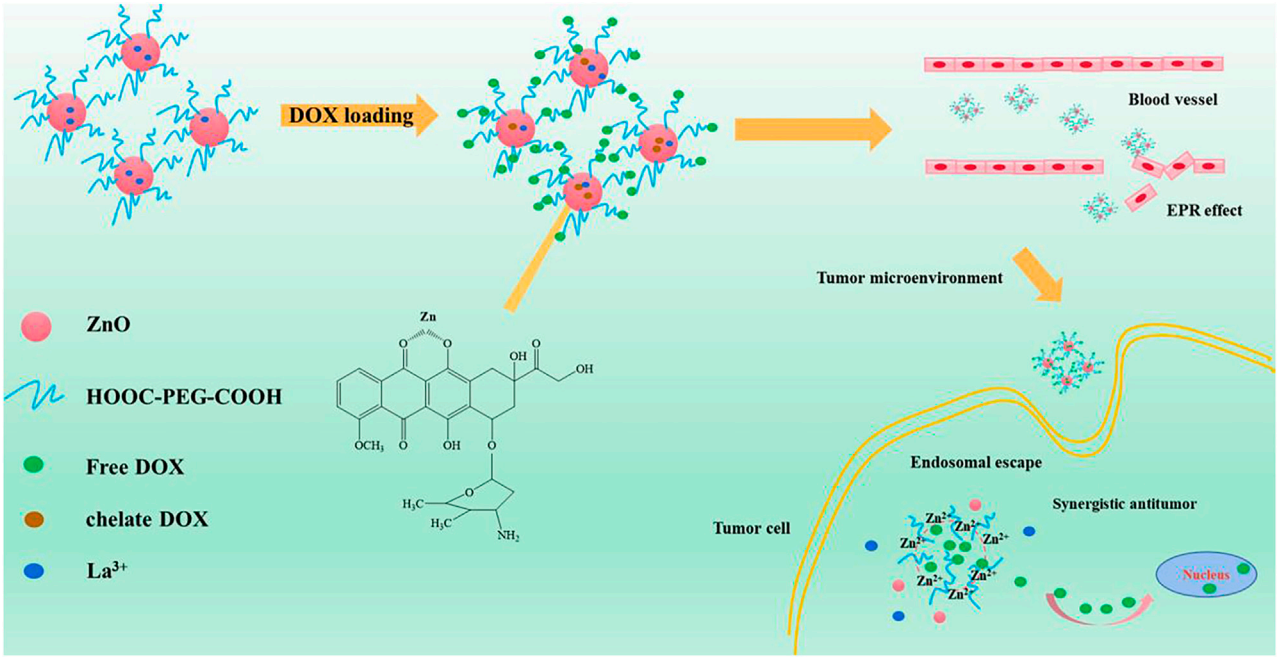

FIGURE 1
Schematic illustration of the preparation of PEG-HA-La-ZnO and its antitumor effects investigate in both *in vitro* and *in vivo*.

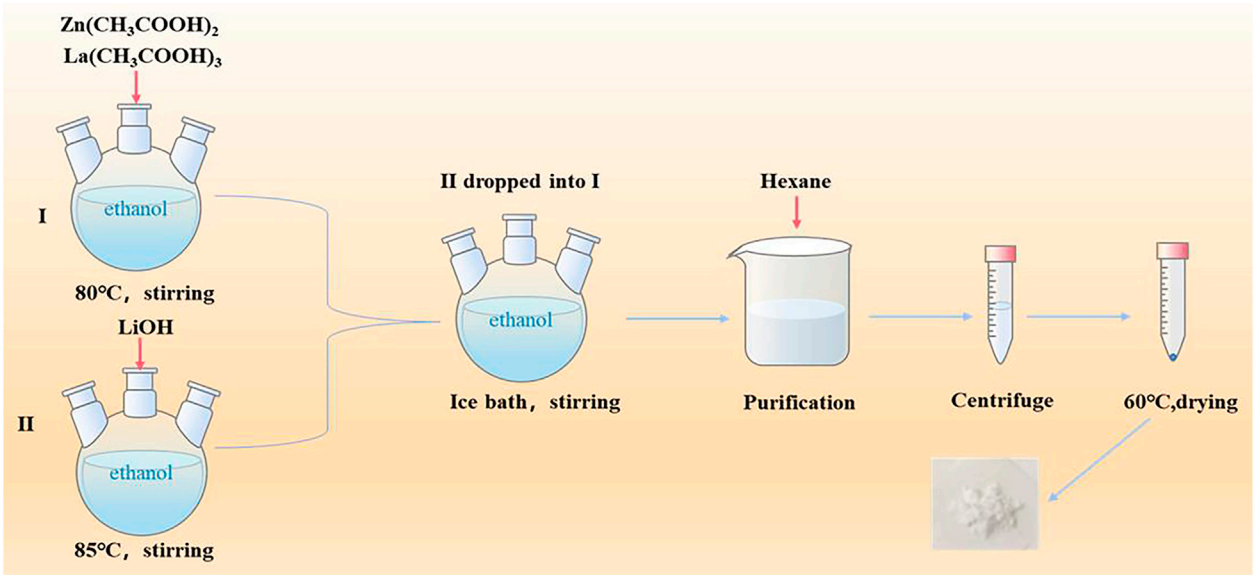

FIGURE 2
Synthesis process of pure and La doped ZnO QDs.

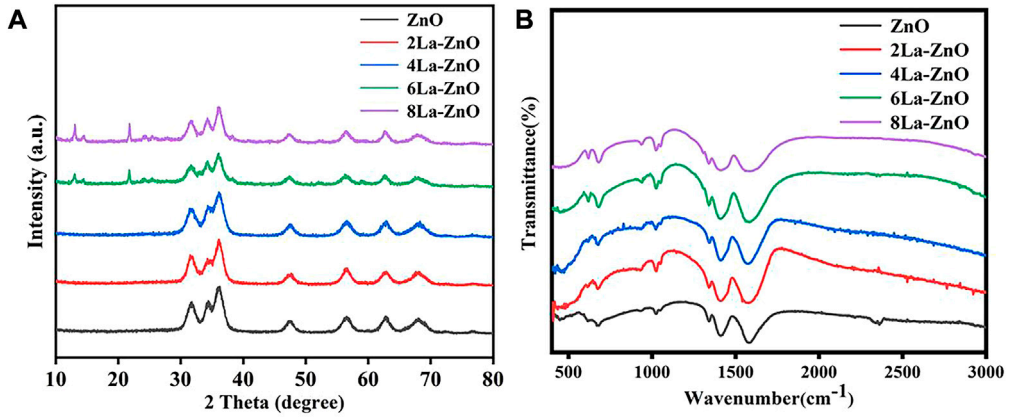

FIGURE 3
(A) XRD pattern and **(B)** FTIR spectra of pure ZnO and La-ZnO QDs.

2.5 Surface modification of PEG-La-ZnO QDs with HA

Firstly, 0.016 mmol of HA was dissolved in 4 ml of ultrapure water, then the pH of the solution was adjusted to four using hydrochloric acid. Then the solution was incubated overnight at room temperature. Afterward, 0.32 mmol EDC/NHS was added to a well-incubated HA solution and activated for 4 h. Finally, 5 mg PEG-La-ZnO QDs were added into the solution and stirred overnight. The obtained HA-PEG-La-ZnO was dialyzed in water with a dialysis bag of molecular weight 3,500 Da for 24 h to remove the excess HA.

2.6 DOX loading (PEG-HA-La-ZnO and PEG-HA-ZnO)

The potential of HA-PEG-ZnO and HA-PEG-La-ZnO nanocomposites *in vitro* drug encapsulation was evaluated. Firstly, 10 mg DOX was put in 10 ml ultrapure water to prepare 1 mg/ml of DOX solution. Afterward, 0.32 mmol of EDC and 0.16 mmol of NHS were mixed with HA-PEG-NH2-ZnO solution and stirred for 30 min, followed by adding 1 ml DOX solution. Then the mixture was stirred overnight in dark. Finally, the reaction products were measured by UV/Vis spectroscopy at 490 nm, and the loading content and loading efficiency of DOX were calculated as follows:

$$\text{Loading content } (\%) = \frac{\text{weight of DOX in nanoparticles}}{\text{weight of nanoparticles taken}} \times 100\% \quad (1)$$

$$\text{Loading efficiency } (\%) = \frac{\text{weight of DOX in nanoparticles}}{\text{weight of DOX added}} \times 100\% \quad (2)$$

2.7 *In vitro* DOX release experiment

PBS buffers (pH = 7.4 and pH = 5.0) were used to simulate the microenvironment of normal cells and cancer cells, respectively. The HA-PEG-La-ZnO DOX sample was put into a dialysis bag with a molecular weight of 3,500 Da and then stirred at the corresponding buffer solution. The fluorescence data were measured at the corresponding time points to obtain the drug release curve.

2.8 Cytotoxicity analysis

2.8.1 Cell culture

B16 cells were cultured in a cell culture flask with DMEM, including 10% fetal bovine serum (FBS) and 1% penicillin-streptomycin solution in a humidified atmosphere incubator with 5% CO2 at 37°C.

2.8.2 MTT assay

To explore the biocompatibility of ZnO, B16 cells were used in the experiment. The cells were cultured in a constant temperature incubator at 37°C and the fourth generation was used for the experiment. To assess the toxicity determined by the MTT method, the 1 × 105 cells were put in 96—well plates with different materials (ZnO, La—ZnO) concentrations of 0 ug/ml, 5 ug/ml, 10 ug/ml, 20 ug/ml, 25 ug/ml, respectively. The experiments were repeated three times for every concentration. After 48 h, MTT solution was added. After 4 h, MTT solution was removed and 150 ul DMSO (Dimethyl sulfoxide) solution was added. Finally, the absorbance of B16 cells was measured by a microplate analyzer.

To explore the therapeutic effect of La-ZnO drug loading system, B16 cells were selected as the experimental cells, and the

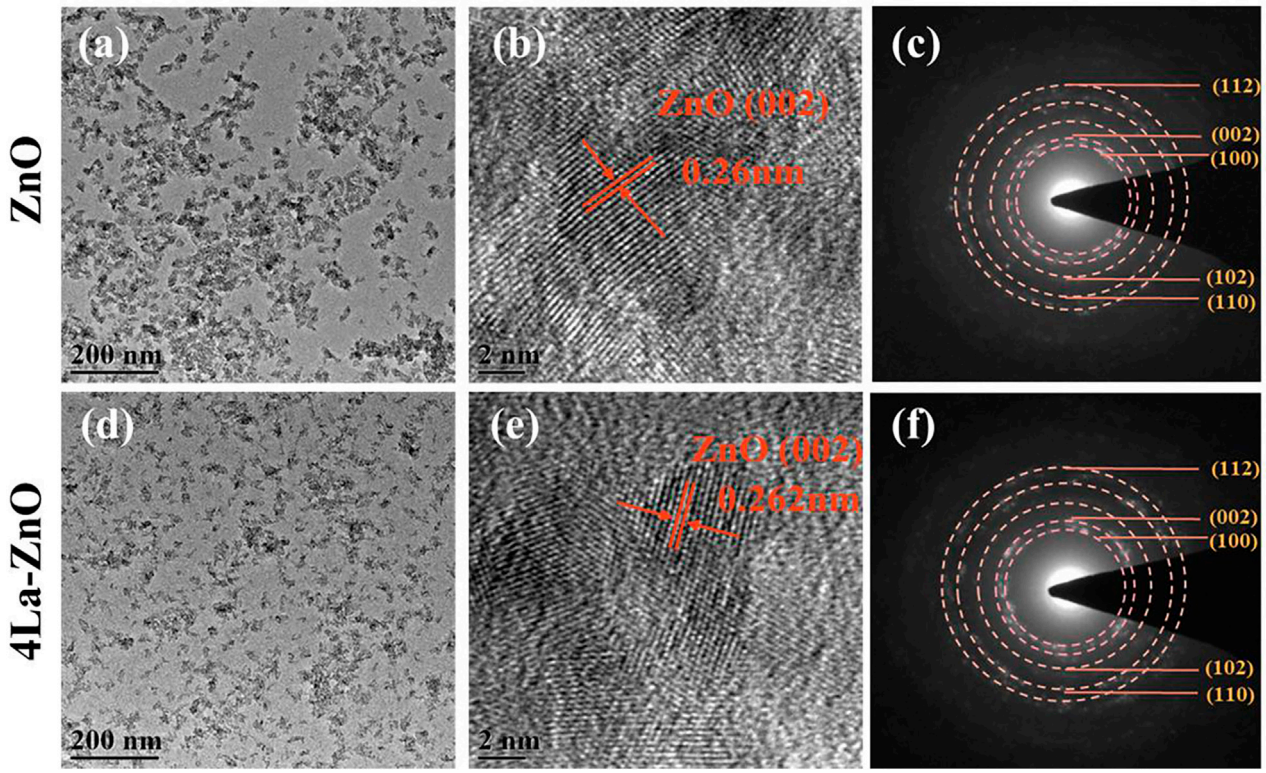

FIGURE 4
TEM **(A,D)**, HR-TEM **(B,E)** and SEAD **(C,F)** patterns of pure and La-ZnO QDs.

MTT method was used to evaluate the toxicity test. Firstly, 1 × 105 cells and different materials (ZnO @ DOX and 4 -La-ZnO @ DOX) were mixed in 96—well plates for 48 h. The concentration of DOX were 0.162 ug/ml, 0.81 ug/ml, 1.62 ug/ml, 2.43 ug/ml, 3.24 ug/ml, 4.05 ug/ml, respectively. Then added MTT solution for 4 h. Removed MTT solution, and added 150 ul DMSO (Dimethyl sulfoxide) solution to lyse cells. Finally, the absorbance of B16 cells was measured by a microplate analyzer to explore the viability of B16 cells.

2.8.3 Fluorescence staining experiment

Fluorescence staining experiment was used to evaluate the B16 cell activity after different treatments. The cells were cultured with different samples for 2 days. Afterward, the cells was wash twice with PBS, then were stained with AM/PI staining for 30 min, followed by washing with PBS for twice, the cells were photographed by a fluorescence microscope (CKX53, OLYMPUS).

2.9 *In vivo* biocompatibility

To evaluate the biocompatibility of ZnO, six tumor-free female C57 mice (4–6 weeks old) were randomly divided into control group and 25 μg/ml ZnO group. Then, bodyweight of the mice in the two groups was recorded with subcutaneous injection of 100 μL of PBS and 25 μg/ml of ZnO solution for 10 consecutive days, and the main organs (liver, heart, spleen, lung, and kidney) were collected for H&E staining.

2.10 *In vivo* antitumor activity

Female C57 mice (4–6 weeks old,16–20 g) were used for antitumor activity assessment. Firstly, 100 uL of B16F10 cell suspension (1 × 107) was injected subcutaneously into the lower hind limb of each mouse. After 6–8 days, the tumor volume was about 80 mm3, and the drug was administered. Eighteen tumor-bearing mice were randomly divided into six groups, PBS, ZnO, 4% La-ZnO, DOX, ZnO@DOX, and 4% La-ZnO@DOX, respectively. The equivalent concentrations of ZnO and 4% La-ZnO in PBS were 25 μg/ml, and the equivalent concentrations of DOX, ZnO@DOX and 4%La-ZnO@DOX in PBS were 4.05ug/mL. The tumor size and weight of mice were recorded once a day. After 10 days of recording, the tumors of each group were collected for H&E

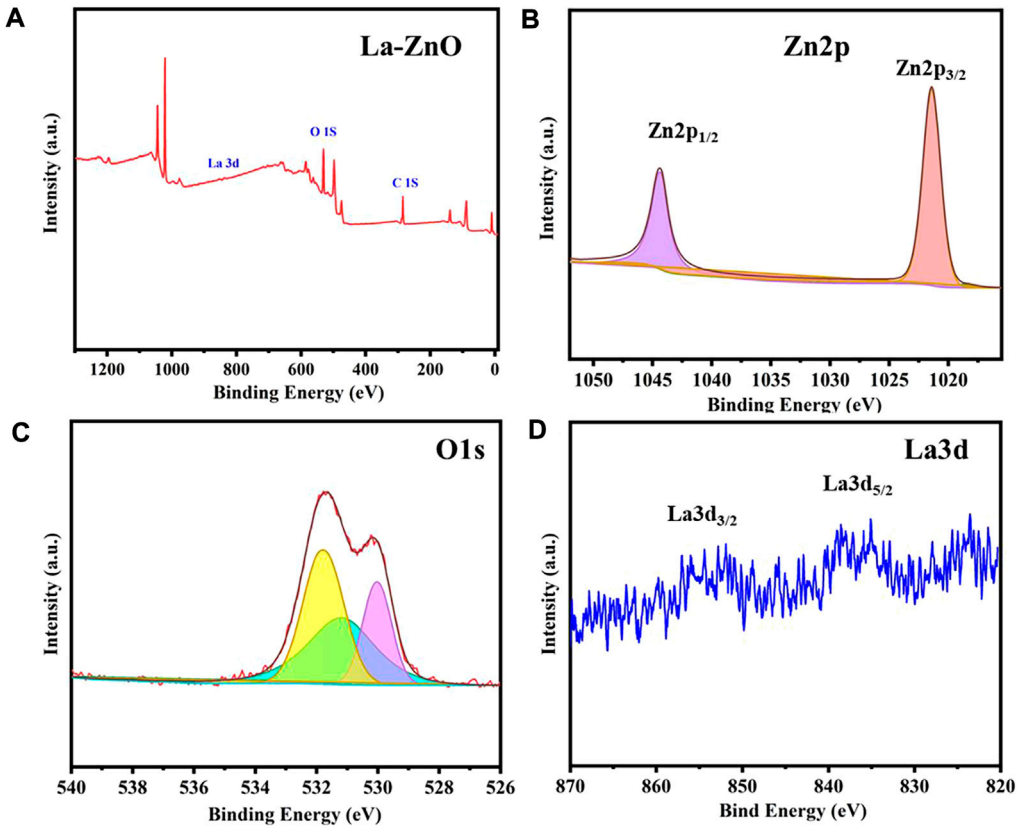

FIGURE 5
(A) XPS survey spectra of La-ZnO. **(B–D)** High-resolution XPS spectra of Zn2p, O1s, and La3d.

staining. The tumor volume was calculated by the following equation:

$$\text{Tumor volume}\,(\text{mm3}) = (l \times W2)/2 \quad (3)$$

where l is the length, and W is the width in mm of tumor.

2.11 Characteristics

The crystal structure and composition were measured through an X-ray powder diffractometer (Shimadzu, Japan, XRD-6100). The morphology and particle size were observed using a field emission transmission electron microscope (FEI Company, United States). Surface functional groups were determined using a Fourier transform infrared spectrometer (IR-960, Tianjin Rui'an Technology Co., Ltd.). The fluorescence performance was tested by a UV spectrophotometer (model UV-2550, Shimadzu, Japan), a PL fluorescence spectroscopy (Beijing ZhuoliHanguang Instrument Co., Ltd.), and a fluorescence spectrometer (Hitachi High-Tech Co., Ltd, Japan).

3. Result and discussion

3.1 Structure and morphology of ZnO QDs

The XRD patterns of ZnO QDs were exhibited in Figure 3A. The diffraction peaks of the pure ZnO and La-ZnO samples and their relative intensities matched well with the standard JCPDS card No. 36–1,451, and both pure ZnO and La-ZnO QDs in this work were hexagonal wurtzite structures. In addition, no other impurities XRD peaks were observed when the doping La is not exceed 4%, which indicated that the doping of La did not change the crystal structure of the ZnO, and it was uniformly dispersed in the ZnO matrix (Manikandan et al., 2017). The reaction was incomplete when the La doping exceed 6%, resulting in a small amount of Zn(OH)2 remained. Next, unless otherwise specified, mentioned La-ZnO is the sample with a La-doping amount of 4%.

The Fourier transform infrared spectra (FTIR) of the pure and La doped ZnO QDs were displayed in Figure 3B. The intensity band at around 465 cm−1 was attributed to the Zn-O stretching vibration. The band at 605 cm-1 indicates the

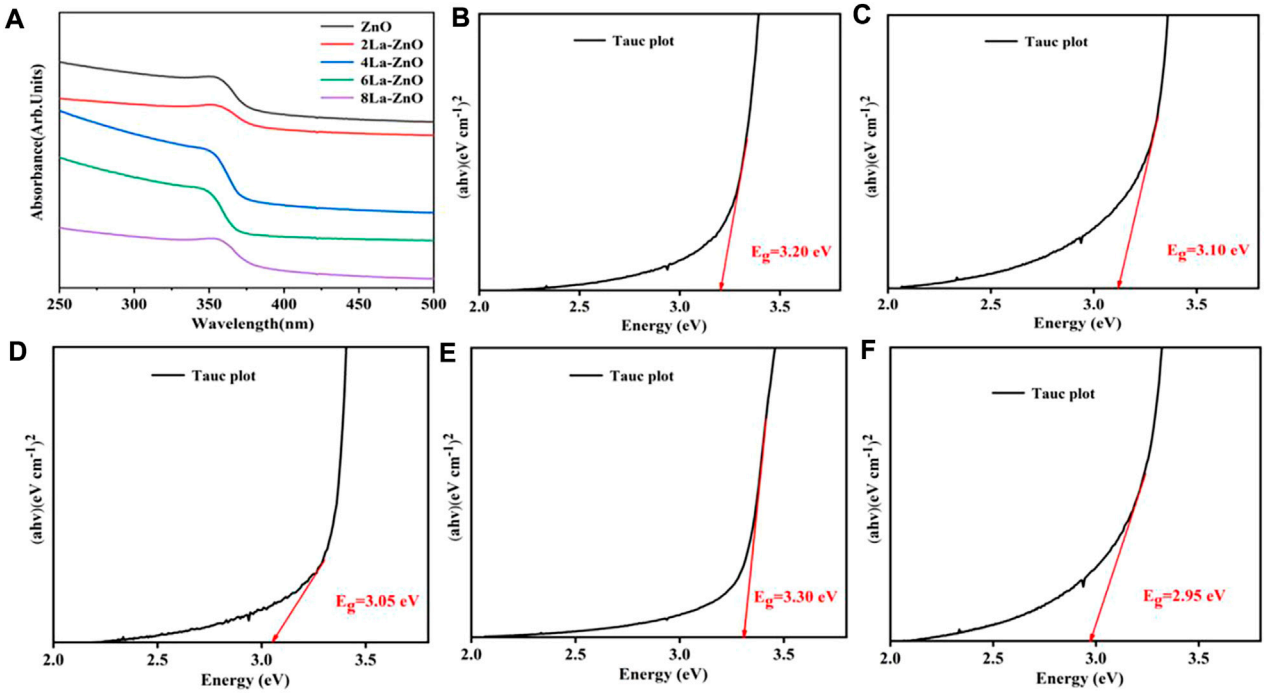

FIGURE 6
(A) UV–vis absorbance spectra of pure ZnO and xLa-ZnO **(B–D)** Tauc plots of (αhν)2 *versus* hν of pure ZnO and xLa-ZnO **(B)** x = 0, **(C)** x = 0.02, **(D)** x = 0.04 and **(E)** x = 0.06, **(F)** x = 0.08.

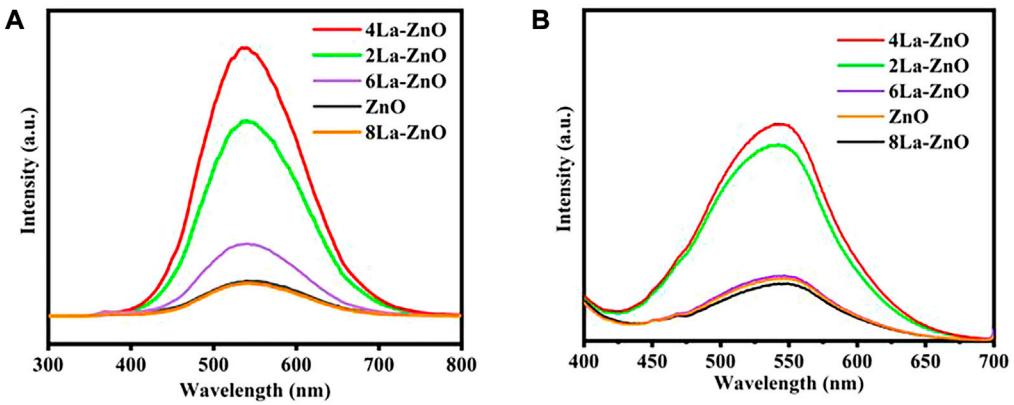

FIGURE 7
(A) PL spectra of pure ZnO QDs and xLa-ZnO QDs. **(B)** Liquid fluorescence spectra of ZnO QDs and xLa-ZnO QDs.

presence of ZnO and La. The intensity band at 1,635 cm-1 may be contributed to the O-H bending mode of the adsorbed water vibration, and the vibration amplitude of La-ZnO is more obvious than that of pure ZnO, indicating the successful incorporation of lanthanum.

To further investigate the microstructure of La-ZnO QDs, transmission electron microscope (TEM) and selected-area electron diffraction (SAED) measurements were carried out. As shown in Figures 4A,D, both pure ZnO and 4La-ZnO QDs were uniformly dispersed without obvious agglomeration. From

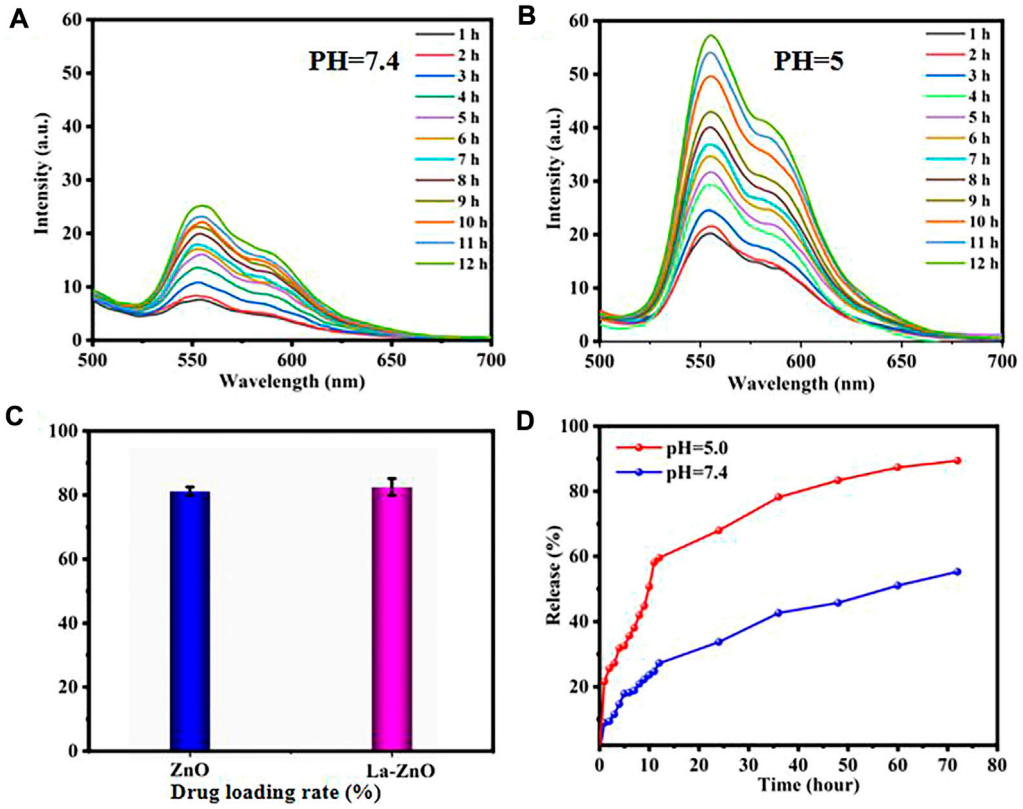

FIGURE 8
Time-dependent fluorescence spectra of DOX release after incubating La-ZnO-DOX at pH 7.4 **(A)** and pH 5.0 **(B)**.**(C)** Drug loading rate of pure ZnO and La-ZnO.**(D)** Drug release rate of HA-PEG-NH2-Zno-DOX drug loading system at pH = 5.0 and 7.4 with time.

the HRTEM images as shown in Figures 4B,E, the pure ZnO exhibited more regular lattice stripes, whereas La-ZnO is less ordered. Besides, the space between the adjacent lattice planes was 0.26 nm, which is consistent with the (002) plane of ZnO (Sun et al., 2012). For La-ZnO QDs, the space lattice plane has increased slightly and reached 0.262 nm, indicating that the doped of rare earth lanthanum causes lattice distortion of ZnO. Selected area electron diffraction patterns (Figures 4C,F) indicate the diffraction ring well corresponds to (112) (002), (100) (102), (110) planes, which is in good agreement with the results of XRD.

The surface element composition and valence of ZnO and La-ZnO QDs were determined by XPS. The binding energy peaks of Zn, La, and O were detected in the La-ZnO composite (Figure 5A), which further confirming the successful doping of lanthanum. Furthermore, high-resolution spectra of Zn2p, O1s, and La3d were provided in Figure 5B, the peaks at 1,023.1 and 1,043.2 eV corresponded to Zn 2p3/2 and Zn 2p1/2, respectively. Figure 5C shows the high resolution of O1 s, the peak at 529.8 eV could be attributed to Zn-O-Zn and the peak at 531.6 eV was attributed to La-O-Zn. It is observed from Figure 5D that the La 3 days spectrum consists of two peaks, the peaks at approximately 836.2 eV and 853.3 eV were ascribed to La3d5/2 and La3d3/2.

UV-vis absorption spectroscopy was used to assess the optical properties of pure ZnO and La-ZnO QDs. As shown in Figure 6A, both pure ZnO and La-ZnO QDs exist band edge-absorption at around 366 nm. There is an extended tail band (from 450 to 800 nm) in the UV spectrum of La-ZnO QDs, indicating that they have optical properties almost in the whole visible spectrum. The optical band gap of pure ZnO and xLa-ZnO was calculated by the following formula:

$$\alpha = A\ (h\upsilon - Eg)n/\ h\upsilon \quad (4)$$

where *a* is the absorption coefficient, A and n are constant, and *?* is the photon frequency.

Figures 6B–F shows the calculated band gaps of the pure ZnO and xLa-ZnO QDs. The doping of lanthanum has a great effect on the bandgap of xLa-ZnO QDs. When the doping amount of lanthanum increased from 0 to 8%, the bandgap was regularly decreased from 3.35 to 2.85 eV. Thus, doping La into ZnO can introduce impurity levels in the bandgap and enhance its visible light response, when the Zn site in ZnO is occupied by La atoms, two main effects can be observed: 1). The impurity band is close

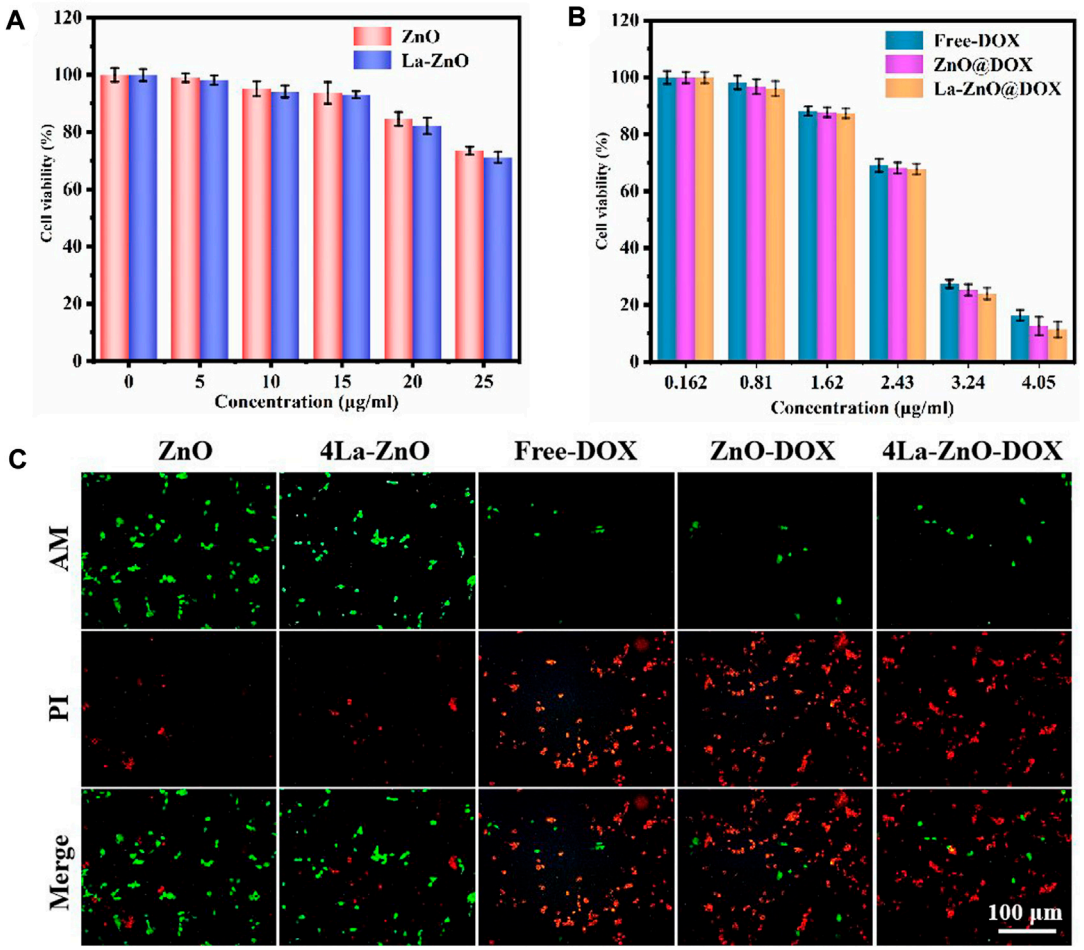

FIGURE 9
Cytotoxicity study of B16 cells after 48 h of incubation with **(A)** ZnO QDs and La-ZnO QDs. **(B)** Free-DOX, ZnO@DOX and 4La-ZnO@DOX. **(C)** The fluorescent images of the cells treated with different groups and stained with AM/PI.

to the edge of the conduction band. 2). Due to the strong orbital coupling between La and O, the obtained band gap decrease (Sun et al., 2012). The results show that the doping concentration of La plays an important role in adjusting the bandgap of La-ZnO, which is conducive to its potential applications in biological imaging.

Figure 7A shows the PL spectra of pure ZnO and La-ZnO QDs. From the spectra, it was observed that all emissions of pure ZnO and La-doped ZnO are concentrated around 530 nm. The small variation of the emission position in the PL spectra may be contributed to the effect of the La doping. The maximum emission intensity was increased significantly with appropriate La doping. When the La doping is 4%, the emission intensity reach the maximum. Besides, we also obtained Fluorescence spectra of different sample in distilled water in Figure 7B, and the 4% La-ZnO also showed highest emission intensity. Therefore, in this research, 4% is the best doping amount, and 4La-ZnO QDs are used for the next biological experiment.

3.2 Drug loading and release efficiency

HA:CD44, a transmembrane glycoprotein with a molecular weight of 85 kDa, is involved in a variety of cellular functions, including cell orientation, adhesion, migration and stromal cell signaling processes. It is over expressed in many solid tumors. Hyaluronic acid (HA), composed of d-glucuronic acid and n-acetylglucosamine, is a negatively charged linear polysaccharide. It specifically recognizes the CD44 glycoprotein and here HA has been used as a targeting ligand to specifically recognize the CD44 glycoprotein overexpression in murine melanoma cells.

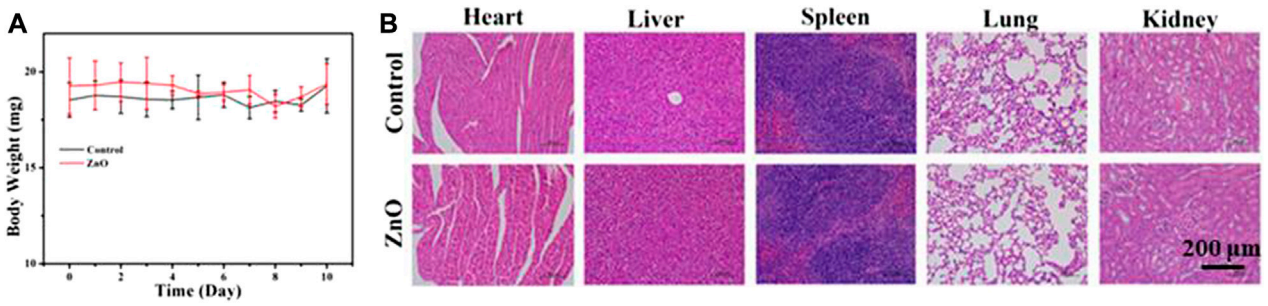

FIGURE 10
(A) The body weight of mice in control group and Zinc oxide group was determined after subcutaneous injection of 100 μL PBS and 25 μg/ml ZnO solution for 10 consecutive days.**(B)** H&E staining images of heart, liver, spleen, lung and kidney after 10 days.

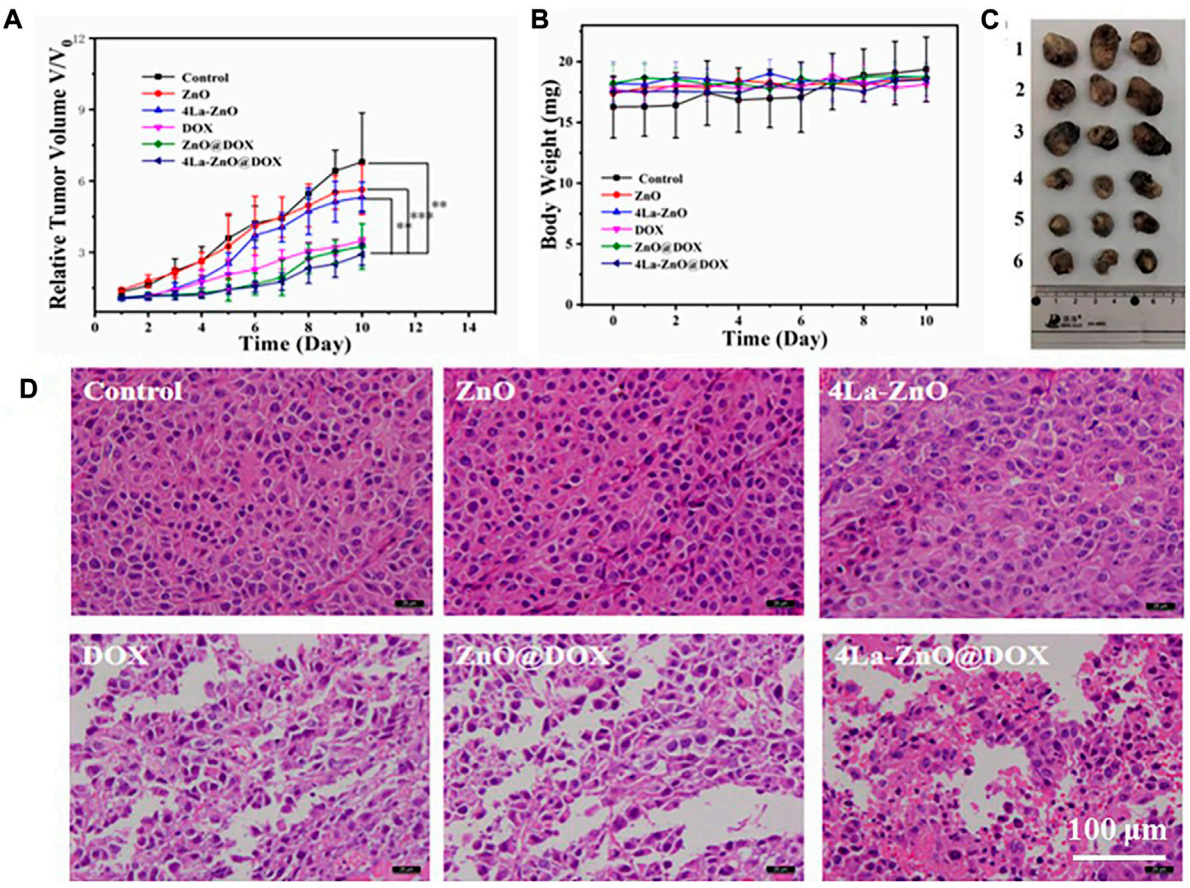

FIGURE 11
In vivo evaluation of antitumor efficacy. **(A)** Mean relative tumor volumes within 10 days.**(B)** The body weight of mice was determined after subcutaneous injection of 100 μL PBS and 25 μg/ml ZnO QDs, La-ZnO QDs, Free-DOX, ZnO@DOX and 4La-ZnO@DOX for 10 consecutive days. **(C)** Representative images of tumors from different groups. Where (1) Control, (2) ZnO, (3) La-ZnO, (4) Free-DOX, (5) ZnO@DOX, (6) 4La-ZnO@DOX. **(D)** Micrographs of H&E stained tumor slices collected from mice of different groups.

PEG has been widely used in drug delivery as a non-toxic modified ligand due to its excellent properties. It not only has good water solubility, high stability, and good biocompatibility. Therefore, using PEG ligand connection of ZnO quantum dot clusters carrier has many advantages, can not only make use of the EPR effect efficient accumulation in the tumor cells but also can realize drug controlled release. In addition, zinc oxide cluster carrier after complete decomposition, side effects, small decomposition Zn2+ can also be generated and synergistic anticancer, improve the effectiveness of the treatment of tumor.

DOX was loaded to the PEG-HA-La-ZnO at a neutral pH of 7.4. DOX can be loaded onto the pure ZnO and La-ZnO by three methods: 1) The complexation of DOX with Zn2+ can provide a payload of DOX molecules. Under acid conditions, the disruption of the coordination bond between Zn2+ and DOX enables the precise release of DOX at the tumor site. 2) DOX can bind to PEG-HA-La-ZnO by an amide bond. 3) Positively charged DOX adsorbed on negatively charged HA-La-ZnO-PEG nanocarriers *via* electrostatic adsorption (Brouet et al., 2008). In this work, DOX loading amounts of PEG-HA-ZnO and PEG-HA-La-ZnO are 81.53% and 81.67%, respectively (Figure 8C).

Generally, TME is acidic and always has a lower pH compared to normal tissues, which is mainly attributed to the production of lactic acid in the anaerobic microenvironment and the formation of hydrolyzed protons during ATP (Adenosine triphosphate) (Vimala et al., 2017; Singh et al., 2018). To improve the therapeutic efficacy of nanoparticles, a large amount of research has been devoted to the fabrication of TME-responsive or cancer-targeted drug delivery platforms. ZnO quantum dots possess pH-responsive release, which exists stably at pH 7.4, but dissolves rapidly at pH < 5.5. To investigate the release of DOX from HA-PEG-La-ZnO quantum dots, PBS buffer solutions (pH = 7.4 and pH = 5) were used to simulate normal cells and tumor microenvironment, respectively. As shown in Figures 8A,B, the fluorescence intensity of DOX at pH = 7.4 is much weaker than in PBS buffer at pH = 5, indicating more DOX was released by ZnO degradation in an acidic environment. In addition, the cumulative release of DOX at different pH was also investigated, as shown in Figure 8D, with the increase of time, DOX was released at a higher rate in pH = 5 solution than in pH = 7 solution. After 72 h of incubation, 70% of DOX was released from the drug-loaded system at pH = 5, while only 32% of DOX was released from the drug-loaded system at pH = 7.4. The above phenomenon is due to the dissolution of ZnO quantum dots and dissociation of drug-metal complexes under acidic conditions, which triggers the release of DOX.

3.3 Cytotoxicity assay *in vitro*

Drug carriers should not only have high drug-carrying abilities and controlled drug-delivery capability but also possess good biocompatibility (Peppicelli et al., 2017). According to the results of PL, 4% La-ZnO is selected to evaluate the effect of La-ZnO on cellular behaviors, and the concentration-dependent cytotoxicity of pure ZnO QDs and La-ZnO QDs was evaluated with B16 cells. The results, as shown in Figures 9A,B, show that there is no significant toxic effect on both groups at concentrations below 15. Significant antitumor effects were exhibited in both groups when the dose exceeded 25 μg/ml, the survival rate of cytotoxic cells was 78% for the pure ZnO group and 74% for the La-ZnO group, which was attributed to ZnO quantum dots dissolving free Zn2+ into tumor cells. Interestingly, compared to pure ZnO, La-ZnO exhibited a stronger tumor-killing effect. This may be due to the addition of lanthanum causing a decrease in the mitochondrial membrane potential of tumor cells and thus increasing the level of reactive oxygen species (ROS) (He and Shi, 2011). In addition, it is positively correlated with the concentration of DOX particles. The same pattern was observed for the drug loading group, and the toxicity of pure DOX was relatively small, while the ZnO-DOX and 4% La-ZnO-DOX groups showed better cell inhibition. At 2.43 μg/ml of DOX, the cell viability of all the groups was reduced to about 70%, with increasing concentration, the cytotoxicity of all groups decreased significantly, and when the concentration was increased to 4.05, the cellular activity of free DOX, ZnO@DOX and La-ZnO@DOX decreased to 18%, 15%, 12%, respectively. Besides, the La-ZnO@DOX also shows a better anti-tumor effect, which indicates that the synthesized La-doped ZnO quantum dots not only have better fluorescence imaging ability, but also have a better anti-tumor effect, and this result is valuable for follow-up research.

Staining of live and dead cells is also effective way to evaluate the antitumor effect of materials (Shuai et al., 2018). It can be seen from Figure 9C that the cell survival rate of the pure ZnO group is higher, indicating that the low concentration of quantum dots is safe and has no toxic effect on normal cells, while the La-ZnO group presents more dead cells, indicating a better anti-tumor effect, which is consistent with the previous MTT experiment. This indicates that lanthanum doping not only improves the fluorescence effect of ZnO but also shows stronger anti-tumor properties than undoped samples. In addition, when the DOX was loaded, all groups showed large areas of dead cells, indicating that powerful anti-tumor effect of La-ZnO@DOX.

3.4 *In vivo* biocompatibility

In this study, the B16F10 melanoma model was used to study the biocompatibility of nano-platform *in vivo*, and the potentially toxic side effects of ZnO as a drug carrier on mice were studied. Six normal C57 mice were randomly divided into two groups, which were subcutaneously injected with 100uL PBS and 100 uL 25ug/mL ZnO, respectively. The body weight of mice was recorded for 10 consecutive days, and then the main organs

(liver, heart, spleen, lung, and kidney) of mice were collected for H&E staining. The body weight of mice at 10 days was recorded, as shown in Figure 10A. The results showed that there was no significant difference in the body weight of mice between the two groups. Figure 10B shows the staining results of the major organs of mice. The staining results showed that there was no significant difference between the major organs of mice treated with ZnO and the control group. The results show that ZnO had good biocompatibility and had no obvious toxic side effects on normal organs of mice. ZnO could be used as an effective drug carrier for anti-tumor research. The anti-tumor mechanism of lanthanum (La) ions may be attributed to the fact that lanthanum ions open the mitochondrial permeability transition pore, blocking the electron transport chain in the mitochondria, thus increasing the level of reactive oxygen species and inducing cancer cell death (Anghileri et al., 1987; Shuai et al., 2018; Vinothini et al., 2019).

3.5 *In vivo* antitumor activity

In this study, the *in vivo* antitumor efficacy of the nanoplatform in C57 mice was investigated using the B16F10 melanoma model. The tumor-bearing mice were divided into six groups: PBS, DOX, ZnO, 4La-ZnO, ZnO@DOX, and 4La-ZnO@DOX groups. The average relative tumor volume was measured daily. Data were processed by the normalization method. As shown in Figure 11A, ZnO, 4La-ZnO, DOX, ZnO@DOX, and 4La-ZnO@DOX all showed a certain degree of tumor inhibition compared with the control group, among which 4La-ZnO@DOX showed a stronger tumor growth inhibition effect, which was consistent with the results of cell experiments and staining experiments. Figure 11B shows the weight change of mice. Within 10 days after treatment, there is no significant difference in the weight of each group, which further verifies that ZnO has no obvious side effects and does not cause other toxic damage to the normal organs of mice, and has good biocompatibility. In addition, Figure 11C shows the size of the mouse tumor. The mean relative tumor volume in the 4La-ZnO@DOX group was smaller than that in the DOX and ZnO@DOX groups, indicating that the antitumor effect of 4La-ZnO@DOX was improved. The tumors of each mouse were collected for HE staining. Figure 11D shows the staining results of tumor sections. Compared with the control group, the tumor sections of the treatment group showed larger areas of necrosis and apoptosis, showing a better tumor inhibition effect. ZnO has the advantages of PH-responsive degradation, good dispersion and biocompatibility, so that 4La-ZnO@DOX has high tumor suppression efficiency. ZnO has the advantages of PH-responsive release and is selectively released in the tumor microenvironment. When the ZnO drug loading system enters the mice and accumulates in the tumor site, ZnO decomposes Zn2 +, which has certain cytotoxicity and can kill cancer cells. La3+ ions can induce endoplasmic reticulum-dependent apoptosis through Bcl-2/Bax cascade, leading to apoptosis of B16 cells (Yu et al., 2015). demonstrated that the antitumor mechanism of La3+ was partly attributed to miRNAs let-7a and Mir-34a (Wu et al., 2013). found that lanthanum induced primary neuronal apoptosis through mitochondrial dysfunction regulated by Ca2 and Bcl-2 families. Therefore, a lanthanum-doped zinc oxide drug delivery system could achieve a stronger antitumor effect.

4 Conclusion

Multifunctional lanthanum-doped zinc oxide (La-ZnO) quantum dots were successfully synthesized. The PEG-HA-La-ZnO QDs has the best fluorescence properties when the doping amount is 4%. PEG-HA-La-ZnO QDs exhibited better anti-tumor effect undoped samples. Dual enhancement of fluorescence and anti-tumor effect by La doping makes La-ZnO QDs promising in drug delivery system applications.

Data availability statement

The raw data supporting the conclusions of this article will be made available by the authors, without undue reservation.

Ethics statement

The animal study was reviewed and approved by the Jiangxi Science and Technology Normal University.

Author contributions

RH and SL: data curation and original draft. FW: review and editing. XP: visualization. JY:review and editing. JW: investigation. HF: methodology. WL: conceptualization, review, and editing.

Funding

This work was financially supported by the Natural Science Foundation of Jiangxi Province (20202BABL203041) and the Research Project of Jiangxi Provincial Department of Education (GJJ190600, GJJ150827).

Conflict of interest

The authors declare that the research was conducted in the absence of any commercial or financial relationships that could be construed as a potential conflict of interest.

Publisher's note

References

Anghileri, L. J., Crone-Escanye, M. C., and Robert, J. (1987). Antitumor activity of gallium and lanthanum: Role of cation-cell membrane interaction. *Anticancer Res.* 7 (6), 1205–1207.

Brouet, V., Yang, W. L., Zhou, X. J., Hussain, Z., Moore, R. G., He, R., et al. (2008). Angle-resolved photoemission study of the evolution of band structure and charge density wave properties inRTe3(R=Y, La, Ce, Sm, Gd, Tb, and Dy). *Phys. Rev. B* 77 (23), 235104. doi:10.1103/PhysRevB.77.235104

Cai, X., Luo, Y., Zhang, W., Du, D., and Lin, Y. (2016). pH-Sensitive ZnO quantum dots–doxorubicin nanoparticles for lung cancer targeted drug delivery. *ACS Appl. Mat. Interfaces* 8 (34), 22442–22450. doi:10.1021/acsami.6b04933

Cai, X., Yan, H., Luo, Y., Song, Y., Zhao, Y., Li, H., et al. (2018). Mesoporous carbon nanospheres with ZnO nanolids for multimodal therapy of lung cancer. *ACS Appl. Bio Mat.* 1 (4), 1165–1173. doi:10.1021/acsabm.8b00381

Cao, S., Zheng, J., Zhao, J., Yang, Z., Li, C., Guan, X., et al. (2017). Enhancing the performance of quantum dot light-emitting diodes using room-temperature-processed Ga-doped ZnO nanoparticles as the electron transport layer. *ACS Appl. Mat. Interfaces* 9 (18), 15605–15614. doi:10.1021/acsami.7b03262

Ge, C., Xie, C., Hu, M., Gui, Y., Bai, Z., and Zeng, D. (2007). Structural characteristics and UV-light enhanced gas sensitivity of La-doped ZnO nanoparticles. *Mater. Sci. Eng. B* 141 (1-2), 43–48. doi:10.1016/j.mseb.2007.05.008

Gomez, K. E., Wu, F., Keysar, S. B., Morton, J. J., Miller, B., Chimed, T. S., et al. (2020). Cancer cell CD44 mediates macrophage/monocyte-driven regulation of head and neck cancer stem cells. *Cancer Res.* 80 (19), 4185–4198. doi:10.1158/0008-5472.CAN-20-1079

Gulia, S., and Kakkar, R. (2013). ZnO quantum dots for biomedical applications. *Adv. Mat. Lett.* 4 (12), 876–887. doi:10.5185/amlett.2013.3440

He, Q., and Shi, J. (2011). Mesoporous silica nanoparticle based nano drug delivery systems: Synthesis, controlled drug release and delivery, pharmacokinetics and biocompatibility. *J. Mat. Chem.* 21 (16), 5845–5855. doi:10.1039/c0jm03851b

Huang, P., Zheng, W., Gong, Z., You, W., Wei, J., and Chen, X. (2019). Rare Earth ion–and transition metal ion–doped inorganic luminescent nanocrystals: From fundamentals to biodetection. *Mater. Today Nano* 5, 100031. doi:10.1016/j.mtnano.2019.100031

Huang, W., Lv, X., Tan, J., Huang, Q., Cheng, H., Feng, J., et al. (2019). Regulable preparation of the oxygen vacancy of ZnO QDs and their fluorescence performance. *J. Mol. Struct.* 1195, 653–658. doi:10.1016/j.molstruc.2019.05.105

Khan, M. I., Hossain, M. I., Hossain, M. K., Rubel, M. H. K., Hossain, K. M., Mahfuz, A. M. U. B., et al. (2022). Recent progress in nanostructured smart drug delivery systems for cancer therapy: A review. *ACS Appl. Bio Mat.* 5 (3), 971–1012. doi:10.1021/acsabm.2c00002

Liu, Y., Miyoshi, H., and Nakamura, M. (2007). Nanomedicine for drug delivery and imaging: A promising avenue for cancer therapy and diagnosis using targeted functional nanoparticles. *Int. J. Cancer* 120 (12), 2527–2537. doi:10.1002/ijc.22709

Maksoudian, C., Saffarzadeh, N., Hesemans, E., Dekoning, N., Buttiens, K., and Soenen, S. J. (2020). Role of inorganic nanoparticle degradation in cancer therapy. *Nanoscale Adv.* 2 (9), 3734–3763. doi:10.1039/d0na00286k

Peppicelli, S., Andreucci, E., Ruzzolini, J., Margheri, F., Laurenzana, A., Bianchini, F., et al. (2017). Acidity of microenvironment as a further driver of tumor metabolic reprogramming. *J. Clin. Cell. Immunol.* 8 (485), 2. doi:10.4172/2155-9899.1000485

Prakash, J., Kumar, A., Dai, H., Janegitz, B. C., Krishnan, V., Swart, H. C., et al. (2021). Novel rare Earth metal–doped one-dimensional TiO2 nanostructures: Fundamentals and multifunctional applications. *Mater. Today Sustain.* 13, 100066. doi:10.1016/j.mtsust.2021.100066

Probst, C. E., Zrazhevskiy, P., Bagalkot, V., and Gao, X. (2013). Quantum dots as a platform for nanoparticle drug delivery vehicle design. *Adv. drug Deliv. Rev.* 65 (5), 703–718. doi:10.1016/j.addr.2012.09.036

Reisch, A., Runser, A., Arntz, Y., Mely, Y., and Klymchenko, A. S. (2015). Charge-controlled nanoprecipitation as a modular approach to ultrasmall polymer nanocarriers: Making bright and stable nanoparticles. *Acs Nano* 9 (5), 5104–5116. doi:10.1021/acsnano.5b00214

Sahu, T., Ratre, Y. K., Chauhan, S., Bhaskar, L. V. K. S., Nair, M. P., and Verma, H. K. (2021). Nanotechnology based drug delivery system: Current strategies and emerging therapeutic potential for medical science. *J. Drug Deliv. Sci. Technol.* 63, 102487. doi:10.1016/j.jddst.2021.102487

Shuai, C., Liu, L., Yang, Y., Gao, C., Zhao, M., Yi, L., et al. (2018). Lanthanum-containing magnesium alloy with antitumor function based on increased reactive oxygen species. *Appl. Sci.* 8 (11), 2109. doi:10.3390/app8112109

Singh, L., Aldosary, S., Saeedan, A. S., Ansari, M. N., and Kaithwas, G. (2018). Prolyl hydroxylase 2: A promising target to inhibit hypoxia-induced cellular metabolism in cancer cells. *Drug Discov. today* 23 (11), 1873–1882. doi:10.1016/j.drudis.2018.05.016

Sun, L. W., Shi, H. Q., Li, W. N., Xiao, H. M., Fu, S. Y., Cao, X. Z., et al. (2012). Lanthanum-doped ZnO quantum dots with greatly enhanced fluorescent quantum yield. *J. Mat. Chem.* 22 (17), 8221–8227. doi:10.1039/c2jm00040g

Thangeeswari, T., Priya, M., and Velmurugan, J. (2015). Enhancement in the optical and magnetic properties of ZnO: Co implanted by Gd3+ nanoparticles. *J. Mat. Sci. Mat. Electron.* 26 (4), 2436–2444. doi:10.1007/s10854-015-2703-2

Verma, R., Pathak, S., Srivastava, A. K., Prawer, S., and Tomljenovic-Hanic, S. (2021). ZnO nanomaterials: Green synthesis, toxicity evaluation and new insights in biomedical applications. *J. Alloys Compd.* 876, 160175. doi:10.1016/j.jallcom.2021.160175

Vimala, K., Shanthi, K., Sundarraj, S., and Kannan, S. (2017). Synergistic effect of chemo-photothermal for breast cancer therapy using folic acid (FA) modified zinc oxide nanosheet. *J. Colloid Interface Sci.* 488, 92–108. doi:10.1016/j.jcis.2016.10.067

Vinothini, K., Jeyaraj, M., Kumar, S. K., and Rajan, M. (2019). Dual role of lanthanum oxide nanoparticles functionalized Co-polymeric micelle for extended anti-cancer drug delivery. *ChemistrySelect* 4 (18), 5206–5213. doi:10.1002/slct.201803339

Wang, Q., Sun, Y., Li, S., Zhang, P., and Yao, Q. (2020). Synthesis and modification of ZIF-8 and its application in drug delivery and tumor therapy. *RSC Adv.* 10 (62), 37600–37620. doi:10.1039/D0RA07950B

Wu, J., Yang, J., Liu, Q., Wu, S., Ma, H., and Cai, Y. (2013). Lanthanum induced primary neuronal apoptosis through mitochondrial dysfunction modulated by Ca2+ and bcl-2 family. *Biol. Trace Elem. Res.* 152, 125–134. doi:10.1007/s12011-013-9601-3

Xiong, H. M. (2013). ZnO nanoparticles applied to bioimaging and drug delivery. *Adv. Mat.* 25 (37), 5329–5335. doi:10.1002/adma.201301732

Yu, L., Xiong, J., Guo, L., Miao, L., Liu, S., and Guo, F. (2015). The effectsof lanthanum chloride on proliferation and apoptosis of CervicalCancer cells: Involvement of let-7a and MiR-34a MicroRNAs. *BioMetals* 28, 879–890. doi:10.1007/s10534-015-9872-6

Yusupov, M., Privat-Maldonado, A., Cordeiro, R. M., Verswyvel, H., Shaw, P., Razzokov, J., et al. (2021). Oxidative damage to hyaluronan–CD44 interactions as an underlying mechanism of action of oxidative stress-inducing cancer therapy. *Redox Biol.* 43, 101968. doi:10.1016/j.redox.2021.10196810.1016/j.redox.2021.101968

Zhao, X., Liu, L., Li, X., Zeng, J., Jia, X., and Liu, P. (2014). Biocompatible graphene oxide nanoparticle-based drug delivery platform for tumor microenvironment-responsive triggered release of doxorubicin. *Langmuir* 30 (34), 10419–10429. doi:10.1021/la502952f

Zheng, L., Zhong, Y., He, T., Peng, S., and Yang, L. (2022). A codispersed nanosystem of silver-anchored MoS2 enhances antibacterial and antitumor properties of selective laser sintered scaffolds. *Int. J. Bioprint.* 8 (3), 577. doi:10.18063/ijb.v8i43.577

Zong, Y., Li, Z., Wang, X., Ma, J., and Men, Y. (2014). Synthesis and high photocatalytic activity of Eu-doped ZnO nanoparticles. *Ceram. Int.* 40 (7), 10375–10382. doi:10.1016/j.ceramint.2014.02.123

Zrazhevskiy, P., Sena, M., and Gao, X. (2010). Designing multifunctional quantum dots for bioimaging, detection, and drug delivery. *Chem. Soc. Rev.* 39 (11), 4326–4354. doi:10.1039/B915139G

frontiers | Frontiers in Chemistry

TYPE Original Research
PUBLISHED 10 October 2022
DOI 10.3389/fchem.2022.1035741

OPEN ACCESS

EDITED BY
He Xiaojun,
Wenzhou Medical University, China

REVIEWED BY
Xiao-Hui Zheng,
Wenzhou Medical University, China
Wei Zhang,
Shenzhen Institutes of Advanced Technology (CAS), China

*CORRESPONDENCE
Jintao Wang,
jintaochem@163.com
Xuemin Duan,
duanxuemin@126.com
Xiangwen Liao,
Liao492008522@163.com

SPECIALTY SECTION
This article was submitted to Medicinal and Pharmaceutical Chemistry, a section of the journal Frontiers in Chemistry

RECEIVED 03 September 2022
ACCEPTED 20 September 2022
PUBLISHED 10 October 2022

CITATION
Jiang L, Ma Y, Xiong Y, Tan Y, Duan X, Liao X and Wang J (2022), Ruthenium polypyridine complexes with triphenylamine groups as antibacterial agents against Staphylococcus aureus with membrane-disruptive mechanism. *Front. Chem.* 10:1035741. doi: 10.3389/fchem.2022.1035741

Ruthenium polypyridine complexes with triphenylamine groups as antibacterial agents against *Staphylococcus aureus* with membrane-disruptive mechanism

Li Jiang[1], Yuanyuan Ma[1], Yanshi Xiong[1], Yanhui Tan[2], Xuemin Duan[1]*, Xiangwen Liao[1]* and Jintao Wang[1]*

[1]Jiangxi Provincial Key Laboratory of Drug Design and Evaluation, School of Pharmacy, Jiangxi Science & Technology Normal University, Nanchang, China, [2]State Key Laboratory for Chemistry and Molecular Engineering of Medicinal Resources, School of Chemistry and Pharmaceutical Sciences, Guangxi Normal University, Guilin, China

Due to the emergence and wide spread of methicillin-resistant *Staphylococcus aureus*, the treatment of this kind of infection becomes more and more difficult. To solve the problem of drug resistance, it is urgent to develop new antibiotics to avoid the most serious situation of no drug available. Three new Ru complexes [Ru (dmob)$_2$PMA] (PF6)$_2$ (**Ru-1**) [Ru (bpy)$_2$PMA] (PF6)$_2$ (**Ru-2**) and [Ru (dmb)$_2$PMA] (PF6)$_2$ (**Ru-3**) (dmob = 4,4′-dimethoxy-2,2′-bipyridine, bpy = 2,2′-bipyridine, dmb = 4,4′-dimethyl-2,2′-bipyridine and PMA = N-(4-(1H-imidazo [4,5-f] [1,10] phenanthrolin-2-yl) -4-methyl-N-(p-tolyl) aniline) were synthesized and characterized by 1H NMR, 13C NMR and HRMS. The detailed molecular structure of **Ru-3** was determined by single crystal X-ray diffraction. Their antibacterial activities against *Staphylococcus aureus* (*Staphylococcus aureus*) were obvious and **Ru-3** showed the best antibacterial effect with the minimum inhibitory concentration value of 4 μg ml^{-1}. Therefore, further study on its biological activity showed that **Ru-3** can effectively inhibit the formation of biofilm and destroy cell membrane. *In vitro* hemolysis test showed that **Ru-3** has almost negligible cytotoxicity to mammalian red blood cells. In the toxicity test of wax moth insect model, **Ru-3** exhibited low toxicity *in vivo*. These results, combined with histopathological studies, strongly suggest that **Ru-3** was almost non-toxic. In addition, the synergistic effect of **Ru-3** with common antibiotics such as ampicillin, chloramphenicol, tetracycline, kanamycin and gentamicin on *Staphylococcus aureus* was detected by chessboard method. Finally, *in vivo* results revealed that **Ru-3** could obviously promote the wound healing of *Staphylococcus aureus* infected mice.

KEYWORDS

Ru(II) complexes, antimicrobial properties, antibiofilm activity, synergistic effect, membrane-disruptive mechanism

Introduction

Since the discovery of penicillin, antibiotics have saved countless lives, prevented fatal infections and made great contributions to the Figureht against human infectious diseases. However, the extensive and evolving pathogenic behavior of bacteria and the abuse and misuse of antibiotics lead to a sharply increase in bacterial drug resistance, which poses a serious threat to public health (Aslam et al., 2018; Tacconelli et al., 2018; Richter and Hergenrother, 2019; De Oliveira et al., 2020; Laxminarayan et al., 2020; Song et al., 2020). It is predicted that drug-resistant infection may cause 10 million deaths every year by 2050 (Piddock, 2016; Abouelhassan et al., 2019). *Staphylococcus aureus* is one of the most common causes of hospital and community-acquired infection, which is closely related to pneumonia, endocarditis, osteomyelitis, arthritis and sepsis (Hussain et al., 2018). Due to the emergence and wide spread of methicillin-resistant *Staphylococcus aureus*, the treatment of this kind of infection becomes more and more difficult. To solve the problem of drug resistance, it is urgent to develop new antibiotics to avoid the most serious situation of no drug available.

It is widely accepted that some transition metal complexes have more advantages than traditional organic molecular drugs, such as easy structural modification, rich photophysical and electrochemical properties (Gitlin and Lill, 2012; Howerton et al., 2012; Knoll and Turro, 2015) Among them, polypyridine ruthenium (II) complexes have a wide range of potential properties, such as DNA binding agents, antibacterial agents and anticancer agents (Li et al., 2015; Mesquita et al., 2018; Moumita et al., 2021). So far, a few ruthenium (II) complexes have been reported as antibacterial agents (Patra, et al., 2012; Gorle et al., 2014; Nyawade, et al., 2015; Srivastava, et al., 2019; Lei, et al., 2020; Singh and Barman, 2021; Sun et al., 2021; Varney et al., 2021) and generally ruthenium (II) complexes were more active than theirs' coordinative ligands (Carlsen et al., 1981; Weber et al., 2016). Moreover, some of that reported Ru(II) polypyridine complexes with different functional groups simultaneously exhibited interesting synergy effects between existing common antibiotics, which were potential adjuvants to enhance the effect of existing antibiotics on *Staphylococcus aureus* (Liao et al., 2020; Zhang et al., 2022).

Recently, Tang and co-workers explored a multifunctional TPA derivative, which showed good selective sterilization effect and targeted Gram-positive bacteria. In addition, that compound could destroy the cell membrane of *Staphylococcus aureus* under white light irradiation and had important anti-infective effect *in vivo* (Kang et al., 2019; Li et al., 2022; Liu et al., 2022). Inspired by the above research, herein, three new Ru(II) complexes (Figure 1) with TPA derivatives were designed and synthesized [Ru $(domb)_2PMA]$ $(PF6)_2$ (**Ru-1**) [Ru $(bpy)_2PMA]$ $(PF6)_2$ (**Ru-2**) and [Ru $(dmb)_2PMA]$ $(PF6)_2$ (**Ru-3**). Their antibacterial activity against *Staphylococcus aureus* was evaluated. In addition, considering the toxicity and drug resistance of **Ru-3** with the best activity, its behaviors concerning antibacterial adjuvant, bacterial biofilm destruction, antibacterial mechanism, antibacterial activity *in vivo* were further explored.

Materials and methods

All reagents and materials were purchased from commercial suppliers used as received without further purification. 4-di-p-tolylamino benzaldehyde and 1,10-phenanthroline-hydrate were purchased from Energy-chemical. Rabbit blood was purchased from Maojie Microbes. 3, 3′-dipropylthiadicarbocyanine iodide [$DiSC_3(5)$] was purchased from Macklin. 4′,6-diamidino-2-phenylindole (DAPI) was purchased from Solarbio and propidium Iodide (PI) was obtained from 3 A Materials. All antibiotics and crystal violet were obtained from Sangon. Tryptic soy broth (TSB) was purchased from Hapebio. Agar powder was purchased from Chembase. *Staphylococcus aureus* strain was obtained from China Center of Industrial Culture Collection (CICC).

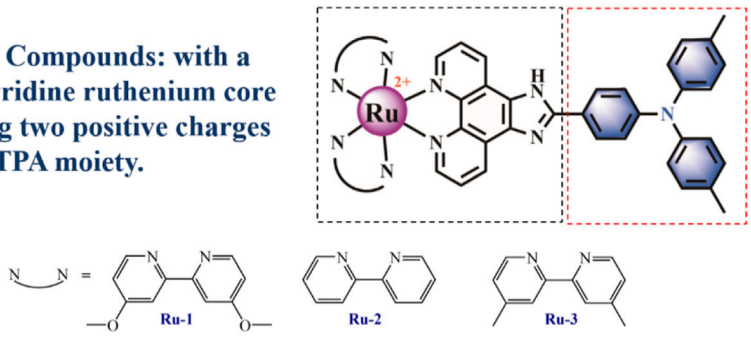

FIGURE 1
Structures and design strategy for target Ru(II) complexes.

The starting materials $[Ru(dmob)_2Cl_2]$ $[Ru(bpy)_2Cl_2]$ and $[Ru(dmb)_2Cl_2]$ were synthesized according to the literature (Sullivan et al., 1978; Collin and Sauvage, 1986; Castellano et al., 1998; Tran et al., 2013).

Nuclear magnetic spectra were recorded on a Bruker AVANCE 400 spectrometer under ambient conditions. High resolution mass spectrometric analysis was carried out on a Waters Xevo G2-XS Q-TOF instrument. A Shimadzu UV-2550 UV-vis spectrophotometer was used for UV scanning. A biochemical incubator and constant temperature culture shaker were purchased from Yiheng Scientific Instruments. Enzyme-labeled instrument was obtained from BioTek Instruments and a fluorescent cell imager was purchased from BIO-RAD.

Synthesis and characterization PMA

The ligand N-(4-(1H-imi-dazo[4,5-f][1,10]phenanthrolin-2-yl(phenyl)-4-methyl-N-(p-tolyl)aniline was synthesized according to the literature (Zhang et al., 2011; Peng et al., 2021). ^{1}H NMR (400 MHz, $CDCl_3$) δ 8.82 (s, 4H), 8.08 (d, J = 8.1 Hz, 2H), 7.39 (s, 2H), 7.05–6.84 (m, 10H), 2.25 (s, 6H). HRMS (acetonitrile) m/z: calcd 492.2144 for $C_{33}H_{25}N_5$, found 492.2185 for $[PAM + H]^+$.

Synthesis and characterization Ru-1

($[Ru(dmob)_2PMA]$ $(PF_6)_2$). A mixture of $[Ru(dmob)_2Cl_2]$ (55.2 mg, 0.1 mmol) and PMA (49.8 mg, 0.1 mmol) in ethylene glycol (10 ml) was heated at 150°C under argon for 8 h to give a clear red solution. After cooling to room temperature, a red precipitate was obtained after 1 mmol KPF_6 aqueous solution (50 ml) was added. The crude product was purified by column chromatography on neutral alumina with a CH_3CN/Xylene mixture as the eluent to obtain a red powder. Yield: 56.5 mg (55.1%). ^{1}H NMR (400 MHz, DMSO-d_6) *d* 14.12 (s, 1H), 9.07 (d, J = 31.6 Hz, 2H), 8.49 (d, J = 18.0 Hz, 4H), 8.14 (d, J = 5.6 Hz, 4H), 7.90 (s, 2H), 7.64 (d, J = 6.4 Hz, 2H), 7.28 (s, 2H), 7.20 (d, J = 8.2 Hz, 6H), 7.06 (t, J = 10.2 Hz, 6H), 6.92 (s, 2H), 4.03 (s, 6H), 3.93 (s, 6H), 2.31 (s, 6H). ^{13}C NMR (101 MHz, DMSO-d_6) *d* 166.46, 166.30, 157.79, 151.85, 151.64, 149.64, 149.50, 143.89, 133.42, 130.18, 129.41, 127.67, 125.85, 125.24, 121.30, 120.07, 114.04, 113.86, 111.16, 56.66, 56.56, 20.32. HRMS (acetonitrile) m/z: calcd 512.6476 for $[C_{57}H_{49}N_9O_4Ru]^{2+}$, found 512.6492 for $[M\text{-}2PF_6]^{2+}$.

Synthesis and characterization Ru-2

($[Ru(bpy)_2PMA]$ $(PF_6)_2$). This complex was synthesized in an identical manner as described for complex **Ru-1** using a mixture of $[Ru(bpy)_2Cl_2]$ (147.4 mg, 0.3 mmol) and PMA (145.3 mg, 0.3 mmol). Yield: 280.8 mg (78.3%). ^{1}H NMR (400 MHz, DMSO-d_6) *d* 14.16 (s, 1H), 9.05 (d, J = 8.2 Hz, 2H), 8.77 (d, J = 8.2 Hz, 4H), 8.39 (s, 4H), 8.20–7.94 (m, 8H), 7.84–7.70 (m, 6H), 7.20 (d, J = 7.9 Hz, 4H), 7.04 (d, J = 8.0 Hz, 6H), 2.31 (s, 6H). ^{13}H NMR (101 MHz, DMSO-d_6) *d* 152.78, 152.68, 152.50, 149.99, 147.16, 147.08, 145.12, 143.87, 136.68, 133.41, 130.34, 130.18, 127.92, 127.64, 126.18, 125.89, 125.24, 120.03, 20.33. HRMS (acetonitrile) m/z: calcd 452.6264 for $[C_{53}H_{41}N_9Ru]^{2+}$, found 452.6285 for $[M\text{-}2PF_6]^{2+}$.

Synthesis and characterization Ru-3

($[Ru(dmb)_2PMA]$ $(PF_6)_2$). This complex was synthesized in an identical manner as described for complex **Ru-1**, with $[Ru(dmb)_2Cl_2]$ in place of $[Ru(domb)_2Cl_2]$. Yield: 121.3 mg (55.6%). ^{1}H NMR (400 MHz, DMSO-d_6) δ 14.09 (s, 1H), 9.04 (s, 2H), 8.71 (d, J = 18.3 Hz, 4H), 8.13 (s, 2H), 8.03 (s, 2H), 7.89 (s, 4H), 7.66 (s, 2H), 7.51 (s, 2H), 7.40 (s, 4H), 7.19 (s, 4H), 7.04 (s, 4H), 2.56 (s, 6H), 2.46 (s, 6H), 2.31 (s, 6H). ^{13}C NMR (101 MHz, DMSO-d_6) δ 156.22, 156.06, 150.26, 149.40, 149.20, 144.80, 143.93, 133.30, 130.14, 129.82, 128.34, 128.21, 127.61, 125.84, 125.14, 124.80, 120.18, 20.59, 20.50, 20.30. HRMS (acetonitrile) m/z: calcd 480.6577 for $[C_{57}H_{49}N_9Ru]^{2+}$, found 480.6597 for $[M\text{-}2PF_6]^{2+}$.

Single crystal X-ray data

Collection and Structure Refinement. The monocrystal data of the **Ru-3** (0.11 × 0.06 × 0.04 mm) were collected using an Agilent Gemini EOS diffractometer with graphite-monochromated with Mo-Kα radiation (λ = 0.71073) at 170 K. An empiric absorption correction was applied. All the non-hydrogen atoms were refined anisotropically and the hydrogen atoms of organic molecule were refined in calculated positions, assigned isotropic thermal parameters, and allowed to ride their parent atoms. All calculations were performed using the SHELX2014 program package (Sheldrick, 2015). Crystallographic data (excluding structure factors) for the structure of **Ru-3** in this paper have been deposited with the Cambridge Crystallographic Data Centre with the reference numbers 2165862.

Antibacterial activity

Antibacterial activity was evaluated by measuring MIC (minimum inhibitory concentration) and MBC (minimum bactericidal concentration) values. The MIC value was measured by the microdilution method using TSB broth with 96 well plates (Carlsen et al., 1981) and the MBC value was determined by LB plates. In brief, the overnight cultured bacteria were 1: 1000 diluted with fresh medium to get a bacterial

suspension. After incubation at 37°C for 20 h, the growth of bacteria is monitored by observing the turbidity of the culture. The bacterial solution was diluted as above method and the complexes were incubated with bacterial solution for 2 h. Then 100 μL bacterial solution was taken for plate coating. The *Staphylococcus aureus* growth inhibition trend in the presence of complexes was obtained. The MBC values of complexes were determined by LB plates after culturing in the same method for 24 h. All experiments were controlled with sterile water and repeated in parallel at least three times.

Hemolytic activity

Obtain red blood cells from fresh sterile rabbit blood and rabbit blood was washed three times with PBS. Ru(II) complexes in 950 μL phosphoric acid buffer (PBS) of different concentrations and 50 μL red blood cells were added into a 1.5 ml sample tube, incubated at 37°C for 30 min. The negative control was red blood cell suspension containing only PBS, and the positive control was PBS containing 0.1% (V/V) Triton X-100. After incubating the mixture was centrifugated (2000 rpm for 2 min) and the supernatant (200 μL) was transfered to another 96 well plate. Finally, the hemolysis rate was calculated by measuring the absorbance at 540 nm.

Effect of ruthenium complex on the growth of *Staphylococcus aureus*

The effect of ruthenium complexes on the growth curve of *Staphylococcus aureus* was determined. Briefly, overnight cultured *Staphylococcus aureus* was diluted 1:1000 with fresh broth medium. Then the bacterial culture and ruthenium complexes were placed in a 24 well Petri dish and shaken at 37°C. After, the OD_{600} of bacteria was measured every 30 min for 20 h. Data analysis was carried out with Graphad Prism.

Determination of distribution coefficient

The partition coefficients of all complexes were determined by standard shake flask method in 1-octanol and buffer liquid system (Yang et al., 2021). In brief, the octanol/water partition coefficient is obtained by the incubation of 2 ml of 25 μg ml^{-1} ruthenium complex 1-octanol and 2 ml PBS samples. After shaking the solution for 6 h, the samples were stood for 2 h. The absorbance of octanol complex at 282 nm before and after oscillation was measured. The absorbance of 1-octanol before oscillation minus the absorbance of 1-octanol after oscillation is the absorbance of the complex in water. Each experiment was repeated three times. The partition coefficient is reported as the number of octanol divided by the number of water.

Effect of Ru-3 on biofilm formation

24 well plate was used for biofilm determination. The overnight cultured *Staphylococcus aureus* strain was diluted 1000 times with fresh TSB medium. Then 2 ml of that diluted bacterial solution was mixed with 500 μL **Ru-3** of different concentrations in a 24 well plate. After incubation at 37°C for 48 h, the bacterial suspension was removed and the plate was washed three times with PBS. The adherent bacteria were dried overnight at 37°C and then dyed through 0.1% crystal violet solution. After 2 min, taking out the crystal violet solution and wash the plate with PBS again. And then, adding 1 ml acetic acid and 1 ml water, the formation of biofilm can be determined by monitoring the absorbance at 595 nm.

Ru-3 killing bacteria in biofilm

To establish bacterial biofilm, the overnight cultured *Staphylococcus aureus* strain was diluted 1000 times with fresh TSB medium, then the bacterial suspension was transferred to 96 well plate and cultured for 24 h. Subsequently, the supernatant was removed and the formed biofilm was washed 3 times with PBS solution. 200 μL solution containing **Ru-3** of different concentrations (512, 256, 128, 64, 32, 16, 8, 4 μg ml^{-1}) were added and further incubated at 37°C for 24 h. Biofilm without **Ru-3** were used as positive controls. Then the supernatant was discarded and the residual biofilm was cleaned using 200 μL PBS 3 times. Next, fresh medium was added to culture for 24 h (Yang et al., 2021). The solution after culture was diluted 1000 times and 100 μL was taken out for plate coating and counting.

Study on drug resistance of bacterial

After *Staphylococcus aureus* was cultured for 5 h, the bacteria were diluted 1000 times with fresh TSB and the MIC of **Ru-3** was measured. The bacterial solution grown at the sub inhibitory concentration of compound **Ru-3** was inoculated into fresh TSB medium for 5 h, then the MIC was measured, and the above procedure was repeated for 20 generations. Ampicillin was used as the control.

Checkerboard assay

Firstly, the MIC of all selected antibiotics was determined by the above method. *Staphylococcus aureus* was cultured overnight and diluted 1000 times with fresh TSB. Then 200 μL the diluted bacterial suspension, 25 μL **Ru-3** of gradient concentrations and 25 μL antibiotics of gradient concentrations were mixed in 96 well plates and further cultured at 37°C for 20 h. MIC values of single drug and the best combination effect

(combination of MICA and MICB) were measured. Graphpad prism software was used to draw the checkerboard map and isoline map.

Secrete toxins

Firstly, *S. aureus* was cultured overnight and diluted 1000 times with fresh TSB, then a mixture of **Ru-3** of 1 μg ml^{-1} or 2 μg ml^{-1} and *Staphylococcus aureus* solution was cultured in a shaking Table at 37°C for 18 h. After culturing, centrifuging (5000 rpm, 2 min) *Staphylococcus aureus* solution. And rabbit blood cells were prepared with PBS buffer (washing rabbit blood three times). Blood cells were collected by centrifugation (2000 rpm, 2 min). Secondly, a mixture containing 1 ml PBS buffer, 150 μL supernatant and 25 μL blood cells was cultured at 37°C for 30 min. Then cultured supernatant was obtained by centrifugation (2000 rpm, room temperature, 2 min). Finally, the optical density of the supernatant was measured at 540 nm.

Nucleic acid leakage

To verify the membrane damage, the loss of 260 nm absorbing material was carried out (Yu et al., 2021). Briefly, overnight cultured bacteria were diluted 1:1000 in fresh TSB and shaken at 37°C for about 5 h until the exponential stage was reached. The supernatant was removed by centrifugation, then the bacteria were resuspended to OD_{600} = 1 with PBS, which was further treated with **Ru-3** or polymyxin B and centrifuged after 2 h to precipitate bacterial cells. Subsequently, the loss of 260 nm absorbing material, including the release of DNA and RNA in the filtrate, was measured at 260 nm.

Effect of Ru-3 on bacterial cell morphology

Scanning electron microscope (SEM) is an important method to observe cell morphology. Briefly, *S. aureus* was cultured in TSB medium to exponential phase, which were collected and washed with PBS three times by centrifugation. After, the bacterial precipitate was diluted to OD_{600} = 0.3 with PBS. Using sterile water as the blank control, **Ru-3** (4 μg ml^{-1}) was added to the bacterial suspension solution for 2 h. After Incubating, the bacteria were fixed with 2.5% glutaraldehyde at 4°C overnight. Pour out the fixed solution and rinse the sample three times with 0.1 M PBS for 15 min each time. The samples were fixed with 1% osmic acid solution for 1–2 h, then the osmic acid was carefully taken out, and the samples were washed three times with 0.1 M PBS for 15 min each time. The samples were then dehydrated by a series of graded concentrations of ethanol (30%, 50%, 70%, 80%, 90% and 95%). The samples were further treated with a mixture of ethanol and isoamyl acetate (V/V = 1/1) for 30 min, then treated with pure isoamyl acetate for overnight. Finally, the treated samples were subjected to critical drying and observed by SEM.

$DiSC_3(5)$ and DAPI/PI fluorescence staining

Firstly, *S. aureus* was cultured in TSB medium to exponential phase. Exponential growth bacteria were collected by centrifugation at 5000 rpm for 2 min, then washed with PBS and diluted to OD_{600} value of 0.3. Secondly, **Ru-3** (4 μg ml^{-1}) was added to the bacterial suspension solution and incubated at 37°C for 2 h, then the supernatant was removed by centrifuging. Thirdly, the bacterial was washed with PBS for three times and suspendedin 500 μL PBS. Subsequently, adding 20 μL $DiSC_3(5)$ (30 μM), incubating for 1 h under dark conditions. For DAPI and PI, adding 20 μL DAPI (10 μg ml^{-1}), incubating for 15 min under dark conditions. Next, adding 20 μL PI (15 μg ml^{-1}) in the same tube, and incubating for 15 min under dark conditions. After that, centrifuge, removing the supernatant. Eventually, suspending with 500 uL PBS and 20 μL samples were transfered on glass slides and observed under fluorescent cell imager.

Study on membrane permeability

O-nitrobenzene-β-D-galactopyranoside (ONPG) was the substrate of intracellular *β*-galactosidase, that was used to determine the permeability of *Staphylococcus aureus* cell membrane. *Staphylococcus aureus* was cultured to logarithmic phase, then washed and cultured in M9 lactose medium, in which lactose was used as the only carbon source of a single colony and stayed overnight at 37°C. After washing three times with PBS, the culture was diluted to OD_{600} = 0.3 (PBS). Subsequently, **Ru-3** (4 μg ml^{-1}) or vancomycin (2 μg ml^{-1}, as positive control) was added to the bacterial suspension solution and then each tube also contains 1.5 mM ONPG, which was further shake at 37°C. The hydrolysis of ONPG to o-nitrophenol over time was monitored by UV every 15 min at 415 nm. A similar procedure was used for untreated cells as control (Xuan et al., 2021).

In vivo antibacterial activity test

S. aureus was cultured in TSB medium to exponential phase. Bacterial precipitates were collected and washed with PBS three times by centrifugation, which was diluted to OD_{600} = 1 (1.02 × 10^8 CFU/ml) with sterile normal saline. The day before the infection, the hair on the back of the mice was shaved off.

Then depilatory cream (Veet®) was used to remove the remaining hair. Subsequently, 100 μL *S. aureus* was injected in subcutaneous and the abscess formed after 12 h later. All mice infected with *S. aureus* were divided into two groups (n = 5 in each group), including control group and treatment group, **Ru-3** (0.05 mg ml^{-1}), which was fully mixed in sterile cream. Afterwards, mouse abscesses were treated with creams containing **Ru-3** 4 times a day. After 10 days, the experiment was ended. The study was conducted in strict accordance with NIH guidelines for the care and use of laboratory animals (NIH Publication No. 85–23, revised in 1985), and was reviewed and approved by the institutional animal care and use Committee of Guangxi Normal University (Guilin, China).

Acute skin irritation test

Female BALB/c mice were randomly divided into three groups, control group, **Ru-3** (0.05 mg ml^{-1}) group and **Ru-3** (0.1 mg ml^{-1}). The day before the experiment, the hair on the back of female mice was removed. The compound and distilled water control were gently attached to the shaving site (about 2 cm^2) once a day for 3 days. On the fourth day, the mice were killed by cervical dislocation. The skin tissue at the site of infections were taken out and fixed in 4% paraformaldehyde at 4°C for 1 day, then embedded in paraffin. Serial sections were prepared for H&E analysis.

Results and discussion

Synthesis and Characterization. All ligands and complexes were prepared according to the procedure shown in (Supplementary Figure S1) and characterized by 1H NMR spectrum, 13C NMR spectrum, HPLC, UV-Vis analysis and HR-MS spectrum. In the case of three ruthenium complexes (Supplementary Figure S2), the UV-Vis spectral data showed that there were strong bands at 264–287 nm, which may be attributed to the p–π* transition, while the relatively weak band in the range of 369–376 nm may correspond to the charge transfer transition from metal to ligand. There cationic complexes were isolated with hexafluorophosphate as the counteranion, making them easy to purify and less moisture-sensitive. Stock solutions (5 mg/ml) of all complexes were prepared in DMSO, which were further diluted using buffer or cell culture medium until working concentrations were achieved. As the complexes need to be stable in the biological environment, the stability of all ruthenium (II) complexes was determined by UV spectra. Three ruthenium (II) complexes dissolved in DMSO was diluted by acetonitrile or H_2O. There was no significant change in the spectral pattern from 0 to 24 h, as shown in Supplementary Figure S17, which suggests the stability of the complexes in solvent and indicates they can be used for antibacterial activities.

Crystal structures

Red crystals were obtained by volatilization from an acetonitrile and water mixture. The **Ru-3** was characterized by single-crystal X-ray crystallography. **Ru-3** crystallizes in the C2 monoclinic space group. Crystallographic data and structural parameters are listed in Table 1. Information concerning X-ray data collection and crystal structure refinement is summarized in Supplementary Table S1, with the selected bond lengths and bond angles listed in Suplementary Table S2. An ORTEP perspective view of the structure is shown in Figure 2, that proved the synthetic complex with the expected structure, and the obtained bond lengths and bond angles are similar to other reported related ruthenium polypyridine complexes (Liu et al., 2001; Singha et al., 2017). Nevertheless, the most interesting feature of the crystal structure is the mode of π-π electron interactions between pyridine rings of adjacent molecules, and the dihedral angle between ring 1 (N8–N9) and ring 2 (C46–C48) is only 14.28°, showing they are nearly parallel (Supplementary Figure S3). The distance between ring one and ring two is 3.710 Å, suggesting that weak intermolecular p-π stacking interactions are involved in stabilizing the monomer structure.

The antibacterial activity studies

The minimum inhibitory concentration (MIC) and the minimum bactericidal concentration (MBC) of three complexes against *S. aureus* were determined. As shown in Table 1, all designed TPA modified complexes showed interesting antibacterial activity, among which **Ru-3** exhibited the best antibacterial activity (MIC = 4 μg ml^{-1}, MBC = 32 μg ml^{-1}). Meanwhile, the MBC values of **Ru-1** and **Ru-2** are 16 μg ml^{-1} and 128 μg ml^{-1}. On the other hand, free TPA ligands and $RuCl_3{\cdot}3H_2O$ showed no antibacterial activity (>256 μg ml^{-1}). Therefore, the antibacterial results showed that the combination of the ligands and Ru was essential for complexes' antibacterial activities. In addition, the % hemolysis at 256 μg/ml values of the **Ru-3** was only 4%. Therefore, in terms of activity and toxicity, **Ru-3** exhibited the most promising antibacterial behavior among them. Herein, different auxiliary ligands affect the physicochemical properties of the complexes, especially hydrophilicity and lipophilicity, which were considered to be closely related to the antibacterial ability (Chopra et al., 2015). The distribution coefficient data show that **Ru-3** (logD o/w of ca. 1.7885) displayed more apparent lipophilicity than **Ru-1** (logD o/w of

10.3389/fchem.2022.1035741

TABLE 1 *In vitro* Antimicrobial Activities Against *S. aureus* and Hemolytic Activities of compounds.

Compounds	MIC μg/mL	MBC μg/mL	% Hemolysis at 256 μg/ml	LgP
Ru-1	16	128	8	1.14
Ru-2	8	16	16	0.97
Ru-3	4	32	4	1.79
PMA	>256	—	—	—
RuCl3·3H2O	>256	—	—	—
Vancomycin	2	—	—	—

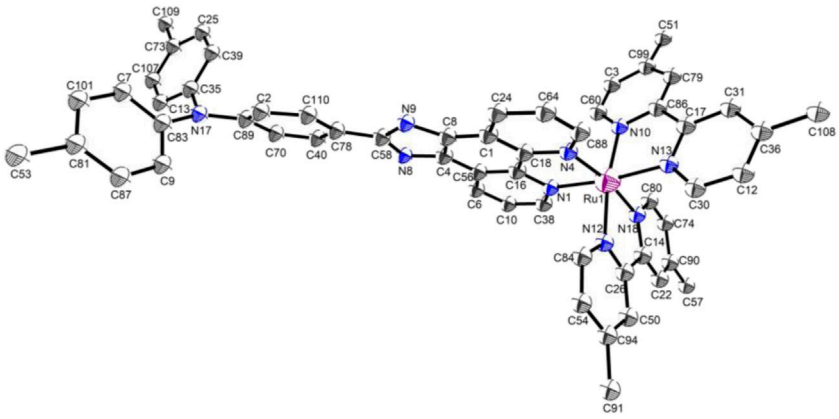

FIGURE 2
Thermal ellipsoid plot of Ru-3 in ORTEP view.

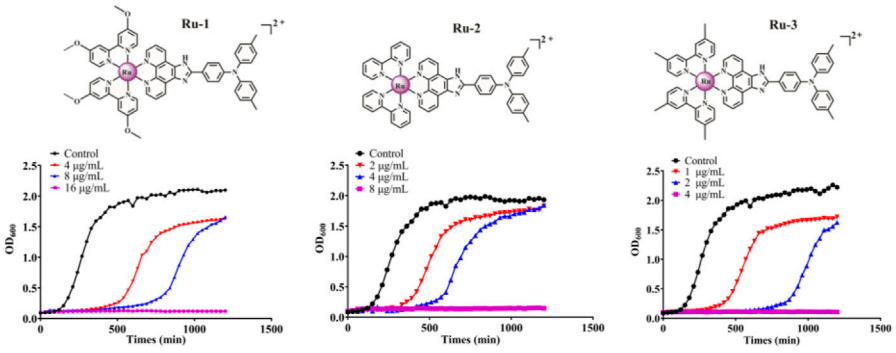

FIGURE 3
The inhibitory effect of Ru-1, Ru-2 and Ru-3 on *Staphylococcus aureus*. The bacterial culture was cultured in a plate reader at 37°C with orbit shaking at 180 rpm. The OD_{600} was recorded at 30 min intervals.

ca. 1.1445) and **Ru-2** (logD o/w of ca. 0.9681). Meanwhile, complexes with two positive charges are favorable for the interaction with negatively charged substances on the bacterial cell membrane, and further lead to destroy the membrane and cause bacterial death. Therefore, herein the polarity of **Ru-3** containing 4,4′- dimethyl-2,2′- bipyridine ligands probably contribute to the antibacterial activity against *Staphylococcus aureus*.

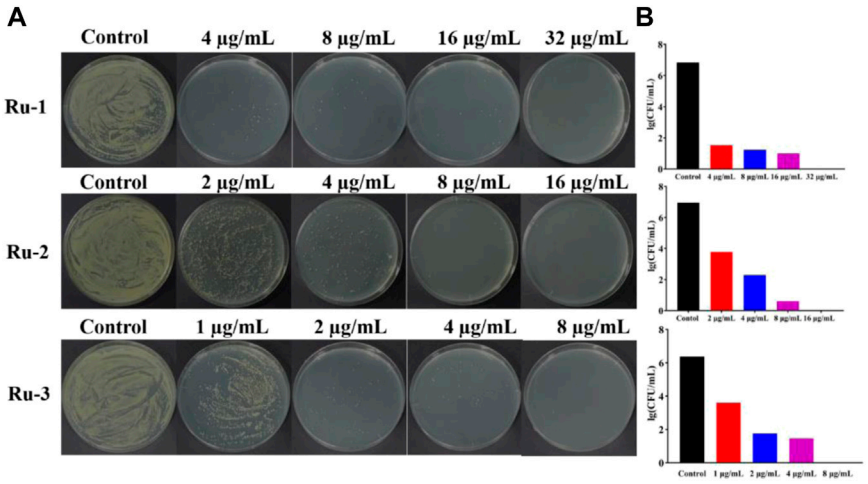

FIGURE 4
Ruthenium complex inhibited the growth of wild-type *Staphylococcus aureus* for 2 h **(A)** the plate experiment diagram. **(B)** the plate counting diagram.

Then, the effects of ruthenium complexes on the growth of *Staphylococcus aureus* was explored by measuring the growth curve of *Staphylococcus aureus*. As shown in Figure 3, the growth curve of three Ru complexes showed a dose-dependent inhibitory effect on *Staphylococcus aureus*. Further quantitative analysis was carried out by colony forming units (CFU) on agar plate to evaluate the activity of the complexes against *Staphylococcus aureus*. As shown in Figure 4, the antibacterial behaviors of **Ru-1**—**Ru-3** were obviously dose-dependent, and **Ru-3** still showed the best antibacterial effect among the three complexes, which was consistent with the experimental results of MIC value determination above.

Inhibit biofilm formation and bacterial biofilm disruption

Bacterial biofilm is a viscous structure formed by bacterial aggregation, which can protect bacterial cells from external influence and effectively resist the action of antibiotics (Chopra et al., 2015), and more than 80% of clinically malignant infections are associated with bacterial biofilm resistance (Conti et al., 2021). According to the above experiments, **Ru-3** was proved as the most effective complex. To further explore whether this complex can inhibit the formation of *S. aureus* biofilm, crystal violet staining method was carried out. **Ru-3** of sub inhibitory concentration was performed to ensure that it affected the formation of biofilm rather than kill bacteria. As shown in Figure 5, biofilm formation in the presence of **Ru-3** was significantly reduced by 27% and 41% at the concentration of 1 μg ml^{-1} and 2 μg ml^{-1}, respectively. These results

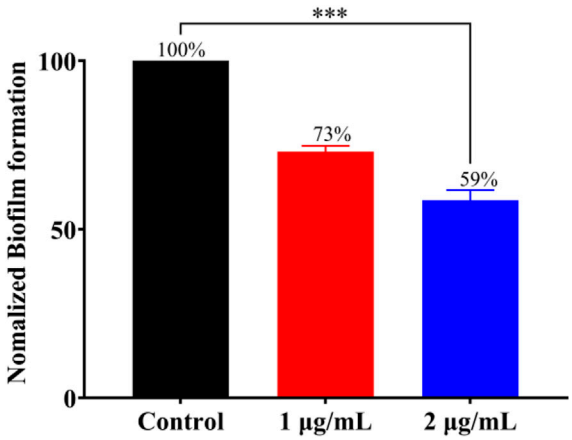

FIGURE 5
The effect of Ru-3 (1 μg ml^{-1} and 2 μg ml^{-1}) on the biofilm formation of *Staphylococcus aureus*.

indicated that **Ru-3** can obviously inhibit the formation of biofilm at sub inhibitory concentratidon.

Then, bacterial biofilm destruction assay was performed to further explore whether **Ru-3** can destroy biofilm, and the results were shown in Figure 6. It was clear that **Ru-3** displayed a significant effect on killing *Staphylococcus aureus* in biofilm, and with the increase of **Ru-3** concentration, the number of living bacteria in biofilm decreased dramatically. The number of the survival *Staphylococcus aureus* in the biofilm decreased from the initial 8.62 to 0 log10 colony-forming units per milliliter (CFU/ml) as the concentration of **Ru-3** was 32 μg ml^{-1}, which was exactly same as

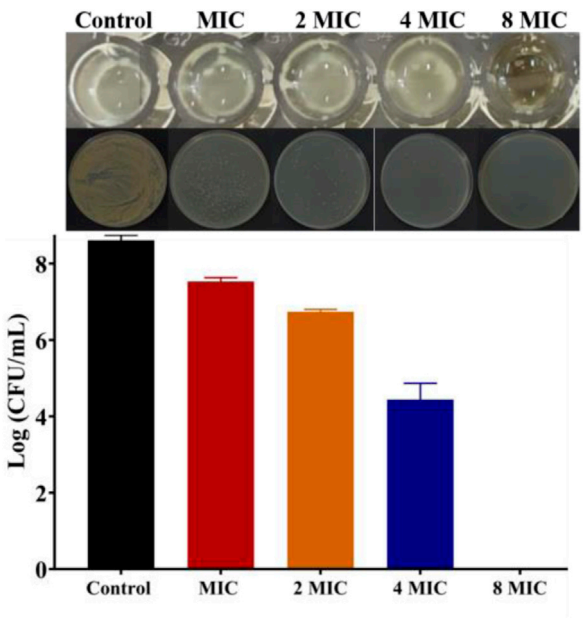

FIGURE 6
The results of killing the *Staphylococcus aureus* in the biofilm and count results of killing *Staphylococcus aureus* in biofilm.

its MBC value. These data indicated that **Ru-3** can inhibit not only the formation of biofilms, but also the already formed bacterial biofilms, suggesting that the antimicrobial behavior of **Ru-3** probably not be prone to drug resistance.

Resistance study

Antibiotic resistance has become an increasingly serious problem (Laxminarayan et al., 2020). To study the possibility of drug resistance induced by **Ru-3**, the drug resistance of *Staphylococcus aureus* for 20 generations was carried out at sublethal concentration. After 20 generations of *Staphylococcus aureus* culture, the MIC value of **Ru-3** increased only four times, indicating that **Ru-3** was not easy to be resistant to *Staphylococcus aureus*. In contrast, the lactam antibiotic ampicillin sodium rapidly induced bacterial drug resistance, and the MIC value increased more than 1024 times after 20 passages (Figure 7A) under the same experimental conditions. This result probably related to the rapid bactericidal effect of **Ru-3** and the destruction of bacterial cell membrane. More importantly, **Ru-3** unexpectedly exhibited apparent antibacterial activity against antibiotics resistant *Staphylococcus aureus*, which were obtained by treating with a variety of antibiotics for 20 generations (Figure 7B). The results showed that the MIC values of **Ru-3** against antibiotic resistant *S. aureus* were almost the same as the wild type *Staphylococcus aureus*. All the results showed that **Ru-3** had strong antibacterial activity against antibiotic resistant bacteria and had no obvious drug resistance.

Hemolysis test

The toxin produced by bacteria is also one of the primary causes of disease. To find whether **Ru-3** can inhibit the produced toxin by *Staphylococcus aureus*, hemolysis test was carried out. As shown in Figure 8, after incubation for 24 h, there was barely different in OD_{600} values between 1 μg ml^{-1}, 2 μg ml^{-1} and control group. Toxin was prominently reduced by 38% and 63% in the presence of **Ru-3** of 1 μg ml^{-1} and 2 μg ml^{-1} respectively. This showed that **Ru-3** could inhibit the toxin production of *Staphylococcus aureus* at sub inhibitory concentration. To verify that the rupture was not caused by buffer (PBS), a sterile control was also performed. The results showed that the red blood cells remained intact, indicating that

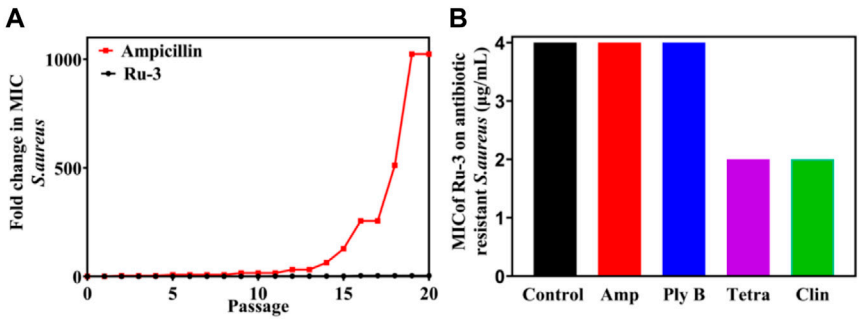

FIGURE 7
Bacterial resistance study of compound Ru-3 against *S. aureus* (Ampicillin was selected as a reference drug). **(A)** Fold changes in MIC values of compound Ru-3 and ampicillin against *Staphylococcus aureus*. **(B)** MIC of Ru-3 on different antibiotic resistant *Staphylococcus aureus*. Control: Wild *Staphylococcus aureus*. Amp: Ampicillin resistant *Staphylococcus aureus*. Ply **(B)** Polymyxin B resistant *Staphylococcus aureus*. Tetra: tetracycline resistant *Staphylococcus aureus*. Clin: Clindamycin resistant *Staphylococcus aureus*.

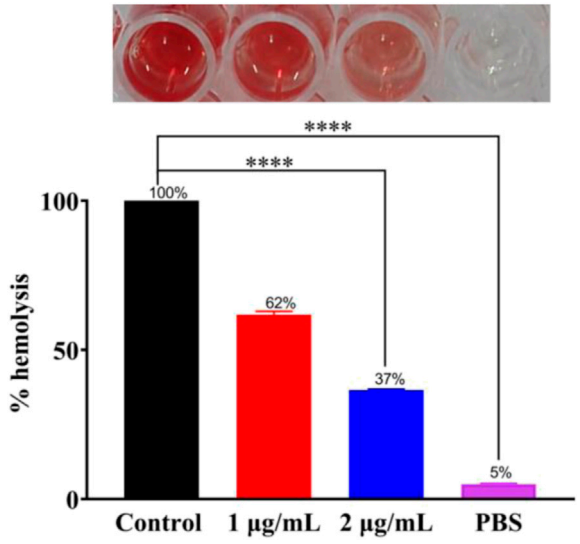

FIGURE 8
Experimental results of Ru-3 inhibitory toxin. Effect of 1 μg ml^{-1} or 2 μg ml^{-1} Ru-3 on the secretion of *Staphylococcus aureus* hemolysin. All experiments had three biological replicates.

the rupture of red blood cells was caused by the secretion of hemolysin by bacteria, and **Ru-3** effectively inhibited the secretion of hemolysin.

Synergistic effects with antibiotics

Antimicrobial adjuvants are considered as magic weapons against drug resistant bacteria. To study whether **Ru-3** can also be used as antibacterial adjuvant, the interactions between **Ru-3** and common antibiotics were performed by checkerboard method (Zhang et al., 2022). Fractional inhibitory concentration index (FICI) is defined as the sum of the MIC of each drug when used in combination divided by the MIC of the drug when used alone (synergism (FICI ≤0.5), preparability (0.5 < FICI ≤1), no difference (1 < FICI ≤2), antagonistic (FICI >2)) (Chen et al., 2021). As shown in Figure 9A, **Ru-3** had synergistic effects with kanamycin, gentamicin, chloramphenicol, ampicillin sodium and tetracycline, which demonstrated that **Ru-3** possessed antibacterial synergistic effect on a variety of antibiotics. To further reveal that synergistic effect, the incubations of the above antibiotics (gentamicin, ampicillin sodium, kanamycin, chloramphenicol and tetracycline) and **Ru-3** of sublethal concentration (0.25 MIC) were used to treat *S. aureus*. (Figure 9D). As expected, the antibacterial activity was significantly enhanced, indicating that there were distinct synergistic effects between them. Therefore, **Ru-3** not only exhibited obvious direct antibacterial activity, but also was a potential antibacterial adjuvant, which can effectively increase antimicrobial activity of some existing antibiotics.

Membrane damage of *Staphylococcus aureus*

The poor permeability of traditional antibiotics is one of the main reasons for the decrease of its therapeutic ability and the increase of multi drug resistant bacteria (Sun et al., 2021; Yan and Bassler, 2019; Gafur et al., 2020). Therefore, excellent membrane damage ability should be an important characteristic of newly developed antibacterial agents (Wang et al., 2019). To elucidate whether **Ru-3** can destroy the integrity of the bacterial membrane, the following experiments were carried out, including membrane depolarization studies, DAPI/PI staining and fluorescence microscope, ONPG experiment, leakage of nucleic acid and SEM.

Firstly, the membrane destruction ability of active molecule **Ru-3** was studied by fluorescence microscopy with 3, 3′-dipropylthiadicarbocyanine iodide [$DiSC_3(5)$]. $DiSC_3$ accumulates in cells on the polarized membrane, resulting in fluorescence self-quenching. However, when the integrity of the cell membrane is damaged by the change of membrane potential, $DiSC_3(5)$ will released from the cell membrane, resulting in a sharp increase in fluorescence intensity (Guo et al., 2021). As shown in Figure 10, the negative group showed no fluorescence in the stained group, while strong green fluorescence occurred in the **Ru-3** treated group. Indicating that compound **Ru-3** has effect on the bacterial cell membranes.

Secondly, 4′, 6-diamino-2-phenylindole (DAPI) and propidium iodide (PI) as staining agents to further analyze the antibacterial mechanism of compound **Ru-3**. DAPI can enter both living and dead cells and produce blue fluorescence, while PI can only enter cells with damaged membrane and combine with nucleic acid to produce red fluorescence (Sun et al., 2021). As shown in Figure 11, only blue fluorescence was observed in the negative control group, suggesting intact cell membranes of *Staphylococcus aureus*. In contrast, blue and red fluorescence was observed for the **Ru-3** groups, indicating that **Ru-3** can effectively disintegrate *S. aureus* membrane.

Thirdly, once the lipid bilayer of bacteria is physically destroyed, the cytoplasmic content will overflow (Rasamiravaka et al., 2015). When the cytoplasmic membrane is permeable, the non-permeable membrane chromogenic substrate o-nitrobenzene-β-Galactoside (ONPG) enters the cytoplasm and is destroyed by *β*-Galactosidase degraded to produce o-nitrophenol, showing special absorbance at 415 nm (Xuan et al., 2021). As shown in Figure 12, the plasma membrane permeability of *Staphylococcus aureus* induced by **Ru-3** increased with time and showed a concentration dependent trend. Compared with vancomycin, **Ru-3** exhibited better membrane permeability. The above results showed that the treatment of **Ru-3** caused damage to *Staphylococcus aureus* cells, which lead to the physical destruction of lipid bilayer and cell membrane, resulting in the serious leakage of cell contents.

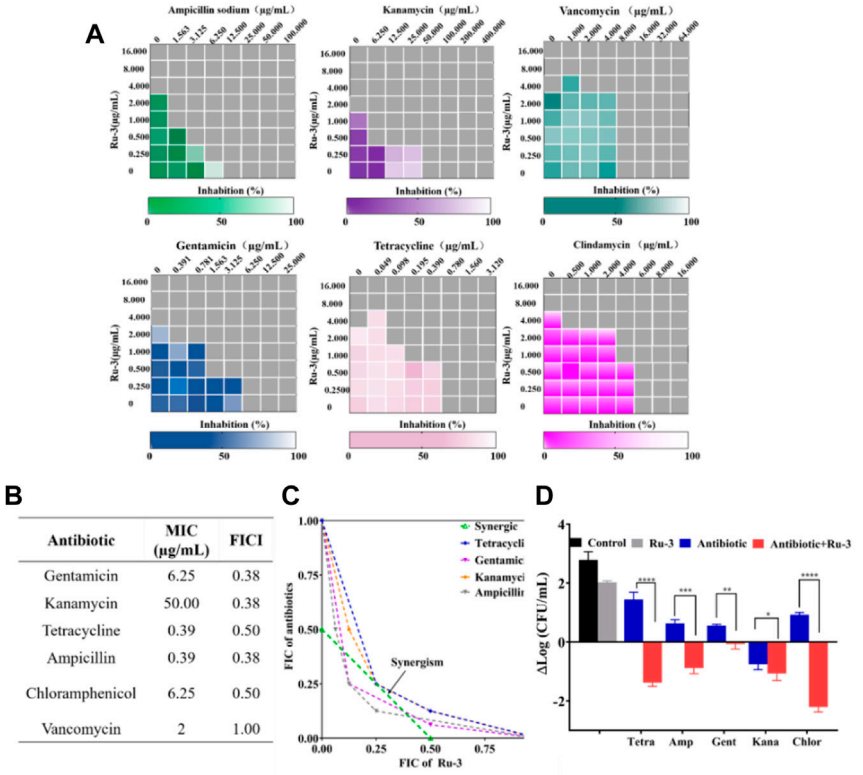

Antibiotic	MIC (μg/mL)	FICI
Gentamicin	6.25	0.38
Kanamycin	50.00	0.38
Tetracycline	0.39	0.50
Ampicillin	0.39	0.38
Chloramphenicol	6.25	0.50
Vancomycin	2	1.00

FIGURE 9
(A) Heat plots of checkerboard assays for Ru-3 in combination with different antibiotics against *Staphylococcus aureus*. **(B)** MIC of antibiotics and fractional inhibitory concentration indices (FIC) of the combination with Ru-3 against *Staphylococcus aureus* **(C)** An isobologram analysis of the synergistic effects of Ru-3 with Ampicillin, Chloramphenicol, Gentamicin, Kanamycin and Tetracyclines. **(D)** Logarithmic change of CFU mL^{-1} (from time zero) of *Staphylococcus aureus* after treatment with Ru-3 (2 μg ml^{-1}) and antibiotics with combined effect (0.25 MIC) for 3 h.

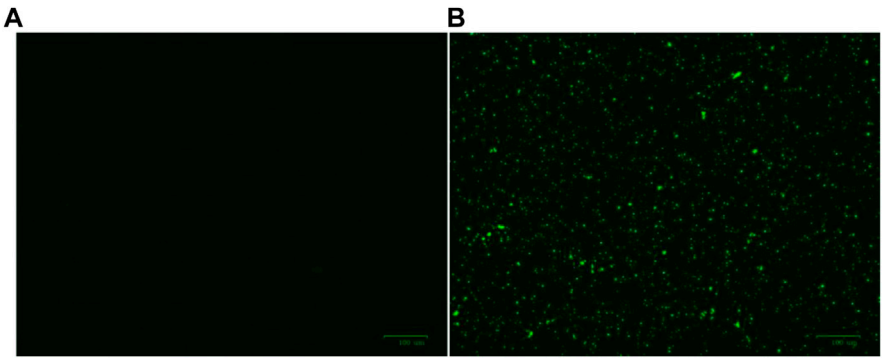

FIGURE 10
Effect of membrane depolarization **(A)** The blank control was bacteria without drug treatment. **(B)** *Staphylococcus aureus* treated with Ru-3 (4 μg ml^{-1}) for 2 h.

Fourthly, the damage of **Ru-3** to the membrane was further verified by measuring the leakage of nucleic acid. Nucleic acids have a characteristic UV absorption at 260 nm, therefore, the degree of cell nucleic acid leakage can be evaluated by observing the change in absorbance at 260 nm of the bacterial solution (Cui et al., 2015). As shown in Figure 13, after treating *S. aureus* with ruthenium **Ru-3** or

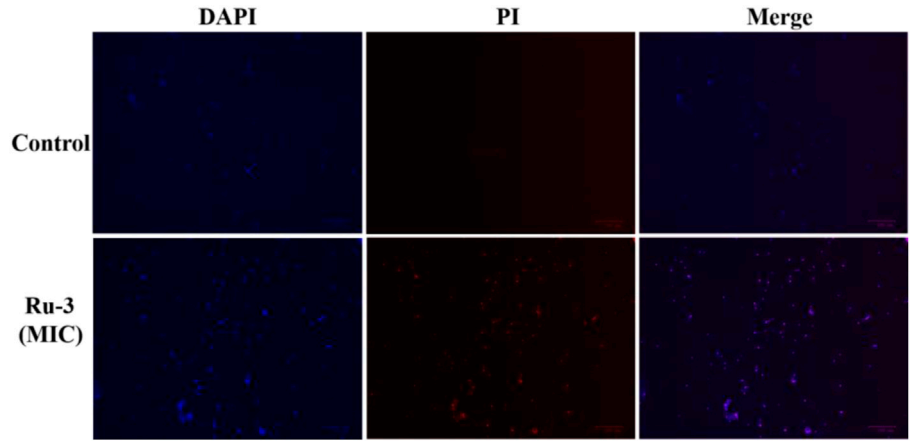

FIGURE 11
Fluorescence images of *Staphylococcus aureus* control or treated with Ru-3 (4 μg ml^{-1}) for 2 h, which stained with DAPI, PI. Scale bar: 100 μm.

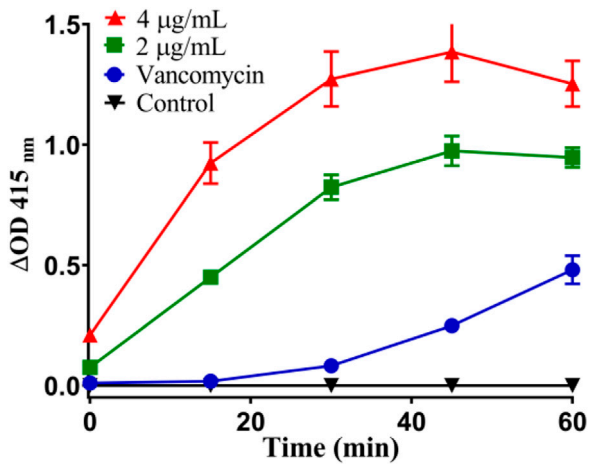

FIGURE 12
Plasma membrane permeability of *Staphylococcus aureus* cells treated with Ru-3 (2 μg/ml or 4 μg/ml) and vancomycin (2 μg/ml).

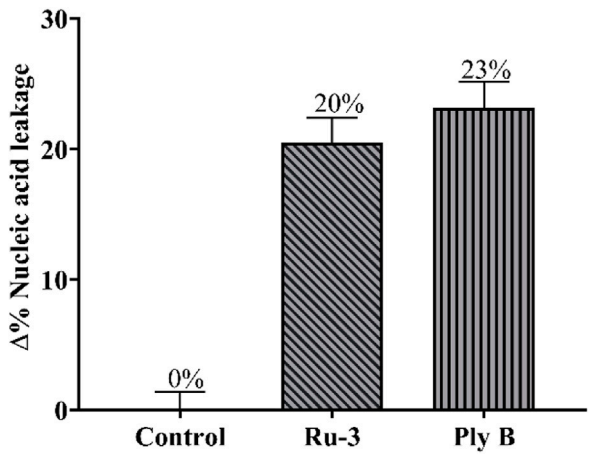

FIGURE 13
Percentage content of leaked nucleic acid from bacterial cells with the treatment of Ru-3 (4 μg/ml) or Ply B (Polymyxin B, 100 μg/ml).

polymyxin B, nucleic acid leakage increased significantly from 0% to 20% and 23%, comparing with the blank. The above results demonstrated that the treatment of **Ru-3** caused damage to *Staphylococcus aureus* cell membrane, resulting in the leakage of intracellular proteins. Importantly, **Ru-3**'s ability to break through cell membranes was much better than polymyxin B, which was a typical antibiotic that disrupted bacterial membrane.

Finally, the morphological observation of bacterial samples provides distinct evidence for the destruction and damage of bacterial cell membrane. As shown in Figures 14A,B, it was obvious that the bacteria in the control group showed a complete and smooth cell surface without rupture. After the treatment with **Ru-3** of a concentration of 4 μg ml^{-1} for 2 h, most of the bacterial structures were deformed, collapsed and many ripples were observed, revealing that the treatment of **Ru-3** would lead to the physical destruction of cell membrane.

Toxicity study

Based on the excellent antibacterial effect of **Ru-3** *in vitro*, its biosafety was further evaluated. Firstly, the hemolytic activity of ruthenium complexes on rabbit red blood cells was measured to study their toxicity. As shown in Figure 15A, **Ru-3** displayed

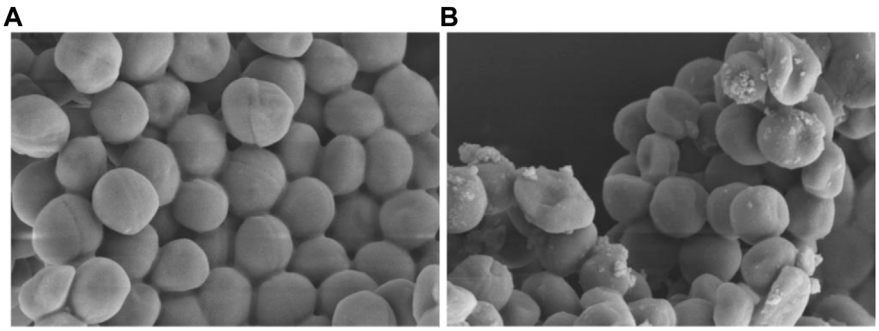

FIGURE 14
Scanning electron microscope (SEM) images of the cell membrane of *Staphylococcus aureus* cells treated with PBS or Ru-3 **(A)** PBS. **(B)** Ru-3 (4 μg/ml).

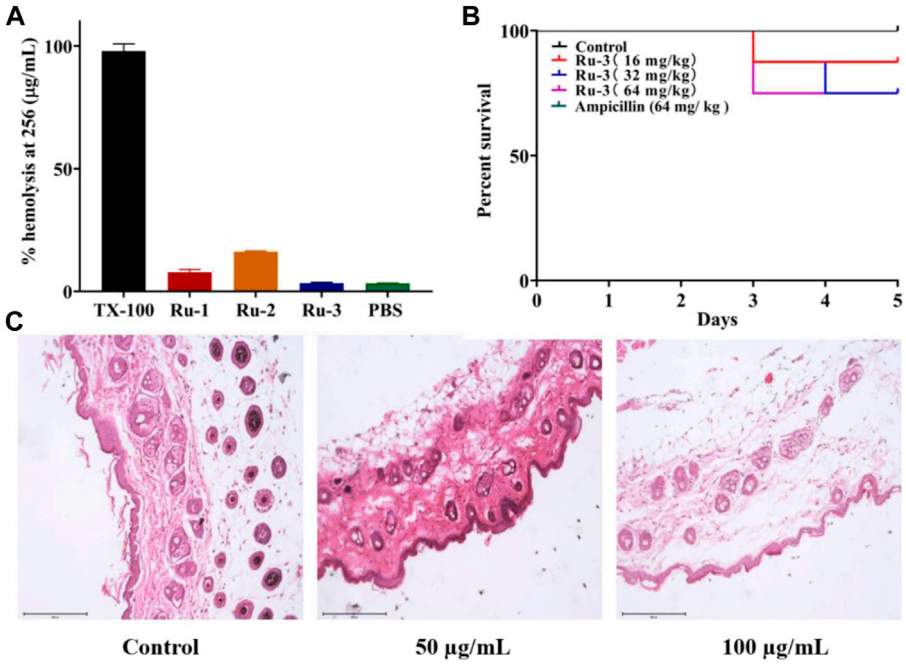

FIGURE 15
Test results of Ru compounds toxicity **(A)** % hemolysis at 256 μg ml^{-1} of Ru compounds. **(B)** Kaplan-Meier survival curves. Determination of Ru-3 toxicity in the insect model Galleria mellonella (Ampcillin's curve coincides with control's curve.) Larvae were injected with 5 μL of water (control), or Ru-3 (4–512 mg kg^{-1}). The larvae were incubated at 37.5°C and live/dead scores were conducted at 120 h **(C)** H&E staining images of the infected tissues with different treatments.

negligible hemolytic activity, even if the concentration was as high as 256 μg ml^{-1}. In view of its good compatibility with mammalian red blood cells, the toxicity of **Ru-3** to eukaryotes was also studied. Herein, **Ru-3** was tested with Gallery melonella larvae. Because its physiology and immune system are extremely similar to mammals, this insect model is widely used as an *in vivo* model, especially in toxicity screening, which produces results comparable to more commonly used mammalian models (Roy et al., 2019). The results were shown in Figure 15B. When the concentration of **Ru-3** was 64 mg kg^{-1}, the survival rate was still 75%. Therefore, it indicated that **Ru-3** has low toxicity and good biocompatibility.

Finally, the skin irritation of **Ru-3** on BALB/c mice was further studied. Hematoxylin eosin (H&E) staining was used to study the pathological changes of muscle tissue caused by **Ru-3** in Figure 15C (Weber et al., 2016). Comparing the images produced by the treated and untreated tissues, the tissue sections of the **Ru-**

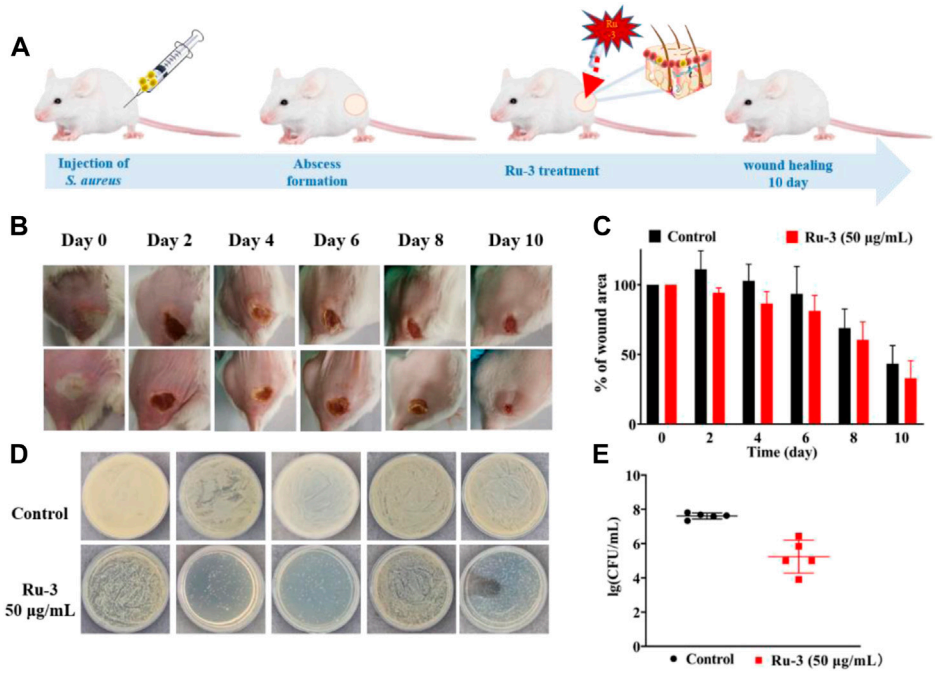

FIGURE 16
Treatment of *Staphylococcus aureus* skin infection *in vivo* **(A)** Scheme illustration of the procedures including the establishment of the *Staphylococcus aureus* infection mouse model and subsequent treatment regime. **(B)** Representative photos of skin abscesses with/without Ru-3 treatment **(C)** Change diagram of mouse wond. **(D)** Plate diagram of mouse wond colony calculation. **(E)** Colony count of wound in mice.

3 treatment group were very similar to the normal mouse tissues, indicating that there were no obvious pathological abnormalities. Therefore, **Ru-3** can be considered as a non-irritating complex and has good antibacterial effect and biocompatibility.

In vivo antibacterial assay

The above results have confirmed that **Ru-3** had good antibacterial activity against *Staphylococcus aureus*. To further explore whether **Ru-3** has significant antibacterial activity *in vivo*, a mouse skin infection model was established. The day before, the hair of the infected part of the mice was removed, then *Staphylococcus aureus* was inoculated to form an abscess on the skin. Subsequently, all mice were divided into two groups, and one group used cream with containing **Ru-3** (50 μg ml^{-1}) and other group used only cream, applying 4 times a day to the abscess. As shown in Figure 16, photos of infected tissue were obtained after 10 days, and subsequent wound healing was used to determine its antibacterial activity. Figure 16A showed a schematic diagram of infection and treatment regimen, and Figure 16B shows changes in wound healing after **Ru-3** (50 μg ml^{-1}, and untreated mice as control) treatment. Obviously, after 4 days of **Ru-3** treatment, the degree of wound healing increased significantly. Which indicates that **Ru-3** also has antibacterial activity *in vivo*.

Conclusions

In conclusion, functionalized ruthenium complex with triphenylamine (TPA) had good antibacterial activity against *Staphylococcus aureus*. **Ru-3** inhibited the formation of biofilm at sublethal concentration and killed the bacteria in the formed biofilm at eight MIC. According to the results of fluorescence staining, ONPG, nucleic acid leakage and scanning electron microscope, it was found that the mechanism of **Ru-3** may be the destruction of bacterial cell membrane. It is exciting to find that **Ru-3** can effectively inhibit the secretion of hemolysin from *Staphylococcus aureus* and has a low rate of auto-hemolysis. More importantly, it has low toxicity and good biocompatibility to the great wax beetle whose physiology and immune system are surprisingly same to mammals. The joint sensitivity test shows that **Ru-3** has synergistic effect on a variety of commonly used antibiotics, and maintains the original MIC value for some antibiotic resistant bacteria, which is helpful to formulate clinical medication plan. Finally, the *in vivo* infection study on mice showed that **Ru-3** significantly improved the wound healing process after skin infection with bacteria, and had no irritating effect on the skin. Obviously, multifunctional Ru complexes modified with TPA have great potential for the development of anti *Staphylococcus aureus* agents.

Data availability statement

The datasets presented in this study can be found in online repositories. The names of the repository/repositories and accession number(s) can be found below: https://www.ccdc.cam.ac.uk/solutions/csd-system/components/csd/.

Ethics statement

The animal study was reviewed and approved by the institutional animal care and use Committee of Guangxi Normal University (Guilin, China).

Author contributions

JL was the study manager. XD conducted statistical analyses on the data. JW co-directed the study and co-wrote the manuscript. YM co-wrote the manuscript. YT co-directed the study. YX oversaw analytical measurements. XL managed manuscript writing and quality control steps. All authors read and approved the final manuscript.

Funding

This work was supported by the National Natural Science Foundation of China (22067007, 22067006), The Natural Science Foundation of Jiangxi, China (20212BAB203007), The department of Education Science and Technology Research Project of Jiangxi, China (GJJ211106), Youth Top Talent Support Program of Jiangxi Science & Technology Normal University (2020QNBJRC007, 2021QNBJRC001).

Conflict of interest

The authors declare that the research was conducted in the absence of any commercial or financial relationships that could be construed as a potential conflict of interest.

Publisher's note

All claims expressed in this article are solely those of the authors and do not necessarily represent those of their affiliated organizations, or those of the publisher, the editors and the reviewers. Any product that may be evaluated in this article, or claim that may be made by its manufacturer, is not guaranteed or endorsed by the publisher.

Supplementary material

The Supplementary Material for this article can be found online at: https://www.frontiersin.org/articles/10.3389/fchem.2022.1035741/full#supplementary-material

References

Abouelhassan, Y., Garrison, A. T., Yang, H., Chávez-Riveros, A., Burch, G. M., and Huigens, R. W. (2019). Recent progress in natural-product-inspired programs aimed to address antibiotic resistance and tolerance. *J. Med. Chem.* 62, 7618–7642. doi:10.1021/acs.jmedchem.9b00370

Aslam, B., Wang, W., Arshad, M. I., Khurshid, M., Muzammil, S., Rasool, M. H., et al. (2018). Antibiotic resistance: a rundown of a global crisis. *Infect. Drug Resist.* 11, 1645–1658. doi:10.2147/IDR.S173867

Carlsen, P. H. J., Katsuki, T., Martin, V. S., and Sharpless, K. B. (1981). A greatly improved procedure for ruthenium tetroxide catalyzed oxidations of organic compounds. *J. Org. Chem.* 46, 3936–3938. doi:10.1021/jo00332a045

Castellano, F. N., Dattelbaum, J. D., and Lakowicz, J. R. (1998). Long-lifetime Ru(II) complexes as labeling reagents for sulfhydryl groups. *Anal. Biochem.* 255, 165–170. doi:10.1006/abio.1997.2468

Chen, J. P., Battini, N., Ansari, M. F., and Zhou, C. H. (2021). Membrane active 7-thiazoxime quinolones as novel DNA binding agents to decrease the genes expression and exert potent anti-methicillin-resistant *Staphylococcus aureus* activity. *Eur. J. Med. Chem.* 217, 113340. doi:10.1016/j.ejmech.2021.113340

Chopra, L., Singh, G., Jena, K. K., and Sahoo, D. K. (2015). Sonorensin: A new bacteriocin with potential of an anti-biofilm agent and a food biopreservative. *Sci. Rep.* 5, 13412. doi:10.1038/srep13412

Collin, J. P., and Sauvage, J. P. (1986). Synthesis and study of mononuclear ruthenium(II) complexes of sterically hindering diimine chelates. Implications for the catalytic oxidation of water to molecular oxygen. *Inorg. Chem.* 25, 135–141. doi:10.1021/ic00222a008

Conti, L., Mengoni, A., Giacomazzo, G. E., Mari, L., Perfetti, M., Fagorzi, C., et al. (2021). Exploring the potential of highly charged Ru(II)- and heteronuclear Ru(II)/Cu(II)-polypyridyl complexes as antimicrobial agents. *J. Inorg. Biochem.* 220, 111467. doi:10.1016/j.jinorgbio.2021.111467

Cui, H. Y., Zhao, C. T., and Lin, L. (2015). Antibacterial activity of Helichrysum italicum oil on VegeTables and its mechanism of action. *J. Food Process. Preserv.* 39, 2663–2672. doi:10.1111/jfpp.12516

De Oliveira, D. M. P., Kidd, B. M., Harris, P. N. A., Beatson, M. A., Beatson, S. A., Paterson, D. L., et al. (2020). Antimicrobial resistance in ESKAPE pathogens. *Clin. Microbiol. Rev.* 33, 001811–e219. doi:10.1128/cmr.00181-19

Gafur, A., Sukamdani, G. Y., Kristi, N., Maruf, A., Xu, J., Chen, X., et al. (2020). From bulk to nano-delivery of essential phytochemicals: recent progress and strategies for antibacterial resistance. *J. Mater. Chem. B* 8, 9825–9835. doi:10.1039/d0tb01671c

Gitlin, J. D., and Lill, R. (2012). Special issue: Cell biology of metals. *Biochim. Biophys. Acta (BBA) - Mol. Cell Res.* 9, 1405–1642. doi:10.1016/j.bbamcr.2012.07.008

Gorle, A. K., Feterl, M., Warner, J. M., Wallace, L., Keene, F. R., and Collins, J. G. (2014). Tri- and tetra-nuclear polypyridyl ruthenium(II) complexes as antimicrobial agents. *Dalton Trans.* 43, 16713–16725. doi:10.1039/c4dt02139h

Guo, Y., Hou, E. H., Wen, T. Y., Yan, X. T., Han, M. Y., Bai, L. P., et al. (2021). Development of membrane-active honokiol/magnolol amphiphiles as potent antibacterial agents against methicillin-resistant *Staphylococcus aureus* (MRSA). *J. Med. Chem.* 64, 12903–12916. doi:10.1021/acs.jmedchem.1c01073

Howerton, B. S., Heidary, D. K., and Glazer, E. C. (2012). Strained ruthenium complexes are potent light-activated anticancer agents. *J. Am. Chem. Soc.* 134, 8324–8327. doi:10.1021/ja3009677

Hussain, S., Joo, J., Kang, J., Kim, B., Braun, G. B., She, Z. G., et al. (2018). Antibiotic-loaded nanoparticles targeted to the site of infection enhance antibacterial efficacy. *Nat. Biomed. Eng.* 2, 95–103. doi:10.1038/s41551-017-0187-5

Kang, M. M., Zhou, C. C., Wu, S. M., Yu, B. G., Zhang, Z. J., Song, N., et al. (2019). Evaluation of structure-function relationships of aggregation-induced emission luminogens for simultaneous dual applications of specific discrimination and efficient photodynamic killing of gram-positive bacteria. *J. Am. Chem. Soc.* 141, 16781–16789. doi:10.1021/jacs.9b07162

Knoll, J. D., and Turro, C. (2015). Control and utilization of ruthenium and rhodium metal complex excited states for photoactivated cancer therapy. *Coord. Chem. Rev.* 282, 110–126. doi:10.1016/j.ccr.2014.05.018

Laxminarayan, R., Boeckel, T. V., Frost, I., Kariuki, S., Khan, E. A., Limmathurotsakul, D., et al. (2020). The lancet infectious diseases commission on antimicrobial resistance: 6 years later. *Lancet Infect. Dis.* 20, e51–e60. doi:10.1016/s1473-3099(20)30003-7

Lei, X. L., Qiu, L., Lan, M., Du, X. C., Zhou, S. W., Cui, P. F., et al. (2020). Antibacterial photodynamic peptides for staphylococcal skin infection. *Biomater. Sci.* 8, 6695–6702. doi:10.1039/d0bm01467b

Li, F. F., Collins, J. G., and Keene, F. R. (2015). Ruthenium complexes as antimicrobial agents. *Chem. Soc. Rev.* 44, 2529–2542. doi:10.1039/c4cs00343h

Li, J. Q., Meng, Z. J., Zhuang, Z. Y., Wang, B. N., Dai, J., Feng, G. X., et al. (2022). Effective therapy of drug-resistant bacterial infection by killing planktonic bacteria and destructing biofilms with cationic photosensitizer based on phosphindole oxide. *Small* 18, 2200743. doi:10.1002/smll.202200743

Liao, X. W., Jiang, G. J., Wang, J. T., Duan, X. M., Liao, Z. Y., Lin, X. L., et al. (2020). Two ruthenium polypyridyl complexes functionalized with thiophen: Synthesis and antibacterial activity against *Staphylococcus aureus*. *New J. Chem.* 44, 17215–17221. doi:10.1039/d0nj02944k

Liu, J. G., Zhang, Q. L., Shi, X. F., and Ji, L. N. (2001). Interaction of $[Ru(dmp)_2(dppz)]^{2+}$ and $[Ru(dmb)_2(dppz)]^{2+}$ with DNA: Effects of the ancillary ligands on the DNA-binding behaviors. *Inorg. Chem.* 40, 5045–5050. doi:10.1021/ic001124f

Liu, S. S., Wang, B. N., Yu, Y. W., Liu, Y. B., Zhuang, Z. Y., Zhao, Z. J., et al. (2022). Cationization-enhanced type I and type II ROS generation for photodynamic treatment of drug-resistant bacteria. *ACS Nano* 16, 9130–9141. doi:10.1021/acsnano.2c01206

Mesquita, M, Q., Dias, C. J., Neves, M. P. M. S., Almeida, A., and Faustino, M. F. (2018). Revisiting current photoactive materials for antimicrobial photodynamic therapy. *Molecules* 23, 2424. doi:10.3390/molecules23102424

Moumita, M. j., Sourav, A., Indira, B., Arnab, G., and Arindam, M. (2021). Effect of an imidazole-containing schiff base of an aromatic sulfonamide on the cytotoxic efficacy of N, N-coordinated half- sandwich ruthenium(II) p-cymene complexes. *Inorg. Chem.* 60, 4744–4754. doi:10.1021/acs.inorgchem.0c03706

Nyawade, E. A., Friedrich, H. B., Omondi, B., and Mpungose, P. (2015). Synthesis and characterization of new (η5-Cyclopentadienyl) dicarbonyl ruthenium(II) amine complexes: Their application as homogeneous catalysts in styrene oxidation. *Organometallics* 34, 4922–4931. doi:10.1021/acs.organomet.5b00564

Patra, M., Gasser, G., and Metzler-Nolte, N. (2012). Small organometallic compounds as antibacterial agents. *Dalton Trans.* 41, 6350–6358. doi:10.1039/c2dt12460b

Peng, Y. B., Tao, C., Tan, C. P., and Zhao, P. (2021). Mitochondrial targeted rhodium(III) complexes: Synthesis, characterized and antitumor mechanism investigation. *J. Inorg. Biochem.* 218, 111400. doi:10.1016/j.jinorgbio.2021.111400

Piddock, L. J. V. (2016). Reflecting on the final report of the O'neill review on antimicrobial resistance. *Lancet Infect. Dis.* 16, 767–768. doi:10.1016/s1473-3099(16)30127-x

Rasamiravaka, T., Labtani, Q., Duez, P., and Jaziri, M. E. (2015). the formation of biofilms by *Pseudomonas aeruginosa*: a review of the natural and synthetic compounds interfering with control mechanisms. *Biomed. Res. Int.* 2015, 1–17. doi:10.1155/2015/759348

Richter, M. F., and Hergenrother, P. J. (2019). The challenge of converting gram-positive-only compounds into broad-spectrum antibiotics. *Ann. N. Y. Acad. Sci.* 1435, 18–38. doi:10.1111/nyas.13598

Roy, S., Mondal, A., Yadav, V., Sarkar, A., Banerjee, R., Sanpui, P., et al. (2019). Mechanistic insight into the antibacterial activity of chitosan exfoliated MoS_2 nanosheets: Membrane damage, metabolic inactivation, and oxidative stress. *ACS Appl. Bio Mater.* 2, 2738–2755. doi:10.1021/acsabm.9b00124

Sheldrick, G. M. (2015). Crystal structure refinement with SHELXL. *Acta Crystallogr. C Struct. Chem.* C71, 3–8. doi:10.1107/s2053229614024218

Singh, A., and Barman, P. (2021). Recent advances in schiff base ruthenium metal complexes: Synthesis and applications. *Top. Curr. Chem. (Cham).* 379, 29–100. doi:10.1007/s41061-021-00342-w

Singha, K., Laha, P., Chandra, F., Dehury, N., Koner, A. L., and Patra, S. (2017). Long-lived polypyridyl based mononuclear ruthenium complexes: Synthesis, structure, and azo dye decomposition. *Inorg. Chem.* 56, 6489–6498. doi:10.1021/acs.inorgchem.7b00536

Song, M., Liu, Y., Huang, X., Ding, S., Wang, Y., Shen, J., et al. (2020). A broad-spectrum antibiotic adjuvant reverses multidrug-resistant Gram-negative pathogens. *Nat. Microbiol.* 5, 1040–1050. doi:10.1038/s41564-020-0723-z

Srivastava, P., Shukla, M., Kaul, G., Chopra, S., and Patra, A. K. (2019). Rationally designed curcumin based ruthenium(II) antimicrobials effective against drug-resistant *Staphylococcus aureus*. *Dalton Trans.* 48, 11822–11828. doi:10.1039/c9dt01650c

Sullivan, B. P., Salmon, D. J. J., and Meyer, T. (1978). Mixed phosphine 2, 2'-bipyridine complexes of ruthenium. *Inorg. Chem.* 17, 3334–3341. doi:10.1021/ic50190a006

Sun, H., Huang, S. Y., Jeyakkumar, P., Cai, G. X., Fang, B., and Zhou, C. H. (2021). Natural berberine-derived azolyl ethanols as new structural antibacterial agents against drug-resistant *Escherichia coli*. *J. Med. Chem.* 65, 436–459. doi:10.1021/acs.jmedchem.1c01592

Sun, W. Z., Jian, Y., Zhou, M. X., Yao, Y. S., Tian, N., Li, C., et al. (2021). Selective and efficient photoinactivation of intracellular *Staphylococcus aureus* and MRSA with little accumulation of drug resistance: Application of a Ru(II) complex with photolabile ligands. *J. Med. Chem.* 64, 7359–7370. doi:10.1021/acs.jmedchem.0c02257

Tacconelli, E., Carrara, E., Savoldi, A., Harbarth, S., Mendelson, M., Monnet, D. L., et al. (2018). Discovery, research, and development of new antibiotics: The WHO priority list of antibiotic-resistant bacteria and tuberculosis. *Lancet Infect. Dis.* 18, 318–327. doi:10.1016/s1473-3099(17)30753-3

Tran, N. H., Nguyen, D., Dwaraknath, S., Mahadevan, S., Chavez, G., Chavez, A., et al. (2013). An efficient light-driven P450 BM3 biocatalyst. *J. Am. Chem. Soc.* 39, 14484–14487. doi:10.1021/ja409337v

Varney, A. M., Smitten, K. L., Thomas, J. A., and McLean, S. (2021). Transcriptomic analysis of the activity and mechanism of action of a ruthenium(II)-Based antimicrobial that induces minimal evolution of pathogen resistance. *ACS Pharmacol. Transl. Sci.* 4, 168–178. doi:10.1021/acsptsci.0c00159

Wang, L. L., Battini, N., Bheemanaboina, R. R. Y., Ansari, M. F., Chen, J. P., Xie, Y. P., et al. (2019). A new exploration towards aminothiazolquinolone oximes as potentially multi-targeting antibacterial agents: Design, synthesis and evaluation acting on microbes, DNA, HSA and topoisomerase IV. *Eur. J. Med. Chem.* 179, 166–181. doi:10.1016/j.ejmech.2019.06.046

Weber, D. K., Sani, M. A., Downton, M. T., Keene, F. R., and Collins, J. G. (2016). Membrane insertion of a dinuclear polypyridyl ruthenium(II) complex revealed by solid-state NMR and molecular dynamics simulation-implications for selective antibacterial activity. *J. Am. Chem. Soc.* 138, 15267–15277. doi:10.1021/jacs.6b09996

Xuan, T. F., Wang, Z. Q., Liu, J., Yu, H. T., Lin, Q. W., Chen, W. M., et al. (2021). Design and synthesis of novel c-di-GMP G-quadruplex inducers as bacterial biofilm inhibitors. *J. Med. Chem.* 64, 11074–11089. doi:10.1021/acs.jmedchem.1c00465

Yan, J., and Bassler, B. L. (2019). Surviving as a community: antibiotic tolerance and persistence in bacterial biofilms. *Cell Host Microbe* 26, 15–21. doi:10.1016/j.chom.2019.06.002

Yang, H. F., Kundra, S., Chojnacki, M., Liu, K., Fuse, M. A., Abouelhassan, Y., et al. (2021). A modular synthetic route involving N-Aryl-2-nitrosoaniline intermediates leads to a new series of 3-substituted halogenated phenazine antibacterial agents. *J. Med. Chem.* 64, 7275–7295. doi:10.1021/acs.jmedchem.1c00168

Yu, J. H., Xu, X. F., Hou, W., Meng, Y., Huang, M. Y., Lin, J., et al. (2021). Synthetic cajaninstilbene acid derivatives eradicate methicillin-resistant *Staphylococcus aureus* persisters and biofilms. *Eur. J. Med. Chem.* 224, 113691. doi:10.1016/j.ejmech.2021.113691

Zhang, H. G., Tao, X. T., Chen, K. S., Yuan, C. X., Yan, S. N., and Jiang, M. H. (2011). Off–on–off luminescent switching of a dye containing imidazo [4, 5-f] [1, 10]phenanthroline. *Chin. Chem. Lett.* 22, 647–650. doi:10.1016/j.cclet.2010.12.005

Zhang, Q., Xiong, Y. S., Cheng, J. X., Tan, Y. H., Liao, X. W., and Wang, J. T. (2022). Synthesis and biological evaluation of ruthenium polypyridine complexes with 18β-glycyrrhetinic acid as antibacterial agents against *Staphylococcus aureus*. *Dalton Trans.* 51, 1099–1111. doi:10.1039/D1DT02692E

frontiers | Frontiers in Chemistry

TYPE Original Research
PUBLISHED 28 October 2022
DOI 10.3389/fchem.2022.1017548

OPEN ACCESS

EDITED BY
He Xiaojun,
Wenzhou Medical University, China

REVIEWED BY
Yuna Qian,
University of Chinese Academy of Sciences, China
Hong Chen,
Luoyang Normal University, China

*CORRESPONDENCE
Hongcai Guan,
1687875577@qq.com

†These authors have contributed equally to this work

SPECIALTY SECTION
This article was submitted to Medicinal and Pharmaceutical Chemistry, a section of the journal Frontiers in Chemistry

RECEIVED 12 August 2022
ACCEPTED 03 October 2022
PUBLISHED 28 October 2022

CITATION
Zheng H, Huang Z, Chen T, Sun Y, Chen S, Bu G and Guan H (2022), Gallium ions incorporated silk fibroin hydrogel with antibacterial efficacy for promoting healing of Pseudomonas aeruginosa-infected wound. *Front. Chem.* 10:1017548. doi: 10.3389/fchem.2022.1017548

Gallium ions incorporated silk fibroin hydrogel with antibacterial efficacy for promoting healing of *Pseudomonas aeruginosa*-infected wound

Hui Zheng[1†], Zhida Huang[1†], Tongxin Chen[2], Yafeng Sun[1], Shouqing Chen[1], Guangming Bu[2] and Hongcai Guan[1*]

[1]Wenzhou Institute of Industry & Science, Wenzhou, Zhejiang, China, [2]Ruibang Laboratories, Wenzhou, Zhejiang, China

The continual resistance to antibiotics and the generation of a series of bacterial infections has emerged as a global concern, which requires appropriate measures and therapeutics to address such a menace. Herein, we report on Silk fibroin (SF) hydrogel with good biocompatibility and biodegradability fabricated through the crosslinking of the SF of different concentrations with Gallium nitrate (Ga $(NO_3)_3$) against *Pseudomonas aeruginosa*. However, the SF: Ga = 500: 1 (w/w) (SF/Ga) demonstrated a good bactericidal and wound healing effect as a result of the moderate and prolonged release of the Ga^{3+} following the gradual degradation of the hydrogel. The Ga^{3+}, known for its innovative nature acted as a crosslinked agent and a therapeutic agent employing the "Trojan horse" strategy to effectively deal with the bacteria. Also, the Ga^{3+}, which is positively charged neutralizes the negative potential value of the SF particles to reduce the charge and further induce the β-sheet formation in the protein structure, a characteristic of gelation in SF. The morphology showed a fabricated homogenous structure with greater storage modulus- G′ with low loss modulus- G″ modulus demonstrating the mechanical performance and the ability of the SF/Ga hydrogel to hold their shape, at the same time allowing for the gradual release of Ga^{3+}. A demonstration of biocompatibility, biodegradability, bactericidal effect and wound healing in *in vitro* and *in vivo* present the SF/Ga hydrogel as an appropriate platform for therapeutic and for antibacterial wound dressing.

KEYWORDS

silk fibroin protein, gallium, hydrogels, against bacterial, wound healing

Introduction

On the one hand, bacterial infections have been on the rise as a result of the uncertain resistance generated by the bacteria following the administration of antibiotics. A condition that has largely been attributed to the misuse and continual use of these antibiotics. As a consequence of these more than 14 million individuals are affected each year and continue to be affected with a substantial rise in the case of morbidity and mortality (Wang et al., 2017). On the other hand, and to a great degree, skin injuries occurring from diverse conditions make the body vulnerable to this bacterial infection and even dehydration (Wu et al., 2019; Yu et al., 2022). Therefore, the upkeeping of an organism's first line of defense from invasion by microorganisms and even homeostasis easily becomes compromised (Zhou et al., 2018; He et al., 2020). All these present the need for a suitable cause of action for the treatment of bacterial infections and rapid means of managing wounds.

Employing polymeric hydrogel owing to its soft tissue-like hydrophilic properties has recently gained prominence when it comes to wound-related cases (Kirker et al., 2002; Mogoşanu and Grumezescu, 2014). Therein, the silk fibroin (SF) a natural protein polymer extracted from the cocoons of the silkworm, *Bombyx mori* have also been extensively studied due to their waterproof nature, biodegradability, gaseous permeation, mild inflammatory potential and homeostatic properties (Minoura et al., 1995; Santin et al., 1999; Gil et al., 2013). These properties allow the SF to easily coordinate between bacteria strains and the antibacterial substance they are reinforced with, thus perfect for antibacterial and wound dressing. Additionally, the modification of the physical parameters of SF aqueous solution, pH, conditions for sonication, and dehydration *via* the addition of ethanol or polymer can trigger the transformation of SF molecules from random-coil/α-helix structures to β-sheets, boosting the physical crosslinking (Hu et al., 2013; Bai et al., 2014; Kambe and Yamaoka, 2019). It is worth noting that, the formation of β-sheets triggers the sol-gel transition of silk fibroin through hydrophobic interaction of molecules, which results in the stabilization of hydrogels (Matsumoto et al., 2006; Nultsch and Germershaus, 2017). Though the influence of mechanical forces and pH on the SF has been extensively studied, the role of ions in the SF hydrogels remains poorly understood. Kelly and co-workers reported that some amino acid residues can emerge as β-turns through chelation with copper ions and subsequently form stable β-sheet by hydrogen bonding (Schneider and Kelly, 1995). Also, some studies show that the folding process of the SF may easily be affected by some ions such as Ca^{2+}, Zn^{2+}, K^{+}, and Na^{+} (Zhou et al., 2004; Zong et al., 2004; Ruan et al., 2008; Ruan and Zhou, 2008). These studies illustrated that the suitable ions may have the ability to induce the sol-gel transition of silk fibroin.

What's more, one crucial nutrient required by the bacteria for the coordination of DNA synthesis, cellular respiration and even eluding of the destructive activity through the generation of ROS is iron (Fe) (Andrews et al., 2003; Hijazi et al., 2018). On the contrary, Ga^{3+} is an anti-infective agent capable of binding to biological complexes containing Fe due to the resemblance in chemical properties, permitting their infiltration into such essential Fe^{3+} binding sites within protein and enzymes. Consequently, this process can alter the Fe content in the bacteria's antioxidant enzymes disrupting the redox-driven process and making the bacteria susceptible to oxidants (Bernstein, 1998; Lemire et al., 2013; Goss et al., 2018; Wang et al., 2019). Ga $(NO_3)_3$ has been reported to have a highly significant bactericidal effect against *P. aeruginosa* even at as low concentrations and is not reduced under physiological conditions (Kaneko et al., 2007; Minandri et al., 2014; Chitambar, 2016). However, no prior research has been reported on the influence of the Ga^{3+}on the SF. In this study, SF: Ga(III) hydrogels were synthesized through the electrostatic adherence of Ga $(NO_3)_3$ into SF with different concentrations to form a new type of antibacterial hydrogel with ideal mechanical properties and for the first time, we report on the effect against the *P. aeruginosa* and for wound healing. The effect of the SF: Ga(III) = 500: 1 (w/w) (SF/Ga) was investigated *in vitro* and *in vivo*. Positively charged Ga^{3+} could "kill two birds with one stone", in addition to antibacterial action, it cause the aggregation of fibroin molecules into hydrophilic regions, forming a SF hydrogel through ionic crosslinks. The SF/Ga hydrogel exhibited a highly effective antibacterial efficiency capacity in the *in vitro* with good biocompatibility. This was confirmed by the *in vivo* experiments where the SF/Ga hydrogel effectively disrupted the *P. aeruginosa via* the slowly and prolonged release of the Ga^{3+} at the same time stepping up with the wound recovery. In all, SF/Ga hydrogel demonstrate great potential for treating bacterial infections and wound dressing.

Experiment section

Materials

Bombyx mori cocoons were provided by Chongqing University (China). Gallium nitrate hydrate (99.9% metals basis) was purchased from MACKLIN. Sodium carbonate (Na_2CO_3), Boric acid, and Sodium chloride (NaCl) were purchased from Sigma. Lithium Bromide salt (LiBr), sodium hydroxide (NaOH) were purchased from Aladdin. Tryptone Broth was purchased from Sangon Biotech. Dialysis bag (MD44, 3.5 K MWCO) was purchased from Solarbio. CCK-8 was purchased from APE×BIO, and DMEM was purchased from Life Technologies Corporation.

Preparation of silk fibroin solution

Bombyx mori cocoons were degummed to remove sericin proteins; silk cocoons were treated in alkaline water baths (0.02 mol/L Na_2CO_3) at 100°C for 2 h. Degummed silk was washed several times in deionized water and dried at room temperature to obtain pure SF fibers. The dried SF was dissolved in 9.3 mol/L LiBr solution and stirred for 1 h at 65 °C. After cooling, the solution was taken out into a dialysis bag, placed in an alkaline buffer solution (Boric acid 18.54 g, NaCl 8.775 g dissolved in 1 L of deionized water, pH titration to 9) dialyzed for 1 day to remove the LiBr salt. The solution was dialyzed against deionized water for 3 days and subsequently filtered. At last, pure SF aqueous solution was obtained, and the final concentration was about 5% (w/v), which was stored at 4°C.

Determination of MIC value of gallium nitrate on *P. aeruginosa*

Using a 96-well plate, the half-dilution method was used to obtain 128 μg/ml to 1 μg/mL Ga $(NO_3)_3$ solution of 50 μL per well, and 50 μL of *P. aeruginosa* bacterial solution with the value of OD_{600} = 0.05 added to each well. The plate was incubated at 37°C in a constant temperature incubator for 24 h. OD_{600} value was measured with a microplate reader (Thermo scientific).

Preparation of silk fibroin-gallium nitrate hydrogel

The SF: Ga (III) hydrogels were prepared by mixing Ga $(NO_3)_3$ with SF in solution. The SF solution and Ga $(NO_3)_3$ were mixed in different ratios for use, specifically, the SF solution concentration was maintained at 5% by changing the blend volume ratio, and the mass ratios of SF and Ga $(NO_3)_3$ were 5000:1, 2500:1, 1000:1, 500:1 and 250:1, which were ultrasonicated for 1 h after mixing, and the state of gelation observed after standing. Based on the gel formation time and properties, SF: Ga(III) = 500: 1 (w/w) is expected to be the best ratio.

SEM and EDS characterizations

The scanning electron microscope (SEM; HITACHI SU8010, Japan) was used to analyze the dried gel morphology. The SF hydrogel and SF/Ga hydrogel were quickly frozen in liquid nitrogen for 10 min, and after, placed in a vacuum freeze dryer (BIOCOOL, China) and freeze-dried at −50°C for 72 h. The sample was pasted on the round sample stage with a conductive double-sided adhesive. Before the test, the sample was processed with gold spray. The thickness of the gold spray was between 20 and 30 nm, and the test was conducted at a temperature of 20°C and relative humidity of 65%.

CD and FTIR characterizations

CD spectra of samples were measured on an Applied Photophysics (Chirascan Plus, England) spectrometer under an N_2 atmosphere. Approximately 20 μL of the samples were evenly placed on a 1 mm thick quartz cuvette and scanned from 180 to 260 nm. Three groups of samples (SF solution, SF solution after 1 h of ultrasound, SF solution, and Ga $(NO_3)_3$ were mixed at a mass ratio of 500:1. The samples for the Fourier transform infrared spectrometer (FTIR, Bruker Tensor II, Germany) were also freeze-dried. The wave number range was 2000–1000 cm^{-1}, the spectral resolution was 4 cm^{-1}, and the scanning range was 4000–400 cm^{-1}.

Rheological test

The mechanical and rheological analyses were carried out using (TA Instrument, New Castle, DE). The elasticity (storage modulus- G') and viscosity (loss modulus- G'') were evaluated at a shear frequency of 1 Hz within a linear viscoelastic region. All frequency sweeps were collected within a frequency range of 0.1–10 Hz rad/s at 25°C. All samples were stabilized and measured, and the process was repeated three times.

Zeta potential

The samples [Mixed Ga $(NO_3)_3$ with SF solution (0.05% wt) at 1000:1, 500:1 (w/w), and SF solution only] were characterized with a nanometer particle size analyzer (Malvern, Zetasizer Nano ZS ZEN3600, England) to determine the change of Zeta potential, and each sample was measured three times repeatedly.

Cell culture and cytotoxicity assay

Human lung fibroblasts (MRC-5) cells were cultured in DMEM medium supplemented with 100 U ml^{-1} penicillin, 0.1 mg ml^{-1} streptomycin, and 10% FBS at 37°C in a humidified incubator under 5% CO_2. After reaching 80% confluence, cells were harvested and seeded in 96-well plates (2×10^4 cells/well). At the same time, 1 ml PBS solution, SF, and SF/Ga hydrogel were separately put into the 6-well plate, sterilized under UV for 30 min and 5 ml DMEM, was added to each well for co-cultivation. After 24 h, the culture medium was replaced with hydrogel leaching solution for each group and cells were cultured for 1 day. The cytotoxicity was measured by the CCK-8 method.

Antibacterial property

The antibacterial activities of the SF/Ga hydrogel against *P. aeruginosa* bacteria were evaluated using the oscillation method. LB culture medium was used to dilute *P. aeruginosa* solution which was recovered for 24 h, OD_{600} = 0.05. The bacterial solutions (4 ml) were added to 15 ml shake tubes and later divided into 3 groups: 1 ml of SF hydrogel, SF/Ga hydrogel, and Ga $(NO_3)_3$ solution. The samples were cultured in a 37°C constant temperature incubator, and Shaked for 7 days. The samples (100 μL) were taken out every day and the OD_{600} was measured.

Wound healing

To evaluate the potential of the SF/Ga hydrogel for wound dressing, an *in vivo* experiment was conducted using a rat model with a *P. aeruginosa*-infected wound. (He et al., 2022a; He et al., 2022b). Six 3-month-old healthy Sprague–Dawley (SD) rats were randomly divided into 2 groups (PBS and SF/Ga hydrogel treatments) and anesthetized with chloral hydrate. The back fur of the mice was shaved, cleaned, and disinfected with 75% alcohol and an 8-mm biopsy punch was used to create circular wounds of full thickness, 8 mm in diameter on each rat. The wounds were infected with 100 μL of 10^8 CFU/mL *P. aeruginosa* solution. Images of the wound area at 0, 1, 2, 3, and 6 days were taken with a digital camera, and the percentage of wound size was calculated using ImageJ software.

Statistical analysis

All the experiments were performed with sample sizes greater than three, and the experimental results were expressed as the mean value ±standard deviation. The difference between the groups was determined using a one-way analysis of variance, and a *p*-value smaller than 0.05 was considered a statistically significant difference.

Result and discussion

Susceptibility of *P. aeruginosa* to Ga $(NO_3)_3$

The release of Ga^{3+} is not able to appropriately replace the Fe^{3+} within the protein binding site of bacteria since the Ga^{3+} transition to Ga^{+} requires much energy compared to the transition of Fe electrons from 3 + to 2 + or *vice versa* (Ma et al., 2013; Nikolova et al., 2016; Best et al., 2020). Hence the disruption of the crucial processes by Ga^{3+} after replacing the Fe^{3+} and the subsequent antibacterial action. The susceptibility of *P. aeruginosa* was investigated to screen the concentration of Ga $(NO_3)_3$ used in the SF: Ga (III) hydrogel fabrication. As shown in Figure 1A, the Minimum inhibition concentration (MIC) of Ga $(NO_3)_3$ was recorded as 16 μg/ml which was sufficient to completely disrupt the *P. aeruginosa*. Also, a measure of the toxicity of the different concentrations of Ga $(NO_3)_3$ on the human lung fibroblast (MRC) using the MTT assay, Figure 1B showed that an increment in the concentration of Ga $(NO_3)_3$ from 16 μg/ml to 1024 μg/ml yielded cell viability which was above 80%. This indicated the negligible toxicity of the concentration of Ga $(NO_3)_3$ within this interval.

Preparation of the SF: Ga (III) hydrogels

The SF: Ga (III) hydrogels were successfully fabricated after sonication for 1 h and standing for 23 h to form a hydrogel with increased stability, the presence of amino and carboxyl groups allowed for the easy chemical modification. Thus, the addition of Ga $(NO_3)_3$ solution of varying concentrations (12.5 μg, 25 μg, 50 μg, 100 μg, and 200 μg) and the subsequent induction of the gelation of the mixed solution *via* sonication, Figure 2A. The even dispersion of Ga $(NO_3)_3$ within the SF formed a hydrogel network SF: Ga (III) resulting from the self-crosslinking. As shown in, Figure 2B, the uniform dispersion allowed SF: Ga (III) to release bioactive Ga^{3+} at the same time providing a moist environment and enough mechanical support while holding their shapes. The antibacterial effect and the gelation time led to the selection of the 100 μg/ml, Ga $(NO_3)_3$, combined with the SF hydrogel to give SF: Ga (III) = 500: 1 (w/w) (SF/Ga), Figure 2C. The time for the gelation is dependent on the concentration of the gelatine and gel strength also significantly increases with an increase in the gelation concentration. Considering the varying ratio of SF: Ga (III), gelation was expected to decrease from the highest concentration (5000–250) to the lowest with time. However, on average the hydrogels demonstrated a shorter gelation time. Hence, a positive correlation in SF/Ga with their crosslinking and other physical properties.

Morphological analysis of the SF/Ga hydrogel

A high proportion of the SF is bound to increase the viscosity of the hydrogel solution, inducing a short gelation time which can restrict the crosslinking and at the same time affect the porosity (Xu et al., 2021). The SEM evaluation of the influence of Ga $(NO_3)_3$ on the micromorphological structure of the hydrogel after dried freezing revealed a lamellar interconnected pores size for SF hydrogel, Figure 3A, and a smaller but increased pore size for Ga $(NO_3)_3$ crosslinked hydrogel SF/Ga, Figure 3B. In all, the morphological evaluation shows the hydrogel was three-dimensionally porous. Elemental analysis of SF/Ga hydrogels with an X-ray energy spectrometer (EDS) attached to the high-

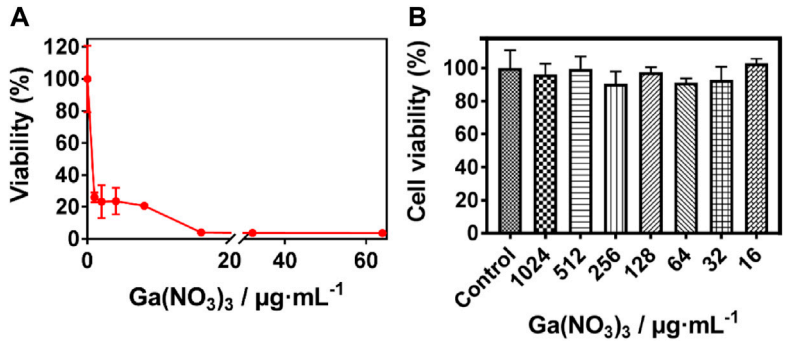

FIGURE 1
Susceptibility of *P. aeruginosa* to Ga $(NO_3)_3$. **(A)** Minimum inhibition concentration of Ga $(NO_3)_3$ against *P. aeruginosa*, **(B)** Cytotoxicity of Ga $(NO_3)_3$ to MRC-5 (mean ± SD, n = 3).

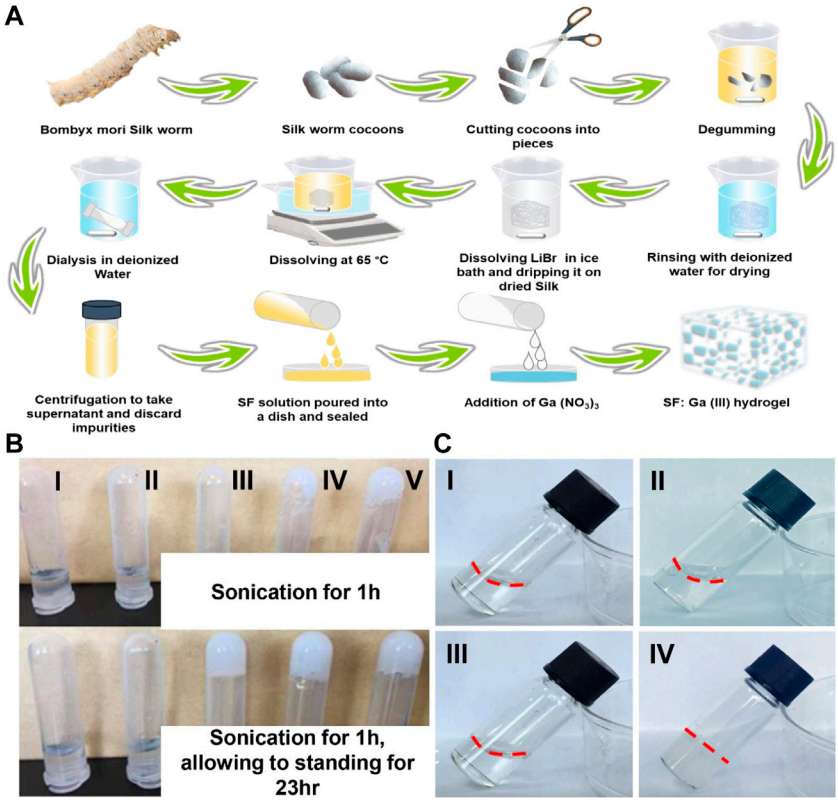

FIGURE 2
Synthesis of hydrogels. **(A)** Schematic illustration of the preparation of SF and SF: Ga (III) hydrogels, **(B)** Digital images of (I) SF: Ga (III) = 5000: 1 (w/w), (II) SF: Ga (III) = 2500: 1 (w/w), (III) SF: Ga (III) = 1000: 1 (w/w), (IV) SF: Ga (III) = 500: 1 (w/w) (SF/Ga) and (V) SF: Ga (III) = 250: 1 (w/w) hydrogels, **(C)** Digital image of SF solution (I, II) and SF: Ga (III) = 500: 1 (w/w) (SF/Ga) hydrogel (III, IV) before and after sonication and standing for 23 h.

resolution electron microscope, confirmed the presence of C, N, O, and Ga elements in the fabricated SF/Ga hydrogel, where C, N, and O are components of silk fibroin and, Ga a mixed component of Ga $(NO_3)_3$, Figure 3C. The changes in the protein secondary structure of the SF/Ga were explored using circular dichroism (CD) and compared with those of unsonicated SF solution and

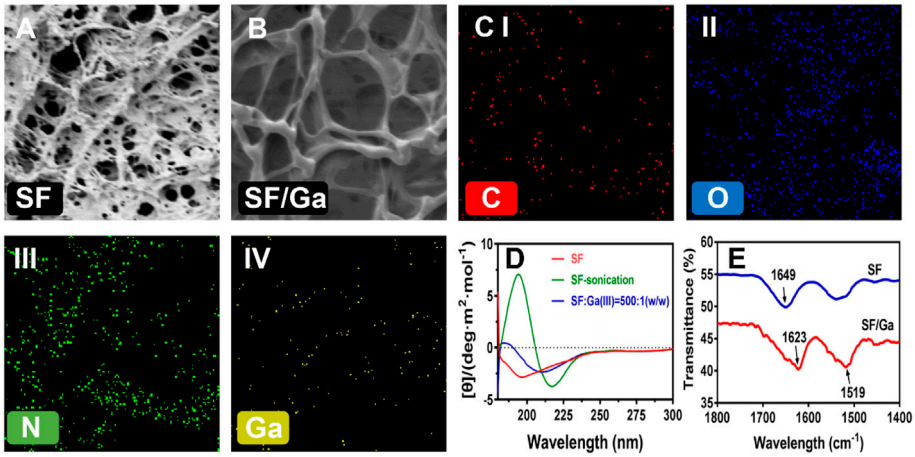

FIGURE 3
Morphological and secondary structural characterization. **(A,B)** SEM images of the surface pore of SF and SF/Ga hydrogel, **(C)** Elemental mapping of SF/Ga hydrogel, **(D)** CD spectrum of unsonicated SF, ultrasonicated SF, and sonicated SF/Ga solutions, **(E)** FTIR of SF and SF/Ga hydrogel.

ultrasonicated SF within 180–260 nm. As shown in Figure 3D, CD spectrum of the unsonicated SF solutions revealed a negative intensity peak close to 195 nm, this indicates a typical random coil structure. In addition, the CD spectrum of the sonicated SF solution showed a negative and positive intensity peak at 217 nm and 198 nm respectively, which is more typical of a characteristic peak within β-sheet conformation. Interestingly addition of Ga $(NO_3)_3$ to the SF demonstrated a change that accompanied the SF/Ga switching from a random coil structure to a β-sheet conformation which was consistent with the change in the conformation of the SF after adding Ga $(NO_3)_3$. Emphasizing that the β-sheet is the dominant secondary structure in the SF/Ga. Figure 3E shows the FTIR spectra which investigated the interaction between Ga $(NO_3)_3$ and the SF, and this reveals a spectra peak of amide I (1700–1600 cm^{-1}) and amide II (1600–1500 cm^{-1}) regions for the SF. The SF conformation comprises a random coil, α-helix, β-sheet, and β-turn. A characteristic peak with the interval of 1625–1640 cm^{-1} (amide I) and 1515–1525 cm^{-1} (amide II) indicated that the secondary structure is related to the β-sheet. Similarly, the peaks of 1640–1660 cm^{-1} (amide I) and 1535–1550 cm^{-1} (amide II) indicated that the secondary structure of the protein is dominated by the α-helix and random coil. However, peaks identified at 1700–1600 cm^{-1} (amid I) and amide II (1600–1500 cm^{-1}) of SF represented relative maturity. Figure 3E, also showed that 1649 cm^{-1}, 1625 cm^{-1}, and 1519 cm^{-1} are characteristic absorption peaks of SF amide I, amide I, and amide II, respectively, indicating that pure silk fibroin has a random coil structure. But the addition of Ga $(NO_3)_3$ to the SF, shifted the position of the characteristic peak of the SF to the right, that is, it changed to the silk II conformation, showing an antiparallel β-sheet. Hence, the β-sheet structure is a significant characteristic of SF, giving SF a good mechanical property. This also shows the successful incorporation of Ga $(NO_3)_3$ in the SF/Ga hydrogel.

Mechanical and rheological properties of SF/Ga

Some reports indicate that the β-sheet is directly responsible for a silk hydrogel mechanical property as a result of improved crosslinks (Hu et al., 2010; Guziewicz et al., 2011; Xu et al., 2021). Hence crosslinking coordinates and improves the mechanical performance of a hydrogel further enabling resistance to easy deformation (Rammensee et al., 2006; Zawko et al., 2009; Jeon et al., 2014). The influence of Ga $(NO_3)_3$ on the SF hydrogels and the viscosity difference were evaluated *via* a dynamic oscillatory rheological measurement of the storage modulus- G' and loss modulus- G" of sample SF and SF/Ga against time and frequency. Mechanical spectra of SF and SF/Ga showed that the storage modulus- G' highly exceeded the loss modulus- G". An indication of a well-obtained hydrogel network, Figures 4A,B. However, a time sweep at a frequency of 1 Hz showed that the SF/Ga had significant stability compared to the SF which could be attributed to Ga $(NO_3)_3$ concentration and the presence of the β-sheet conformation from the cross-linking. The Zeta potential is the magnitude of change that determines the stability of a colloidal suspension. As shown in Figure 4C, the SF revealed a negative Zeta potential value of about −30 mV. However, an increase in the content of Ga $(NO_3)_3$ in the hydrogel significantly decreases the value of the Zeta potential. An indication of possible electrostatic adsorption between the positively charged Ga^{3+}, of Ga $(NO_3)_3$, and the negatively charged SF.

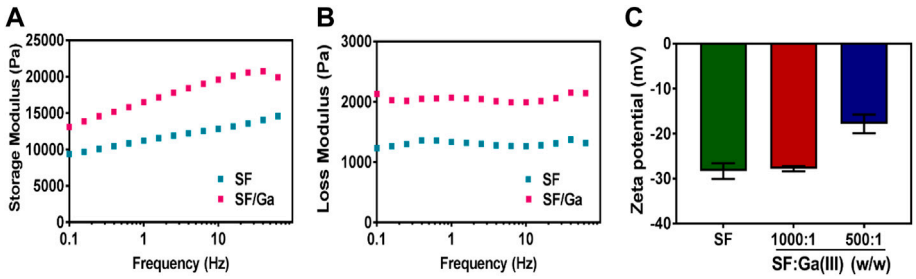

FIGURE 4
(A,B) Rheological characterization and **(C)** Zeta-potentials **(B)** of SF and SF/Ga hydrogel (mean ± SD, *n* = 3).

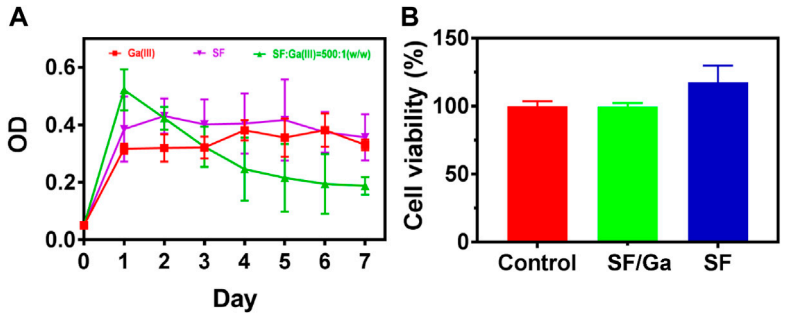

FIGURE 5
In vitro antibacterial activity **(A)** and biocompatibility **(B)** of SF/Ga hydrogel (mean ± SD, n = 3).

Also, this demonstrated that the configuration of the SF and SF: Ga (III) = 1000: 1 (w/w) were random coils, whereas the neutralization process by the positively charged Ga^{3+} yielded a β-sheet in the SF/Ga.

In vitro antibacterial activity and biocompatibility

Gallium compounds have been employed in many areas in the biomedical field for the treatment of many infectious diseases and even in cancer treatment (Rudnev et al., 2006; Rzhepishevska et al., 2011; Deliormanlı, 2015). Thus, we investigated the antibacterial efficiency of the SF/Ga against *P. aeruginosa*. The effect of 100 μg/mL Ga $(NO_3)_3$ solution, 50 mg/ml pure SF solution, and SF/Ga on the growth of *P. aeruginosa* showed a lower OD value for Ga $(NO_3)_3$ group compared to the SF/Ga group and a high OD value for the SF group, Figure 5A. The significant antibacterial activity observed in Ga $(NO_3)_3$ could be attributed to the release of Ga^{3+} while the high OD value in the SF hydrogel group, indicated the insignificant antibacterial effect. Results from the second day showed the gradual degradation of the hydrogel in the SF/Ga group with a gradual decline in the OD value. The gradual decline in the OD value demonstrated the gradual release of Ga^{3+} as the hydrogel gradually degrades. Extension of time to the 7th day demonstrated a significantly reduced OD value in the SF/Ga group compared to the other two groups. Intriguingly a critical observation of the OD value showed that the bacteria suspension in the Ga $(NO_3)_3$ group began to rise steadily from the 3rd day. This can be ascribed to the hydrolysis of Ga $(NO_3)_3$ which reduces the activity of Ga $(NO_3)_3$ and permitted the bacteria regrowth. This also proves the SF/Ga hydrogel can present a prolonged and efficient antibacterial effect. Also, apart from the antibacterial activity, biocompatibility serves as a direct prerequisite for a biomedical purposes. The *in vitro* cytocompatibility was examined using human lung fibroblast (MRC -5) cells in a CCK-8 assay. As shown in Figure 5B, cells inoculated with SF and SF/Ga hydrogels leaching solution for 24 h demonstrated a cell activity of about 100% relative to the control group, indicating negligible cytotoxicity. However, cells in the SF hydrogels group demonstrated an obvious cell proliferation effect. SF/Ga hydrogel proves good biocompatibility with an efficient antibacterial effect.

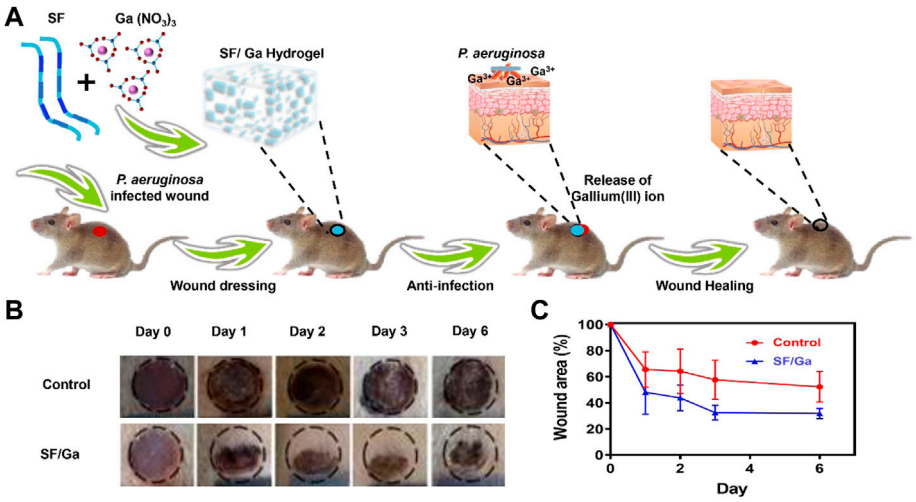

FIGURE 6
In vivo antibacterial activity of SF/Ga hydrogel. **(A)** Schematic illustration of SF/Ga hydrogel promotion of healing of a *P aeruginosa*-infected wound, **(B)** Digital images of *P. aeruginosa* infected wound covered with PBS, and SF/Ga hydrogel **(C)** Quantitative curve of wound area for treatment groups, PBS and SF/Ga hydrogel (mean ± SD, n = 6).

In vivo antibacterial activity

The result from the *in vitro* antibacterial activity and biocompatibility inspired us to further investigate the *in vivo* antibacterial activity of SF/Ga hydrogel. A *P. aeruginosa* infection model in the SD rats was created by making skin incisions on the back of the rats, PBS solution, and SF/Ga hydrogel were applied separately, Figure 6A. The wound recovery in the control group was very slow. In contrast, the SF/Ga group demonstrated a better and more pronounced wound recovery effect Figure 6B. Images of wounds taken at a separate time interval from 0,1,2,3 to 6 days showed that the wound treated with SF/Ga hydrogel exhibited a wound area of about 70% relative to the control group on the 3rd day, an indication of the release of Ga^{3+} for bactericidal effect in the SF/Ga group and with time the wound size began to decrease Figure 6C. On the 6th day, the wound scar rate and closure of the wound in the SF/Ga group were observed to be better compared to the other group, indicating the SF/Ga hydrogel which contains Ga $(NO_3)_3$ wielded the potential to effectively disrupt bacterial activity and at the same time accelerating the wound healing process. This confirms results from the *in vitro* antibacterial activity and presents SF/Ga as an appropriate biomaterial for antibacterial effects and wound healing.

Conclusion

In summary, we successfully prepared SF/Ga hydrogel and systematically investigated the therapeutic and wound healing ability against *P. aeruginosa*. The SF/Ga hydrogel showed a good water content, biocompatibility, mechanical strength, and biodegradability. The hydrogel allowed the gradual and prolonged release of Ga^{3+} which in turn gradually disrupted the bacteria. Besides SF/Ga hydrogel demonstrated negligible toxicity towards human lung fibroblast (MRC-5) cells affirming their biocompatibility. More importantly, the SF/Ga hydrogel effect on *P. aeruginosa* infected wound exhibited effective recovery confirming its ability to disrupt bacteria and at the same time induce wound healing. Therefore SF/Ga hydrogel can serve as an excellent multifunctional candidate for wound dressing with a prolonged antibacterial effect.

Data availability statement

The original contributions presented in the study are included in the article/supplementary materials, further inquiries can be directed to the corresponding author.

Ethics statement

The animal study was reviewed and approved by Animal Ethics Association of Wenzhou Institute of Industry & Science.

Author contributions

Credit Author Statement HZ and ZH: Conceptualization, Methodology, Software. GB: Data curation, Writing-Original draft preparation. YS: Visualization, Investigation. HG: Supervision, Funding acquisition, Project administration. SC:

Software, Validation. TC, HZ, and HG: Writing—Reviewing and Editing.

Funding

This work was financially supported by Wenzhou Science and Technology Plan Project (ZG2021035).

Conflict of interest

Authors TC and GB were employed by Ruibang Laboratories.

The remaining authors declare that the research was conducted in the absence of any commercial or financial relationships that could be construed as a potential conflict of interest.

Publisher's note

References

Andrews, S. C., Robinson, A. K., and Rodríguez-Quiñones, F. (2003). Bacterial iron homeostasis. *FEMS Microbiol. Rev.* 27, 215–237. doi:10.1016/s0168-6445(03)00055-x

Bai, S., Zhang, X., Lu, Q., Sheng, W., Liu, L., Dong, B., et al. (2014). Reversible hydrogel–solution system of silk with high beta-sheet content. *Biomacromolecules* 15, 3044–3051. doi:10.1021/bm500662z

Bernstein, L. R. (1998). Mechanisms of therapeutic activity for gallium. *Pharmacol. Rev.* 50, 665–682.

Best, M. G., Cunha-Reis, C., Ganin, A. Y., Sousa, A., Johnston, J., Oliveira, A. L., et al. (2020). Antimicrobial properties of gallium(III)- and iron(III)-Loaded polysaccharides affecting the growth of *Escherichia coli*, *Staphylococcus aureus*, and *Pseudomonas aeruginosa*, *in vitro*. *ACS Appl. Bio Mat.* 3, 7589–7597. doi:10.1021/acsabm.0c00811

Chitambar, C. R. (2016). Gallium and its competing roles with iron in biological systems. *Biochimica Biophysica Acta - Mol. Cell Res.* 1863, 2044–2053. doi:10.1016/j.bbamcr.2016.04.027

Deliormanlı, A. M. (2015). Synthesis and characterization of cerium- and gallium-containing borate bioactive glass scaffolds for bone tissue engineering. *J. Mater. Sci. Mater. Med.* 26, 1–13.

Gil, E. S., Panilaitis, B., Bellas, E., and Kaplan, D. L. (2013). Functionalized silk biomaterials for wound healing. *Adv. Healthc. Mater.* 2, 206–217. doi:10.1002/adhm.201200192

Goss, C. H., Kaneko, Y., Khuu, L., Anderson, G. D., Ravishankar, S., Aitken, M. L., et al. (2018). Gallium disrupts bacterial iron metabolism and has therapeutic effects in mice and humans with lung infections. *Sci. Transl. Med.* 10, eaat7520. doi:10.1126/scitranslmed.aat7520

Guziewicz, N., Best, A., Perez-Ramirez, B., and Kaplan, D. L. (2011). Lyophilized silk fibroin hydrogels for the sustained local delivery of therapeutic monoclonal antibodies. *Biomaterials* 32, 2642–2650. doi:10.1016/j.biomaterials.2010.12.023

He, X., Dai, L., Ye, L., Sun, X., Enoch, O., Hu, R., et al. (2022). A vehicle-free antimicrobial polymer hybrid gold nanoparticle as synergistically therapeutic platforms for *Staphylococcus aureus* infected wound healing. *Adv. Sci.* 9, 2105223. doi:10.1002/advs.202105223

He, X., Hou, J.-T., Sun, X., Jangili, P., An, J., Qian, Y., et al. (2022). NIR-II photo-amplified sonodynamic therapy using sodium molybdenum bronze nanoplatform against subcutaneous *Staphylococcus aureus* infection. *Adv. Funct. Mat.* 32, 2203964. doi:10.1002/adfm.202203964

He, X., Liu, X., Yang, J., Du, H., Chai, N., Sha, Z., et al. (2020). Tannic acid-reinforced methacrylated chitosan/methacrylated silk fibroin hydrogels with multifunctionality for accelerating wound healing. *Carbohydr. Polym.* 247, 116689. doi:10.1016/j.carbpol.2020.116689

Hijazi, S., Visaggio, D., Pirolo, M., Frangipani, E., Bernstein, L., and Visca, P. (2018). Antimicrobial activity of gallium compounds on ESKAPE pathogens. *Front. Cell. Infect. Microbiol.* 8, 316. doi:10.3389/fcimb.2018.00316

Hu, X., Lu, Q., Sun, L., Cebe, P., Wang, X., Zhang, X., et al. (2010). Biomaterials from ultrasonication-induced silk Fibroin–Hyaluronic acid hydrogels. *Biomacromolecules* 11, 3178–3188. doi:10.1021/bm1010504

Hu, X., Tang-Schomer, M. D., Huang, W., Xia, X. X., Weiss, A. S., and Kaplan, D. L. (2013). Charge-tunable autoclaved silk-tropoelastin protein alloys that control neuron cell responses. *Adv. Funct. Mat.* 23, 3875–3884. doi:10.1002/adfm.201202685

Jeon, O., Samorezov, J. E., and Alsberg, E. (2014). Single and dual crosslinked oxidized methacrylated alginate/PEG hydrogels for bioadhesive applications. *Acta biomater.* 10, 47–55. doi:10.1016/j.actbio.2013.09.004

Kambe, Y., and Yamaoka, T. (2019). Biodegradation of injectable silk fibroin hydrogel prevents negative left ventricular remodeling after myocardial infarction. *Biomater. Sci.* 7, 4153–4165. doi:10.1039/c9bm00556k

Kaneko, Y., Thoendel, M., Olakanmi, O., Britigan, B. E., and Singh, P. K. (2007). The transition metal gallium disrupts Pseudomonas aeruginosa iron metabolism and has antimicrobial and antibiofilm activity. *J. Clin. Invest.* 117, 877–888. doi:10.1172/jci30783

Kirker, K. R., Luo, Y., Nielson, J. H., Shelby, J., and Prestwich, G. D. (2002). Glycosaminoglycan hydrogel films as bio-interactive dressings for wound healing. *Biomaterials* 23, 3661–3671. doi:10.1016/s0142-9612(02)00100-x

Lemire, J. A., Harrison, J. J., and Turner, R. J. (2013). Antimicrobial activity of metals: Mechanisms, molecular targets and applications. *Nat. Rev. Microbiol.* 11, 371–384. doi:10.1038/nrmicro3028

Ma, H., Darmawan, E. T., Zhang, M., Zhang, L., and Bryers, J. D. (2013). Development of a poly(ether urethane) system for the controlled release of two novel anti-biofilm agents based on gallium or zinc and its efficacy to prevent bacterial biofilm formation. *J. Control. Release* 172, 1035–1044. doi:10.1016/j.jconrel.2013.10.005

Matsumoto, A., Chen, J., Collette, A. L., Kim, U.-J., Altman, G. H., Cebe, P., et al. (2006). Mechanisms of silk fibroin Sol–Gel transitions. *J. Phys. Chem. B* 110, 21630–21638. doi:10.1021/jp056350v

Minandri, F., Bonchi, C., Frangipani, E., Imperi, F., and Visca, P. (2014). Promises and failures of gallium as an antibacterial agent. *Future Microbiol.* 9, 379–397. doi:10.2217/fmb.14.3

Minoura, N., Aiba, S.-I., Higuchi, M., Gotoh, Y., Tsukada, M., and Imai, Y. (1995). Attachment and growth of fibroblast cells on silk fibroin. *Biochem. biophysical Res. Commun.* 208, 511–516. doi:10.1006/bbrc.1995.1368

Mogoşanu, G. D., and Grumezescu, A. M. (2014). Natural and synthetic polymers for wounds and burns dressing. *Int. J. Pharm.* 463, 127–136. doi:10.1016/j.ijpharm.2013.12.015

Nikolova, V., Angelova, S., Markova, N., and Dudev, T. (2016). Gallium as a therapeutic agent: A thermodynamic evaluation of the competition between Ga^{3+} and Fe^{3+} ions in metalloproteins. *J. Phys. Chem. B* 120, 2241–2248. doi:10.1021/acs.jpcb.6b01135

Nultsch, K., and Germershaus, O. (2017). Silk fibroin degumming affects scaffold structure and release of macromolecular drugs. *Eur. J. Pharm. Sci.* 106, 254–261. doi:10.1016/j.ejps.2017.06.012

Rammensee, S., Hümmerich, D., Hermanson, K. D., Scheibel, T., and Bausch, A. R. (2006). Rheological characterization of hydrogels formed by recombinantly produced spider silk. *Appl. Phys. A* 82, 261–264. doi:10.1007/s00339-005-3431-x

Ruan, Q. X., Zhou, P., Hu, B. W., and Ji, D. (2008). An investigation into the effect of potassium ions on the folding of silk fibroin studied by generalized two-dimensional NMR-NMR correlation and Raman spectroscopy. *FEBS J.* 275, 219–232. doi:10.1111/j.1742-4658.2007.06191.x

Ruan, Q. X., and Zhou, P. (2008). Sodium ion effect on silk fibroin conformation characterized by solid-state NMR and generalized 2D NMR–NMR correlation. *J. Mol. Struct.* 883-884, 85–90. doi:10.1016/j.molstruc.2007.11.055

Rudnev, A. V., Foteeva, L. S., Kowol, C., Berger, R., Jakupec, M. A., Arion, V. B., et al. (2006). Preclinical characterization of anticancer gallium(III) complexes: Solubility, stability, lipophilicity and binding to serum proteins. *J. Inorg. Biochem.* 100, 1819–1826. doi:10.1016/j.jinorgbio.2006.07.003

Rzhepishevska, O., Ekstrand-Hammarström, B., Popp, M., Björn, E., Bucht, A., Sjöstedt, A., et al. (2011). The antibacterial activity of Ga^{3+} is influenced by ligand complexation as well as the bacterial carbon source. *Antimicrob. Agents Chemother.* 55, 5568–5580. doi:10.1128/aac.00386-11

Santin, M., Motta, A., Freddi, G., and Cannas, M. (1999). In Vitro Evaluation of the Inflammatory Potential of the Silk Fibroin. *J. Biomed. Mater. Res.* 46. 382–389.

Schneider, J. P., and Kelly, J. W. (1995). Templates that induce .alpha.-Helical, beta.-sheet, and loop conformations. *Chem. Rev.* 95, 2169–2187. doi:10.1021/cr00038a015

Wang, Y., Han, B., Xie, Y., Wang, H., Wang, R., Xia, W., et al. (2019). Combination of gallium(iii) with acetate for combating antibiotic resistant *Pseudomonas aeruginosa*. *Chem. Sci.* 10, 6099–6106. doi:10.1039/c9sc01480b

Wang, Z., Dong, K., Liu, Z., Zhang, Y., Chen, Z., Sun, H., et al. (2017). Activation of biologically relevant levels of reactive oxygen species by Au/g-C3N4 hybrid nanozyme for bacteria killing and wound disinfection. *Biomaterials* 113, 145–157. doi:10.1016/j.biomaterials.2016.10.041

Wu, J., Chen, A., Zhou, Y., Zheng, S., Yang, Y., An, Y., et al. (2019). Novel H2S-Releasing hydrogel for wound repair via *in situ* polarization of M2 macrophages. *Biomaterials* 222, 119398. doi:10.1016/j.biomaterials.2019.119398

Xu, Z., Chen, T., Zhang, K. Q., Meng, K., and Zhao, H. (2021). Silk fibroin/chitosan hydrogel with antibacterial, hemostatic and sustained drug-release activities. *Polym. Int.* 70, 1741–1751. doi:10.1002/pi.6275

Yu, Y., Yang, B., Tian, D., Liu, J., Yu, A., and Wan, Y. (2022). Thiolated hyaluronic acid/silk fibroin dual-network hydrogel incorporated with bioglass nanoparticles for wound healing. *Carbohydr. Polym.* 288, 119334. doi:10.1016/j.carbpol.2022.119334

Zawko, S. A., Suri, S., Truong, Q., and Schmidt, C. E. (2009). Photopatterned anisotropic swelling of dual-crosslinked hyaluronic acid hydrogels. *Acta Biomater.* 5, 14–22. doi:10.1016/j.actbio.2008.09.012

Zhou, P., Xie, X., Knight, D. P., Zong, X. H., Deng, F., and Yao, W. H. (2004). Effects of pH and calcium ions on the conformational transitions in silk fibroin using 2D Raman correlation spectroscopy and ^{13}C solid-state NMR. *Biochemistry* 43, 11302–11311. doi:10.1021/bi049344i

Zhou, Q., Kang, H., Bielec, M., Wu, X., Cheng, Q., Wei, W., et al. (2018). Influence of different divalent ions cross-linking sodium alginate-polyacrylamide hydrogels on antibacterial properties and wound healing. *Carbohydr. Polym.* 197, 292–304. doi:10.1016/j.carbpol.2018.05.078

Zong, X. H., Zhou, P., Shao, Z. Z., Chen, S. M., Chen, X., Hu, B. W., et al. (2004). Effect of pH and copper(II) on the conformation transitions of silk fibroin based on EPR, NMR, and Raman spectroscopy. *Biochemistry* 43, 11932–11941. doi:10.1021/bi049455h

frontiers | Frontiers in Chemistry

TYPE Original Research
PUBLISHED 03 November 2022
DOI 10.3389/fchem.2022.1053675

OPEN ACCESS

EDITED BY
Yu Huo,
Sichuan Normal University, China

REVIEWED BY
Hang Gao,
Taiyuan University of Technology, China
Bingchao Qiang,
Baiyao Group Co. Ltd. New medicine R&D, China

*CORRESPONDENCE
Haifeng Zhou,
zhouhf@ctgu.edu.cn
Hong Chen,
chenwexpo@sina.com

SPECIALTY SECTION
This article was submitted to Medicinal and Pharmaceutical Chemistry, a section of the journal Frontiers in Chemistry

RECEIVED 26 September 2022
ACCEPTED 20 October 2022
PUBLISHED 03 November 2022

CITATION
Qi Y, Xue B, Chen S, Wang W, Zhou H and Chen H (2022), Synthesis, biological evaluation, and molecular docking of novel hydroxyzine derivatives as potential AR antagonists.
Front. Chem. 10:1053675.
doi: 10.3389/fchem.2022.1053675

Synthesis, biological evaluation, and molecular docking of novel hydroxyzine derivatives as potential AR antagonists

Yueheng Qi[1], Baoli Xue[1,2], Shijin Chen[1], Wang Wang[1], Haifeng Zhou[2]* and Hong Chen[1]*

[1]Luoyang Key Laboratory of Organic Functional Molecules, College of Food and Drug, Luoyang Normal University, Luoyang, Henan, China, [2]Hubei Key Laboratory of Natural Products Research and Development, College of Biological and Pharmaceutical Sciences, China Three Gorges University, Yichang, China

Prostate cancer (PCa) is a malignant tumor with a higher mortality rate in the male reproductive system. In this study, the hydroxyazine derivatives were synthesized with different structure from traditional anti-prostate cancer drugs. In the evaluation of *in vitro* cytotoxicity and antagonistic activity of PC-3, LNCaP, DU145 and androgen receptor, it was found that the mono-substituted derivatives on the phenyl group (**4**, **6**, **7**, and **9**) displayed strong cytotoxic activities, and compounds **11**–**16** showed relatively strong antagonistic potency against AR (Inhibition% >55). Docking analysis showed that compounds **11** and **12** mainly bind to AR receptor through hydrogen bonds and hydrophobic bonds, and the structure-activity relationship was discussed based on activity data. These results suggested that these compounds may have instructive implications for drug structural modification in prostate cancer.

KEYWORDS

hydroxyzine derivatives, cytotoxic activity, antagonistic activity, docking study, AR antagonists

1 Introduction

Targeted anti-tumor drugs are the focus of modern anti-cancer research, because of their special targeting, they can greatly reduce the toxicity to normal cells (Falciani et al., 2010). In addition, cells in rapid division were more sensitive to the most drugs due to the differences in cell dynamics (Tannock, 1978). Therefore, targeted antitumor drugs can simultaneously inhibit the proliferation and differentiation of tumor cells and greatly accelerate the death of tumor cells (Vinaya et al., 2011). Prostate cancer (PCa) is a malignant tumor with a higher mortality rate in the male reproductive system (Greenlee et al., 2001). Prostate cancer is driven by the androgen receptor (Yap et al., 2016; Dai et al., 2017), and is directly associated with nuclear steroidal AR (Bentel and Tilley, 1996; Culig et al., 2002; Gelmann, 2002). Androgens bind to the AR and form a hormone-receptor complex, which can bind to the DNA and induce downstream biological effects (Dehm and Tindall, 2007). This complex also induces the proliferation of prostate cells, and

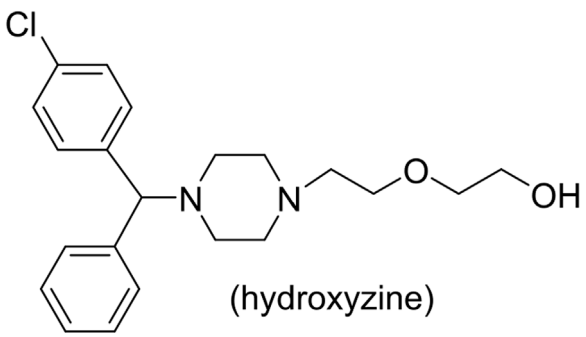

FIGURE 1
Structures of hydroxyzine.

ultimately causes tumorigenesis (Heinlein and Chang, 2004). Although some current treatments (hormonotherapy, radical prostatectomy, chemotherapy, or local radiotherapy) can treat androgen-dependent prostate cancer (Frydenberg et al., 1997). However, drug resistance problems hinder its therapeutic efficacy. Therefore, early detection and elimination of both types of prostate cancer cells are very important for decreasing prostate cancer-related death (Feldman and Feldman, 2001).

Piperazine moieties play an important role in many drugs (Chaudhary et al., 2006), and piperazine derivatives also have exhibited biological importance, such as receptor high-affinity properties (Leopoldo et al., 2007; Romeiro et al., 2011; Chen et al., 2012; Ananthan et al., 2014; Baran et al., 2014) and anti-proliferative properties (Berardi et al., 2008; Lee et al., 2010; Abate et al., 2011; Cao et al., 2013; Liu et al., 2013; Arnatt et al., 2014; Guo et al., 2015). Hydroxyzine (Figure 1) has antihistamine effect and can be quickly absorbed and distributed by oral or muscle injection. The arylpiperazine derivatives were reported to exhibit significant antagonism against AR with an IC_{50} of 0.11 μM, whereas the IC_{50} of bicaluramide is 50 μM. Results of animal experiments have shown that the mass of prostate in rats is significantly reduced, and the concentration of serum testosterone is not significantly changed (Kinoyama et al., 2004; Kinoyama et al., 2005; Gupta et al., 2016). However, there have been few studies on hydroxyzine derivatives. Based on the results of our group's previous anti-prostate cancer study (Chen et al., 2016; Chen et al., 2017; Chen et al., 2018a; Chen et al., 2019a; Chen et al., 2019b; Qi et al., 2022), we tried to design and synthesize a series of novel hydroxyzine derivatives (Scheme 1) with 2-p-tolylethanol group instead of 2-ethoxyethanol group in hydroxyzine. Unexpectedly, some derivatives exhibited strong anti-cancer activities and antagonistic

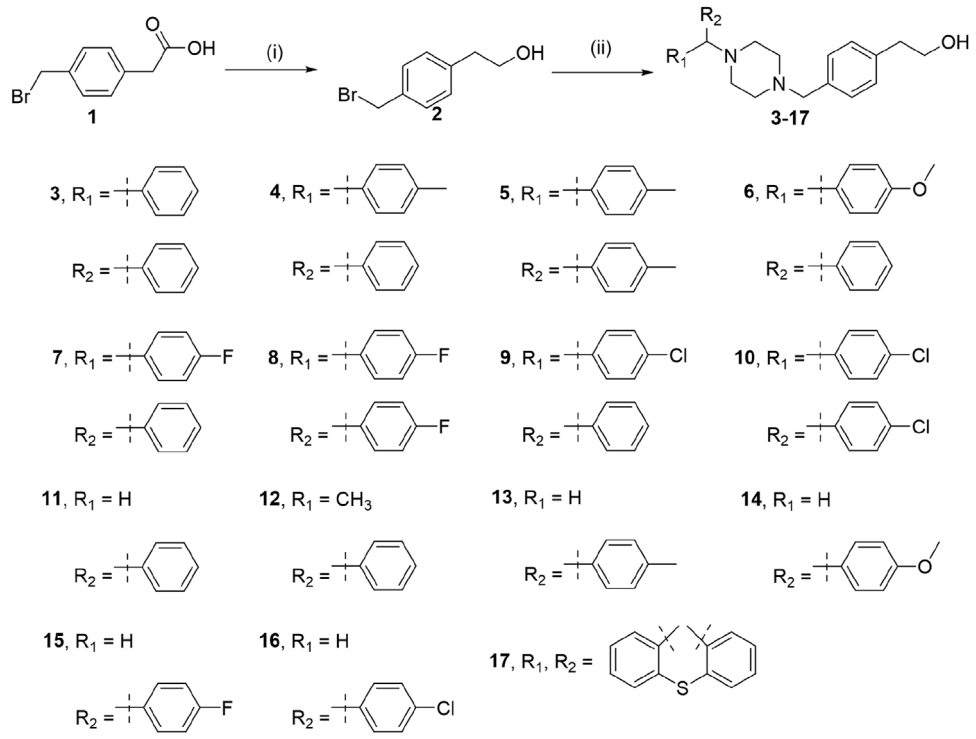

SCHEME 1
Reagents and conditions: (i) $BH_3.S(CH_3)_2$, THF, 0°C for 1 h, and room temperature for 10 h; (ii) Piperazines, K_2CO_3, CH_3CN, reflux, 16 h.

activities. These results can provide valuable information for further designing hydroxyzine derivatives as potential prostate cancer therapeutics.

2 Materials and methods

2.1 Materials and instruments

Reagents and solvents were of analytical purity and dried and using standard procedures. The melting point was measured using the Shanghai electrical optical SGW X-4 micromelting point instrument. The HRMS mass spectrometry was measured using the LCQ DECA XP LC-MS. The NMR spectra were measured using the Bruker AV-400 NB, with TMS as the internal standard, and DMSO-d_6 or $CDCl_3$ as the solvent. Column chromatography silica gel was the 300–400 mesh silicone of Qingdao Marine Chemical Plant.

2.2 Synthesis of 2-[4-(bromomethyl) phenyl]ethanol (2)

The borane–dimethyl sulfide (20.0 ml, 0.038 mol, 2 M in THF) was added to the tetrahydrofuran (THF, 100 ml) solution, supplemented with carboxylic acid **1** (5 g, 0.021 mol), and stirred at 0°C for 1 h. Then stirred at r. t. for 10 h. Extracted with ethyl acetate (100 ml) and water (20 ml). Concentrated organic phase, the resulting residue was directly used without further purification.

2.3 Preparation of derivatives 3–17

Piperazines (1.3 equiv), potassium carbonate (5.5 equiv), acetonitrile (CH_3CN, 10 ml), and **2** (50 mg, 0.11 mmol) were successively added to the flask, stirred with reflux for 10 h. The reaction solution was filtered and concentrated, and purified by silica gel column chromatography (ethyl acetate/petroleum ether = 1/5).

2.3.1 2-(4-((4-benzhydrylpiperazin-1-yl)methyl) phenyl)ethan-1-ol (**3**)

White solid (ethyl acetate), yield: 85% (from compound **1**); M.p. 122°C–123°C; ^{1}H NMR (400 MHz, DMSO-d_6) δ in ppm: 7.75–7.10 (m, 14H), 4.26 (br s, 2H), 3.64 (br s, 10H), 3.56 (t, J = 6.9 Hz, 2H), 2.70 (t, J = 6.9 Hz, 2H); MS (ESI, m/z): 387.1 $[M+1]^+$; HRMS (EI) calcd for $C_{26}H_{29}ClN_2O$, 386.2358; found, 386.2354.

2.3.2 2-(4-((4-(phenyl(p-tolyl)methyl)piperazin-1-yl)methyl)phenyl)ethan-1-ol (**4**)

White solid (ethyl acetate), yield: 82% (from compound **1**); M.p. 125°C–126°C; ^{1}H NMR (400 MHz, DMSO-d_6) δ in ppm: 7.80–7.11 (m, 13H), 4.27 (br s, 2H), 3.66 (br s, 10H), 3.57 (t, J = 6.9 Hz, 2H), 2.72 (t, J = 6.9 Hz, 2H); 2.34 (s, 3H), MS (ESI, m/z): 401.2 $[M+1]^+$; HRMS (EI) calcd for $C_{27}H_{32}N_2O$, 400.2515; found, 400.2510.

2.3.3 2-(4-((4-(di-p-tolylmethyl)piperazin-1-yl) methyl)phenyl)ethan-1-ol (**5**)

White solid (ethyl acetate), yield: 82% (from compound **1**); M.p. 128°C–129°C; ^{1}H NMR (400 MHz, DMSO-d_6) δ in ppm: 7.75 (br s, 4H), 7.45 (d, J = 8.0 Hz, 2H), 7.23 (d, J = 8.0 Hz, 2H), 7.16 (t, J = 8.1 Hz, 4H), 4.25 (br s, 2H), 3.64 (br s, 10H), 3.56 (t, J = 6.9 Hz, 2H), 2.71 (t, J = 6.9 Hz, 2H); 2.36 (s, 6H), MS (ESI, m/z): 415.1 $[M+1]^+$; HRMS (EI) calcd for $C_{28}H_{34}N_2O$, 414.2671; found, 414.2668.

2.3.4 2-(4-((4-((4-methoxyphenyl)(phenyl) methyl)piperazin-1-yl)methyl)phenyl)ethan-1-ol (**6**)

White solid (ethyl acetate), yield: 87% (from compound **1**); M.p. 116°C–117°C; ^{1}H NMR (400 MHz, DMSO-d_6) δ in ppm: 7.76–7.13 (m, 13H), 4.25 (br s, 2H), 3.77 (s, 3H), 3.67 (br s, 10H), 3.54 (t, J = 6.9 Hz, 2H), 2.74 (t, J = 6.9 Hz, 2H), MS (ESI, m/z): 417.1 $[M+1]^+$; HRMS (EI) calcd for $C_{27}H_{32}N_2O_2$, 416.2464; found, 416.2462.

2.3.5 2-(4-((4-((4-fluorophenyl)(phenyl)methyl) piperazin-1-yl)methyl)phenyl)ethan-1-ol (**7**)

White solid (ethyl acetate), yield: 87% (from compound **1**); M.p. 116°C–117°C; ^{1}H NMR (400 MHz, DMSO-d_6) δ in ppm: 7.70–7.11 (m, 13H), 4.27 (br s, 2H), 3.64 (br s, 10H), 3.57 (t, J = 6.9 Hz, 2H), 2.72 (t, J = 6.9 Hz, 2H), MS (ESI, m/z): 405.1 $[M+1]^+$; HRMS (EI) calcd for $C_{26}H_{29}FN_2O$, 404.2264; found, 404.2260.

2.3.6 2-(4-((4-(bis(4-fluorophenyl)methyl) piperazin-1-yl)methyl)phenyl)ethanol (**8**)

White solid (ethyl acetate), yield: 70% (from compound **1**); M.p. 133°C–134°C; ^{1}H NMR (400 MHz, DMSO-d_6) δ in ppm: 1H NMR (400 MHz, DMSO-d6) δ 7.70 (br s, 4H), 7.46 (d, J = 8.0 Hz, 2H), 7.22 (d, J = 8.0 Hz, 2H), 7.18 (t, J = 8.2 Hz, 4H), 4.27 (br s, 2H), 3.66 (br s, 10H), 3.55 (t, J = 6.9 Hz, 2H), 2.68 (t, J = 6.9 Hz, 2H); MS (ESI, m/z): 423.2 $[M+1]^+$; HRMS (EI) calcd for $C_{26}H_{28}F_2N_2O$, 422.2170; found, 422.2168.

2.3.7 2-(4-((4-((4-chlorophenyl)(phenyl)methyl) piperazin-1-yl)methyl)phenyl)ethanol (**9**)

White solid (ethyl acetate), yield: 75% (from compound **1**); M.p. 130°C–131°C; ^{1}H NMR (400 MHz, DMSO-d_6) δ in ppm: 7.89–7.13 (m, 13H), 4.29 (br s, 2H), 3.66 (br s, 10H), 3.57 (t, J = 6.9 Hz, 2H), 2.71 (t, J = 6.9 Hz, 2H); MS (ESI, m/z): 421.1 $[M+1]^+$; HRMS (EI) calcd for $C_{26}H_{29}ClN_2O$, 420.1968; found, 420.1962.

2.3.8 2-(4-((4-(bis(4-chlorophenyl)methyl) piperazin-1-yl)methyl)phenyl)ethan-1-ol (**10**)

White solid (ethyl acetate), yield: 72% (from compound **1**); M.p. 127°C–128°C; ^{1}H NMR (400 MHz, DMSO-d_6) δ in ppm: 7.67 (br s, 4H), 7.42 (d, J = 8.0 Hz, 2H), 7.23 (d, J = 8.0 Hz, 2H), 7.16 (t, J = 8.0 Hz, 4H), 4.23 (br s, 2H), 3.68 (br s, 10H), 3.57 (t, J = 6.9 Hz, 2H), 2.66 (t, J = 6.9 Hz, 2H); MS (ESI, m/z): 455.2 $[M+1]^+$; HRMS (EI) calcd for $C_{26}H_{28}Cl_2N_2O$, 454.1579; found, 454.1575.

2.3.9 2-(4-((4-benzylpiperazin-1-yl)methyl) phenyl)ethan-1-ol (**11**)

White solid (ethyl acetate), yield: 82% (from compound **1**); M.p. 119°C–120°C; ^{1}H NMR (400 MHz, $CDCl_3$) δ in ppm: 7.43 (d, J = 8.0 Hz, 2H), 7.32 (t, J = 8.0 Hz, 2H), 7.24 (d, J = 8.0 Hz, 2H), 7.05 (d, J = 7.8 Hz, 2H), 6.98 (t, J = 7.6 Hz, 1H), 4.25 (s, 2H), 3.76 (t, J = 6.8 Hz, 2H), 3.62 (s, 2H), 3.54 (t, J = 5.0 Hz, 4H), 2.72 (t, J = 6.8 Hz, 2H), 2.68 (t, J = 5.0 Hz, 4H); MS (ESI, m/z): 311.1 $[M+1]^+$; HRMS (EI) calcd for $C_{20}H_{26}N_2O$, 310.2045; found, 310.2040.

2.3.10 2-(4-((4-(1-phenylethyl)piperazin-1-yl) methyl)phenyl)ethan-1-ol (**12**)

White solid (ethyl acetate), yield: 78% (from compound **1**); M.p. 114°C–115°C; ^{1}H NMR (400 MHz, $CDCl_3$) δ in ppm: 7.58–7.09 (m, 9H), 4.23 (q, J = 6.6 Hz, 1H), 3.64 (br s, 8H), 3.62 (t, J = 6.8 Hz, 2H), 3.55 (s, 2H), 2.68 (t, J = 6.8 Hz, 2H), 1.12 (d, J = 6.6 Hz, 3H); MS (ESI, m/z): 325.2 $[M+1]^+$; HRMS (EI) calcd for $C_{21}H_{28}N_2O$, 324.2202; found, 324.2200.

2.3.11 2-(4-((4-(4-methylbenzyl)piperazin-1-yl) methyl)phenyl)ethan-1-ol (**13**)

White solid (ethyl acetate), yield: 75% (from compound **1**); M.p. 112°C–113°C; ^{1}H NMR (400 MHz, $CDCl_3$) δ in ppm: 7.41 (d, J = 8.0 Hz, 2H), 7.30 (t, J = 8.0 Hz, 2H), 7.22 (d, J = 8.0 Hz, 2H), 7.02 (d, J = 8.0 Hz, 2H), 4.27 (s, 2H), 3.74 (t, J = 6.8 Hz, 2H), 3.66 (s, 2H), 3.56 (t, J = 5.0 Hz, 4H), 2.70 (t, J = 6.8 Hz, 2H), 2.64 (t, J = 5.0 Hz, 4H); MS (ESI, m/z): 325.1 $[M+1]^+$; HRMS (EI) calcd for $C_{21}H_{28}N_2O$, 324.2202; found, 324.2200.

2.3.12 2-(4-((4-(4-methoxybenzyl)piperazin-1-yl)methyl)phenyl)ethan-1-ol (**14**)

White solid (ethyl acetate), yield: 82% (from compound **1**); M.p. 117°C–118°C; ^{1}H NMR (400 MHz, $CDCl_3$) δ in ppm: 7.43 (d, J = 8.0 Hz, 2H), 7.31 (t, J = 8.0 Hz, 2H), 7.23 (d, J = 8.0 Hz, 2H), 7.00 (d, J = 8.0 Hz, 2H), 4.25 (s, 2H), 3.81 (s, 3H), 3.72 (t, J = 6.8 Hz, 2H), 3.67 (s, 2H), 3.54 (t, J = 5.0 Hz, 4H), 2.72 (t, J = 6.8 Hz, 2H), 2.62 (t, J = 5.0 Hz, 4H); MS (ESI, m/z): 341.0 $[M+1]^+$; HRMS (EI) calcd for $C_{21}H_{28}N_2O_2$, 340.2151; found, 340.2149.

2.3.13 2-(4-((4-(4-fluorobenzyl)piperazin-1-yl) methyl)phenyl)ethan-1-ol (**15**)

White solid (ethyl acetate), yield: 70% (from compound **1**); M.p. 114°C–115°C; ^{1}H NMR (400 MHz, $CDCl_3$) δ in ppm: 7.42 (d, J = 8.0 Hz, 2H), 7.32 (t, J = 8.0 Hz, 2H), 7.21 (d, J = 8.0 Hz, 2H), 7.03 (d, J = 8.0 Hz, 2H), 4.26 (s, 2H), 3.70 (t, J = 6.8 Hz, 2H), 3.64 (s, 2H), 3.55 (t, J = 5.0 Hz, 4H), 2.70 (t, J = 6.8 Hz, 2H), 2.63 (t, J = 5.0 Hz, 4H); MS (ESI, m/z): 329.1 $[M+1]^+$; HRMS (EI) calcd for $C_{20}H_{25}FN_2O$, 328.1951; found, 328.1948.

2.3.14 2-(4-((4-(4-chlorobenzyl)piperazin-1-yl) methyl)phenyl)ethan-1-ol (**16**)

White solid (ethyl acetate), yield: 72% (from compound **1**); M.p. 109°C–110°C; ^{1}H NMR (400 MHz, $CDCl_3$) δ in ppm: 7.43 (d, J = 8.0 Hz, 2H), 7.33 (t, J = 8.0 Hz, 2H), 7.20 (d, J = 8.0 Hz, 2H), 7.01 (d, J = 8.0 Hz, 2H), 4.24 (s, 2H), 3.72 (t, J = 6.8 Hz, 2H), 3.67 (s, 2H), 3.56 (t, J = 5.0 Hz, 4H), 2.72 (t, J = 6.8 Hz, 2H), 2.66 (t, J = 5.0 Hz, 4H); MS (ESI, m/z): 345.1 $[M+1]^+$; HRMS (EI) calcd for $C_{20}H_{25}ClN_2O$, 344.1655; found, 344.1653.

2.3.15 2-(4-((4-(9H-thioxanthen-9-yl)piperazin-1-yl)methyl)phenyl)ethan-1-ol (**17**)

White solid (ethyl acetate), yield: 78% (from compound **1**), M.p. 121°C–122°C; ^{1}H NMR (400 MHz, DMSO-d_6) δ in ppm: 7.73–7.08 (m, 12H), 4.24 (br s, 2H), 3.67 (br s, 10H), 3.57 (t, J = 6.9 Hz, 2H), 2.74 (t, J = 6.9 Hz, 2H); MS (ESI, m/z): 417.1 $[M+1]^+$; HRMS (EI) calcd for $C_{26}H_{28}N_2OS$, 416.1922; found, 416.1920.

2.4 Biological evaluation

2.4.1 Cell culture

LNCaP, PC-3 and WPMY-1 cells were cultured in Ham's F-12K (PM150910) supplemented with 10% FBS (164210-50) and 1% P/S (PB180120). DU145 cells were cultured in MEM (PM150410) supplemented with 10% FBS (164210–50) and 1% P/S (PB180120). The cells were incubated at 37°C with 5% CO_2 (Qi et al., 2022).

2.4.2 Assessment of antitumor activity by CCK-8 assay

Cell proliferation was measured using the CCK-8 assay kit (Kaspers et al., 1997; Kaspers et al., 1998; Ding et al., 2010). Cells were seeded into 96-well plates (>5*10^4) with approximately 100 ul of cell suspension per well and incubated in 37°C incubator for 4 h. Various concentrations of the compounds were then added and incubated for a further 24 h in a 37°C incubator. Finally, 10 ul CCK8 was added and incubated for 0.5–4 h, absorbance at 450 nm was determined. (Guo et al., 2021; He et al., 2022a; Hu et al., 2022).

2.5 AR reporter gene assay

Firefly and Renilla luciferase activities, were determined using the Dual-Glo™luciferase assay kit. RLUs were determined using the GloMax®96-Microplate Luminometer.

10.3389/fchem.2022.1053675

TABLE 1 *In vitro* cytotoxicity of derivatives 3–17.

Compd.	IC_{50} (μM)[a]			
	PC-3	LNCaP	DU145	WPMY-1
3	8.13 ± 0.12	6.14 ± 0.58	11.12 ± 0.76	>50
4	2.56 ± 0.32	4.67 ± 1.02	6.14 ± 0.24	>50
5	12.14 ± 0.29	3.73 ± 0.58	9.82 ± 0.24	37.51 ± 0.37
6	3.15 ± 0.48	6.17 ± 1.02	2.17 ± 0.72	>50
7	1.87 ± 0.22	5.17 ± 0.63	2.17 ± 1.12	48.26 ± 0.41
8	10.12 ± 0.08	4.92 ± 0.29	12.35 ± 0.16	35.53 ± 0.13
9	1.53 ± 0.16	4.13 ± 0.06	7.63 ± 0.12	>50
10	15.24 ± 0.14	7.14 ± 0.29	10.78 ± 1.14	>50
11	20.36 ± 0.48	11.24 ± 0.14	11.26 ± 0.27	>50
12	13.67 ± 1.12	7.76 ± 0.19	16.28 ± 0.63	>50
13	15.36 ± 0.42	22.13 ± 0.76	17.17 ± 1.02	47.14 ± 0.42
14	11.13 ± 0.67	16.16 ± 0.53	24.14 ± 0.47	>50
15	10.46 ± 1.14	18.45 ± 0.16	16.17 ± 0.62	>50
16	14.42 ± 0.35	16.41 ± 0.19	31.46 ± 1.21	>50
17	6.42 ± 0.52	5.61 ± 0.86	8.35 ± 0.28	>50
Finasteride	17.80	13.53	14.55	—
Naftopidil	42.10 ± 0.79	22.36 ± 0.61	34.58 ± 0.31	>50

[a]IC_{50} values are taken as means ± standard deviation from three experiments.

TABLE 2 AR antagonist activity of compounds 3–17.

Compd.	AR antagonistic activity % (10 μM)
3	40.17 ± 0.24
4	32.46 ± 0.65
5	22.68 ± 0.72
6	30.75 ± 0.17
7	38.67 ± 0.83
8	25.16 ± 0.71
9	28.42 ± 0.25
10	20.47 ± 0.18
11	65.15 ± 0.57
12	68.62 ± 0.38
13	64.18 ± 0.45
14	58.88 ± 0.23
15	64.35 ± 0.17
16	60.25 ± 0.35
17	36.49 ± 0.79
R1881	N.E[a]
Enzalutamide	84.7 ± 1.4

[a]N.E, no antagonistic effect.

IC_{50} was calculated using the GraphPad Prism 5.0 (He et al., 2022b; Qi et al., 2022).

2.6 Molecular docking simulation

Binding mechanism experiments performed docking analysis of the three active pockets (LBP, AF2 and BF3) (Axerio-Cilies et al., 2011; Lack et al., 2011) in AR receptors using AutoDock software (Trott and Olson, 2010). Its PDB protein data (2OZ7, 2YHD and 2YLO) was downloaded from the protein data bank (PDB) (Rose et al., 2011), and the proteins were optimized by the addition of hydrogen atoms and the removal of foreign ligands before docking. A docking space of 40 Å × 40 Å × 30 Å was constructed centered on the ligand of the AR active pocket, with compounds **11** and **12** as template molecules, docked into the optimized cavity and repeated 10 times to find a conformation of the one with the lowest binding free energy.

3 Results and discussions

3.1 Chemistry

Compounds **3–17** were synthesized by the following two-step method as depicted in Scheme 1. The compound **1** was reduced to compound **2** with $BH_3.S(CH_3)_2$. Then, the compound **2** was heated at reflux with various piperines in an alkaline environment for 16 h.

3.2 Cytotoxic activity and AR antagonist activity

The *in vitro* cytotoxic activity results of the synthesized derivatives **3–17** against human prostate cancer lines (PC-3, LNCaP, and DU145) and the human prostate epithelial cell line (WPMY-1) were evaluated, as shown in Table 1.

The compounds **3–10** and **12–17** showed strong cytotoxic activity against PC-3 cells and were more potent than finasteride; the compounds **3–12** and **17** showed strong cytotoxic activity against LNCaP cells; the compounds **3–11** and **17** showed strong cytotoxic activity against DU145 cells. In addition, mono-substituted derivatives on the phenyl group (**4**, **6**, **7**, and **9**) displayed strong cytotoxic activities against all the tested cancer cells. And these compounds exhibited low cytotoxicity to normal human prostate epithelial WPMY-1 cells.

Structure-activity relationship investigation was focused on the effects of changes in different substituents on the phenyl group. For instance, compared to compound **3**, the compounds with mono-substituted group on the phenyl group (**4**, **6**, **7**, and **9**) exhibited potent anticancer activity against LNCaP, DU145, and PC-3 cells. However, Dimethyl-substituted derivative **5** displayed moderate activity against PC-3 and DU145 cells, compounds **8**

TABLE 3 The binding affinities (kcal/mol) of compounds 11 and 12 in three binding sites of AR.

Binding site	Compound 11	Compound 12
LBP (PDB ID: 2OZ7)	−8.1	−8.5
AF2 (PDB ID: 2YHD)	−5.9	−6.0
BF3 (PDB ID: 2YLO)	−6.5	−6.6

and **10** also had the similar properties. Moreover, compound **6** with electron-donating group also demonstrated strong cytotoxic activities against all the tested cancer cells. In order to compare the cytotoxic activity of compounds **3–10**, the compounds **11–16** were synthesized, and the substitution of R1 and R2 groups with two phenyl groups showed high cytotoxic activity against the tested cancer cells. In summary, the introduction of this piperazine moiety contributes to its activity. Both PC-3 and

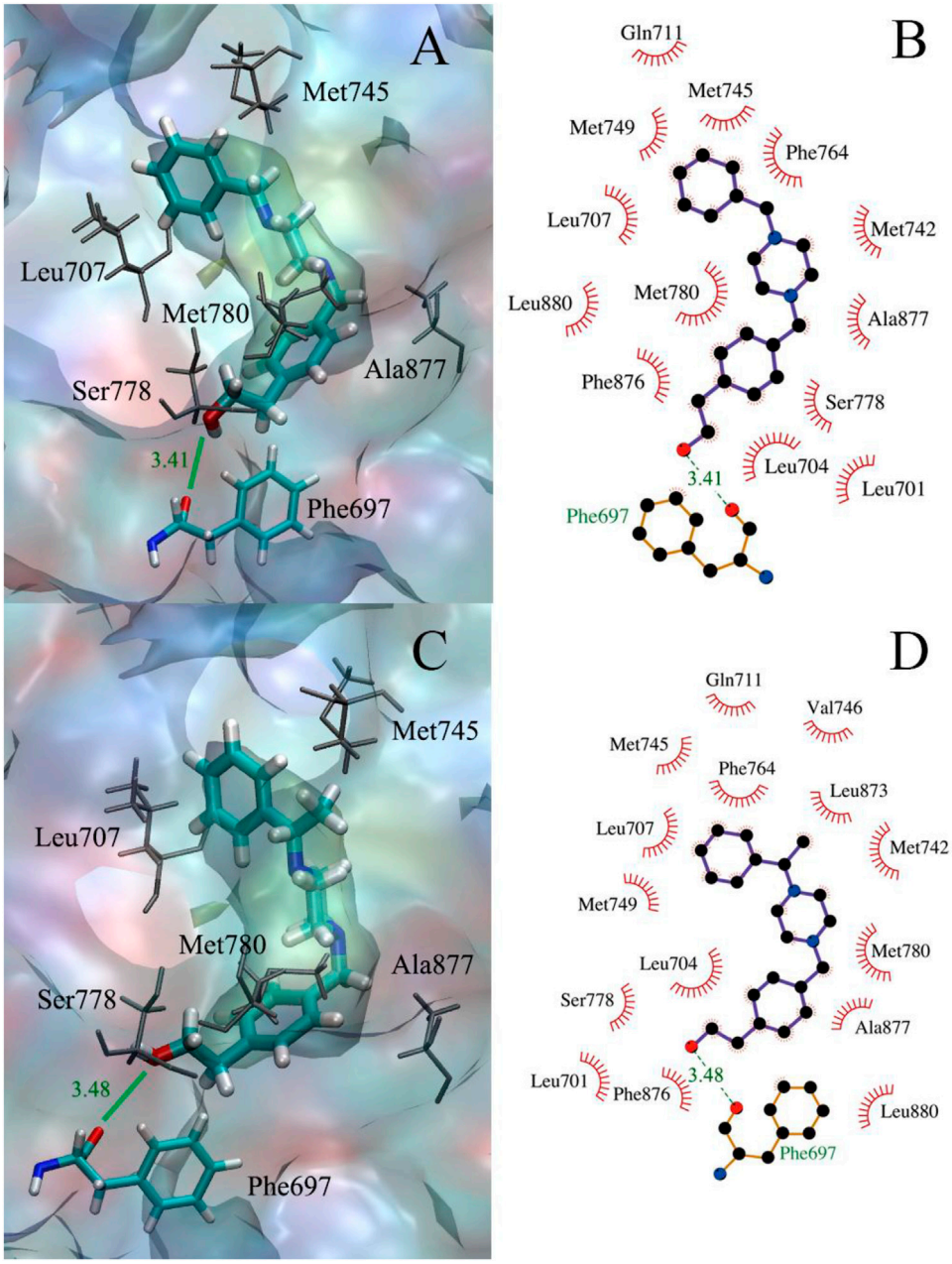

FIGURE 2
(A,B) The docking of compound **11** to the AR receptor; **(C,D)** The docking of compound **12** to the AR receptor.

DU145 cells are androgen-insensitive cell lines, but the compounds have different inhibitory activities against PC-3 and DU145 cells. The p53 is one of the most commonly mutated genes in human cancer, and the expression of p53 gene may be a key determinant of derivatives sensitivity in prostate cancer DU145 cells (Liu et al., 2013b). The literatures have reported that the p53 in DU145 cells were significantly activated by drugs, but in PC-3 cells the expression of the p53 gene was undetectable (Isaacs et al., 1991; Mashimo et al., 2000). So the compounds have different inhibitory activities against PC-3 and DU145 cells, and PC-3 cells are insensitive to derivatives.

The antagonistic activity of these derivatives against AR was assessed using luciferase assays (Xu et al., 2014; Xu et al., 2015; Zuo et al., 2017; Xu et al., 2018). As shown in Table 2, the compounds **3–10** exhibited weak antagonistic potency against AR. However, compounds **11–16** demonstrated relatively potent antagonistic potency (>55% inhibition).The above results were be contrary to the tested cancer cells antiproliferation activity. The results indicated that a small group introduction to the piperazine ring may be helpful for antagonistic activity against AR.

3.3 Docking study

In order to better understand the binding site of derivatives targets, the docking simulation into the three binding sites of AR (LBP, AF2, and BF3) of compounds **11** and **12** were performed using AutoDock Vina software, as shown in Table 3.

As displayed in Table 3, the binding free energies of the compounds **11** and **12** to all three sites of the AR were calculated, both of the LBP sites had the lowest binding free energy, as measured at −8.1 and −8.5 kcal/mol, respectively. As shown in Figure 2, both compounds **11** and **12** could form hydrophobic interactions with over a dozen amino acid residues, such as Gln711, Met745, and Ala877. More importantly, they were all able to form hydrogen bonds with the amino acid residue Phe697, at a distance of between 3.5 Å.

4 Conclusion

In summary, in this study a series of novel hydroxyazine derivatives were synthesized and evaluated for antagonistic activity against AR and cytotoxic activity against human prostate cancer cells. The results showed that the derivative **4**, **6**, **7**, and **9** displayed strong cytotoxic activities against the LNCaP, DU145 and PC-3 cells, and compounds **11–16** showed strong AR antagonism (Inhibition% >55). The SAR results suggested that mono-substituted derivatives on the phenyl group contributed to improve the cytotoxic activity against human prostate cancer cells. These hydroxyzazine piperazine derivatives may be instructive for structural modification of novel anti-prostate cancer drugs.

Data availability statement

The original contributions presented in the study are included in the article/Supplementary Material, further inquiries can be directed to the corresponding authors.

Author contributions

YQ, BX, and SC performed synthesis experiments. YQ, BX, and WW conducted the biological evaluation and molecular docking. YQ, HZ, and HC designed experiments. YQ and HC interpreted the data and wrote the paper. All authors contributed to the article and approved the submitted version.

Funding

The work was supported by the Henan Province Science and Technology Attack Plan Foundation (Nos 212102110241 and 222102310356), the Key Scientific Research Project of Higher Education of Henan Province (Nos 21A350006 and 22B350004), the National Natural Science Foundation of China (No. 22278244), and 111 Project (No. D20015).

Conflict of interest

The authors declare that the research was conducted in the absence of any commercial or financial relationships that could be construed as a potential conflict of interest.

Publisher's note

Supplementary material

The Supplementary Material for this article can be found online at: https://www.frontiersin.org/articles/10.3389/fchem.2022.1053675/full#supplementary-material

References

Abate, C., Niso, M., Contino, M., Colabufo, N. A., Ferorelli, S., Perrone, R., et al. (2011). 1-Cyclohexyl-4-(4-arylcyclohexyl) piperazines: Mixed σ and human Δ(8)-Δ(7) sterol isomerase ligands with antiproliferative and P-glycoprotein inhibitory activity. *ChemMedChem* 6, 73–80. doi:10.1002/cmdc.201000371

Ananthan, S., Saini, S. K., Zhou, G., Hobrath, J. V., Padmalayam, I., Zhai, L., et al. (2014). Design, synthesis, and structure-activity relationship studies of a series of [4-(4-carboxamidobutyl)]-1-arylpiperazines: Insights into structural features contributing to dopamine D3 versus D2 receptor subtype selectivity. *J. Med. Chem.* 57, 7042–7060. doi:10.1021/jm500801r

Arnatt, C. K., Adams, J. L., Zhang, Z., Haney, K. M., Li, G., and Zhang, Y. (2014). Design, syntheses, and characterization of piperazine based chemokine receptor CCR5 antagonists as anti-prostate cancer agents. *Bioorg. Med. Chem. Lett.* 24, 2319–2323. doi:10.1016/j.bmcl.2014.03.073

Axerio-Cilies, P., Lack, N. A., Nayana, M. R., Chan, K. H., Yeung, A., Leblanc, E., et al. (2011). Inhibitors of androgen receptor activation function-2 (AF2) site identified through virtual screening. *J. Med. Chem.* 54, 6197–6205. doi:10.1021/jm200532b

Baran, M., Kepczynska, E., Zylewski, M., Siwek, A., Bednarski, M., and Cegla, M. T. (2014). Studies on novel pyridine and 2-pyridone derivatives of N-arylpiperazine as α-adrenoceptor ligands. *Med. Chem. Los. Angeles.* 10, 144–153. doi:10.2174/09298673209991311221149 22

Bentel, J. M., and Tilley, W. D. (1996). Androgen receptors in prostate cancer. *J. Endocrinol.* 151, 1–11. doi:10.1677/joe.0.1510001

Berardi, F., Abate, C., Ferorelli, S., De Robertis, A. F., Leopoldo, M., Colabufo, N. A., et al. (2008). Novel 4-(4-Aryl)cyclohexyl-1-(2-pyridyl)piperazines as Δ_8–Δ_7 sterol isomerase (emopamil binding protein) selective ligands with antiproliferative activity. *J. Med. Chem.* 51, 7523–7531. doi:10.1021/jm800965b

Cao, S. L., Han, Y., Yuan, C. Z., Wang, Y., Xiahou, Z. K., Liao, J., et al. (2013). Synthesis and antiproliferative activity of 4-substituted-piperazine-1-carbodithioate derivatives of 2, 4-diaminoquinazoline. *Eur. J. Med. Chem.* 64, 401–409. doi:10.1016/j.ejmech.2013.04.017

Chaudhary, P., Kumar, R., Verma, A. K., Singh, D., Yadav, V., Chhillar, A. K., et al. (2006). Synthesis and antimicrobial activity of N-alkyl and N-aryl piperazine derivatives. *Bioorg. Med. Chem.* 14, 1819–1826. doi:10.1016/j.bmc.2005.10.032

Chen, H., Liang, X., Sun, T., Qiao, X. G., Zhou, Z., Li, Z. Y., et al. (2018a). Synthesis and biological evaluation of estrone 3-O-ether derivatives containing the piperazine moiety. *Steroids* 134, 101–109. doi:10.1016/j.steroids.2018.02.002

Chen, H., Wang, C. L., Sun, T., Zhou, Z., Niu, J. X., Tian, X. M., et al. (2018b). Synthesis, biological evaluation and SAR of naftopidil-based arylpiperazine derivatives. *Bioorg. Med. Chem. Lett.* 28, 1534–1539. doi:10.1016/j.bmcl.2018.03.070

Chen, H., Xu, B. B., Sun, T., Zhou, Z., Ya, H. Y., and Yuan, M. (2017). Synthesis and antitumor activity of novel arylpiperazine derivatives containing the saccharin moiety. *Molecules* 22, 1857. doi:10.3390/molecules22111857

Chen, H., Xu, F., Xu, B. B., Xu, J. Y., Shao, B. H., Huang, B. Y., et al. (2016). Design, synthesis and biological evaluation of novel arylpiperazine derivatives on human prostate cancer cell lines. *Bioorg. Med. Chem. Lett.* 27, 285–287. doi:10.1016/j.bmcl.2014.11.049

Chen, H., Yu, Y. Z., Tian, X. M., Wang, C. L., Qian, Y. N., Deng, Z. A., et al. (2019a). Synthesis and biological evaluation of arylpiperazine derivatives as potential anti-prostate cancer agents. *Bioorg. Med. Chem.* 27, 133–143. doi:10.1016/j.bmc.2018.11.029

Chen, H., Zhang, J. X., Hu, P. X., Qian, Y. N., Li, J., and Shen, J. L. (2019b). Synthesis, biological evaluation and molecular docking of 4-Amino-2Hbenzo[h] chromen-2-one (ABO) analogs containing the piperazine moiety. *Bioorg. Med. Chem.* 27, 115081. doi:10.1016/j.bmc.2019.115081

Chen, X., Sassano, M. F., Zheng, L. Y., Setola, V., Chen, M., Bai, X., et al. (2012). Structure–functional selectivity relationship studies of β-arrestin-biased dopamine D_2Receptor agonists. *J. Med. Chem.* 55, 7141–7153. doi:10.1021/jm300603y

Culig, Z., Klocker, H., Bartsch, G., Hobishc, A., and Hobisch, A. (2002). Androgen receptors in prostate cancer. *Endocr. Relat. Cancer* 9, 155–170. doi:10.1677/erc.0.0090155

Dai, C., Heemers, H., and Sharifi, N. (2017). Androgen signaling in prostate cancer. *Cold Spring Harb. Perspect. Med.* 7, a030452. doi:10.1101/cshperspect.a030452

Dehm, S. M., and Tindall, D. J. (2007). Androgen receptor structural and functional elements: Role and regulation in prostate cancer. *Mol. Endocrinol.* 21, 2855–2863. doi:10.1210/me.2007-0223

Ding, J., Huang, S. L., Wu, S. Q., Zhao, Y. J., Liang, L. H., Yan, M. X., et al. (2010). Gain of miR-151 on chromosome 8q24.3 facilitates tumour cell migration and spreading through downregulating RhoGDIA. *Nat. Cell Biol.* 12, 390–399. doi:10.1038/ncb2039

Falciani, C., Brunetti, J., Pagliuca, C., Menichetti, S., Vitellozzi, L., Lelli, B., et al. (2010). Design and *in vitro* evaluation of branched peptide conjugates: Turning nonspecific cytotoxic drugs into tumor-selective agents. *ChemMedChem* 5, 567–574. doi:10.1002/cmdc.200900527

Feldman, B. J., and Feldman, D. (2001). The development of androgen-independent prostate cancer. *Nat. Rev. Cancer* 1, 34–45. doi:10.1038/35094009

Frydenberg, M., Stricker, P. D., and Kaye, K. W. (1997). Prostate cancer diagnosis and management. *Lancet* 349, 1681–1687. doi:10.1016/S0140-6736(96)07393-X

Gelmann, E. P. (2002). Molecular biology of the androgen receptor. *J. Clin. Oncol.* 20, 3001–3015. doi:10.1200/JCO.2002.10.018

Greenlee, R. T., Murray, T., Hill-Harmon, M. B., and Thun, M. J. (2001). Cancer statistics, 2001. *CA A Cancer J. Clin.* 51, 15–36. doi:10.3322/canjclin.51.1.15

Guo, F. J., Sun, J., Gao, L. L., Wang, X. Y., Zhang, Y., Qian, S. S., et al. (2015). Discovery of phenylpiperazine derivatives as IGF-1R inhibitor with potent antiproliferative properties *in vitro*. *Bioorg. Med. Chem. Lett.* 25, 1067–1071. doi:10.1016/j.bmcl.2015.01.011

Guo, Z. H., Shi, L. Q., Feng, H. Y., Yang, F., Li, Z. R., Zhang, J. J., et al. (2021). Reduction-sensitive nanomicelles: Delivery celastrol for retinoblastoma cells effective apoptosis. *Chin. Chem. Lett.* 32, 1046–1050. doi:10.1016/j.cclet.2020.03.066

Gupta, S., Pandey, D., Mandalapu, D., Bala, V., Sharma, V., Shukla, M., et al. (2016). Design, synthesis and biological profiling of aryl piperazine based scaffolds for the management of androgen sensitive prostatic disorders. *MedChemComm* 7, 2111–2121. doi:10.1039/C6MD00426A

He, X. J., Dai, L. X., YeSun, L. S. X. S., Enoch, O., Hu, R. D., Zan, X. J., et al. (2022b). A vehicle-free antimicrobial polymer hybrid gold nanoparticle as synergistically therapeutic platforms for staphylococcus aureus infected wound healing. *Adv. Sci. (Weinh).* 9 (14), 2105223. doi:10.1002/advs.202105223

He, X. J., Hou, J. T., Sun, X. S., Jangili, P., An, J., Qian, Y., et al. (2022a). Nir-ii photo-amplified sonodynamic therapy using sodium molybdenum bronze nanoplatform against subcutaneous staphylococcus aureus infection. *Adv. Funct. Mat.* 32 (38), 2203964. doi:10.1002/adfm.202203964

Heinlein, C. A., and Chang, C. (2004). Androgen receptor in prostate cancer. *Endocr. Rev.* 25, 276–308. doi:10.1210/er.2002-0032

Hu, F. Y., Song, B., Wang, X. H., Bao, S., Shang, S. Y., Lv, S. P., et al. (2022). Green rapid synthesis of Cu2O/Ag heterojunctions exerting synergistic antibiosis. *Chin. Chem. Lett.* 33, 308–313. doi:10.1016/j.cclet.2021.07.018

Isaacs, W. B., Carter, B. S., and Ewing, C. M. (1991). Wild-type p53 suppresses growth of human prostate cancer cells containing mutant p53 alleles. *Cancer Res.* 51, 4716–4720.

Kaspers, G. J., Pieters, R., Van Zantwijk, C. H., VanWering, E. R., Van Der Does-Van Den Berg, A., and Veerman, A. J. (1998). Prednisolone resistance in childhood acute lymphoblastic leukemia: Vitro-vivo correlations and cross-resistance to other drugs. *Blood* 92, 259–266. doi:10.1182/blood.V92.1.259.413k21_259_266

Kaspers, G. J., Veerman, A. J., Pieters, R., Van Zantwijk, C. H., Smets, L. A., Van Wering, E. R., et al. (1997). *In vitro* cellular drug resistance and prognosis in newly diagnosed childhood acute lymphoblastic leukemia. *Blood* 90, 2723–2729. doi:10.1182/blood.V90.7.2723.2723_2723_2729

Kinoyama, I., Taniguchi, N., Kawaminami, E., Nozawa, E., Koutoku, H., Furutani, T., et al. (2005). N-arylpiperazine-1-carboxamide derivatives: A novel series of orally active nonsteroidal androgen receptor antagonists. *Chem. Pharm. Bull.* 53, 402–409. doi:10.1248/cpb.53.402

Kinoyama, I., Taniguchi, N., Yoden, T., Koutoku, H., Furutani, T., Kudoh, M., et al. (2004). Synthesis and pharmacological evaluation of novel arylpiperazine derivatives as nonsteroidal androgen receptor antagonists. *Chem. Pharm. Bull.* 52, 1330–1333. doi:10.1248/cpb.52.1330

Lack, N. A., Axeriocilies, P., Tavassoli, P., Han, F. Q., Chan, K. H., Feau, C., et al. (2011). Targeting the binding function 3 (BF3) site of the human androgen receptor through virtual screening. *J. Med. Chem.* 54, 8563–8573. doi:10.1021/jm201098n

Lee, Y. B., Gong, Y. D., Yoon, H., Ahn, C. H., Jeon, M. K., and Kong, J. Y. (2010). Synthesis and anticancer activity of new 1-[(5 or 6-substituted 2-alkoxyquinoxalin-3-yl)aminocarbonyl]-4-(hetero)arylpiperazine derivatives. *Bioorg. Med. Chem.* 18, 7966–7974. doi:10.1016/j.bmc.2010.09.028

Leopoldo, M., Lacivita, E., Passafiume, E., Contino, M., Colabufo, N. A., Berardi, F., et al. (2007). 4-[ω-[4-Arylpiperazin-1-yl]alkoxy]phenyl)imidazo[1, 2-*a*]pyridine Derivatives: fluorescent high-affinity dopamine D_3 receptor ligands as potential probes for receptor visualization. *J. Med. Chem.* 50, 5043–5047. doi:10.1021/jm070721+

Lin, H. H., Wu, W. Y., Cao, S. L., Liao, J., Ma, L., Gao, M., et al. (2013). Synthesis and antiproliferative evaluation of piperazine-1-carbothiohydrazide derivatives of indolin-2-one. *Bioorg. Med. Chem. Lett.* 23, 3304–3307. doi:10.1016/j.bmcl.2013.03.099

Liu, C., Zhu, Y., Lou, W., Nadiminty, N., Chen, X., Zhou, Q., et al. (2013b). Functional p53 determines docetaxel sensitivity in prostate cancer cells. *Prostate* 73, 418–427. doi:10.1002/pros.22583

Liu, W. H., Chang, J. X., Liu, Y., Luo, J. W., and Zhang, J. W. (2013a). Design, synthesis and activities of novel benzothiazole derivatives containing arylpiperazine. *Acta Pharm. Sin.* 48, 1259–1265. doi:10.16438/j.0513-4870.2013.08.002

Mashimo, T., Bandyopadhyay, S., Goodarzi, G., Watabe, M., Pai, S. K., Gross, S. C., et al. (2000). Activation of the tumor Metastasis suppressor gene, KAI1, by Etoposide is mediated by p53 and c-jun genes. *Biochem. Biophys. Res. Commun.* 274, 370–376. doi:10.1006/bbrc.2000.3139

Qi, Y. H., Chen, H., Chen, S. J., Shen, J. L., and Li, J. G. (2022). Synthesis, bioactivity, and molecular docking of novel arylpiperazine derivatives as potential AR antagonists. *Front. Chem.* 10, 947065. doi:10.3389/fchem.2022.947065

Romeiro, L. A., Da Silva Ferreira, M., Da Silva, L. L., Castro, H. C., Miranda, A. L., ilva, S. C. L., et al. (2011). Discovery of LASSBio-772, a 1, 3-benzodioxole N-phenylpiperazine derivative with potent alpha 1A/D-adrenergic receptor blocking properties. *Eur. J. Med. Chem.* 46, 3000–3012. doi:10.1016/j.ejmech.2011.04.032

Rose, P. W., Beran, B., Bi, C., Bluhm, W. F., Dimitropoulos, D., Goodsell, D. S., et al. (2011). The RCSB protein data bank: Redesigned web site and web services. *Nucleic Acids Res.* 39, D392–D401. doi:10.1093/nar/gkq1021

Shen, W. C., Hu, T. T., Liu, X. Y., Zha, J. J., Meng, F. Q., Wu, Z. K., et al. (2022). Defect engineering of layered double hydroxide nanosheets as inorganic photosensitizers for NIR-III photodynamic cancer therapy. *Nat. Commun.* 13, 3384. doi:10.1038/s41467-022-31106-9

Tannock, I. (1978). Cell kinetics and chemotherapy: A critical review. *Cancer Treat. Rep.* 62, 1117–1133.

Trott, O., and Olson, A. J. (2010). AutoDock Vina: Improving the speed and accuracy of docking with a new scoring function, efficient optimization, and multithreading. *J. Comput. Chem.* 31, 455–461. doi:10.1002/jcc.21334

Vinaya, K., Kavitha, C. V., Chandrappa, S., Prasanna, D. S., Raghavan, S. C., and Rangappa, K. S. (2011). Synthesis and antileukemic activity of novel 4-(3-(piperidin-4-yl) propyl)piperidine derivatives. *Chem. Biol. Drug Des.* 78, 622–630. doi:10.1111/j.1747-0285.2011.01184.x

Xu, F., Chen, H., He, X. L., Xu, J. Y., Xu, B. B., Huang, B. Y., et al. (2014). Identification of two novel α1-AR agonists using a high-throughput screening model. *Molecules* 19, 12699–12709. doi:10.3390/molecules190812699

Xu, F., Chen, H., Xu, J. Y., Liang, X., He, X. L., Shao, B. H., et al. (2015). Synthesis, structure-activity relationship and biological evaluation of novel arylpiperzines as α1A/1D-AR subselective antagonists for BPH. *Bioorg. Med. Chem.* 23, 7735–7742. doi:10.1016/j.bmc.2015.11.020

Xu, X., Ge, R., Li, L., Wang, J., Lu, X., Xue, S., et al. (2018). Exploring the tetrahydroisoquinoline thiohydantoin scaffold blockade the androgen receptor as potent anti-prostate cancer agents. *Eur. J. Med. Chem.* 143, 1325–1344. doi:10.1016/j.ejmech.2017.10.031

Yap, T. A., Smith, A. D., Ferraldeschi, R., Al-Lazikani, B., Workman, P., and de Bono, J. S. (2016). Drug discovery in advanced prostate cancer: Translating biology into therapy. *Nat. Rev. Drug Discov.* 15, 699–718. doi:10.1038/nrd.2016.120

Zhou, Z., Wang, Y. L., Peng, F., Meng, F. Q., Zha, J. J., Ma, L., et al. (2022). Intercalation-activated layered MoO3 nanobelts as biodegradable nanozymes for tumor-specific photo-enhanced catalytic therapy. *Angew. Chem. Int. Ed. Engl.* 61, e202115939. doi:10.1002/anie.202115939

Zuo, M., Xu, X., Xie, Z., Ge, R., Zhang, Z., Li, Z., et al. (2017). Design and synthesis of indoline thiohydantoin derivatives based on enzalutamide as antiproliferative agents against prostate cancer. *Eur. J. Med. Chem.* 125, 1002–1022. doi:10.1016/j.ejmech.2016.10.049

frontiers | Frontiers in Chemistry

TYPE Original Research
PUBLISHED 09 November 2022
DOI 10.3389/fchem.2022.1054739

OPEN ACCESS

EDITED BY
Yu Huo,
Sichuan Normal University, China

REVIEWED BY
You Zhang,
Dongguan University of Technology, China
Hong Chen,
Luoyang Normal University, China

*CORRESPONDENCE
Bailin Xiang,
xsz96@163.com
Jianliang Shen,
shenjl@wiucas.ac.cn

†These authors have contributed equally to this work

SPECIALTY SECTION
This article was submitted to Medicinal and Pharmaceutical Chemistry, a section of the journal Frontiers in Chemistry

RECEIVED 27 September 2022
ACCEPTED 06 October 2022
PUBLISHED 09 November 2022

CITATION
Obeng E, Feng J, Wang D, Zheng D, Xiang B and Shen J (2022), Multifunctional phototheranostic agent ZnO@Ag for anti-infection through photothermal/photodynamic therapy. *Front. Chem.* 10:1054739. doi: 10.3389/fchem.2022.1054739

Multifunctional phototheranostic agent ZnO@Ag for anti-infection through photothermal/photodynamic therapy

Enoch Obeng[1†], Jiayao Feng[2†], Danyan Wang[3], Dongyang Zheng[3], Bailin Xiang[4*] and Jianliang Shen[1,3*]

[1]School of Ophthalmology and Optometry, School of Biomedical Engineering, Wenzhou Medical University, Wenzhou, Zhejiang, China, [2]Ningbo Eye Hospital, Ningbo, Zhejiang, China, [3]Wenzhou Institute, University of Chinese Academy of Sciences, Wenzhou, China, [4]College of Chemistry and Materials Engineering, Huaihua University, Huaihua, China

To overcome the limitations of traditional therapeutics, nanotechnology offers a synergistic therapeutic approach for the treatment of bacterial infection and biofilms that has attracted attention. Herein, we report on a ZnO@Ag nanocomposite with good biocompatibility synthesized by doping ZnO NPs with silver nanoparticles (Ag NPs). ZnO@Ag nanocomposites were synthesized with varying ratios of Ag NPs (0.5%, 2%, 8%). Under the same experimental conditions, ZnO@8%Ag exhibited outstanding properties compared to the other nanocomposites and the pristine ZnO NPs. ZnO@8%Ag demonstrated excellent photothermal and photodynamic properties. Also, ZnO@8%Ag demonstrated over 99% inhibition of *Staphylococcus aureus* (*S. aureus*) under photothermal therapy (PTT) or photodynamics therapy (PDT) as a result of the excessive generation of reactive oxygen species (ROS) by the Ag^+ released, while the pristine ZnO showed an insignificant inhibition rate compared to the PBS group (control). Furthermore, ZnO@8%Ag completely disrupted *S. aureus* biofilm under a combined PTT/PDT treatment, a synergetic trimodal therapy, although the molecular mechanism of biofilm inhibition remains unclear. Hence, the excellent photothermal, photodynamic, biocompatibility, and bactericidal properties of ZnO@8%Ag present it as an appropriate platform for bacterial and biofilm treatment or other biomedically related applications.

KEYWORDS

ZnO@Ag nanocomposite, photothermal therapy, photodynamic therapy, synergistic effect, anti-infective therapy

1 Introduction

Bacterial infection is a principal problem of great concern to public health as a result of the inability of traditional antibacterial therapies to completely or efficiently eliminate bacterial infections that form biofilm over time. The approach was a therapeutic practice in the 1930s (Boucher et al., 2009; Courtney et al., 2016; Jia et al., 2017), but its current

ineffectiveness has been attributed to environmental pollution and the uncontrolled use of antibiotics that have contributed to the resistance mounted by bacteria. As a result, a global crisis is facing the world with billions of dollars of estimated annual costs (Stewart and Costerton, 2001; Darouiche, 2004; Wright, 2011). Hence, researchers are responding to an urgent call for an alternative therapy to address the shortcomings of the traditional antibacterial approach. The nanotechnology-based antibacterial approach has presented a novel strategy for eradicating bacteria and, in so doing, attracted much attention, owing to its antibacterial activity and stability (Pelgrift and Friedman, 2013; Duncan et al., 2015; Liu et al., 2016). Their material presents unique characteristics such as adjustable size, shape, and structure that offer an antibacterial advantage. Not all nanomaterials have the intrinsic ability to kill bacteria. However, silver nanoparticles (Ag NPs) bear this ability and are capable of influencing cell membrane integrity, respiration, and the ATP production of the bacteria due to their shape, size, and surface charge (Morones et al., 2005; Vikesland and Wigginton, 2010; Hassan et al., 2012; Rajavel et al., 2014; Tian et al., 2014). Ag NPs exhibit tremendous effectiveness against a wide variety of microbes that are Gram-positive and Gram-negative inclusive through the release of silver ions (Ag^+). This results in the generation of reactive oxygen species (ROS) and, at the same time, facilitates wound healing through the induction of metalloproteinase activity and enhanced neutrophil apoptosis (Kirsner et al., 2001; Chaloupka et al., 2010; Chernousova and Epple, 2013; Zheng et al., 2016; Sarfraz and Qayyum, 2018).

Zinc oxide nanoparticles (ZnO NPs) have acquired great attention and have extensively been studied due to their physical, chemical, high reflective index, and easy means of synthesis. However, their wide bandgap (3.37 eV), large exciton binding energy (around 60 MeV), low charge separation efficiency, and fast recombination rate present limitations, making ZnO NPs an inactive photocatalyst within a visible light spectrum but active in the UV region (Huang et al., 2001; Kudo and Miseki, 2009; Grumezescu et al., 2014; Ali et al., 2019). Intriguingly, modification of the ZnO NPs with noble metals such as Au, Ag, Ru, and Pt helps circumvent these drawbacks (Zheng et al., 2008; Yuan et al., 2010; Zhang et al., 2010). Studies indicate that modification of the ZnO NPs with noble metals allows the formation of a Schottky barrier to promote photogenerated charge separation, subsequently improving the material's photocatalytic activity and making it an appropriate choice. Although UV may be required for ROS generation, the insufficient penetration depth and possible tissue damage calls off UV light for an alternative approach to a photo-responsive approach for antibacterial therapy (Kuriakose et al., 2014; Lu et al., 2016; Sun et al., 2019).

Photothermal therapy (PTT) and photodynamic therapy (PDT) are the photo-responsive bacteria-killing methods that have been used in recent years. The near-infrared (NIR) range from 700 to 1000 nm (biological window) may present a controllable cause of tissue damage and an efficient therapeutic effect, depending on their mode of usage (Chang et al., 2013; Hou et al., 2015; Li et al., 2018). However, the single-modal use therapy of the former has been reported to pose a high risk of thermal damage or inflammation (Yang et al., 2017; Zhang et al., 2018; Liu et al., 2019a; Gao et al., 2019), making the PTT-based multimodal therapy with NP dosage the best alternative due to reduced irradiation time and improved antibacterial efficiency. In such instances, the enhanced ROS generation contributes to the multimodal therapy approach for bacteria eradication (Hou et al., 2012; Liu et al., 2019b; Wang et al., 2019). The synergism of the PTT and PDT also presents a great advantage and is considered a trimodal therapy.

In this study, we fabricated ZnO NPs and ZnO@Ag nanocomposite doped with different molar ratios of Ag (0.5%, 2%, 8%), using silver nitrate ($AgNO_3$) as the precursor for improving the charge transfer and ROS generation. For the first time, we report on the bacterial inhibition response. ZnO@8%Ag was later selected due to its excellent photo-responsiveness under NIR irradiation and biocompatibility. The previous research report indicates that the best photocatalytic activity of Ag in ZnO@Ag was evident when the Ag content was 8% (Nie et al., 2020). ZnO@8%Ag's excellent performance under PTT and PDT together with the biocompatibility performance was investigated. Also, the synergistic effect of ZnO@8% Ag in combination with PTT and PDT against *Staphylococcus aureus* (*S. aureus*) *in vitro* and *in vivo* was investigated. *In vitro* experiments revealed that, under NIR irradiation (808 nm), ZnO@8%Ag exhibited a tremendous bactericidal effect against *S. aureus*. The effect was similar under PDT treatment of ZnO@8%Ag. Both displayed a bacterial inhibition of over 99%, revealing the synergistic effect for rapid and improved release of Ag^+. However, the impact of each multimodal treatment of ZnO@8%Ag was the same even after the combination of both PTT and PDT in a trimodal approach. Intriguingly, the biofilm test proved ZnO@8%Ag could disrupt a junk portion of *S. aureus* biofilm even at a low concentration but revealed the complete disruption of biofilm under PTT + PDT trimodal treatment. This finding revealed that a prolonged time is required to release Ag^+ upon irradiation. *In vivo* examination confirmed that ZnO@8%Ag could effectively compromise *S. aureus* in an infected wound while accelerating the wound healing. In all, ZnO@8%Ag's outstanding biocompatibility and synergistic effect in combination with PTT and PDT for the release of Ag^+ and wound healing demonstrate an efficient and potential platform for the treatment of bacteria-infected wounds.

2 Experimental section

2.1 Materials and reagent

Zinc nitrate ($Zn(NO_3)_2$ $6H_20$) >99.0 purity, silver nitrate ($AgNO_3$) > 99% purity, sodium hydroxide (NaOH) > 99%, and

citric acid ($C_6H_8O_7$) >99.0 purity were purchased from Sigma-Aldrich. All other chemicals and reagents were purchased from Aladdin Chemical Reagent Co., Ltd. (Shanghai, China). All working solutions were used in their originally received state without further modification. Other preparations were made with deionized water.

2.2 Synthesis of ZnO and ZnO@Ag (0.5%, 2%, and 8%)

ZnO was prepared as reported by Bai et al. (2017) and Nie et al. (2020). During the synthesis process, citric acid was used as fuel. Zinc nitrate and silver nitrate served as the oxidizing reactant, and sodium hydroxide was used to adjust the pH between 12 and 13. A stoichiometric ratio of oxidizers (zinc nitrate) to the citric acid was added to a petri dish and mixed with 40 ml H_2O. The mixture was stirred for a few minutes to develop uniformity. The dish containing the mixture was introduced into a muffled furnace maintained at 400°C. The mixture was made to undergo dehydration and decomposition under the smoldering combustion reaction to give a nanocrystalline ZnO within 5–7 min. The product was further calcined at 500°C for 3 h. A similar procedure was used in the synthesis of the ZnO@Ag with the mole ratio of 1 ZnO to 0.005, 0.02, and 0.08 of Ag to give ZnO@0.5%Ag, Zno@2%Ag, and ZnO@8%Ag.

2.3 Characterization

The morphology of the samples was characterized with a Tecnai G2 F20 microscope to obtain the high-resolution transmission electron microscopy (HRTEM) images. The X-ray diffraction patterns (XRD) were determined with a D/MAX 2005 Rigaku X-ray diffractometer (Japan). The XPS was determined with a Thermo Fisher X-ray photoelectron spectrophotometer K-alpha (United States), and the UV-Vis spectroscopy was performed with a CARY 5000 spectrophotometer (Agilent Technologies, United States).

2.4 Photothermal and photodynamic properties

Detection of $^1O_2$ and the peroxidase-like activity after PTT treatment was conducted using 1,3-diphenylisobenzofuran (DPBF) and *o*-phenylenediamine (OPD) as chemical probes. The steady-state kinetic assay for PBS, ZnO, and ZnO@8%Ag with/without PTT treatment was determined after coincubation. A measure of 10 µL (100 µg/ml) of DPBF and OPD were separately added to the samples and subsequently analyzed with the UV-Vis spectrophotometer. The absorbances of DPBF and OPD were collected at 410 and 492 nm, respectively. The results were analyzed and plotted with GraphPad Prism 8.0.

2.5 Photothermal performance and photothermal conversion efficiency

A gradient concentration of the ZnO@8%Ag aqueous solution (100 µL) in a 0.5-ml Eppendorf tube was irradiated with NIR laser light (808 nm) at power densities of 0.5, 1.0, and 2.0 W/cm^2. The temperature of the solution was monitored and recorded with a thermal imager. The temperature of the PBS and ZnO were also monitored and recorded using the same approach following the irradiation of the different laser power densities used (0.5, 1.0, and 2.0 W/cm^2). The turn-off/cooling cycle for ZnO@8%Ag (100 µg/ml) using a 2.0 W/cm^2 laser was accomplished with an irradiation time of 10 min, repeated five times. The photothermal conversion efficiency of ZnO@8%Ag was determined as follows.

$$\eta = hs(T_{max} - T_0)/\left(I\left(1 - 10^{-A\lambda}\right)\right)$$

where η represents the photothermal conversion co-efficient; A is the surface area of the container; T_{max} is the maximum steady temperature, T_0 is the minimum steady temperature; I is the laser power, and A_λ is the value of absorbance of ZnO@8%Ag at 808 nm.

$$\tau_s = \sum mC_p/hA \text{ meanwhile } hA = \sum mC_p/\tau_s$$

where τ_s represents the slope of the fitting line between t and $-\ln\theta$, m is the mass of ZnO@8%Ag, and C_p is the specific heat capacity.

$$\theta = T - T_{sur}/T_{max} - T_0$$

T represents the corresponding cooling time temperature.

2.6 Cell culture and cytotoxicity

Murine fibroblast cells (L929) purchased from America Type Culture Collection (ATCC) were used to evaluate the cytotoxicity of the nanocomposite. Cells were cultured with Dulbecco modified Eagle medium (DEME) at 5% CO_2 and 37°C with 10% fetal bovine serum (FBS), penicillin (100 units m/L), and streptomycin (100 mg/ml). L929 cells at a density of 5×10^3/well were seeded into a 96-well plate and cultured for 24 h. Different concentrations of ZnO@8%Ag (0, 50, 100, and 200 µg/ml) were suspended in DEME, added to the 96-well plate, and irradiated with 2 W/cm^2 lasers for 5 min. Following 48 h of incubation, 10 µL of MTT solution (5 mg/ml) was added to the solution, and PBS was used as a control. A microplate (Varioskan LUX multimode microplate reader, Thermo Fisher Scientific Co.,

United States) was used to measure the absorbance at 570 nm after 4 h of incubation. The viability of the control cells was estimated at 100% to determine the relative viability of the other cells.

$$\text{Cell Viability}\,(\%) = \frac{A_e}{A_o} \times 100\%,$$

where A_e and A_o denote the experimental and the control groups, respectively.

2.7 *In vitro* antibacterial test

S. aureus (New man strain) was used as a model strain for the evaluation of the antibacterial properties of the nanomaterials. *S. aureus* was grown in a sterilized tryptic soy broth (TSB) and solid broth (SB). A mixture of bacteria concentration of 50 µL define by the $O.D_{600}$ = 0.05 with 50 µL of ZnO, ZnO@8%Ag, and PBS were separately added to a 96-well plate. Following 30 min of incubation at 37°C, the mixtures in the plate were irradiated with an 808 nm laser (2.0 W/cm^2) for 10 min and then incubated for 2 h. After serially diluting the mixtures with sterile LB, 100 µL of each sample was spread on an agar plate. Following 12 h incubation at 37°C, colonies formed were counted for further evaluation.

$$\text{Survival rate}\,(\%) = \frac{CFU_e}{CFU_o} \times 100\%,$$

where CFU_e and CFU_o represent the number of colonies formed in the experimental and control groups, respectively.

2.7.1 Bacteria morphology study

The morphologies of the bacteria treated with PBS and the nanomaterials (ZnO and ZnO@8%Ag) with/without PTT were examined with SEM. These varying solutions of bacteria were fixed with 2% glutaraldehyde for 4 h and subsequently dehydrated with a series of ethanol solutions (50%, 70%, 90%, 95%, and 100%), 10 min for each dehydration step. Samples were blown dried under nitrogen gas; silicon wafers were coated with ultrathin gold by sputtering, and the morphology of the bacteria was imaged at 3.0 kV with a Hitachi Su 8010 instrument, Japan.

2.7.2 *In vitro* antibacterial evaluation with confocal microscopy

Bacterial suspension treated with different materials was collected by washing with PBS and centrifugation. Aliquots (10 µL each) of calcein acetoxymethyl ester (calcein-Am, 10 µg/ml, Solarbio) and propidium iodide (PI, 10 µg/ml, Solarbio) were incubated with 20 µL of the collected bacterial suspension in room temperature for 15 min. Fluorescent images of bacteria samples were captured by confocal microscopy (Nikon A1 Confocal Laser Scanning Microscope, Japan) and analyzed with NIS—Element viewer, Nikon.

2.8 *In vitro* anti-biofilm test

S. aureus suspension in TSB was cultured for 48 h at 37°C in a 6-well plate overnight to form a static biofilm. Bacterial cultures were diluted with tryptic soy LB OD_{600} = 0.05 and incubated in a 96-well plate for 24 h at 37°C. Following incubation, the bacterial suspension was removed, and the well was rinsed three times with PBS. Aliquots (50 µL each) of PBS and the materials (ZnO, ZnO@8%Ag) were added to the wells and treated with/without PTT or PDT for 10 min. After the wells were rinsed three times with deionized water (ddH_2O), crystal violet (0.05%, 50 µL) was added to each well and incubated for 15 min. The dye was discarded and unbounded by rinsing with PBS three times. Acetic acid (33%, 200 µL) was added to each well to release the dye bound to the remaining biofilm for quantification. Quantification was performed with a Thermo Fisher Scientific Multiskan Sky microplate reader, OD_{550}. Each experiment was performed in triplicate.

2.8.1 Anti-biofilm evaluation with confocal microscopy

A coverslip was dropped at the bottom of a 24-well plate. A 20 µL aliquot of the *S. aureus* bacteria OD_{600} = 0.05 was added to the well, followed by 1000 µL of TSB, and the samples were incubated for 24 h. The coverslip was removed and rinsed with PBS three times, following treatment of the coverslip with PBS, ZnO, and ZnO@8%Ag with/without PTT/PDT. The biofilm was rinsed once again with PBS, and the coverslip was stained with 2 µM calcein-Am and 1 µM propidium for 15–20 min. Fluorescent images of bacteria were captured with a Nikon A1 confocal laser scanning microscope, and the images were analyzed with NIS—Element viewer, Nikon. Bacteria with intact and damaged membranes appeared green and red, respectively.

2.9 Hemolysis assay

A hemolysis assay was performed with the fresh blood of a healthy mouse by collecting blood from the eyeballs. The blood was centrifuged (12,000 rpm, 5 min) and rinsed with PBS (0.02 M, pH = 7.4) three times. The red blood cells (RBC) obtained were diluted to a 4:5 volume ratio with PBS, water, and varying concentration of ZnO@8%Ag (20, 25, 75, 100, 125, and 200 µg/ml). The PBS and water acted as the positive and negative controls, respectively. The mixtures were carefully suspended and incubated at 37°C for 1 h. Samples were centrifuged at 3000 rpm for 5 min. The supernatant was collected, and the absorbance was determined at OD_{595}. The

hemolysis rate was calculated according to the following equation:

$$\text{Hemolysis rate}\,(\%) == \frac{OD_e - OD_-}{OD_+ - OD_-} \times 100\%$$

where OD_e, OD_-, and OD_+ represent the OD of the treatment group, the OD of the negative control group, and the OD of the positive control group, respectively.

2.10 *In vivo* antibacterial and wound healing

All animal experiments were performed according to the guidelines and rules approved by the Animal Ethics Committee of Wenzhou Medical University (SYXK-2021-0020).

To further evaluate the practical application of ZnO@8% Ag, BALB/c mice at 7–8 weeks were divided into five groups: PBS, ZnO, ZnO + PTT, ZnO@8%Ag, and ZnO@8%Ag + PTT. Following anesthesia, a wound (4 mm in diameter) was created at the back of the mice and injected with (20 μL, 1 × 10^8 CFU m/L) of *S. aureus* to establish the mouse model. The surface of the wound was covered with PBS and the nanomaterials and further exposed to NIR irradiation for 10 min. This process was monitored and recorded with a thermal imager. Images of the nature and state of the wound were taken for 0, 2, 4, 6, and 10 days. ImageJ was used to monitor the different treatments for the groups.

2.11 Tissue toxicological analysis

A histological examination of the skin and other internal organs (lung, liver, kidneys, and heart) was conducted after 10 days. These organs were fixed with 4% paraformaldehyde; organs were sectioned and stained with hematoxylin and eosin (H&E). Samples were observed with an Olympus BX51 fluorescence imaging microscope. Fluorescence imaging was conducted with an Olympus BX51 fluorescence microscope (Olympus Co., Ltd., Japan).

2.12 Statistical analysis

Experimental data were expressed as mean ± standard deviation (SD). Statistical analysis among groups was evaluated with Student's t-test, with the difference being statistically significant when $p < 0.05$ and highly significant when $p < 0.01$. The graph plots and analysis were performed using GraphPad Prism 8.0 (Graph Pad Software, United States).

3 Result and discussion

3.1 Synthesis and characterization of nanomaterials

The nanocomposites were successfully prepared, and the TEM images showed the morphology and structures of ZnO and ZnO@8% Ag. This shows that the ZnO is characterized by a size range of 74.18–161.20 nm with an average size of 109.26 nm (Figure 1A). Similarly, Figure 1B shows that the ZnO@8%Ag has an average size of 43.33 nm with a range of 31.01–55.91 nm, exhibiting the good deposition of the Ag on the surface of ZnO without agglomeration and growing in the direction that is misaligned from the normal direction. The HRTEM of ZnO shows an interplanar spacing of 0.18 and 0.07 nm in the direction of ZnO along (110) and Ag along (220), respectively (Figures 1C,D). The crystallinity, structural phase, and purity of ZnO and ZnO@8%Ag nanocomposites were identified by the XRD patterns for ZnO indexed to a hexagonal wurtzite structure (JCPDS 36-1451), where the diffraction peaks corresponding to (100), (002), (101), (102), (110), (103) (112), (201), and (202) appeared at the 2θ with values of 31.66°, 34.45°, 36.24°, 47.60°, 56.57°, 62.74°, 67.93°, 69.12°, and 77.29° (Figure 1E). In addition, the doping of ZnO unveiled distinct peaks marked with (*) in the ZnO@8%Ag at 38.23°,44.21°, and 64.34° that corresponded to (111), (200), and (220). The presence of well-defined peaks demonstrated the absence of impurities in the nanocomposites.

The appearance of new peaks in the ZnO@8%Ag nanocomposite demonstrated that the Ag^+ with a high atomic radius had displaced the Zn^{2+}, showing the successful incorporation of Ag^+ into ZnO. XPS was employed to further evaluate the surface structure and chemical compositions of the nanocomposites. The full XPS spectrum shows the presence of Zn, O, Ag, and C elements, further demonstrating the successful synthesis of the nanocomposite without impurities (Figure 1F). The XPS spectrum of Zn 2p reveals binding energy peak positions of Zn2p with 1021.05 and 1044.12 eV in ZnO and 1021.13 and 1044.12 eV in ZnO@8%Ag. These peaks resemble each other, further confirming Zn in the nanocomposites (Figure 1G). This phenomenon was evident in element O, and the presence of element C could be attributed to the XPS instrument (Figure 1H). All of these match findings of other earlier reports (Fageria et al., 2014; Jaramillo-Páez et al., 2017). Similarly, the binding energy peak positions of 368.01 eV ($3d_{5/2}$) and 373.05 eV ($3d_{3/2}$) were in tandem with what had been reported earlier as the binding energies of Ag (Figure 1I) (Pande et al., 2007; Ahmad et al., 2011).

Elemental mapping confirmed the presence of Zn and O in the ZnO nanocomposite and ZnO and Ag in the ZnO@8%Ag nanocomposites (Supplementary Figures S1A,B). This demonstrated the perfect distribution of the Ag in the different regions. Supplementary Figure S1C displays the UV-Vis absorption spectra of the nanocomposites. The peaks corresponding to ZnO absorption demonstrated a strong

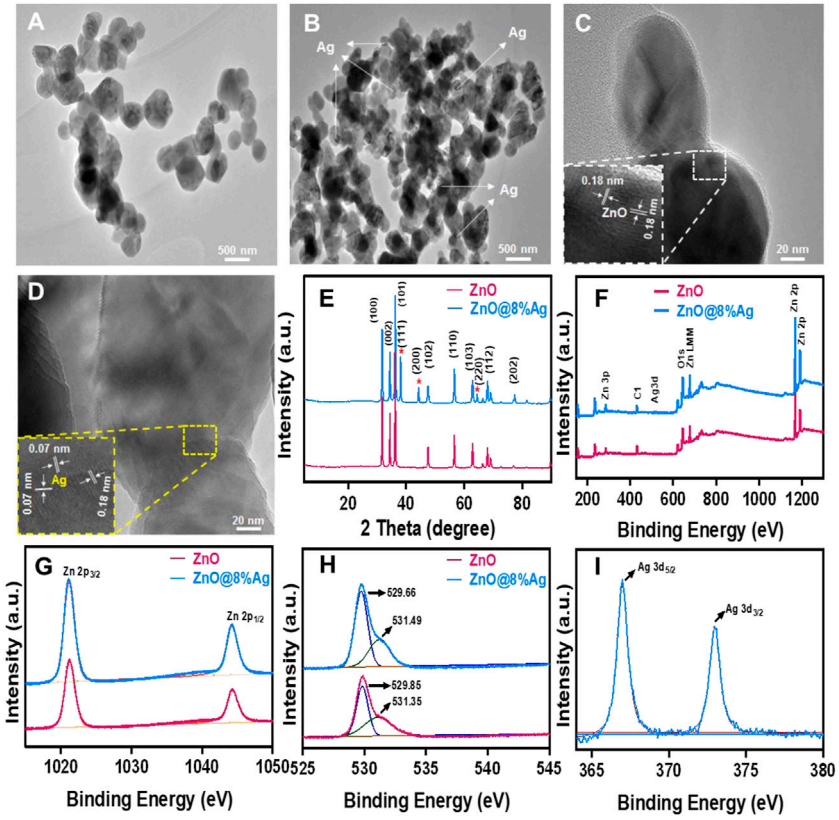

FIGURE 1
Characterization of ZnO and ZnO@8%Ag. **(A,B)** TEM images, **(C,D)** HRTEM images, **(E)** X-ray diffraction (XRD) patterns, **(F)** full XPS survey spectrum of ZnO and ZnO@8%Ag, **(G)** XPS spectra of Zn 2p region, **(H)** O1s region, **(I)** Ag 3d region.

absorption in the UV region for the ZnO@8%Ag, with the Fermi level being established due to the transfer of free radicals from Ag to ZnO. This result further demonstrates how ZnO@8%Ag can be active in both the UV and the visible light region.

3.2 Photothermal and photodynamic performance

The photothermal effect was explored under 808 nm laser irradiation with power densities of 0.5, 1, and 2 W/cm^2 for 5 min, as shown in (Figures 2A–C). Temperature higher than 50°C but lower than 60°C can destroy proteins and enzymes as well as crucial intracellular reactions (Wu et al., 2013; Pan et al., 2016; Liu et al., 2018). Upon irradiation at 808 nm, 2 W/cm^2 for 5 min, the temperature of the solutions was elevated as follows: PBS (17–34°C), ZnO (17–32°C), ZnO@0.5%Ag (17–40°C), ZnO@2% Ag (17–44°C), and ZnO@8%Ag (17–50.5°C) at a concentration 100 μg/ml (Figure 2C). The rapid temperature elevation in ZnO@8%Ag reveals the superior photothermal property and safety that it will render to normal cells. The cooling circles (Figure 2D) and also the photothermal conversion efficiency exhibited no significant attenuation of the temperature, which reveals high photothermal stability (Figures 2E,F). In contrast, PBS, ZnO, and ZnO@2%Ag reached maximum temperatures of less than 50°C under the same conditions. Therefore, the superior photothermal performance exhibited by ZnO@8%Ag makes it promising for eradicating bacteria cells. Based on the different laser power, the enhanced temperature for an equal concentration of ZnO@8%Ag proved that the temperature rise also depended on the kind of laser power employed.

Finally, we investigated the photodynamic property through the NIR-triggered ROS generation with DBPF and OPD. Upon exposure to single NIR (808 nm, 2 W/cm^2) irradiation, DPBF absorption for ZnO@8%Ag gradually decreases due to the presence of $^1O_2$ (Figure 2H), as the absorbance of the OPD increases due to the peroxidase-like activity (Figure 2I). This indicated that the Ag incorporation in ZnO increased the ROS generation of the nanocomposite. Ag in the nanocomposite acted as an efficient sink with photogenerated electrons flowing from the ZnO to Ag to prevent recombination with holes (Figure 3). Surface modification of oxides of a semiconductor influences

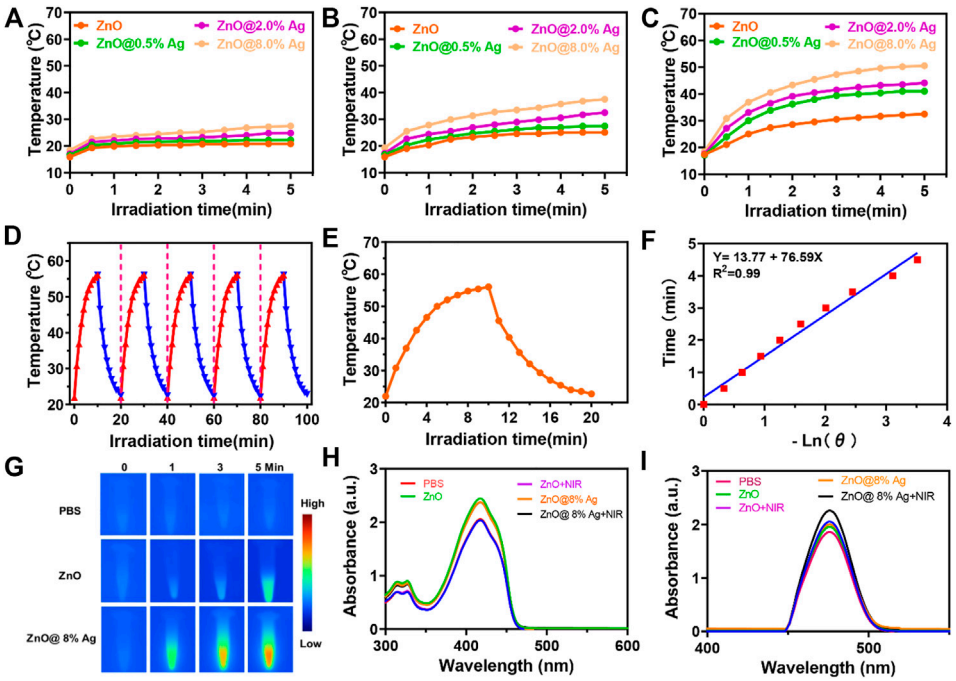

FIGURE 2
Activatable NIR photothermal and photodynamic properties of ZnO@8%Ag. **(A)** Temperature elevation curves of ZnO and ZnOAg with varying ratios of Ag (0.2%, 0.5%, and 8%) under NIR irradiation (808 nm, 0.5 W/cm^2, 5 min), **(B)** photothermal evolution curves of ZnO and ZnO@Ag with varying ratios of Ag (0.2%, 0.5%, and 8%) under NIR irradiation (808 nm, 1 W/cm^2, 5 min), **(C)** temperature variations of ZnO and ZnO@Ag with varying ratios of Ag (0.2%, 0.5%, and 8%) under NIR irradiation (808 nm, 2 W/cm^2, 5 min), **(D)** recycling heating profiles of ZnO@8%Ag under irradiation for five on/off cycles, **(E)** heating and cooling of ZnO@8%Ag under NIR irradiation (808 nm, 2 W/cm^2, 5 min), **(F)** linear correlation of the cooling time of ZnO@8%Ag, **(G)** thermal images of PBS, ZnO, and ZnO@8%Ag under NIR irradiation (808 nm, 2 W/cm^2, 5 min),**(H)** UV spectra following the absorption of DPBF in PBS, ZnO, and ZnO@8%Ag with/without NIR irradiation (808 nm, 2 W/cm^2, 5 min), and **(I)** spectra of changes for the absorption of OPD in PBS, ZnO, and ZnO@8%Ag with/without NIR irradiation (808 nm, 2 W/cm^2, 5 min).

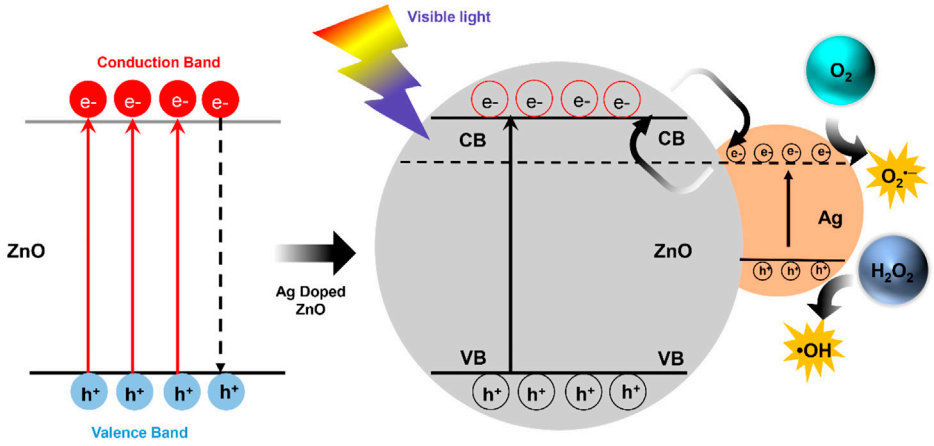

FIGURE 3
Schematic representation of the movement of electrons in ZnO@Ag under visible light.

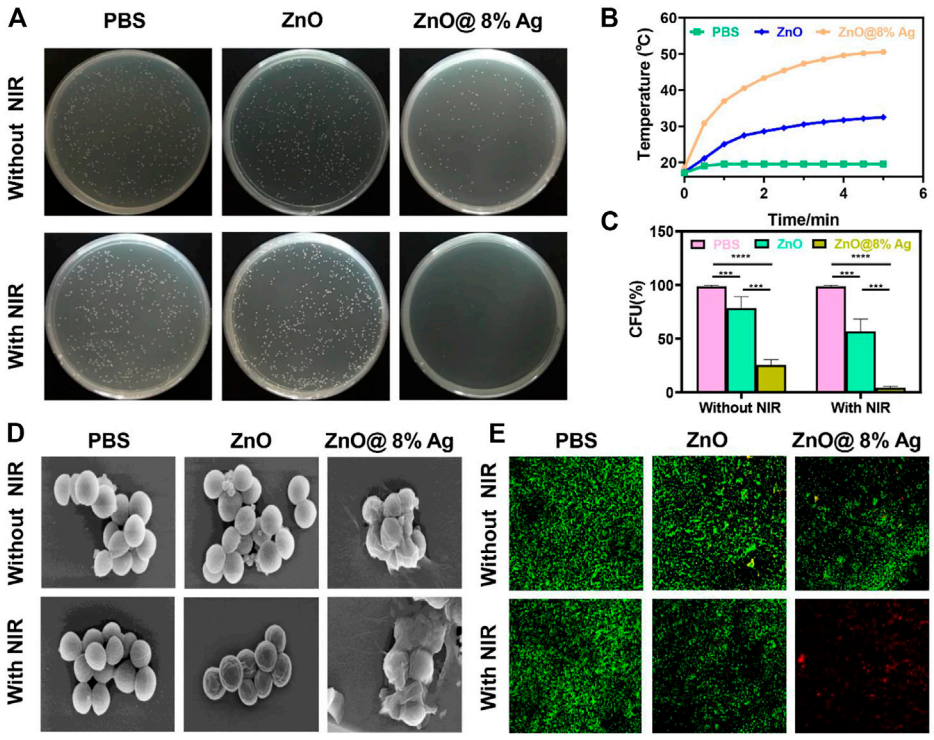

FIGURE 4
In vitro antibacterial activity of ZnO@8%Ag. **(A)** Bactericidal effect of PBS, ZnO, and ZnO@8%Ag against *S. aureus* with/without NIR irradiation (808 nm, 2 W/cm^2, 10 min), **(B)** temperature elevation curve corresponding to **(A)**, **(C)** survival rate of *S. aureus* corresponding to **(B)** $^{**}p < 0.01$, **(D)** SEM images of *S. aureus* treated with PBS, ZnO, and ZnO@8%Ag under NIR irradiation (808 nm, 2 W/cm^2, 10 min), and **(E)** live/dead staining assay of *S. aureus* corresponding to **(D)**.

photocatalysis, creating an electron-hole pair within the bandgap as holes are generated in the valence band and electrons in the conduction band (Hu et al., 2010; Adarakatti and Malingappa, 2016; Nagaraju et al., 2017). Photon energy that is equal to or greater than the bandgap is absorbed as an electron is promoted from the valence band to the conduction band and creating an equivalent number of holes in the valence band. However, the difference in the energy level of the conduction band of ZnO and the Fermi level of Ag presents the Ag as an efficient sink with the photogenerated electrons flowing from the ZnO to Ag to prevent recombination with the holes (Figure 3) (Nagaraju et al., 2017). These photogenerated electrons and holes can react with O_2 and H_2O_2 molecules to form superoxide anion and hydroxyl radicals, respectively (Arsana et al., 2012; Kuriakose et al., 2014). This process is an indication of the role played by Ag^+ in the enhanced generation of ROS.

3.3 *In vitro* antibacterial activity assay

As shown in Figures 2C–I, ZnO@8%Ag exhibited excellent PTT and PDT ability. An Ag-based nanocomposite demonstrated effective antibacterial capacity compared to some antibiotics (Singh et al., 2017; Francis et al., 2018; Hu et al., 2018). Ag release can also be dependent on temperature, causing the photogenerated free radicals to penetrate cell walls to induce cell death. The material is also reported to rapidly and strongly bind to the thiol groups in enzymes and proteins located on the surface of bacteria, subsequently inducing cell death (Liu and Hurt, 2010; Shao et al., 2015). However, a higher amount of Ag can result in resistance, cytotoxicity, and aggregation of the Ag, which can further result in the instability of the nanomaterial and its ability to effectively deal with bacteria (Wiesenthal et al., 2011; Zhang et al., 2014; El Yamani et al., 2017). Nie et al. (2020) indicated that the best photocatalytic activity of Ag in ZnOAg nanocomposite was evident when the Ag content was 8%. ZnO@8%Ag (100 μg/ml) was, therefore, chosen for further future studies considering the cytotoxicity, photothermal, photodynamic, and bactericidal effects (Supplementary Figures S2, S3). Due to the aforementioned results, we evaluated the *in vitro* antibacterial effect of ZnO and ZnO@8%Ag with/without single NIR (808 nm, 2 W/cm^2) for 10 min (Figure 4A) against *S. aureus* using the colony-forming count approach. After different treatments and cultures there was no significant reduction in the

number of bacteria in the PBS, ZnO, Figure 4A. They exhibited negligible antibacterial activity with a bacterial viability rate of about 90%, although ZnO@8%Ag showed some bactericidal effect from the release of Ag^+. Upon NIR irradiation, the colony count decreased but with a significant reduction in the ZnO@8%Ag + PTT group (Figure 4C). Results were the same for groups with/without PDT (Supplementary Figures S4A–C). These findings revealed that the release of Ag^+ and its subsequent enhancement by the NIR irradiation proved a synergistic therapeutic effect efficient against *S. aureus*, making neither PTT nor the Ag^+ solely responsible for killing the bacteria completely. Intriguingly, in the ZnO + PTT group, the survival rate of bacteria was substantial, indicating the negligible impact of the heat stability exhibited by ZnO, confirmed in (Figure 4B). ZnO@8%Ag exposure to a combination of PTT and PDT for 5 and 10 min against *S. aureus* (Supplementary Figures S5A,B) exhibited similar results as those observed in Supplementary Figures S3, S4A during a multimodal treatment with either PTT or PDT. To further explore the *in vitro* antibacterial effect mentioned earlier, the SEM observation and live/dead staining assay were employed. Like the control group (PBS treatment), the morphology of bacteria treated with ZnO and ZnO + PTT retained a smooth structure and remained intact. However, after treatment with ZnO@8%Ag and ZnO@8%Ag + PTT, some shrinks and wrinkles appeared on the surface of *S. aureus* (Figure 4D). The results from the live/dead staining assay confirmed these observations. Bacteria with intact membranes were stained with green fluorescence by calcein-Am, while those with damaged membranes were stained with red fluorescence by PI (Figure 4E). The intense green, evident in the PBS, ZnO, and ZnO + NIR, demonstrated that PTT alone was not sufficient to impact bacterial viability. Small red fluorescence indicated weak antibacterial activity, and strong red fluorescence in ZnO@8%Ag + PTT group indicated that the integrity of the bacteria cell membrane was greatly compromised and appeared damaged and shrunken as a result of ROS induced by the Ag^+ released from PTT treatment. Mei et al. and others have reported that NIR promoted the effective release of Ag^+ in killing bacteria (Tsuchido et al., 1985; Gao et al., 2018; Mei et al., 2020). Thus, the effectiveness is demonstrated by the synergistic role of Ag^+ and PTT or PDT.

3.4 Biofilm inhibition test

Aggregation of sessile microbial particles and the subsequent formation of the extracellular matrix comprising a protein and polysaccharides grant microorganisms the ability to persist and survive in adverse environments (Donlan and Costerton, 2002; Vadyvaloo and Martínez, 2014; Fonseca et al., 2019). This condition makes them drug-resistant and gives them the capability to induce chronic bacterial infections. The anti-biofilm capability will validate the recognition of antibacterial materials as promising clinical translations. To study the biofilm capability, the conventional crystal violet method was employed and further confirmed with a live/dead staining assay. As shown in Figure 5A, biofilms in ZnO, ZnO + PDT group were densely distributed compared with ZnO@8%Ag and ZnO@8%Ag + PDT group. About 20 % biofilm in the ZnO@8%Ag group which was obviously due to Ag^+ release and about 50 % in ZnO@8%Ag + PDT group which may be due to the ability of Ag^+ under-PDT of which ZnO lacks that ability. This demonstrated the antibacterial efficacy exhibited through the release of Ag^+. Under the biofilm treatment, in most cases, the NPs themselves are incapable of entirely eradicating the biofilm matrix and require an alternative mechanical process to deal with the biofilm matrix (Jiang et al., 2013; Fonseca et al., 2019). Compared with the ZnO + PTT group, the ZnO@8%Ag + PTT group exhibited a significantly lower biofilm rate due to the excellent photothermal ability of ZnO@8%Ag (Figure 5B). Surprisingly, all biofilms were completely eradicated in the ZnO@8%Ag + PTT + PDT group, but some significant amount of biofilm remained in the ZnO + PTT + PDT group, which indicated the effectual disruption of biofilm by the ZnO@8%Ag + PTT + PDT, a trimodal synergism. The live/dead staining assay further confirmed the antibiofilm capability of the ZnO@8%Ag + PTT + PDT (Figure 5C). Biofilm in this group was completely disrupted. In contrast, the ZnO@8%Ag + PTT group exhibited a good antibacterial effect from the PTT treatment with potential biofilm inhibition application, as the effect in the remaining groups can be considered negligible. The antibiofilm capability was performed with the same concentration used in the antibacterial test (100 μg/ml). This demonstrated that even at the low concentration, ZnO@8%Ag + PTT could effectively eradicate a significant portion of bacteria. However, the molecular mechanism of the antibiofilm activity of the ZnO@8%Ag + PTT + PDT group remains to be studied.

3.5 *In vitro* cytotoxicity test and hemolysis

Biocompatibility is a crucial concern for nanoparticles and a prerequisite for *in vivo* applications. Hence, biocompatibility was evaluated using the cytotoxicity test and hemolysis. L929 cells were co-cultured with varying concentrations of ZnO@8%Ag with/without PTT/PDT treatment for 5 min (25, 50, 75, 100, and 200 μg/ml) for 24 h. The cellular compatibility of ZnO@8%Ag was determined using an MTT assay. The viability of cells was over 70% even at the highest concentration of ZnO@8%Ag when exposed to PTT/PDT, indicating that ZnO@8%Ag or

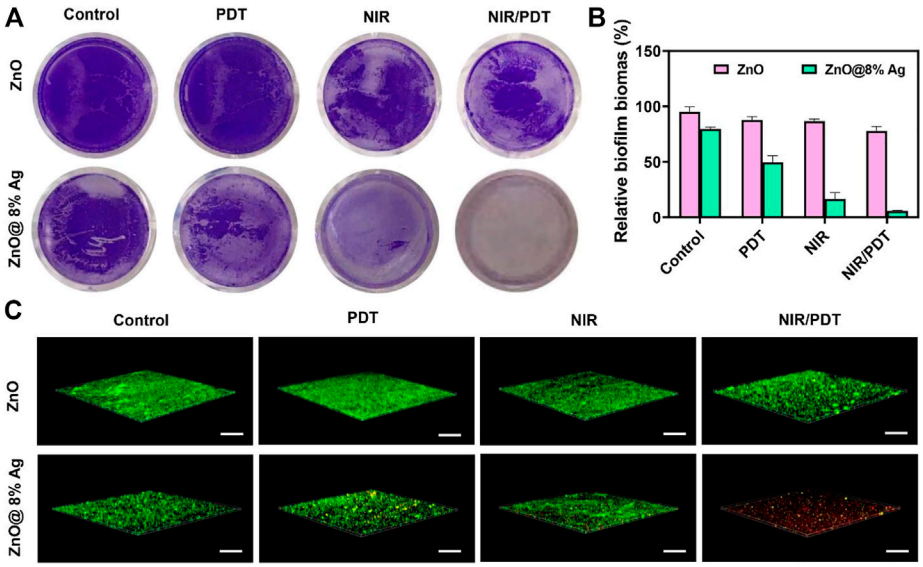

FIGURE 5
Inhibition of *S. aureus* biofilm. **(A)** Representative images of biofilm treated with ZnO, ZnO@8%Ag, ZnO + PDT, ZnO@8%Ag + PDT, ZnO + PTT, ZnO@8%Ag + PTT, ZnO + PTT + PDT, and ZnO@8%Ag + PTT + PDT, **(B)** quantitative analysis corresponding to **(A)** $^{**}p < 0.01$, and **(C)** live/dead staining assay of *S. aureus* in biofilms corresponding to **(A)**.

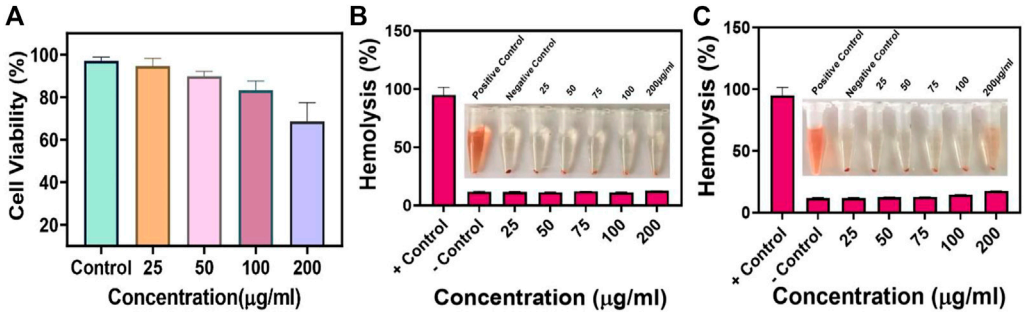

FIGURE 6
Biocompatibility of ZnO@8%Ag. **(A)** Cytotoxicity of ZnO@8%Ag under PTT/PDT in L929 cells, hemolysis rate of ZnO@8%Ag under PTT/PDT, inserted image of blood treated with varying concentrations of ZnO@8%Ag (25, 50, 75, 100, and 200 μg/ml) aqueous solutions ddH_2O (positive control) and PBS (negative control), **(B)** after 30 min, **(C)** after 1 h.

ZnO@8%Ag + PTT + PDT irradiation did not induce toxicity in healthy tissues. This result is shown in Figure 6A. Similarly, hemolytic evaluation of mouse erythrocytes confirmed that the ddH_2O (positive control) group caused the release of erythrocytes from the hemoglobin, showing the induction of hemolysis. In contrast, after 30 min, ZnO@8% Ag induced negligible hemolysis with no significant difference compared to the PBS (positive control) group, even after increasing the concentration (Figure 6B). Intriguingly, ZnO@8%Ag did not induce any significant damage to the erythrocyte even after 1 h (Figure 6C), demonstrating the biosafety of ZnO@8%Ag in blood circulation and indicating good biocompatibility.

3.6 *In vivo* antibacterial activity and biosafety evaluation

Inspired by the *in vitro* antibacterial and biocompatibility results of ZnO@8%Ag, we further studied the *in vivo*

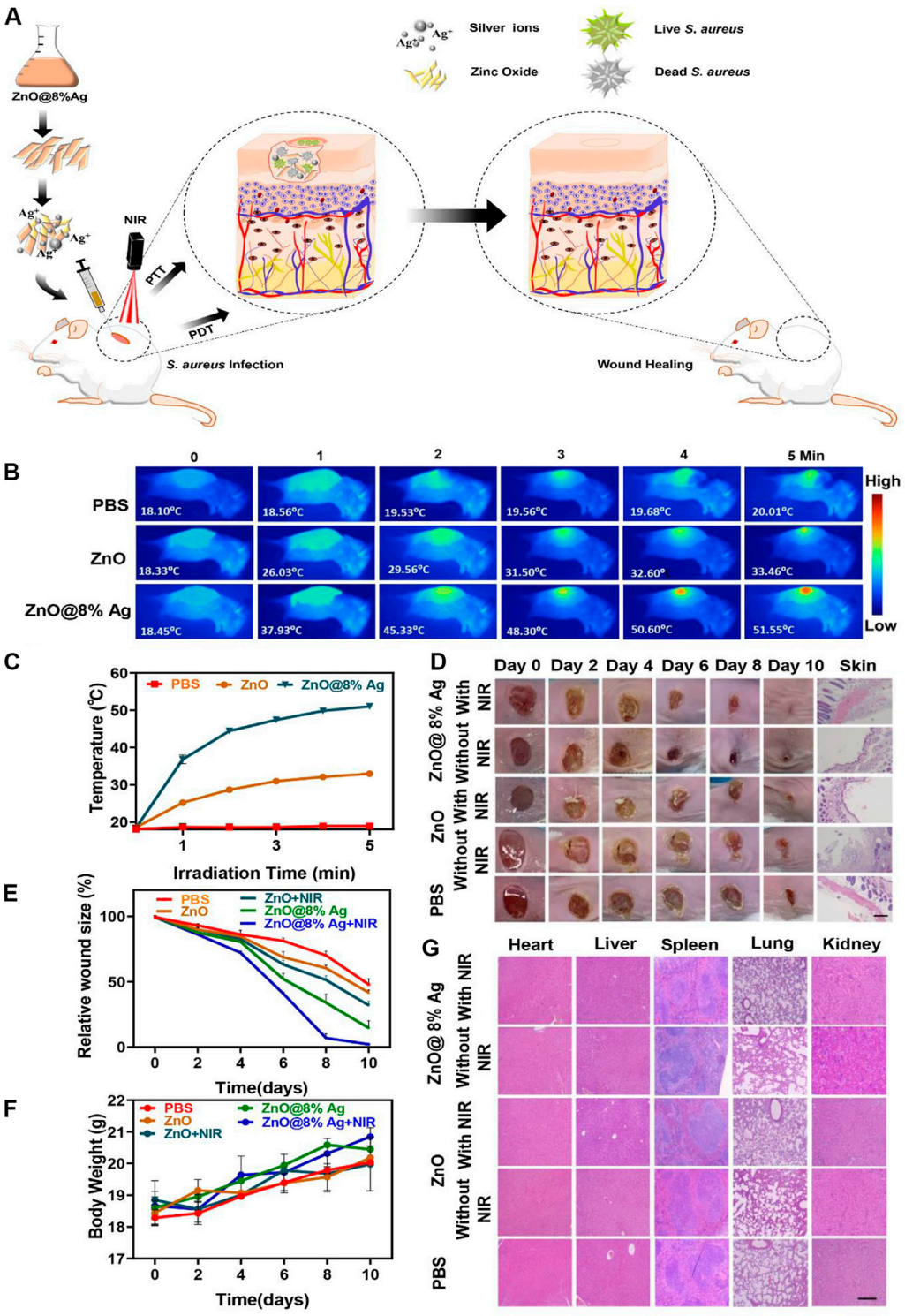

FIGURE 7
In vivo antibacterial activity of ZnO@8%Ag. **(A)** Schematic illustration of the fabricated ZnO@8%Ag and the corresponding antibacterial effect *in vivo* under PTT and PDT, **(B)** thermal images of PBS, ZnO, and ZnO@8%Ag under NIR irradiation (808 nm, 2 W/cm^2, 5 min), **(C)** temperature variation curve corresponding to **(B)**, **(D)**representative images of *S. aureus* infected wound after treatment, **(E)** quantitative curve of the wound size over time for the treatment groups, **(F)** bodyweight variation curve for the different treatment groups over time, and **(G)** tissue slices of major organs (the heart, liver, spleen, lung and kidney) stained with H&E, after treatment, scale bar 100 μm.

bactericidal activity by developing an *S. aureus* infection model in BALB/c mice and evaluated the effect of ZnO@8%Ag on wound healing under NIR irradiation. The PBS and nanocomposites (ZnO, ZnO@8%Ag) were applied to the dorsal excisional (4 mm) wound inoculated with *S. aureus* (1×10^8 CFU m/L, 20 μL) (Figure 7A). After 5 min of irradiation, the temperature of the wound region of the mice rose from 18°C to 52°C, without a rise in the temperature of the normal skin, compared to the PBS and ZnO groups (Figures 7B,C), demonstrating the potential of ZnO@8%Ag as a photothermal therapeutic agent. The wound healing process was monitored with digital camera, and the weight of mice within each group was recorded with a Sartorius balance. Images of the wound were taken at separate time intervals of 0, 2, 4, 6, and 10 days. As shown in Figure 7D, on day 2, all treatment groups showed scars except for the PBS group. The scar rate of the ZnO@8%Ag and ZnO@8%Ag + PTT groups was observed to be better than the other groups. On day 10, the scar in the ZnO@8%Ag + PTT group was absent, and the wound was obviously healed, demonstrating the excellent bactericidal effect of Ag from ZnO@8%Ag under NIR irradiation that enables it to facilitate wound healing by preventing wound infection (Figure 7E). In contrast, the scar remained visible in other groups with decreasing wound area in the following order: ZnO@8%Ag, ZnO + PTT, ZnO, and PBS, indicating a low bactericidal effect. Also, the weight of mice increased rapidly after day 2 of *S. aureus* infection in the ZnO@8%Ag + PTT group (Figure 7F). This may be due to the effect of the wound infection on the mice's physiological activity and the subsequent normalization of the physiological activity by ZnO@8%Ag + PTT. However, in the control group (PBS treatment), the weight of the mice increased very slowly with time, indicating the disruption of the physiological activity, which may have led to the loss of appetite in those groups. The key organs (the heart, liver, spleen, lung, kidney and skin) sections were examined using H & E staining to evaluate the inflammatory and tissue repair response of the treatment groups under PTT treatment (Figure 7G). The results showed the number of inflammatory cells and serious infections in the control groups (PBS treatment), ZnO, and ZnO + PTT groups. The image exhibited disorganized tissue granulation with loose and irregular epithelial cells. Also, ZnO@8%Ag induced tissue regeneration, emphasizing the wound-healing ability of Ag. Remarkably, the wound treated with ZnO@8% Ag exhibited negligible inflammation, with the epithelial layer and the dermis appearing to be well organized on day 10. This phenomenon was observed in the multimodal treatment with PDT (Supplementary Figures S6A–D). This demonstrated that ZnO@8%Ag under PTT or PDT poses no long-term histological toxicity, and the material's excellent bactericidal effect under PTT or PDT further accelerates wound healing.

4 Conclusion

In summary, we have successfully designed a nanocomposite (ZnO@8%Ag) with good biocompatibility and an efficient antimicrobial, antibiofilm and wound-healing effect that can combine solely with either PTT or PDT. The nanocomposite combinational use of NIR raises the temperature and unleashes ROS induction from the Ag^+. In contrast, the trimodal treatment (ZnO@8%Ag + PTT + PDT) against *S. aureus* demonstrated a similar effect when employed multimodally, either as ZnO@8% Ag + PTT or as ZnO@8%Ag + PDT, although the PTT effect appears to be more pronounced. However, ZnO@8%Ag + PDT + PTT showed a remarkable and complete disruption of biofilm. Wound healing results further confirm the effective ability of the ZnO@8%Ag to induce negligible inflammation with accelerated tissue regeneration and wound healing under PTT or PDT. Cytotoxicity results demonstrated the biocompatibility of ZnO@8%Ag without any adverse histological toxicity to mammalian cells, even under NIR irradiation and PDT treatment. Therefore, ZnO@8%Ag under PTT/PDT presents a promising application in antibacterial biofilm and wound healing therapies.

Data availability statement

The original contributions presented in the study are included in the article and Supplementary Material. Further inquiries can be directed to the corresponding authors.

Ethics statement

The animal study was reviewed and approved by the Animal Ethics Committee of Wenzhou Medical University (SYXK-2021-0020).

Author contributions

EO: conceptualization, methodology, and writing—original draft. JF: conceptualization, methodology, writing–original draft, and resources. DW: conceptualization and methodology. DZ: methodology and investigation. JS and BX: resources, writing—review and editing, validation, and supervision.

Funding

This work was financially supported by the National Natural Science Foundation of China (21977081), the Zhejiang Provincial Natural Science of Foundation of China

(LZ19H180001), Wenzhou Medical University (KYYW201901), the University of Chinese Academy of Sciences (WIBEZD2017001-03), the Zhejiang Qianjiang Talent Plan (QJD20020224), and the Wenzhou Science and Technology Plan Project (ZG2021035).

Conflict of interest

The authors declare that the research was conducted in the absence of any commercial or financial relationships that could be construed as a potential conflict of interest.

The reviewer HC declared a past co-authorship with the author JS to the handling editor.

Publisher's note

Supplementary material

The supplementary material for this article can be found online at: https://www.frontiersin.org/articles/10.3389/fchem.2022.1054739/full#supplementary-material

References

Adarakatti, P. S., and Malingappa, P. (2016). Amino-calixarene-modified graphitic carbon as a novel electrochemical interface for simultaneous measurement of lead and cadmium ions at picomolar level. *J. Solid State Electrochem.* 20, 3349–3358. doi:10.1007/s10008-016-3306-4

Ahmad, M., Yingying, S., Nisar, A., Sun, H., Shen, W., Wei, M., et al. (2011). Synthesis of hierarchical flower-like ZnO nanostructures and their functionalization by Au nanoparticles for improved photocatalytic and high performance Li-ion battery anodes. *J. Mat. Chem.* 21, 7723–7729. doi:10.1039/c1jm10720h

Ali, G., Abd El-Moez, S. I., and Abdel-Fattah, W. I. (2019). Synthesis and characterization of nontoxic silver nano-particles with preferential bactericidal activity. *Biointerface Res. Appl. Chem.* 9, 4617–4623. doi:10.33263/BRIAC00.00000

Arsana, P., Bubpa, C., and Sang-aroon, W. (2012). Photocatalytic activity under solar irradiation of silver and copper doped zincoxide: Photodeposition versus liquid impregnation methods. *J. Appl. Sci.* 12, 1809–1816. doi:10.3923/jas.2012.1809.1816

Bai, D. S., Ramesh Kumar, V., and Survana, R. P. (2017). Synthesis and characterization of zinc oxide nanoparticles by solution combustion method: DC conductivity studies. *Indian J. Adv. Chem. Sci.* 5, 137–141. doi:10.22607/IJACS.2017.503004

Boucher, H. W., Talbot, G., Bradley, J., Edwards, J., Gilbert, D., Rice, L., et al. (2009). Bad bugs, no drugs: No ESKAPE! An update from the infectious diseases society of America. *Clin. Infect. Dis.* 48, 1–12. doi:10.1086/595011

Chaloupka, K., Malam, Y., and Seifalian, A. M. (2010). Nanosilver as a new generation of nanoproduct in biomedical applications. *Trends Biotechnol.* 28, 580–588. doi:10.1016/j.tibtech.2010.07.006

Chang, J., Ning, Y., Wu, S., Niu, W., and Zhang, S. (2013). Effectively utilizing NIR light using direct electron injection from up-conversion nanoparticles to the TiO2 photoanode in dye-sensitized solar cells. *Adv. Funct. Mat.* 23, 5910–5915. doi:10.1002/adfm.201301158

Chernousova, S., and Epple, M. (2013). Silver as antibacterial agent: Ion, nanoparticle, and metal. *Angew. Chem. Int. Ed.* 52, 1636–1653. doi:10.1002/anie.201205923

Courtney, C. M., Goodman, S. M., McDaniel, J. A., Madinger, N. E., Chatterjee, A., and Nagpal, P. (2016). Photoexcited quantum dots for killing multidrug-resistant bacteria. *Nat. Mat.* 15, 529–534. doi:10.1038/nmat4542

Darouiche, R. O. (2004). Treatment of infections associated with surgical implants. *N. Engl. J. Med.* 350, 1422–1429. doi:10.1056/nejmra035415

Donlan, R. M., and Costerton, J. W. (2002). Biofilms: Survival mechanisms of clinically relevant microorganisms. *Clin. Microbiol. Rev.* 15, 167–193. doi:10.1128/cmr.15.2.167-193.2002

Duncan, B., Li, X., Landis, R. F., Kim, S. T., Gupta, A., Wang, L. S., et al. (2015). Nanoparticle-stabilized capsules for the treatment of bacterial biofilms. *ACS Nano* 9, 7775–7782. doi:10.1021/acsnano.5b01696

El Yamani, N., Collins, A. R., Runden-Pran, E., Fjellsbo, L. M., Shaposhnikov, S., Zielonddiny, S., et al. (2017). *In vitro* genotoxicity testing of four reference metal nanomaterials, titanium dioxide, zinc oxide, cerium oxide and silver: Towards reliable hazard assessment. *Mutagenesis* 32, 117–126. doi:10.1093/mutage/gew060

Fageria, P., Gangopadhyay, S., and Pande, S. (2014). Synthesis of ZnO/Au and ZnO/Ag nanoparticles and their photocatalytic application using UV and visible light. *RSC Adv.* 4, 24962–24972. doi:10.1039/c4ra03158j

Fonseca, B. B., Silva, P. L. A. P. A., Silva, A. C. A., Dantas, N. O., de Paula, A. T., Olivieri, O. C. L., et al. (2019). Nanocomposite of Ag-Doped ZnO and AgO nanocrystals as a preventive measure to control biofilm formation in eggshell and salmonella spp. Entry into eggs. *Front. Microbiol.* 10, 217. doi:10.3389/fmicb.2019.00217

Francis, S., Joseph, S., Koshy, E. P., and Mathew, B. (2018). Microwave assisted green synthesis of silver nanoparticles using leaf extract of elephantopus scaber and its environmental and biological applications. *Artif. Cells Nanomed. Biotechnol.* 46, 795–804. doi:10.1080/21691401.2017.1345921

Gao, D., Ji, X., Wang, J. L., Wang, Y. T., Li, D. L., Liu, Y. B., et al. (2018). Engineering a protein-based nanoplatform as an antibacterial agent for light activated dual-modal photothermal and photodynamic therapy of infection in both the NIR I and II windows. *J. Mat. Chem. B* 6, 732–739. doi:10.1039/c7tb02990j

Gao, G., Jiang, Y. W., Jia, H. R., and Wu, F. G. (2019). Near-infrared light-controllable on-demand antibiotics release using thermo-sensitive hydrogel-based drug reservoir for combating bacterial infection. *Biomaterials* 188, 83–95. doi:10.1016/j.biomaterials.2018.09.045

Grumezescu, A. M., Gestal, M., Holban, A., Grumezescu, V., Vasile, B., Mogoanta, L., et al. (2014). Biocompatible Fe_3O_4 increases the efficacy of amoxicillin delivery against Gram-positive and Gram-negative bacteria. *Molecules* 19, 5013–5027. doi:10.3390/molecules19045013

Hassan, M., Kjos, M., Nes, I., Diep, D., and Lotfipour, F. (2012). Natural antimicrobial peptides from bacteria: Characteristics and potential applications to fight against antibiotic resistance. *J. Appl. Microbiol.* 113, 723–736. doi:10.1111/j.1365-2672.2012.05338.x

Hou, Y., Li, X., Zhao, Q., Chen, G., and Raston, C. L. (2012). Role of hydroxyl radicals and mechanism of *Escherichia coli* inactivation on Ag/AgBr/TiO_2 nanotube array electrode under visible light irradiation. *Environ. Sci. Technol.* 46, 4042–4050. doi:10.1021/es204079d

Hou, Z., Zhang, Y., Deng, K., Chen, Y., Li, X., Deng, X., et al. (2015). UV-Emitting upconversion-based TiO2 photosensitizing nanoplatform: Near-infrared light mediated *in vivo* photodynamic therapy via mitochondria-involved apoptosis pathway. *ACS Nano* 9, 2584–2599. doi:10.1021/nn506107c

Hu, M., Li, X., Zhou, M., Sun, J., Sheng, F., Shi, S., et al. (2018). Zinc oxide/silver bimetallic nanoencapsulated in PVP/PCL nanofibres for improved antibacterial activity. *Artif. Cells Nanomed. Biotechnol.* 46, 1248–1257. doi:10.1080/21691401.2017.1366339

Hu, X., Li, G., and Yu, J. C. (2010). Design, fabrication, and modification of nanostructured semiconductor materials for environmental and energy applications. *Langmuir* 26, 3031–3039. doi:10.1021/la902142b

Huang, M. H., Mao, S., Feick, H., Yan, H., Wu, Y., Kind, H., et al. (2001). Room-temperature ultraviolet nanowire nanolasers. *Science* 292 (5523), 1897–1899. doi:10.1126/science.1060367

Jaramillo-Páez, C., Navio, J., Hidalgo, M., and Macias, M. (2017). High UV-photocatalytic activity of ZnO and Ag/ZnO synthesized by a facile method. *Catal. Today* 284, 121–128. doi:10.1016/j.cattod.2016.11.021

Jia, X., Ahmad, I., Yang, R., and Wang, C. (2017). Versatile graphene-based photothermal nanocomposites for effectively capturing and killing bacteria, and for destroying bacterial biofilms. *J. Mat. Chem. B* 5, 2459–2467. doi:10.1039/c6tb03084j

Jiang, L.-Y., Zhang, Y. Y., Li, Z., and Liu, J. Z. (2013). Metabolic engineering of Corynebacterium glutamicum for increasing the production of L-ornithine by increasing NADPH availability. *J. Ind. Microbiol. Biotechnol.* 40, 1143–1151. doi:10.1007/s10295-013-1306-2

Kirsner, R. S., Orsted, H. L., and Wright, J. P. (2001). The role of silver in wound healing part 3 matrix metalloproteinases in normal and impaired wound healing: A potential role of nanocrystalline silver. *Wounds* 13, X–12. doi:10.1201/b14164

Kudo, A., and Miseki, Y. (2009). Heterogeneous photocatalyst materials for water splitting. *Chem. Soc. Rev.* 38, 253–278. doi:10.1039/b800489g

Kuriakose, S., Choudhary, V., Satpati, B., and Mohapatra, S. (2014). Enhanced photocatalytic activity of Ag-ZnO hybrid plasmonic nanostructures prepared by a facile wet chemical method. *Beilstein J. Nanotechnol.* 5, 639–650. doi:10.3762/bjnano.5.75

Li, Y., Liu, X., Tan, L., Cui, Z., Yang, X., Zheng, Y., et al. (2018). Rapid sterilization and accelerated wound healing using Zn^{2+} and graphene oxide modified g-C3N4 under dual light irradiation. *Adv. Funct. Mat.* 28, 1800299. doi:10.1002/adfm.201800299

Liu, J., and Hurt, R. H. (2010). Ion release kinetics and particle persistence in aqueous nano-silver colloids. *Environ. Sci. Technol.* 44, 2169–2175. doi:10.1021/es9035557

Liu, M., He, D., Yang, T., Liu, W., Mao, L., Zhu, Y., et al. (2018). An efficient antimicrobial depot for infectious site-targeted chemo-photothermal therapy. *J. Nanobiotechnology* 16, 23. doi:10.1186/s12951-018-0348-z

Liu, Y., Busscher, H. J., Zhao, B., Zhang, Z., Ren, Y., van der Mei, H. C., et al. (2016). Surface-adaptive, antimicrobially loaded, micellar nanocarriers with enhanced penetration and killing efficiency in staphylococcal biofilms. *ACS Nano* 10, 4779–4789. doi:10.1021/acsnano.6b01370

Liu, Y., Guo, Z., Li, F., Xiao, Y., Zhang, Y., Bu, T., et al. (2019). Multifunctional magnetic copper ferrite nanoparticles as Fenton-like reaction and near-infrared photothermal agents for synergetic antibacterial therapy. *ACS Appl. Mat. Interfaces* 11, 31649–31660. doi:10.1021/acsami.9b10096

Liu, Y., Zhen, W., Wang, Y., Liu, J., Jin, L., Zhang, T., et al. (2019). One-dimensional Fe2P acts as a Fenton agent in response to NIR II light and ultrasound for deep tumor synergetic theranostics. *Angew. Chem. Int. Ed. Engl.* 131, 2429–2434. doi:10.1002/ange.201813702

Lu, J., Wang, H., Peng, D., Chen, T., Dong, S., and Chang, Y. (2016). Synthesis and properties of Au/ZnO nanorods as a plasmonic photocatalyst. *Phys. E Low-dimensional Syst. Nanostructures* 78, 41–48. doi:10.1016/j.physe.2015.11.035

Mei, Z., Gao, D., Hu, D., Zhou, H., Huang, L., Liu, X., et al. (2020). Activatable NIR-II photoacoustic imaging and photochemical synergistic therapy of MRSA infections using miniature Au/Ag nanorods. *Biomaterials* 251, 120092. doi:10.1016/j.biomaterials.2020.120092

Morones, J. R., Elechiguerra, J. L., Camacho, A., Holt, K., Kouri, J. B., Ramirez, J. T., et al. (2005). The bactericidal effect of silver nanoparticles. *Nanotechnology* 16, 2346–2353. doi:10.1088/0957-4484/16/10/059

Nagaraju, G., Prashanth, S. A., Shastri, M., Yathish, K., et al. (2017). Electrochemical heavy metal detection, photocatalytic, photoluminescence, biodiesel production and antibacterial activities of Ag–ZnO nanomaterial. *Mat. Res. Bull.* 94, 54–63. doi:10.1016/j.materresbull.2017.05.043

Nie, M., Sun, H., Cai, H., Xue, Z., Yang, C., Li, Q., et al. (2020). Study on electrocatalytic property of ZnO and Ag/ZnO. *Mat. Lett.* 271, 127785. doi:10.1016/j.matlet.2020.127785

Pan, W. Y., Huang, C. C., Lin, T. T., Hu, H. Y., Lin, W. C., Li, M. J., et al. (2016). Synergistic antibacterial effects of localized heat and oxidative stress caused by hydroxyl radicals mediated by graphene/iron oxide-based nanocomposites. *Nanomedicine Nanotechnol. Biol. Med.* 12, 431–438. doi:10.1016/j.nano.2015.11.014

Pande, S., Ghosh, S. K., Praharaj, S., Panigrahi, S., Basu, S., Jana, S., et al. (2007). Synthesis of normal and inverted gold– silver core– shell architectures in β-cyclodextrin and their applications in SERS. *J. Phys. Chem. C* 111, 10806–10813. doi:10.1021/jp0702393

Pelgrift, R. Y., and Friedman, A. J. (2013). Nanotechnology as a therapeutic tool to combat microbial resistance. *Adv. Drug Deliv. Rev.* 65, 1803–1815. doi:10.1016/j.addr.2013.07.011

Rajavel, K., Gomathi, R., Manian, S., and Rajendra Kumar, R. T. (2014). *In vitro* bacterial cytotoxicity of CNTs: Reactive oxygen species mediate cell damage edges over direct physical puncturing. *Langmuir* 30, 592–601. doi:10.1021/la403332b

Sarfraz, R. A., and Qayyum, A. (2018). *Mechanism of action of bio-inspired nanosilver particles*. Thomas Telford Ltd.

Shao, W., Liu, X., Min, H., Dong, G., Feng, Q., and Zuo, S. (2015). Preparation, characterization, and antibacterial activity of silver nanoparticle-decorated graphene oxide nanocomposite. *ACS Appl. Mat. Interfaces* 7, 6966–6973. doi:10.1021/acsami.5b00937

Singh, H., Du, J., and Yi, T. H. (2017). Biosynthesis of silver nanoparticles using Aeromonas sp. THG-FG1. 2 and its antibacterial activity against pathogenic microbes. *Artif. Cells Nanomed. Biotechnol.* 45, 584–590. doi:10.3109/21691401.2016.1163715

Stewart, P. S., and Costerton, J. W. (2001). Antibiotic resistance of bacteria in biofilms. *Lancet* 358, 135–138. doi:10.1016/s0140-6736(01)05321-1

Sun, J., Song, L., Fan, Y., Tian, L., Luan, S., Niu, S., et al. (2019). Synergistic photodynamic and photothermal antibacterial nanocomposite membrane triggered by single NIR light source. *ACS Appl. Mat. Interfaces* 11, 26581–26589. doi:10.1021/acsami.9b07037

Tian, Y., Qi, J., Zhang, W., Cai, Q., and Jiang, X. (2014). Facile, one-pot synthesis, and antibacterial activity of mesoporous silica nanoparticles decorated with well-dispersed silver nanoparticles. *ACS Appl. Mat. Interfaces* 6, 12038–12045. doi:10.1021/am5026424

Tsuchido, T., Katsui, N., Takeuchi, A., Takano, M., and Shibasaki, I. (1985). Destruction of the outer membrane permeability barrier of *Escherichia coli* by heat treatment. *Appl. Environ. Microbiol.* 50, 298–303. doi:10.1128/aem.50.2.298-303.1985

Vadyvaloo, V., and Martínez, L. (2014). Mechanisms of post-transcriptional gene regulation in bacterial biofilms. *Front. Cell. Infect. Microbiol.* 4, 38. doi:10.3389/fcimb.2014.00038

Vikesland, P. J., and Wigginton, K. R. (2010). Nanomaterial enabled biosensors for pathogen monitoring - a review. *Environ. Sci. Technol.* 44, 3656–3669. doi:10.1021/es903704z

Wang, P., Shi, Y., Zhang, S., Huang, X., Zhang, J., Zhang, Y., et al. (2019). Hydrogen peroxide responsive iron-based nanoplatform for multimodal imaging-guided cancer therapy. *Small* 15, e1803791. doi:10.1002/smll.201803791

Wiesenthal, A., Hunter, L., Wang, S., Wickliffe, J., and Wilkerson, M. (2011). Nanoparticles: Small and mighty. *Int. J. Dermatol.* 50, 247–254. doi:10.1111/j.1365-4632.2010.04815.x

Wright, G. D. (2011). Molecular mechanisms of antibiotic resistance. *Chem. Commun.* 47, 4055–4061. doi:10.1039/c0cc05111j

Wu, M.-C., Deokar, A. R., Liao, J. H., Shih, P. Y., and Ling, Y. C. (2013). Graphene-based photothermal agent for rapid and effective killing of bacteria. *ACS Nano* 7, 1281–1290. doi:10.1021/nn304782d

Yang, Y., Zhu, W., Dong, Z., Chao, Y., Xu, L., Chen, M., et al. (2017). 1D coordination polymer nanofibers for low-temperature photothermal therapy. *Adv. Mat.* 29, 1703588. doi:10.1002/adma.201703588

Yuan, J., Choo, E. S. G., Tang, X., Sheng, Y., Ding, J., and Xue, J. (2010). Synthesis of ZnO-Pt nanoflowers and their photocatalytic applications. *Nanotechnology* 21, 185606. doi:10.1088/0957-4484/21/18/185606

Zhang, K., Meng, X., Cao, Y., Yang, Z., Dong, H., Zhang, Y., et al. (2018). Metal–organic framework nanoshuttle for synergistic photodynamic and low-temperature photothermal therapy. *Adv. Funct. Mat.* 28, 1804634. doi:10.1002/adfm.201804634

Zhang, T., Wang, L., Chen, Q., and Chen, C. (2014). Cytotoxic potential of silver nanoparticles. *Yonsei Med. J.* 55, 283–291. doi:10.3349/ymj.2014.55.2.283

Zhang, Y., Xu, J., Xu, P., Zhu, Y., Chen, X., and Yu, W. (2010). Decoration of ZnO nanowires with Pt nanoparticles and their improved gas sensing and photocatalytic performance. *Nanotechnology* 21, 285501. doi:10.1088/0957-4484/21/28/285501

Zheng, K., Setyawati, M. I., Lim, T. P., Leong, D. T., and Xie, J. (2016). Antimicrobial cluster bombs: Silver nanoclusters packed with daptomycin. *ACS Nano* 10, 7934–7942. doi:10.1021/acsnano.6b03862

Zheng, Y., Chen, C., Zhan, Y., Lin, X., Zheng, Q., Wei, K., et al. (2008). Photocatalytic activity of Ag/ZnO heterostructure nanocatalyst: Correlation between structure and property. *J. Phys. Chem. C* 112, 10773–10777. doi:10.1021/jp8027275

frontiers | Frontiers in Chemistry

TYPE Original Research
PUBLISHED 24 November 2022
DOI 10.3389/fchem.2022.1093073

OPEN ACCESS

EDITED BY
He Xiaojun,
Wenzhou Medical University, China

REVIEWED BY
Jianxun Ding,
Changchun Institute of Applied Chemistry (CAS), China
Kelong Fan,
Institute of Biophysics (CAS), China

*CORRESPONDENCE
Zheng Lian,
20052430@ppsuc.edu.cn

SPECIALTY SECTION
This article was submitted to Medicinal and Pharmaceutical Chemistry, a section of the journal Frontiers in Chemistry

RECEIVED 08 November 2022
ACCEPTED 14 November 2022
PUBLISHED 24 November 2022

CITATION
Lian Z, Lu C, Zhu J, Zhang X, Wu T, Xiong Y, Sun Z and Yang R (2022), Mo@ZIF-8 nanozyme preparation and its antibacterial property evaluation. *Front. Chem.* 10:1093073. doi: 10.3389/fchem.2022.1093073

Mo@ZIF-8 nanozyme preparation and its antibacterial property evaluation

Zheng Lian[1,2]*, Chunqing Lu[1], Jiangqi Zhu[1,3], Xining Zhang[2], Ting Wu[2], Youlin Xiong[2], Zhiyi Sun[1] and Rong Yang[2]

[1]School of Criminal Investigation, People's Public Security University of China, Beijing, China, [2]CAS Key Laboratory for Biomedical Effects of Nanomaterials and Nanosafety, Center of Materials Science and Optoelectronics Engineering, CAS Center for Excellence in Nanoscience, National Center for Nanoscience and Technology, University of Chinese Academy of Sciences, Beijing, China, [3]Institute of Evidence Law and Forensic Science, China University of Politic Science and Law, Beijing, China

Types of nanozymes can produce free radicals and/or reactive oxygen species (ROS) to serve as broad spectrum antibacterial materials. Developing nanozyme-based antibacterial materials with good biocompatibility exhibits promising application prospects. In this study, we doped Mo to ZIF-8 (both components have good biocompatibility) to prepare a new nanozyme, Mo@ZIF-8, which can produce hydroxyl radicals (•OH) triggered by a low dosage of hydrogen peroxide (H_2O_2), exhibiting effective antibacterial capability against both Gram-negative bacteria (*Escherichia coli*) and Gram-positive bacteria (*Staphylococcus aureus*). This work provides a reference for the design of antibacterial nanozymes with good biocompatibility.

KEYWORDS

peroxidase-like nanozyme, metal organic framework, ZIF-8, molybdenum, antibacterial therapy

1 Introduction

Bacterial-related diseases has been one of public safety issues that greatly threaten the health of humankind. (Reverter et al., 2020; Yu et al., 2022; Ding et al., 2022). Antibiotics have been the most widely accepted treatment for bacterial infection diseases. (Stracy et al., 2022). However, the abuse of antibiotics attribute to the emergence of drug-resistant bacteria, which may threaten the global health and environment. (Lakemeyer et al., 2018; Serwecińska, 2020). Therefore, effective and broad-spectrum antibacterial agents are urgently needed.

Currently, types of materials, such as metals (Gu et al., 2020; Tian et al., 2021), metal oxides (Li et al., 2018; Dong et al., 2022), carbon materials (Bi et al., 2022), single-atom materials (Cai et al., 2022) and MXenes (Yu et al., 2022b), have been verified to have peroxidase (POD)-like activity when they are fabricated to nanoscale. These nanozymes can convert H_2O_2 into OH radicals to effectively kill bacteria.

Metal organic frameworks (MOFs) have large surface area and pore structures, which provides scaffold for the enzymatic (catalytic) performance. (Ma et al., 2020). Here, we developed a new type of antibacterial nanozyme (Mo@ZIF-8) by doping Mo to ZIF-8.

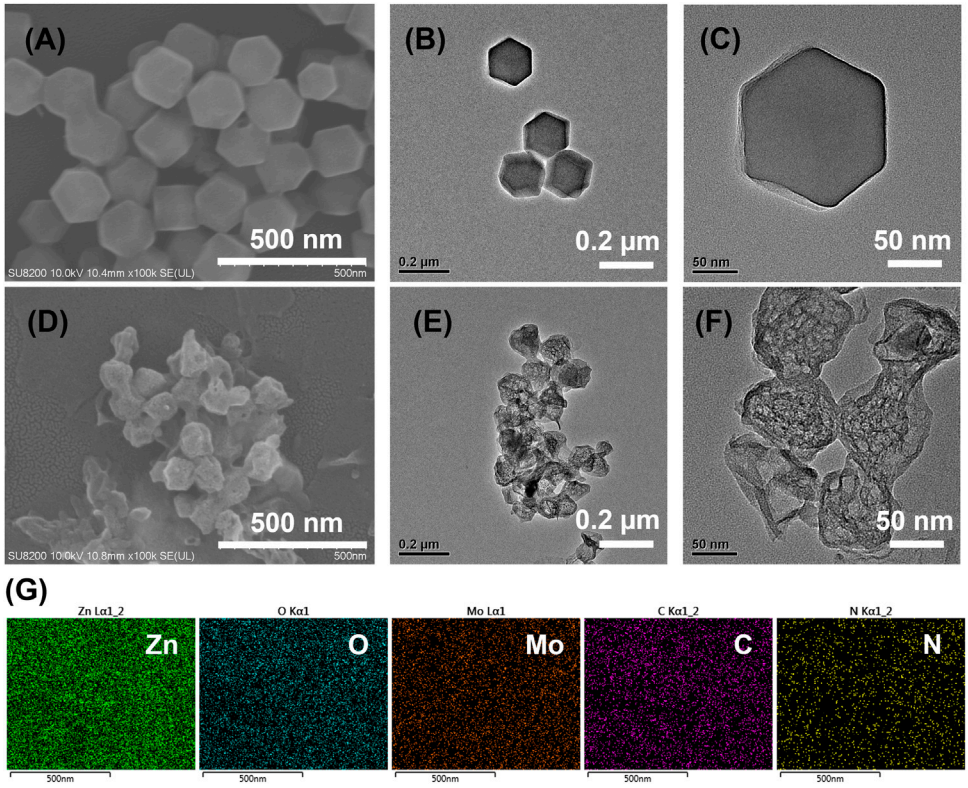

FIGURE 1
Characterizations of nanostructures from electron microscopy technique. **(A)** SEM image of ZIF-8. **(B,C)** TEM images of ZIF-8 at different magnifications. **(D)** SEM image of Mo@ZIF-8. **(E,F)** TEM images of Mo@ZIF-8 at different magnifications. **(G)** EDX analysis of Mo@ZIF-8. The images indicated that Mo had been doped to the nanostructures.

Briefly, the prepared hexahedron-shaped ZIF-8 (150 nm) was refluxed with Na_2MoO_4 solution and subsequent pyrolyzed at 600°C. The prepared Mo@ZIF-8 exhibited promising capability producing •OH and killing both Gram-negative (*E. coli*) and Gram-positive (*S. aureus*) bacteria at a low dosage of H_2O_2 (10^{-5} M). Due to the high biocompatibility of Mo and ZIF-8, this rationally designed nanozyme has the potential to be an effective antibacterial agent.

2 Experimental

2.1 Synthesis of hollow Mo@ZIF-8 nanostructures

0.595 g $Zn(NO_3)_2{\cdot}6H_2O$ was dissolved in 20 mL methanol (solution A). 0.656 g 2-methylimidazole (2-MIM) was dissolved in 20 mL methanol (solution B). Then solution B was rapidly added into solution A under vigorous for 15 min stirring at room temperature. The mixed solution was stand for 3 h at room temperature. After washing with methanol for three times, the white powder was collected by centrifugation and dried at 40°C.

To prepare Mo@ZIF-8 nanostructures, 0.075 g of as-prepared ZIF-8 was dispersed in 30 mL ethanol. Then 15 mL of Na_2MoO_4 solution (containing 0.0375 g $Na_2MoO_4{\cdot}2H_2O$) was mixed with ZIF-8 solution, then the mixed suspension refluxed at 82°C for 2 h. The precipitation was collected and wash by methanol for three times. The product was dried at 40°C and further annealed in Argon atmosphere at 600°C for 2 h with the rate of 5°C/min.

2.2 Enzyme-like activity and catalytic kinetics studies

The peroxidase-like activity of Mo@ZIF-8 nanostructures was tested by 3,3′,5,5′-tetramethylbenzidine (TMB) as substrate in the presence of H_2O_2. First, the Mo@ZIF-8 catalysts were dispersed in water with ultrasonication. Then, 1 mg/mL (50 μl) suspension was added to 450 μl NaAc–HAc buffer (0.1 M pH 3.0) containing 1 mM TMB and 2 mM H_2O_2. After incubation at room temperature for 20 min, the UV-vis absorption of the mixture was recorded. The influence of pH (2–9) and temperature (20–80°C) on the catalytic performance of Mo@ZIF-8 were also evaluated.

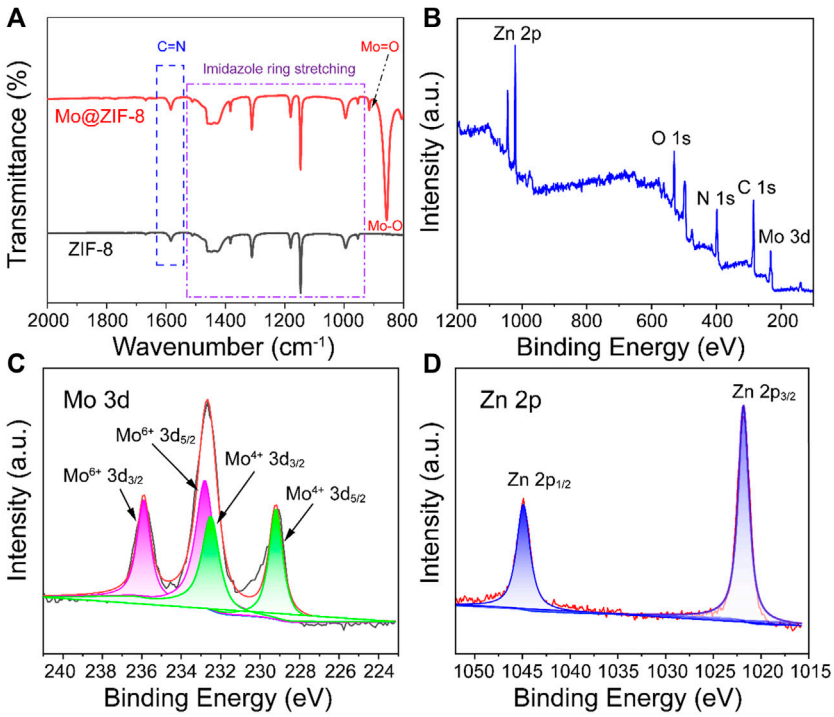

FIGURE 2
Characterizations of Mo@ZIF-8. **(A)** The FT-IR spectra of ZIF-8 and Mo@ZIF-8. The stretching peaks in the ZIF-8 and Mo@ZIF-8 were labeled. **(B–D)** XPS spectra of Mo@ZIF-8. **(B)** Survey spectrum. High-resolution XPS spectra of **(C)** Mo 3d, **(D)** Zn 2p.

The steady-stated kinetic experiments were carried out in 500 μL NaAc–HAc buffer (0.1 M pH 3.0) containing 100 μg/mL Mo@ZIF-8, 1 mM TMB and H_2O_2 ranging from 0 to 2.0 mM, or containing 100 μg/mL Mo@ZIF-8, 2 mM H_2O_2 and TMB ranging from 0 to 2.0 mM. The absorbance changes at 652 nm were constantly monitored in time-scan mode. The kinetic parameters were determined by the following equation:

$$\frac{1}{v} = \left(\frac{K_m}{V_{max}}\right)\left(\frac{1}{[S]}\right) + \frac{1}{V_{max}} \quad (1)$$

where v was the initial velocity, V_{max} was the maximal reaction velocity, K_m was the Michaelis–Menten constant and [S] was the substrate (TMB or H_2O_2) concentration, respectively.

2.3 Antibacterial experiments

Gram-positive *S. aureus* and Gram-negative *E. coli* were used for the antibacterial experiments. Typically, the experiments for each bacterium were divided into four groups: 1) bacteria, 2) bacteria + H_2O_2, 3) bacteria + Mo@ZIF-8, 4) bacteria + Mo@ZIF-8 + H_2O_2. The concentration of H_2O_2 used in the process was 10^{-5} M and the concentration of Mo@ZIF-8 was 2, 5 and 10 μg/mL. The bacteria were incubated with above solution for 4 h, then 30 μl of the suspension (1.0×10^7 CFU/mL *S. aureus* or *E. coli*) were spread on Luria-Bertani (LB) solid medium. These plates were kept at 37°C for 18 h, and bacterial colonies were counted.

Scanning electron microscopy (SEM) was used to observe the morphological change of the bacteria after antibacterial experiments. Groups: 1) control (bacteria without any treatment), 2) 10^{-5} M H_2O_2, 3) 5 μg/mL Mo@ZIF-8, 4) 5 μg/mL Mo@ZIF-8 + 10^{-5} M H_2O_2. After incubated for 4 h, the bacterial suspensions were collected and dropped onto silicon slides. Subsequently, bacterial cells were prefixed with 2.5% glutaraldehyde for 4 h, and dehydrated by a graded series of ethanol (30%, 50%, 70%, 80%, 90%, and 100%, respectively). The bacteria were finally dried for observation by scanning electron microscope.

3 Results and discussion

3.1 Structure characterizations

The SEM and TEM characterizations showed a hexahedron shape for ZIF-8 with the size of about 150 nm. (Figures 1A–C).

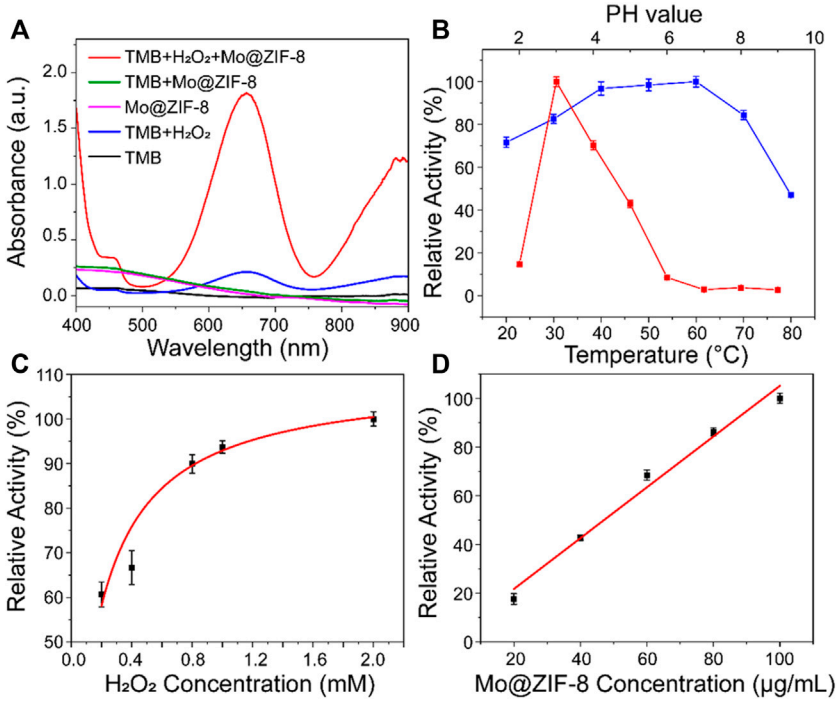

FIGURE 3
The peroxidase-like activity of the Mo@ZIF-8. **(A)** Absorbance spectra of TMB in different systems. **(B)** pH (red) and temperature (blue) dependence of Mo@ZIF-8 peroxidase activity. **(C)** H_2O_2 concentration dependence of the peroxidase-like activity of Mo@ZIF-8. **(D)** Concentration dependence of peroxidase activity of Mo@ZIF-8. In **(B–D)**, data are presented as mean ± SD (n = 3).

Meanwhile, TEM images showed the smooth surface of the ZIF-8 crystals (Figures 1B,C). After refluxing with Na_2MoO_4, the product became rounded and the corner disappeared. The size of the product was smaller than ZIF-8, which was about 100 nm. (Supplementary Figure S1A,B). The product was annealed at 600°C in Argon atmosphere and Mo@ZIF-8 formed. The Mo@ZIF-8 exhibited rough surfaces and hollow structures, shown in Figures 1D–F. TEM revealed their hollow and spongy structure, and the average diameter of the Mo@ZIF-8 was about 100 nm. (Figure 1F).

The incorporation of Mo element into ZIF-8 was confirmed by Energy Dispersive X-Ray Spectroscopy (EDX). The element distribution of Mo@ZIF-8 was shown in Figure 1G, demonstrating a homogeneous distribution of Zn, O, Mo, C, N elements in the nanocomposites.

FT-IR spectra of ZIF-8 and Mo@ZIF-8 were performed to demonstrate the successful incorporation of Mo, as shown in Figure 2A. The FT-IR spectra of ZIF-8 and Mo@ZIF-8 exhibited the characteristic peaks of 953–1,511 cm^{-1} and 1,582 cm^{-1}, which corresponded to the signals of the imidazole ring stretching and C=N bond of ZIF-8. (Wang et al., 2016; Zhang and Park, 2019). This revealed that the introduction of Mo did not destroy the imidazole ring. For the Mo@ZIF-8, new peaks appeared at 857 cm^{-1} and 916 cm^{-1}, which might be attributed to the stretching vibration of Mo-O and Mo=O bond, respectively. (Lin et al., 2020).

Furthermore, X-ray photoelectron spectroscopy (XPS) was explored the chemical composition and element valence state of Mo@ZIF-8 nanocomposites. Wide-scan XPS spectrum (Figure 2B) indicated the presence of C, O, N, Zn, and Mo in the Mo@ZIF-8 nanocomposites, confirming that Mo was successfully loaded on ZIF-8. Figure 2C was the high-resolution XPS spectrum of Mo 3d. Three bands at 235.9 , 232.6, and 229.2 eV could be assigned to Mo 3d doublets. The fitted Mo 3d peaks positioned at 229.2 and 232.5 eV were corresponding to Mo (IV). While, the doublet peaks at 232.8 and 235.9 eV were indexed to Mo (VI). (Zheng et al., 2017; Lian et al., 2022). As displayed in Figure 2D, the binding energy for Zn 2p3/2 and 2p1/2 were 1,021.8 and 1,044.8 eV, respectively. (Hua et al., 2019).

3.2 The peroxidase mimetic activity of Mo@ZIF-8

TMB, a classical chromogenic substrate, was used to test the peroxide-like activity of Mo@ZIF-8 nanocomposites in the presence of H_2O_2. (Wang et al., 2019). As shown in Figure 3A, Mo@ZIF-8 exhibited highest absorbance at 652 nm, illustrating the high peroxidase-like activity. However, ZIF-8 showed negligible enzymatic activity under the same

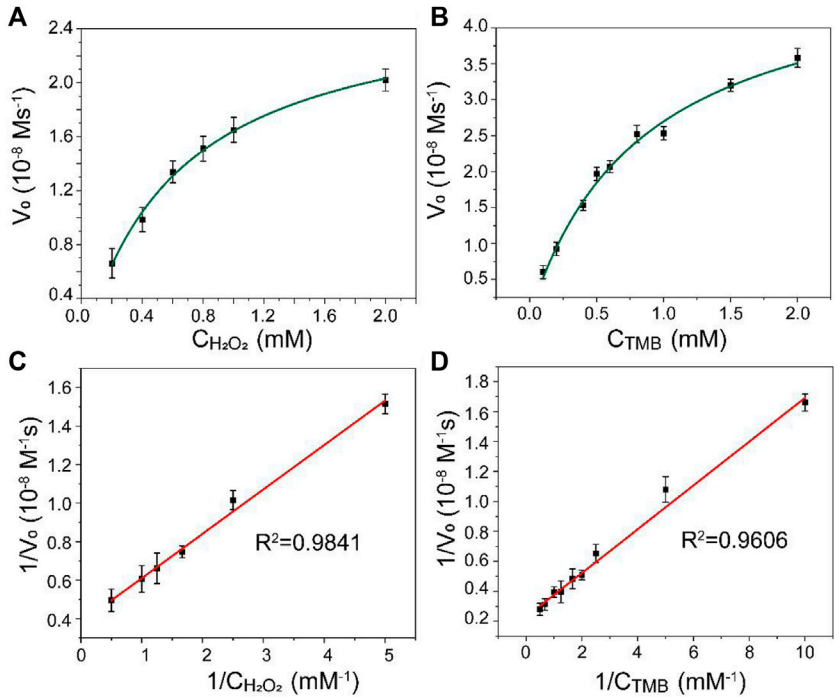

FIGURE 4
Steady-state kinetic analysis for Mo@ZIF-8-catalyzed TMB oxidation. **(A,B)** Michaelis–Menten model analysis. **(C,D)** Lineweaver–Burk models analysis. Data are presented as mean ± SD (n = 3).

condition, (Supplementary Figure S2), which indicated that the introduction of Mo element played a key role during the catalytic process. In contrast, H_2O_2 alone did not show significant absorption at 652 nm. The catalytic performance of enzyme was highly dependent on pH, temperature, concentration of H_2O_2 and nanozyme. Experiments were carried out at different pH (2–9) and temperature (20–80°C), and the optimum condition for the peroxide-like activity of Mo@ZIF-8 was found to be pH 3 and 60°C. (Figure 3B). Notably, Mo@ZIF-8 exhibited high catalytic activity in a broad temperature range, illustrating its low sensitivity towards temperature. Furthermore, the catalytic activity of Mo@ZIF-8 was directly enhanced by the increasing concentration of H_2O_2 (Figure 3C). And there was almost a linear relationship between the concentration of Mo@ZIF-8 and its relative catalytic activity (Figure 3D).

The kinetic analysis of Mo@ZIF-8 was further investigated using steady-state kinetic experiments. The data were collected by using a series of TMB concentrations with constant H_2O_2 concentration and *vice versa*. The Michaelis–Menten constant (K_m) and the maximum initial velocity (V_{max}) could be calculated from Lineweaver–Burk double reciprocal plots, which showed a good linear-ship between v^{-1} and $[S]^{-1}$. (Figure 4). The K_m values of Mo@ZIF-8 were 0.62 and 0.86 mM with H_2O_2 and TMB as the substrates, respectively, and the corresponding V_{max} values were 26.64 nM s^{-1} and 50.15 nM s^{-1}.

The mechanism of Mo@ZIF-8 peroxidase-like activity was investigated. Assuming that Mo@ZIF-8 could convert H_2O_2 into hydroxyl radicals (•OH) through the POD-like activity, terephthalic acid (TA) was used to confirm the production of •OH during the catalytic progress. TA was a nonfluorescent molecule, but it could easily react with •OH to generate highly fluorescent 2-hydroxy terephthalic acid. (Wang et al., 2018). As shown in Supplementary Figure S3, the enhancement in fluorescence intensity was significant when compared with the control group, confirming the production of hydroxyl radicals by Mo@ZIF-8 in the presence of H_2O_2. All the results indicated that Mo@ZIF-8 showed POD enzyme mimicking activity and was suitable and efficient for killing bacteria.

3.3 Antibacterial experiments

The antibacterial effect of the Mo@ZIF-8 nanocomposites was evaluated with the assistance of H_2O_2. The bacterial viability was measured by counting the colonies forming units. During the antibacterial experiments, the concentration of H_2O_2 was 10^{-5} M, which hardly affect the survival of both *E. coli* and *S. aureus*. Figure 5 showed the images of bacteria colonies on LB agar with various treatments. As shown, Mo@ZIF-8 alone showed a dose-dependent inhibition effect. However, Mo@ZIF-8 combined with low

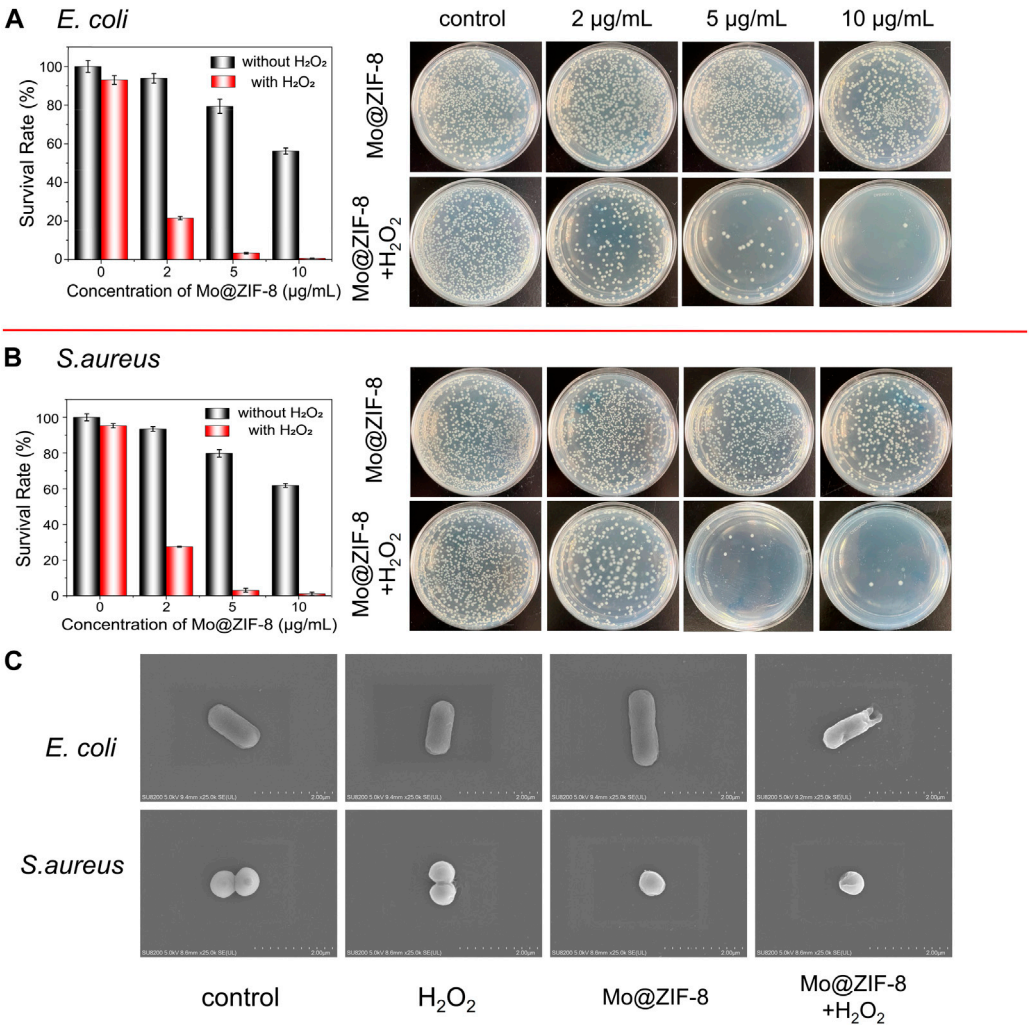

FIGURE 5
Antibacterial capability of Mo@ZIF-8. Bacterial proliferation and the corresponding images of bacterial colonies on LB agar at different concentration with and without H_2O_2. **(A)** Antibacterial capability of Mo@ZIF-8 to *E. coli* (Gram-negative). **(B)** Antibacterial capability of Mo@ZIF-8 to *S. aureus* (Gram-positive). In **(A)** and **(B)**, data are presented as mean ± SD (n = 3). **(C)** Representative morphologies of bacteria in different groups imaged by SEM.

concentration H_2O_2 (10^{-5} M) exhibited excellent antibacterial effect, and the inhibition efficiency towards *E. coli* and *S. aureus* reached to 99.2% and 99.4%, respectively, when the concentration of Mo@ZIF-8 was 10 μg/mL. These results illustrated that Mo@ZIF-8 could be used as an efficient antibacterial agent.

The morphological changes of *E. coli* and *S. aureus* were investigated after various treatment by SEM. In Figure 5C, as for *E. coli*, no obvious morphological change was observed in the control, H_2O_2 and Mo@ZIF-8 groups, and *E. coli* cells showed rod-shape, with intact and smooth cell walls. As for the groups with treatment of both Mo@ZIF-8 and H_2O_2, *E. coli* cells lost their cellular integrity, with noticeable holes on its cell wall. For *S. aureus*, the results were similar. *S. aureus* in the control, H_2O_2 and Mo@ZIF-8 groups exhibited a sphere shape, a well-defined and even cell wall. Nevertheless, the morphology of *S. aureus* cells incubated with Mo@ZIF-8 and H_2O_2 were changed. In this group, *S. aureus* cells were damaged, even with intracellular components leaked. These results demonstrated excellent antibacterial capability of Mo@ZIF-8 with the assistant of H_2O_2.

4 Conclusion

In summary, we fabricated a new nanozyme, Mo@ZIF-8 nanocomposites through refluxing Na_2MoO_4 solution with ZIF-8 and pyrolyzing at 600°C. This nanocomposite exhibited peroxide-like activity and achieved a wide range of antibacterial capability against both Gram-negative (*E. coli*) and Gram-

positive (*S. aureus*) bacteria through producing •OH. Due to the high biocompatibility of the selected components, Mo and ZIF-8, the Mo@ZIF-8 nanozyme has the potential to be an effective antibacterial agent applied in biomedical field.

Data availability statement

The original contributions presented in the study are included in the article/Supplementary Material, further inquiries can be directed to the corresponding author.

Author contributions

ZL: Methodology, formal analysis, investigation, writing—original draft, writing—review and editing, funding. CL: Formal analysis, methodology. JZ: investigation, resources. XZ: Formal analysis, investigation. TW: Formal analysis, investigation. YX: Formal analysis, investigation. ZS: Formal analysis. RY: Conceptualization, writing—review and editing, supervision, project administration.

Funding

This project was financially supported by the Fundamental Research Funds for the Central Universities (2021JKF210) awarded by the People's Public Security University of China.

Acknowledgments

The authors would like to express sincere thanks to the professors and technicists of National Center for Nanoscience and Technology for their supports and assistance.

Conflict of interest

The authors declare that the research was conducted in the absence of any commercial or financial relationships that could be construed as a potential conflict of interest.

Publisher's note

All claims expressed in this article are solely those of the authors and do not necessarily represent those of their affiliated organizations, or those of the publisher, the editors and the reviewers. Any product that may be evaluated in this article, or claim that may be made by its manufacturer, is not guaranteed or endorsed by the publisher.

Supplementary material

The Supplementary Material for this article can be found online at: https://www.frontiersin.org/articles/10.3389/fchem.2022.1093073/full#supplementary-material

References

Bi, X., Bai, Q., Wang, L., Du, F., Liu, M., Yu, W. W., et al. (2022). Boron doped graphdiyne: A metal-free peroxidase mimetic nanozyme for antibacterial application. *Nano Res.* 15, 1446–1454. doi:10.1007/s12274-021-3685-4

Cai, S., Liu, J., Ding, J., Fu, Z., Li, H., Xiong, Y., et al. (2022). Tumor-microenvironment-Responsive cascade reactions by a cobalt-single-atom nanozyme for synergistic nanocatalytic chemotherapy. *Angew. Chem. Int. Ed. Engl.* 16, e202204502. doi:10.1002/anie.202204502

Ding, J., Xiao, H., and Chen, X. (2022). Advanced biosafety materials for prevention and theranostics of biosafety issues. *Biosaf. Health* 4, 59–60. doi:10.1016/j.bsheal.2022.03.011

Dong, H., Du, W., Dong, J., Che, R., Kong, F., Cheng, W., et al. (2022). Depletable peroxidase-like activity of Fe_3O_4 nanozymes accompanied with separate migration of electrons and iron ions. *Nat. Commun.* 13, 5365. doi:10.1038/s41467-022-33098-y

Gu, H., Huang, Q., Zhang, J., Li, W., and Fu, Y. (2020). Heparin as a bifunctional biotemplate for Pt nanocluster with exclusively peroxidase mimicking activity at near-neutral PH. *Colloids Surfaces A Physicochem. Eng. Aspects* 606, 125455. doi:10.1016/j.colsurfa.2020.125455

Hua, Y., Li, X., Zhang, X., Zhang, L., Shu, Y., Sheng, H., et al. (2019). Active anchoring polysulfides of ZnS-decorated porous carbon aerogel for a high-performance lithium-sulfur battery. *ChemElectroChem* 6, 2570–2577. doi:10.1002/celc.201900556

Lakemeyer, M., Zhao, W. N., Mandl, F. A., Hammann, P., and Sieber, S., and(2018). Thinking outside the box-novel antibacterials to tackle the resistance crisis. *Angew. Chem. Int. Ed.* 57, 14440–14475. doi:10.1002/anie.201804971

Li, D., Liu, B., Huang, P., Zhang, Z., and Liu, J. (2018). Highly active fluorogenic oxidase mimicking NiO nanozymes. *Chem. Commun.* 54, 12519–12522. doi:10.1039/c8cc07062h

Lian, Z., Li, H., Wu, T., Zhao, J., Cai, S., and Yang, R. (2022). Vapor deposition of MoO_x/MoS_2 films on silicon wafer with visible-light responsive photocatalytic antibacterial properties. *Appl. Surf. Sci.* 606, 154874. doi:10.1016/j.apsusc.2022.154874

Lin, Z., Zhang, X., Liu, S., Zheng, L., Bu, Y., Deng, H., et al. (2020). Colorimetric acid phosphatase sensor based on MoO_3 nanozyme. *Anal. Chim. Acta* 1105, 162–168. doi:10.1016/j.aca.2020.01.035

Ma, L., iang, F., Fan, X., Wang, L., He, C., Zhou, M., et al. (2020). Metal-organic-framework-engineered enzyme-mimetic catalysts. *Adv. Mat.* 32, e2003065. doi:10.1002/adma.202003065

Reverter, M., Sarter, S., Caruso, D., Avarre, J. C., Combe, M., Pepey, E., et al. (2020). Aquaculture at the crossroads of global warming and antimicrobial resistance. *Nat. Commun.* 11, 1870. doi:10.1038/s41467-020-15735-6

Serwecińska, L. (2020). Antimicrobials and antibiotic-resistant bacteria: A risk to the environment and to public health. *Water* 12, 3313. doi:10.3390/w12123313

Stracy, M., Snitser, O., Yelin, I., Amer, Y., Parizade, M., Katz, R., et al. (2022). Minimizing treatment-induced emergence of antibiotic resistance in bacterial infections. *Science* 375, 889–894. doi:10.1126/science.abg9868

Tian, Y., Chen, Y., Chen, M., Song, Z., Xiong, B., and Zhang, X. (2021). Peroxidase-like Au@Pt nanozyme as an integrated nanosensor for Ag^+ detection by LSPR spectroscopy. *Talanta* 221, 121627. doi:10.1016/j.talanta.2020.121627

Wang, H., Li, P., Yu, D., Zhang, Y., Wang, Z., Liu, C., et al. (2018). Unraveling the enzymatic activity of oxygenated carbon nanotubes and their application in the treatment of bacterial infections. *Nano Lett.* 18, 3344–3351. doi:10.1021/acs.nanolett.7b05095

Wang, H., Wan, K., and Shi, X. (2019). Recent advances in nanozyme research. *Adv. Mat.* 31, e1805368. doi:10.1002/adma.201805368

Wang, X., Liu, J., Leong, S., Lin, X., Wei, J., Kong, B., et al. (2016). Rapid construction of ZnO@ZIF-8 heterostructures with size-selective photocatalysis properties. *ACS Appl. Mat. Interfaces* 8, 9080–9087. doi:10.1021/acsami.6b00028

Yu, L., Chang, J., Zhuang, X., Li, H., Hou, T., and Li, F. (2022). Two-dimensional cobalt-doped Ti_3C_2 MXene nanozyme-mediated homogeneous electrochemical strategy for pesticides assay based on *in situ* generation of electroactive substances. *Anal. Chem.* 94, 3669–3676. doi:10.1021/acs.analchem.1c05300

Yu, Y., Ding, J., Zhou, Y., Xiao, H., and Wu, G. (2022). Biosafety chemistry and biosafety materials: A new perspective to solve biosafety problems. *Biosaf. Health* 4, 15–22. doi:10.1016/j.bsheal.2022.01.001

Zhang, Y., and Park, S. (2019). Facile construction of MoO_3@ZIF-8 core-shell nanorods for efficient photoreduction of aqueous Cr (VI). *Appl. Catal. B Environ.* 240, 92–101. doi:10.1016/j.apcatb.2018.08.077

Zheng, Z., Cong, S., Gong, W., Xuan, J., Li, G., Lu, W., et al. (2017). Semiconductor SERS enhancement enabled by oxygen incorporation. *Nat. Commun.* 8 (1), 1993. doi:10.1038/s41467-017-02166-z

frontiers | Frontiers in Chemistry

TYPE Original Research
PUBLISHED 09 March 2023
DOI 10.3389/fchem.2023.1148354

OPEN ACCESS

EDITED BY
Wansong Chen,
Central South University, China

REVIEWED BY
Tang Yufu,
National University of Singapore, Singapore
Zhou Guoyong,
Guizhou Minzu University, China

*CORRESPONDENCE
Jingguo Li,
lijingguo@zzu.edu.cn
Zhan Zhou,
zhouzhan@lynu.edu.cn

SPECIALTY SECTION
This article was submitted to Nanoscience, a section of the journal Frontiers in Chemistry

RECEIVED 23 January 2023
ACCEPTED 17 February 2023
PUBLISHED 09 March 2023

CITATION
Chen H, Zhao X, Cui B, Cui H, Zhao M, Shi J, Li J and Zhou Z (2023), Peroxidase-like MoS_2/Ag nanosheets with synergistically enhanced NIR-responsive antibacterial activities.
Front. Chem. 11:1148354.
doi: 10.3389/fchem.2023.1148354

Peroxidase-like MoS_2/Ag nanosheets with synergistically enhanced NIR-responsive antibacterial activities

Huiying Chen[1,2], Xinshuo Zhao[3], Bingbing Cui[1,2], Haohao Cui[1,2], Mengyang Zhao[1], Jun Shi[2], Jingguo Li[1]* and Zhan Zhou[1,3]*

[1]Henan Provincial People's Hospital, People's Hospital of Zhengzhou University, Zhengzhou, China, [2]School of Materials Science and Engineering, Zhengzhou University, Zhengzhou, China, [3]Henan Key Laboratory of Function-Oriented Porous Materials, College of Chemistry and Chemical Engineering, Luoyang Normal University, Luoyang, China

Pathogenic microbial infections have been threatening public health all over the world, which makes it highly desirable to develop an antibiotics-free material for bacterial infection. In this paper, molybdenum disulfide (MoS_2) nanosheets loaded with silver nanoparticles (Ag NPs) were constructed to inactive bacteria rapidly and efficiently in a short period under a near infrared (NIR) laser (660 nm) in the presence of H_2O_2. The designed material presented favorable features of peroxidase-like ability and photodynamic property, which endowed it with fascinating antimicrobial capacity. Compared with free MoS_2 nanosheets, the MoS_2/Ag nanosheets (denoted as MoS_2/Ag NSs) exhibited better antibacterial performance against *Staphylococcus aureus* by the generated reactive oxygen species (ROS) from both peroxidase-like catalysis and photodynamic, and the antibacterial efficiency of MoS_2/Ag NSs could be further improved by increasing the amount of Ag. Results from cell culture tests proved that MoS_2/Ag3 nanosheets had a negligible impact on cell growth. This work provided new insight into a promising method for eliminating bacteria without using antibiotics, and could serve as a candidate strategy for efficient disinfection to treat other bacterial infections.

KEYWORDS

two-dimensional, silver nanoparticles, photo-responsive, peroxidase-like activity, synergistic antibacterial

1 Introduction

Bacterial infection, a major case resulting in pathological disorder, remains challenging to treat in terms of its highly horrible morbidity and mortality (Fisher et al., 2017; Qi et al., 2017). With the discovery and application of penicillin, human health and care present prosperous prospects in the field of fighting against microbes. However, bacteria continue to evolve and the abuse of anti-biotic leads to rapid and widespread drug resistance (Roope et al., 2019; Li et al., 2023a), which results in the increasingly difficult treatment of bacterial infections. Antibiotics administration against the bacterial infections can no longer catch up with the pace of bacterial evolution (Chen et al., 2023). According to statistics, 600 to −700 species of microbes have been identified on the planet, and with the bacteria still evolving and mutating, bacterial infections remain one of the greatest challenges to human health (Bakkeren et al., 2020; Li et al., 2021). It is imperative to

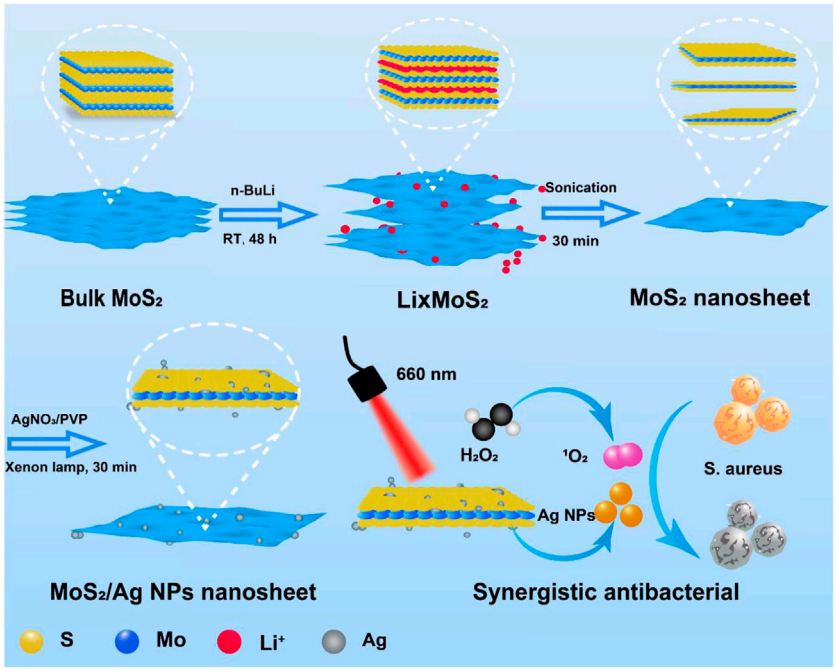

SCHEME 1
The schematic diagram for the preparation and synergistic antibacterial of MoS_2/Ag nanosheets.

develop a novel and favorable antimicrobial strategy with desired properties such as antibiotic-free, and biocompatible.

Due to the minimal likelihood of developing drug resistance and indeed the reliance on photo-responsive materials to carry out the operation (Zhu et al., 2020; He et al., 2022b), the photodynamic antibacterial method has drawn tremendous attention in microbiological applications (Yang et al., 2018; Chauhan et al., 2019; Chen et al., 2019; Han et al., 2020; Zhao et al., 2022b). Numerous cutting-edge substances, including nano-metal oxides (Ning et al., 2017; Jin et al., 2019; He et al., 2022a), two-dimensional (2D) materials (Liu et al., 2016; Zhao et al., 2023), and other photosensitive substances (Liu et al., 2019), can produce electron-hole pairs when exposed to certain wavelengths of light. The ejected electrons can then be captured by the oxygen in the environment to create reactive oxygen species (ROS), which can cause the death of pathogenic or diseased cells (Chen et al., 2022a; Zhou et al., 2022b; Hu et al., 2023). In particular, versus traditional chemotherapy, photodynamic therapy (PDT) manages to avoid the progression of drug resistance by primarily acting its biocidal activity through the oxidative damage of biological macromolecules such as lecithin, enzymes, nutrients, and DNA in cell membranes (Zhang et al., 2022b; Xiu et al., 2022).

MoS_2 has been utilized in the departments of catalysis (Wu et al., 2022), drug delivery (Zhang et al., 2019a), and biomedicine (Yadav et al., 2019; Hu et al., 2022b) for the sake of its superior biocompatibility, high specific surface area, ultrathin atomic layer structure in two dimensions (2D) (Huang et al., 2022). Additionally, the photo-responsive properties of MoS_2 from UV to near-infrared light, and the human-friendly elements of sulfur and molybdenum make it available for photodynamic therapy (Zhou et al., 2022a; Sethulekshmi et al., 2022). However, the small band gap of MoS_2 makes it easier for electron-hole pairs to combine, which can reduce its photodynamic activity (Zhu et al., 2020). Hence, it is required to identify other appropriate materials to combine with MoS_2. By accelerating the movement of electrons, the combination of precious metals with semiconductor materials can considerably enhance the photodynamic characteristics of semiconductor materials (Xia et al., 2015; Raza et al., 2017). The superior conductivity and inherent antibacterial properties of Ag make it a suitable precious metal material (Li et al., 2022b). More importantly, the Ag also have the effect of surface plasmon resonance, which allows electrons to escape from the outermost surface and be captured by the surrounding oxygen to produce ROS (Zhu et al., 2020). The local $^1O_2$ produced by MoS_2 with 660 nm laser irradiation can create a highly oxidized environment for the activation of metal nanoparticles, resulting in highly toxic metal ions that can induce oxidative stress to kill bacteria (Wei et al., 2021; Hu et al., 2022a; Li et al., 2022a; Xue et al., 2023). Another advantage of MoS_2 is that it can produce ROS when reacts with hydrogen peroxide (H_2O_2) (Li et al., 2023b), hastening the death of bacteria (Zhao et al., 2015). Therefore, combining the characteristics of photodynamic and peroxidase, nanocomposites based on MoS_2 nanosheets could provide a promising alternative for resistant bacterial infections.

Herein, MoS_2/Ag nanosheets (denoted as MoS_2/Ag NSs) with rapidly adjustable antibacterial properties was constructed by a simple chemical exfoliation and xenon lamp reduction method (Scheme 1). Ag NPs and MoS_2 together increased the energy evolution routes and electron transport at the interface, considerably raising the photodynamic activity of MoS_2 and, as a result, the amount of ROS produced when irradiated by 660 nm near-infrared light. Meanwhile, a low concentration of H_2O_2 could

be catalyzed into detrimental ROS by the intrinsic peroxidase-like property of MoS_2/Ag NSs, which was vital in attacking the bacterial membranes. As a result, this work displayed remarkable promise in the practical treatment of inflammatory diseases while also offering a promising strategy for swift and efficient sterilization.

2 Experimental details

2.1 Chemicals

Molybdenum disulfide (MoS_2) layered bulk crystals, n-Butyllithium (2.5 M in cyclohexane) were purchased from Sigma Aldrich (United States). Polyvinylpyrrolidone (PVP) with the average MW 58000 was purchased from Aladdin Reagent Company (China). $AgNO_3$ was obtained from Macklin. Ag nanoparticles were successfully grown on MoS_2 nanosheets by 300 W xenon lamp (PLS-SXE100) irradiation. 3-(4,5-Dimethylthiazol-2-yl)-2,5-diphenyl tetrazolium bromide (MTT) was provided from Sigma Biochemical Technology Co., Ltd. (Shanghai, China). LIVE/DEAD™ Baclight™ Bacterial Viability Kit (L7012) was purchased from Invitrogen (China). Cell counting Kit-8 (CCK-8) was purchased from Beyotime (China). *Staphylococcus aureus* and L929 cells were supplied by the Henan Eye Institute.

2.2 Characterization

Scanning electron Microscope (SEM) images were captured Field Launch Scanning Electron Microscope (Zeiss Sigma 500, Germany). Transmission electron microscope (TEM) images taken on by field emission transmission electron microscope (JEM-2100F, Japan). The diameter of particles and zeta potential of MoS_2/Ag NSs were detected by Malvern ZEM 3700 equipment. The antibacterial property of samples with MTT was investigated by 2,104 Multilabel Microplate Reader (PerkinElmer). UV-Vis-NIR spectra were detected with a spectrophotometer from Agilent Technologies (Cary 5,000). Fluorescence pictures of microbial were observed with a Nikon 80i fluorescence microscope.

2.3 Synthesis of MoS_2 nanosheets

The similar approach outlined in the prior research was used to prepare the MoS_2 nanosheets (Chen et al., 2022b). The specific steps were as follows: the grinded MoS_2 crystals (100 mg) were immersed in a solution of n-butyllithium (2.5 M in cyclohexane, 5 mL) and kept in glove boxes for 48 h to obtain lithium intercalation compounds. The precipitate at the bottom was washed three times with hexane after taking of the upper layer of n-butyllithium, followed by adding 50 mL of water and sonicated for 30 min to produce a homogeneous suspension. The large-size nanosheets were removed by centrifuging at 5,000 rpm for 10 min. The supernatant was further centrifugation products at 5,000–12000 rpm were collected and washed three times with DI water to obtain MoS_2 nanosheets.

2.4 Preparation of MoS_2/Ag NSs

40 mg PVP was added to 20 mL of synthesized MoS_2 suspension in triplicate, and the $AgNO_3$ (1 mg/mL) solution with various volumes (0.5, 1, and 2 mL) was added to the mixture. After stirring evenly, the mixture was lit under a xenon lamp at 300 W for 30 min. The crude products with different silver content were denoted as MoS_2/Ag1, MoS_2/Ag2, and MoS_2/Ag3 and were washed two times with DI water to get the MoS_2/Ag nanosheets with different silver contents.

2.5 Cytotoxicity tests

Using the Cell Counting Kit-8, the cytotoxicity of MoS_2/Ag3 NSs was determined (CCK-8, Beyotime). Each well plate was injected with 7 to 8 10^3 L929 cells for 24 h in a thermostatic incubator set to 37°C with 5% CO_2, and then the wells were filled with 100 μL of the MoS_2/Ag3 NSs solution for another 24 h. Subsequently, a fresh medium (100 μL) containing 10% CCK-8 agentia was added. This medium was then cultured for 4 h in a thermostatic incubator. Enzyme labeling (PerkinElmer Envision, England) was used to detect the optical density and cell viability at 450 nm.

2.6 Antibacterial test

Staphylococcus aureus (*S. aureus*) was used as the bacterial model. Frozen strains were first resuspended and transferred to columbia blood agar plates to be incubated overnight in a 37°C incubator, and then took a single colony by inoculation loops and transferred it to 4 mL LB medium and incubated for 12 h at 220 rpm on a shaker. Bacterial suspension was diluted to 10^7 CFU/mL for inhibition experiments. Microdilution, plate counting, fluorescence staining, and scanning electron microscopy were used to examine the antibacterial activity and mechanism of MoS_2/Ag nanosheets against *S. aureus*.

2.6.1 Plate colony counting assay

The plate colony counting assay was employed to investigate the antibacterial performance. Firstly, *S. aureus* was mixed with different concentrations (10, 20, 30, 40, 50 μg/mL) of sample groups MoS_2, MoS_2/Ag1, MoS_2/Ag2, MoS_2/Ag3 in 96-well plates, respectively. All groups were irradiated with a 660 nm laser for 10 min and treated with hydrogen peroxide (H_2O_2) at a final concentration of 100 μM. Furthermore, *S. aureus* treated with H_2O_2 under laser irradiation was taken as the control. To further determine the effect of H_2O_2 or laser on the antimicrobial properties of the materials, four groups of each kind of material: I) bacteria control, II) bacteria + H_2O_2, III) bacteria + material, IV) bacteria + material + H_2O_2 were treated without or with NIR laser (660 nm) irradiation for 10 min. All experiments were carried out according to the following procedure, after culturing at 37°C for 3 h, 100 μL of diluted bacterial suspension was taken out and evenly spread on the blood agar plates and placed at 37°C for 12 h. The antibacterial ability of the material was determined by the colonies that grew on

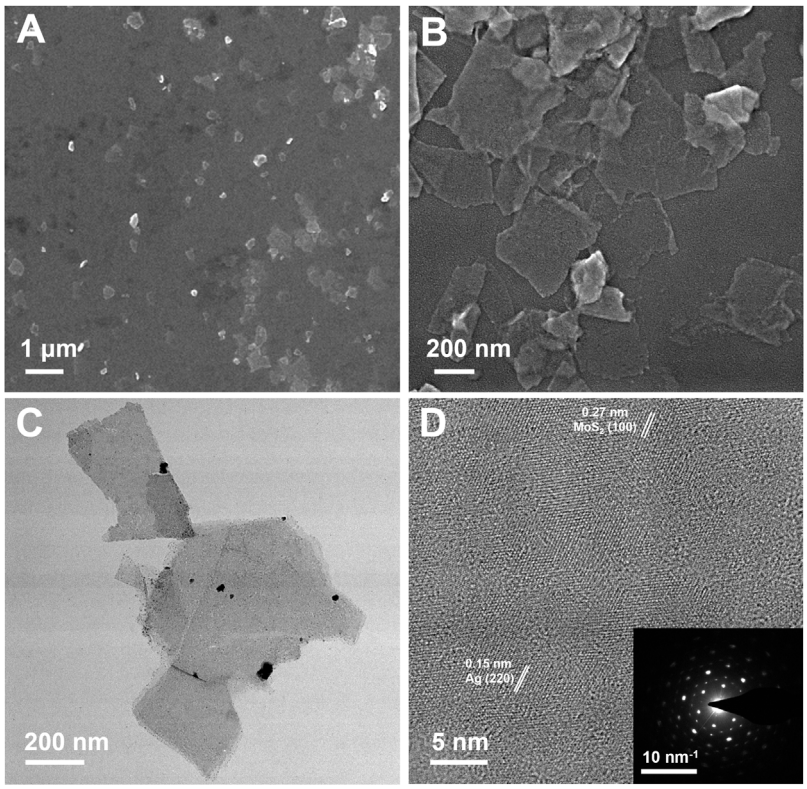

FIGURE 1
(A, B) SEM, **(C)** TEM, and **(D)** HR-TEM images of MoS_2/Ag3 nanosheets. Inset in **(D)** is the SAED pattern of MoS_2/Ag3 nanosheets.

the blood agar plates. Each experiment was conducted at least three times.

2.6.2 The cell viability of *S. aureus* assay

The premise of the test is that tetrazole is converted to blue crystalline methionine by the enzyme succinate dehydrogenase of live cells (Cheng et al., 2022). The percentage of living cells is proportional to the amount of blue-purple crystalline methionine produced. By using a microplate equipment to evaluate the optical density (OD_{600}) of various holes, the bacterial survival rate was examined by comparing the optical density data.

Briefly, MTT solution (10 μL, 5 mg/mL) was mixed with *S. aureus* treated with the material and hatched in a constant temperature incubator at 37°C for 4 h. The survival rate of *S. aureus* was obtained by detecting the value of optical-density at 600 nm for 0 and 4 h with a micropore meter.

2.6.3 Live/dead *S. aureus* staining experiment

SYTO™-9 is a green fluorescent nucleic acid dye that can penetrate cell membranes. PI is a nuclear stain that can penetrate the damaged cells, making the nucleus red. PBS or MoS_2/Ag3 nanosheets (30 μg/mL) were mixed with a suspension of *S. aureus* treated by laser or H_2O_2 (100 μM), respectively. After being exposed to a 660 nm laser for 10 min, the cells were placed in an incubator at a constant temperature for 3 h, and the combination was then incubated at ambient temperature for 15 min without illumination. The stained *S. aureus* suspension (10 μL) was put on a slide, covered with the coverslip, and the excess dye was removed. Finally, bacterial staining images were observed by using a fluorescence microscope.

2.6.4 Micromorphology of bacteria

S. aureus under different conditions were collected by centrifugation (4,000 rpm, 5 min). The *S. aureus* was fixed with 2.5% glutaraldehyde for 12 h and washed twice with PBS at room temperature. Next, the bacteria were treated with 10%, 25%, 50%, 75%, and 100% ethanol successively and gradually dehydrated for 15 min. For SEM observation, the final bacterial solution was dropped onto a silica substrate and sprayed with gold.

3 Results and discussion

3.1 Preparation and characterization of MoS_2/Ag NSs

The synthesis process of MoS_2/Ag nanosheets was schematically stated in Scheme 1. The MoS_2 nanosheets were fabricated and obtained according the previous procedure (Chen et al., 2022b). To load the silver nanoparticles (Ag NPs) onto the surface of MoS_2 nanosheets, $AgNO_3$ was first mixed with MoS_2 nanosheets solution

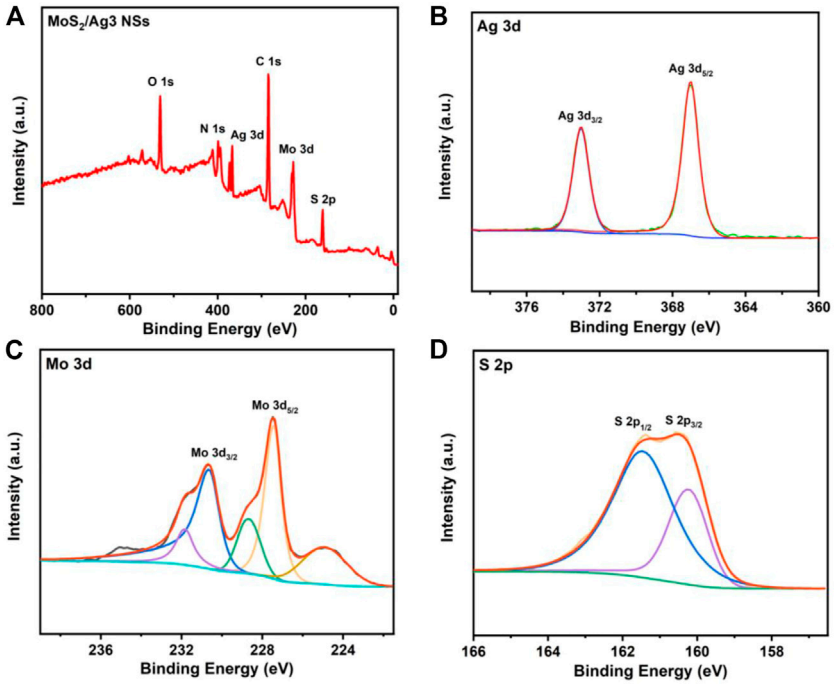

FIGURE 2
(A) X-ray photoelectron spectra of MoS_2/Ag3 NSs. **(B)** Ag 3d, **(C)** Mo 3d, and **(D)** S 2p spectra of MoS_2/Ag3 NSs.

and then reduced under the irradiation of a Xenon lamp, the highly dispersed Ag NPs could be obtained. The scanning electron microscope (SEM) images clearly showed that the MoS_2/Ag3 NSs exhibited the uniform nanosheet morphology with a size around 200–400 nm (Figures 1A, B). The TEM images disclosed that the Ag NPs were successfully dispersed on the surface of MoS_2 nanosheets (Figure 1C), and its high-resolution transmission electron microscopy (HRTEM) image (Figure 1D) further presented that the lattice fringes of 0.27 and 0.15 nm belonged to planes of MoS_2 (100) and Ag (220), respectively, indicating Ag NPs were successfully loaded onto the surface of nanosheets. Promisingly, the selected area electron diffraction (SAED) pattern of MoS_2/Ag3 NSs was characterized by the presence of bright diffraction spots with regular hexagon (inset of Figure 1D), signifying its single-crystalline nature.

Both the MoS_2 and MoS_2/Ag3 NSs were further characterized by X-ray photoelectron spectroscopy (XPS). The XPS survey spectra revealed the presence of six elements (C, N, O, S, Mo, and Ag) in MoS_2/Ag3 NSs (Figure 2A), while the MoS_2 nanosheets were found to lack the Ag element (Supplementary Figure S1A). Compared with the XPS Ag 3d spectrum of MoS_2 nanosheets (Supplementary Figure S1B), that of MoS_2/Ag3 NSs exhibited two distinct peaks at 372.98 eV and 366.98 eV corresponding to Ag $3d_{3/2}$ and Ag $3d_{5/2}$ of Ag (0) (Figure 2B) (Qiao et al., 2017; Li et al., 2022a), which indicated the fabrication of MoS_2/Ag NSs. As shown in Figure 2C, the high-resolution XPS Mo 3d spectrum of the MoS_2/Ag3 NSs given two main peaks at 230.68 eV and 227.48 eV, which belonged to Mo $3d_{3/2}$ and Mo $3d_{5/2}$ of Mo (IV), respectively (Chen et al., 2022a). The characteristic peaks at 161.38 eV and 160.48 eV (Figure 2D) originated from S $2p_{1/2}$ and S $2p_{3/2}$ of S (II) (Zhou et al., 2020), respectively. The UV-Vis absorption spectroscopy data (Supplementary Figure S2) were used to confirm that Ag NPs had been synthesized without structural alteration of MoS_2. Moreover, it was found that the augmentation of silver content had negligible effect on particle size and Zeta potential of MoS_2/Ag3 NSs (Supplementary Figure S3).

3.2 Antibacterial activity *in vitro*

As shown in Figure 3A, we evaluated the cytotoxicity of MoS_2/Ag NSs with the highest silver content (MoS_2/Ag3) by CCK-8 experiment in L929 cells. The viability of L929 cells was still higher than 85% after the treatment with MoS_2/Ag3 at the concentration of 50 μg/mL, showing that excellent biocompatibility and the great potential for *in vivo* and *in vitro* antibacterial applications.

Considering its great photodynamic performance and promising peroxidase-like ability (Supplementary Figure S4), the germproof capacity against *S. aureus* was further appraised by plate counting method. After co-incubation with the designed materials, it was found that the group of H_2O_2 or laser irradiation had a negligible antimicrobial effect against *S. aureus* (Figure 3B). Therefore, the optimal inhibitory concentration of all samples was determined under laser irradiation at the presence of H_2O_2. As presented in Figure 3B, the visual colony dramatically decreased with increasing concentrations of antibacterial agents, which showed the fascinating concentration-dependent bactericidal capacity. It was noting that the antibacterial effect was further enhanced with increasing density of Ag NPs (30 μg/mL),

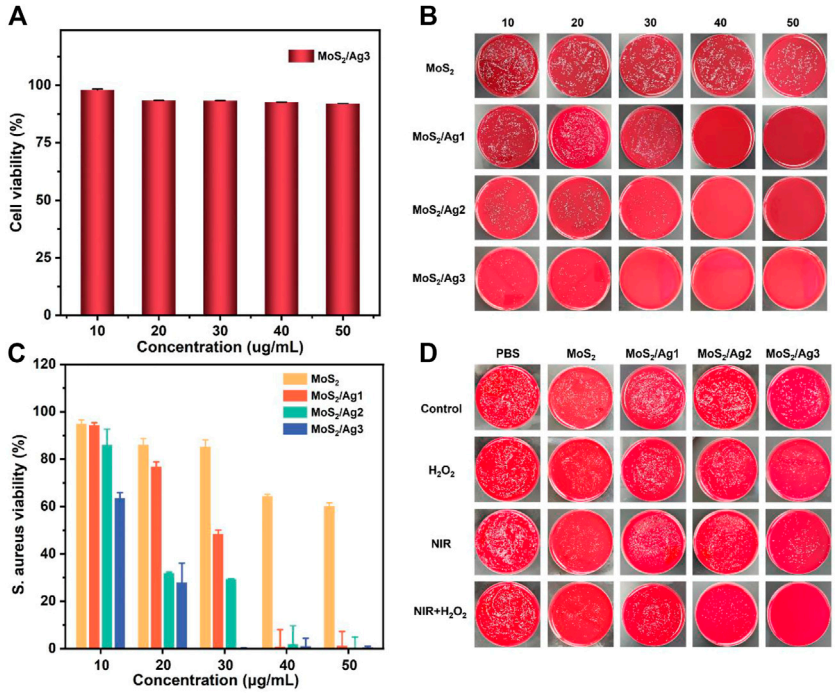

FIGURE 3
(A) Cell viability of L929 cells after treated with MoS_2/Ag3. **(B)** *S. aureus* bacterial colony development after treating with various doses of MoS_2, MoS_2/Ag1, MoS_2/Ag2, and MoS_2/Ag3, respectively. **(C)** Bacterial survival rate of *S. aureus* after treatment with several groups. All groups were treated with H_2O_2 (100 μM) under the 660 nm irradiation for 10 min (1 W/cm^2). **(D)** *S. aureus* bacterial colony development after treatment with different groups (PBS, MoS_2, MoS_2/Ag1, MoS_2/Ag2, MoS_2/Ag3) in the conditions of H_2O_2, NIR, NIR + H_2O_2, respectively.

implying that maybe more ROS were activated to grievously destroy the morphology of bacteria. The antibacterial properties of MoS_2 NSs were also determined in terms of MTT assay. The results demonstrated that only a survival rate of 0.12% was performed in the group of MoS_2/Ag3 with the concentration of 30 μg/mL, but obvious colonies were observed in other groups (Figures 3B, C). Interestingly, an impressive bactericidal effect against *S. aureus* was observed when the concentration of MoS_2/Ag nanosheets was raised.

In order to intuitively observe the inhibitory effect against *S. aureus* under irradiation of laser (660 nm) or in the presence of H_2O_2, we kept up with the plate-counting antibacterial experiment with MoS_2/Ag nanosheets at the concentration of 30 μg/mL. It has been reported that H_2O_2 (100 μM) together with near-infrared irradiation exhibited hardly inhibitory effect (Wei et al., 2021). Although the growth of microorganisms was not completely suppressed, H_2O_2 or laser irradiation had a more conspicuous antibacterial effect than only material in other groups (Figure 3D), suggesting that the ROS was insufficient to kill *S. aureus* at the current concentration. Following the combination of laser irradiation and H_2O_2 therapy, *S. aureus* survival rate continued to decline, indicating synergistically antibacterial capacity with regard to photodynamic therapy and peroxidase-like strategy (Li et al., 2020; Zhang et al., 2022a). Compared to the other groups, MoS_2/Ag3 exhibited the most robust antimicrobial ability and almost all bacteria were inactivated, demonstrating the antibacterial effectiveness might be improved with the addition of Ag. Thus, it could be speculated that the practical bactericidal process under irradiation was dominated by the synergistic impact of MoS_2 and Ag NPs to boost ROS formation.

MoS_2/Ag3 NSs (30 μg/mL) was utilized to carry out the live-dead bacteria staining experiment for the sake of investigating the antibacterial mechanism. All *S. aureus* could be stained by green fluorescence (SYTO™-9) and only damaged *S. aureus* presented red fluorescence (PI). Fluorescence images showed (Supplementary Figure S5) that membranes of *S. aureus* would not be destroyed in terms of free H_2O_2, NIR irradiation (10 min), or combination of H_2O_2 and NIR irradiation (10 min). Since the red fluorescence in the H_2O_2 condition only was practically identical to that of a single laser irradiation in Figure 4A, so it is almost harmless to conduct independent action. But the peroxidase-like activity of MoS_2/Ag3 NSs could kill off large numbers of bacteria in the presence of H_2O_2, implying that the synergistic effect made *S. aureus* unable to survive.

To further appraise the antimicrobic capacity of MoS_2/Ag3 NSs, surface morphologies of antibacterial with different treatment were detected by SEM. It was observed that the bacteria of the PBS group maintained a smooth and unbroken membrane, meanwhile the *S. aureus* treated by H_2O_2 or NIR revealed no evident difference with the PBS group, suggesting the intact structure of *S. aureus* (Figure 4B). However, obvious wrinkles and destruction of *S. aureus* were observed in the MoS_2/Ag3, MoS_2/Ag3 + H_2O_2, and MoS_2/Ag3 + NIR groups (Figure 4B). Promisingly, the bacterial membranes shrunk more seriously and even destroyed (signaled by yellow

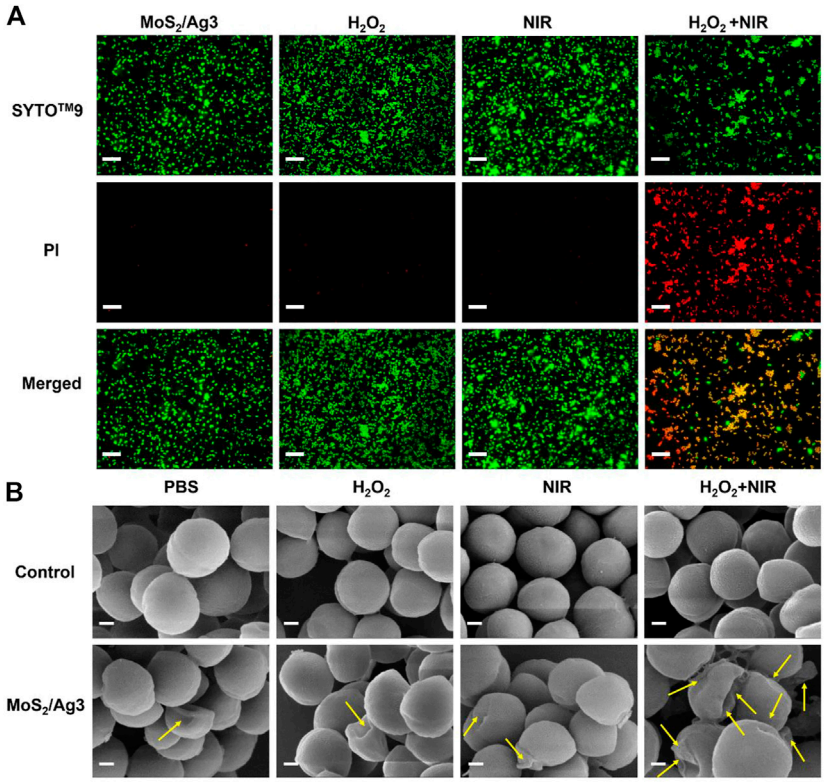

FIGURE 4
(A) Fluorescent images of *S. aureus* incubated with different conditions (MoS_2/Ag3 (30 μg/mL), MoS_2/Ag3 (30 μg/mL) + H_2O_2 (100 μM), MoS_2/Ag3 (30 μg/mL) + H_2O_2 (100 μM) + NIR (irradiation by a 660 nm laser with 1 W/cm^2 for 10 min), Scale bar: 5 μm. **(B)** SEM pictures of *S. aureus* after various treatments, Scale bar: 200 nm.

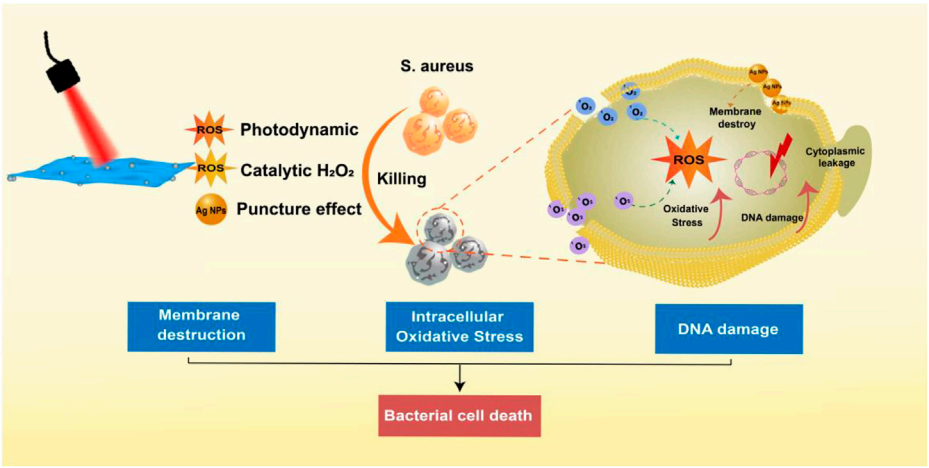

FIGURE 5
The multi-level synergistic antibacterial mechanism of MoS_2/Ag nanosheets.

arrows) in the MoS_2/Ag3 + H_2O_2 + NIR group (Figure 4B), which attributed to the ample ROS synergistically generated by the catalysis of MoS_2/Ag3 under the NIR laser irradiation in the presence of H_2O_2.

Inspired by the results of the *in vitro* antibacterial assays described above, we hypothesized a multi-level synergistic antibacterial mechanism (Figure 5). The sterilization mechanism of Ag NPs was mainly to puncture the cell membrane of their tiny size (Akter et al.,

2018). When irradiated by a 660 nm laser, the valence band electrons of MoS_2 were stimulated to change into the conduction band and produce electron-hole pairs (Zhu et al., 2020). Additionally, combining Ag NPs and MoS_2 could facilitate electron transport and prevent the compounding of electron-hole pairs, generating a significant amount of photoelectrons and holes (Ma et al., 2016). Virtually, the positively charged holes had a robust oxidability and could yield $^1O_2$ when reacted with oxygen (Karkhanechi et al., 2014; Zhang et al., 2020; Zhao et al., 2022a; Luo et al., 2022). Importantly, H_2O_2 could be catalyzed to produce ROS for the sake of the peroxidase-like ability of MoS_2 (Wang et al., 2016). As a result, when bacteria were exposed to near-infrared laser, the synergistic action assaulted the bacterial membrane, causing the bacterial metabolic barrier and ultimately causing bacterial mortality.

4 Conclusion

In conclusion, a facile artificial nanosheet of MoS_2/Ag was designed by a simple method for synergistic photodynamic and peroxidase-like catalytic antibacterial treatment. The developed MoS_2/Ag nanosheets may effectively inactivate bacteria by producing poisonous ROS supported to assault the membranes. Importantly, MoS_2/Ag3 nanosheets exhibited an antimicrobial efficiency of 99.88% against *S. aureus* within 10 min under 660 nm illumination in the presence of H_2O_2. Owing to the modification of PVP, the biocompatibility of MoS_2/Ag3 NSs was significantly improved. This particular type of photo-responsive material demonstrated prominent effectivity in antimicrobial treatment with minimal cytotoxicity, which could serve as a promising candidate of antibiotic-free treatment of bacterial infections.

Data availability statement

The original contributions presented in the study are included in the article/Supplementary Material, further inquiries can be directed to the corresponding authors.

Author contributions

ZZ and JL conceived and supervised the project. HC, XZ, BC, and HC performed all the experiments. MZ and JS wrote the manuscript. All authors read and approved the manuscript.

Funding

This work is supported by the National Natural Science Foundation of China (52173143 and 52102348), the China Postdoctoral Science Foundation (No. 2021M701113) and the Key Scientific Research Project of Higher Education of Henan Province (21A150003).

Conflict of interest

The authors declare that the research was conducted in the absence of any commercial or financial relationships that could be construed as a potential conflict of interest.

Publisher's note

All claims expressed in this article are solely those of the authors and do not necessarily represent those of their affiliated organizations, or those of the publisher, the editors and the reviewers. Any product that may be evaluated in this article, or claim that may be made by its manufacturer, is not guaranteed or endorsed by the publisher.

Supplementary material

The Supplementary Material for this article can be found online at: https://www.frontiersin.org/articles/10.3389/fchem.2023.1148354/full#supplementary-material

References

Akter, M., Sikder, M. T., Rahman, M. M., Ullah, A. A., Hossain, K. F. B., Banik, S., et al. (2018). A systematic review on silver nanoparticles-induced cytotoxicity: Physicochemical properties and perspectives. *J. Adv. Res.* 9, 1–16. doi:10.1016/j.jare.2017.10.008

Bakkeren, E., Diard, M., and Hardt, W. D. (2020). Evolutionary causes and consequences of bacterial antibiotic persistence. *Nat. Rev. Microbiol.* 18, 479–490. doi:10.1038/s41579-020-0378-z

Chauhan, M., Sharma, B., Kumar, R., Chaudhary, G. R., Hassan, A. A., and Kumar, S. (2019). Green synthesis of CuO nanomaterials and their proficient use for organic waste removal and antimicrobial application. *Environ. Res.* 168, 85–95. doi:10.1016/j.envres.2018.09.024

Chen, H., Guan, X., Liu, Q., Yang, L., Guo, J., Gao, F., et al. (2022a). Co-Assembled nanocarriers of de novo thiol-activated hydrogen sulfide donors with an RGDFF pentapeptide for targeted therapy of non-small-cell lung cancer. *ACS Appl. Mater Interfaces* 14, 53475–53490. doi:10.1021/acsami.2c14570

Chen, H., He, X., Zhou, Z., Wu, Z., Li, H., Peng, X., et al. (2022b). Metallic phase enabling MoS_2 nanosheets as an efficient sonosensitizer for photothermal-enhanced sonodynamic antibacterial therapy. *J. Nanobiotechnology* 20, 136. doi:10.1186/s12951-022-01344-6

Chen, H., Ji, P., Qi, Y., Chen, S. J., Wang, C. Y., Yang, Y. J., et al. (2023). Inactivation of *Pseudomonas aeruginosa* biofilms by thymoquinone in combination with nisin. *Front. Microbiol.* 13, 1029412. doi:10.3389/fmicb.2022.1029412

Chen, W., Chen, J., Li, L., Wang, X., Wei, Q., Ghiladi, R. A., et al. (2019). Wool/acrylic blended fabrics as next-generation photodynamic antimicrobial materials. *ACS Appl. Mater Interfaces* 11, 29557–29568. doi:10.1021/acsami.9b09625

Cheng, B., Cui, H., Zhang, N., Feng, H., Chu, D., et al. (2022). Antibiotic-free self-assembled polypeptide nanomicelles for bacterial keratitis. *ACS Appl. Polym. Mater* 4, 7250–7257. doi:10.1021/acsapm.2c01099

Fisher, R. A., Gollan, B., and Helaine, S. (2017). Persistent bacterial infections and persister cells. *Nat. Rev. Microbiol.* 15, 453–464. doi:10.1038/nrmicro.2017.42

Han, D., Ma, M., Han, Y., Cui, Z., Liang, Y., Liu, X., et al. (2020). Eco-friendly hybrids of carbon quantum dots modified MoS_2 for rapid microbial inactivation by strengthened photocatalysis. *ACS Sustain Chem. Eng.* 8, 534–542. doi:10.1021/acssuschemeng.9b06045

He, X., Dai, L., Ye, L., Sun, X., Enoch, O., Hu, R., et al. (2022a). A vehicle-free antimicrobial polymer hybrid gold nanoparticle as synergistically therapeutic platforms for *Staphylococcus aureus* infected wound healing. *Adv. Sci.* 9, 2105223. doi:10.1002/advs.202105223

He, X., Hou, J., Sun, X., Jangili, P., An, J., Qian, Y., et al. (2022b). NIR-II photo-amplified sonodynamic therapy using sodium molybdenum bronze nanoplatform against subcutaneous Staphylococcus aureus infection. *Adv. Funct. Mater* 32, 2203964. doi:10.1002/adfm.202203964

Hu, F., Gu, Z., Williams, G. R., Strimaite, M., Zha, J., Zhou, Z., et al. (2022b). Layered double hydroxide-based nanomaterials for biomedical applications. *Chem. Soc. Rev.* 51, 6126–6176. doi:10.1039/D2CS00236A

Hu, F., Song, B., Wang, X., Bao, S., Shang, S., Lv, S., et al. (2022a). Green rapid synthesis of Cu_2O/Ag heterojunctions exerting synergistic antibiosis. *Chin. Chem. Lett.* 33, 308–313. doi:10.1016/j.cclet.2021.07.018

Hu, T., Xue, B., Meng, F., Ma, L., Du, Y., Yu, S., et al. (2023). Preparation of 2D polyaniline/MoO_{3-x} superlattice nanosheets via intercalation-induced morphological transformation for efficient chemodynamic therapy. *Adv. Healthc. Mater* 22, e2202911. doi:10.1002/adhm.202202911

Huang, H., Zha, J., Li, S., and Tan, C. (2022). Two-dimensional alloyed transition metal dichalcogenide nanosheets: Synthesis and applications. *Chin. Chem. Lett.* 33, 163–176. doi:10.1016/j.cclet.2021.06.004

Jin, Y., Long, J., Ma, X., Zhou, T., Zhang, Z., Lin, H., et al. (2019). Synthesis of caged iodine-modified ZnO nanomaterials and study on their visible light photocatalytic antibacterial properties. *Appl. Catal. B Environ.* 256, 117873. doi:10.1016/j.apcatb.2019.117873

Karkhanechi, H., Takagi, R., and Matsuyama, H. (2014). Biofouling resistance of reverse osmosis membrane modified with polydopamine. *Desalination* 336, 87–96. doi:10.1016/j.desal.2013.12.033

Li, G., Lai, Z., and Shan, A. (2023a). Advances of antimicrobial peptide-based biomaterials for the treatment of bacterial infections. *Adv. Sci.* 2023, 2206602. doi:10.1002/advs.202206602

Li, G., Zhao, S., Wang, Z., and Li, F. (2023b). Controllable preparation of 2D V_2O_5 peroxidase-mimetic nanozyme to develop portable paper-based analytical device for intelligent pesticide assay. *Small* 2023, 2206465. doi:10.1002/smll.202206465

Li, Q., Hu, B., Yang, Q., Cai, X., Nie, M., Jin, Y., et al. (2020). Interaction mechanism between multi-layered MoS_2 and H_2O_2 for self-generation of reactive oxygen species. *Environ. Res.* 191, 110227. doi:10.1016/j.envres.2020.110227

Li, W., Thian, E. S., Wang, M., Wang, Z., and Ren, L. (2021). Surface design for antibacterial materials: From fundamentals to advanced strategies. *Adv. Sci.* 8, 2100368. doi:10.1002/advs.202100368

Li, X., Zhang, X., Xue, N., Li, J., Wu, T., Xu, Z., et al. (2022b). Hierarchical self-assembly of Ag-coordinated motifs on Ag (111). *Acta Phys. -Chim. Sin.* 38, 2011060. doi:10.3866/PKU.WHXB202011060

Li, X., Zhao, X., Chu, D., Zhu, X., Xue, B., Chen, H., et al. (2022a). Silver nanoparticle-decorated 2D Co-TCPP MOF nanosheets for synergistic photodynamic and silver ion antibacterial. *Surf. Interfaces* 33, 102247. doi:10.1016/j.surfin.2022.102247

Liu, C., Kong, D., Hsu, P-C., Yuan, H., Lee, H. W., Liu, Y., et al. (2016). Rapid water disinfection using vertically aligned MoS_2 nanofilms and visible light. *Nat. Nanotechnol.* 11, 1098–1104. doi:10.1038/nnano.2016.138

Liu, Y., Meng, X., and Bu, W. (2019). Upconversion-based photodynamic cancer therapy. *Coord. Chem. Rev.* 379, 82–98. doi:10.1016/j.ccr.2017.09.006

Luo, B., Li, X., Liu, P., Cui, M., Zhou, G., Long, J., et al. (2022). Self-assembled NIR-responsive MoS_2@quaternized chitosan/nanocellulose composite paper for recyclable antibacteria. *J. Hazard Mater* 434, 128896. doi:10.1016/j.jhazmat.2022.128896

Ma, S., Zhan, S., Jia, Y., Shi, Q., and Zhou, Q. (2016). Enhanced disinfection application of Ag-modified g-C_3N_4 composite under visible light. *Appl. Catal. B Environ.* 186, 77–87. doi:10.1016/j.apcatb.2015.12.051

Ning, S., Lin, H., Tong, Y., Zhang, X., Lin, Q., Zhang, Y., et al. (2017). Dual couples Bi metal depositing and Ag@AgI islanding on BiOI 3D architectures for synergistic bactericidal mechanism of *E. coli* under visible light. *Appl. Catal. B Environ.* 204, 1–10. doi:10.1016/j.apcatb.2016.11.006

Qi, B., Zhang, D., Liu, F-H., Qiao, Z. Y., and Wang, H. (2017). An "on-site transformation" strategy for treatment of bacterial infection. *Adv. Mater* 29, 1703461. doi:10.1002/adma.201703461

Qiao, X., Zhang, Z., Tian, F., Hou, D. F., and Li, D. S. (2017). Enhanced catalytic reduction of p-nitrophenol on ultrathin MoS_2 nanosheets decorated with noble metal nanoparticles. *Cryst. Growth Des.* 17, 3538–3547. doi:10.1021/acs.cgd.7b00474

Raza, F., Yim, D., Park, J. H., Kim, H. I., Jeon, S. J., and Kim, J. H. (2017). Structuring Pd nanoparticles on 2H-WS_2 nanosheets induces excellent photocatalytic activity for cross-coupling reactions under visible light. *J. Am. Chem. Soc.* 139, 14767–14774. doi:10.1021/jacs.7b08619

Roope, S. J., Smith, R. D., Pouwels, K. B., Buchanan, J., Abel, L., Eibich, P., et al. (2019). The challenge of antimicrobial resistance: What economics can contribute. *Science* 364, eaau4679. doi:10.1126/science.aau4679

Sethulekshmi, A. S., Saritha, A., Joseph, K., Aprem, A. S., and Sisupal, S. B. (2022). MoS_2 based nanomaterials: Advanced antibacterial agents for future. *J. Control. Release* 348, 158–185. doi:10.1016/j.jconrel.2022.05.047

Wang, X., Nakamoto, T., Dulińska-Molak, I., Kawazoe, N., and Chen, G. (2016). Regulating the stemness of mesenchymal stem cells by tuning micropattern features. *J. Mater Chem. B* 4, 37–45. doi:10.1039/C5TB02215K

Wei, F., Cui, X., Wang, Z., Dong, C., Li, J., and Han, X. (2021). Recoverable peroxidase-like Fe_3O_4@MoS_2-Ag nanozyme with enhanced antibacterial ability. *Chem. Eng. J.* 408, 127240. doi:10.1016/j.cej.2020.127240

Wu, K., Li, X., Wang, W., Huang, Y., and Jiang, Q. (2022). Creating edge sites within the basal plane of a MoS_2 catalyst for substantially enhanced hydrodeoxygenation activity. *ACS Catal.* 12, 8–17. doi:10.1021/acscatal.1c03669

Xia, D., Shen, Z., Huang, G., Wang, W., Yu, J. C., and Wong, P. K. (2015). Red phosphorus: An earth-abundant elemental photocatalyst for "green" bacterial inactivation under visible light. *Environ. Sci. Technol.* 49, 6264–6273. doi:10.1021/acs.est.5b00531

Xiu, W., Wan, L., Yang, K., Li, X., Yuwen, L., Dong, H., et al. (2022). Potentiating hypoxic microenvironment for antibiotic activation by photodynamic therapy to combat bacterial biofilm infections. *Nat. Commun.* 13, 3875. doi:10.1038/s41467-022-31479-x

Xue, B., Geng, X., Cui, H., Chen, H., Wu, Z., Chen, H., et al. (2023). Size engineering of 2D MOF nanosheets for enhanced photodynamic antimicrobial therapy. *Chin. Chem. Lett.* 2023, 108140. doi:10.1016/j.cclet.2023.108140

Yadav, V., Roy, S., Singh, P., Khan, Z., and Jaiswal, A. (2019). 2D MoS_2-based nanomaterials for therapeutic, bioimaging, and biosensing applications. *Small* 15, 1803706. doi:10.1002/smll.201803706

Yang, C., Chen, Y., Guo, W., Gao, Y., Song, C., Zhang, Q., et al. (2018). Bismuth ferrite-based nanoplatform design: An ablation mechanism study of solid tumor and NIR-triggered photothermal/photodynamic combination cancer therapy. *Adv. Funct. Mater* 28, 1706827. doi:10.1002/adfm.201706827

Zhang, H., Deng, L., Chen, J., Zhang, Y., Liu, M., Han, Y., et al. (2022a). How MoS_2 assisted sulfur vacancies featured Cu_2S in hollow Cu_2S@MoS_2 nanoboxes to activate H_2O_2 for efficient sulfadiazine degradation? *Chem. Eng. J.* 446, 137364. doi:10.1016/j.cej.2022.137364

Zhang, H., Jia, Q., Yue, Z., Huo, J., Chai, J., Yu, L., et al. (2022b). An electroluminodynamic flexible device for highly efficient eradication of drug-resistant bacteria. *Adv. Mater* 34, 2200334. doi:10.1002/adma.202200334

Zhang, L., Cheng, Q., Li, C., Zeng, X., and Zhang, X. Z. (2020). Near infrared light-triggered metal ion and photodynamic therapy based on AgNPs/porphyrinic MOFs for tumors and pathogens elimination. *Biomaterials* 248, 120029. doi:10.1016/j.biomaterials.2020.120029

Zhang, X., Wu, J., Williams, G. R., Yang, Y., Niu, S., Qian, Q., et al. (2019a). Dual-responsive molybdenum disulfide/copper sulfide-based delivery systems for enhanced chemo-photothermal therapy. *J. Colloid Interface Sci.* 539, 433–441. doi:10.1016/j.jcis.2018.12.072

Zhao, K., Gu, W., Zheng, S., Zhang, C., and Xian, Y. (2015). SDS–MoS_2 nanoparticles as highly-efficient peroxidase mimetics for colorimetric detection of H_2O_2 and glucose. *Talanta* 141, 47–52. doi:10.1016/j.talanta.2015.03.055

Zhao, M., He, X., Hou, A., Cheng, C., Wang, X., Yue, Y., et al. (2022b). Growth of Cu_2O nanoparticles on two-dimensional Zr–Ferrocene–Metal–Organic framework nanosheets for photothermally enhanced chemodynamic antibacterial therapy. *Inorg. Chem.* 61, 9328–9338. doi:10.1021/acs.inorgchem.2c01091

Zhao, M., Yang, R., Wei, Y., Su, J., Wang, X., Zhang, N., et al. (2022a). Dual isolated bimetal single-atom catalysts for tumor ROS cycle and parallel catalytic therapy. *Nano Today* 44, 101493. doi:10.1016/j.nantod.2022.101493

Zhao, X., Qiu, H., Shao, Y., Wang, P., Yu, S., Li, H., et al. (2023). Silver nanoparticle-modified 2D MOF nanosheets for photothermally enhanced silver ion release antibacterial treatment. *Acta phys.-chim. Sin.* 39, 2211043. doi:10.3866/PKU.WHXB202211043

Zhou, Z., Li, B., Shen, C., Wu, D., Fan, H., Zhao, J., et al. (2020). Metallic 1T phase enabling MoS_2 nanodots as an efficient agent for photoacoustic imaging guided photothermal therapy in the near-infrared-II window. *Small* 16, 2004173. doi:10.1002/smll.202004173

Zhou, Z., Li, X., Hu, T., Xue, B., and Chen, H. (2022a). Molybdenum-based nanomaterials for photothermal cancer therapy. *Adv. NanoBiomed Res.* 2, 2200065. doi:10.1002/anbr.202200065

Zhou, Z., Wang, Y., Peng, F., Meng, F., Zha, J., Ma, L., et al. (2022b). Intercalation-activated layered MoO_3 nanobelts as biodegradable nanozymes for tumor-specific photo-enhanced catalytic therapy. *Angew. Chem. Int. Ed.* 61, e202115939. doi:10.1002/anie.202115939

Zhu, M., Liu, X., Tan, L., Cui, Z., Liang, Y., Li, Z., et al. (2020). Photo-responsive chitosan/Ag/MoS_2 for rapid bacteria-killing. *J. Hazard Mater* 383, 121122. doi:10.1016/j.jhazmat.2019.121122

Frontiers in Chemistry

Explores all fields of chemical science across the periodic table

Advances our understanding of how atoms, ions, and molecules come together and come apart. It explores the role of chemistry in our everyday lives - from electronic devices to health and wellbeing.

Discover the latest Research Topics

See more →

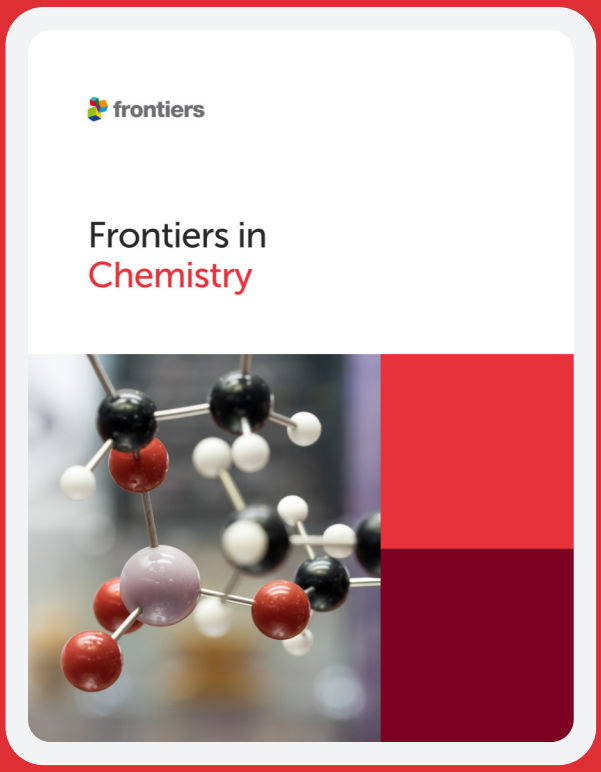

Frontiers

Avenue du Tribunal-Fédéral 34
1005 Lausanne, Switzerland
frontiersin.org

Contact us

+41 (0)21 510 17 00
frontiersin.org/about/contact